

# **Analysis of Repaired/Strengthened R.C. Structures Using Composite Materials: Punching Shear**

A thesis submitted to The University of Manchester for the  
degree of Doctor of Philosophy in the Faculty of  
Engineering and Physical Sciences

**2010**

**AHMAD MAHMOUD ABDULLAH**

**SCHOOL OF MECHANICAL, AEROSPACE AND CIVIL  
ENGINEERING**

# Table of content

<b>TABLE OF CONTENT .....</b>	<b>2</b>
<b>LIST OF FIGURES .....</b>	<b>6</b>
<b>LIST OF TABLES .....</b>	<b>12</b>
<b>ABSTRACT .....</b>	<b>13</b>
<b>DECLARATION.....</b>	<b>14</b>
<b>COPYRIGHT STATEMENT .....</b>	<b>15</b>
<b>ACKNOWLEDGEMENTS.....</b>	<b>16</b>
<b>NOTATION .....</b>	<b>17</b>
<b><u>CHAPTER 1 INTRODUCTION .....</u></b>	<b><u>19</u></b>
1.1. INTRODUCTION .....	19
1.2. RESEARCH OBJECTIVES.....	21
1.3. OUTLINE OF THE THESIS .....	22
<b><u>CHAPTER 2 LITERATURE REVIEW .....</u></b>	<b><u>24</u></b>
2.1. INTRODUCTION .....	24
2.2. PUNCHING SHEAR BEHAVIOUR OF RC SLABS .....	24
2.2.1. PARAMETERS INFLUENCING PUNCHING SHEAR STRENGTH OF COLUMN-SLAB CONNECTIONS.....	29
2.2.1.1. Concrete strength .....	29
2.2.1.2. Flexural and compression reinforcement.....	30
2.2.1.2.1. Strength and ratio of flexural reinforcement .....	30
2.2.1.2.2. Pattern of flexural reinforcement .....	33
2.2.1.2.3. Arrangement of flexural reinforcement.....	33
2.2.1.2.4. Compression reinforcement.....	35
2.2.1.3. Shear reinforcement .....	35
2.2.1.4. In plane restraints .....	39
2.2.1.5. Size and shape of loaded area .....	40
2.2.1.6. Size effect (span-depth ratio and aggregate size) .....	42
2.3. PUNCHING SHEAR STRENGTHENING OF SLABS WITH FRP .....	43
2.3.1. DIRECT SHEAR STRENGTHENING .....	44
2.3.2. INDIRECT (FLEXURAL) SHEAR STRENGTHENING.....	46
2.3.2.1. Prestressed composites for external reinforcement.....	54
2.4. FAILURE MODES OF SLABS STRENGTHENING WITH FRP .....	55
2.4.1. FULL COMPOSITE ACTION FAILURE MODES .....	55
2.4.2. LOSS OF COMPOSITE ACTION FAILURE MODES .....	57
2.4.2.1. Debonding failure mode .....	57
2.4.2.2. Peeling-off failure mode.....	59
2.4.2.3. Code provisions to maintain composite action .....	60
2.4.2.3.1. ACI.....	60
2.4.2.3.2. CEB-FIB Bulletin No.14.....	61

2.5. BOND BEHAVIOUR OF FRP-CONCRETE INTERFACES .....	61
2.5.1. BOND-SLIP RELATIONSHIP .....	63
2.6. PUNCHING SHEAR ANALYSIS OF RC FLAT SLABS STRENGTHENED WITH EBR ....	66
2.6.1. CLASSICAL ANALYSIS APPROACHES.....	67
2.6.1.1. Yield line model by Rankin and Long .....	68
2.6.1.2. Modified Rankin and Long model by Ebead and Marzouk .....	69
2.6.1.3. Critical shear crack model .....	70
2.6.1.4. Analytical model by Menetrey.....	70
2.6.1.5. Enhancements to Menetrey's model.....	72
2.7. TREATMENT OF PUNCHING SHEAR IN CODES OF PRACTICE .....	74
2.7.1.1. Eurocode 2 and CEB-FIB model code 1990.....	75
2.7.1.2. British Standard BS 8110 .....	76
2.7.1.3. American code ACI 318-05 .....	78
2.8. CONCLUSION .....	79

### **CHAPTER 3 EXPERIMENTAL PROGRAMME.....81**

3.1. INTRODUCTION .....	81
3.2. STRUCTURAL TESTS.....	81
3.2.1. DETAILS OF TEST SPECIMEN .....	83
3.2.2. EXPERIMENTAL PARAMETERS .....	83
3.2.3. PREPARATION METHOD .....	84
3.2.3.1. Mould.....	84
3.2.3.2. Reinforcement.....	85
3.2.3.3. Casting and curing.....	86
3.2.4. APPLICATION OF PRESTRESSING TECHNIQUE.....	87
3.2.4.1. Description of prestressing Device .....	87
3.2.4.2. Surface preparation and bonding process .....	93
3.2.4.3. Application of plate prestress.....	94
3.2.5. INSTRUMENTATION .....	97
3.2.5.1. Strain gauges .....	97
3.2.5.2. Linear potentiometer (pots) .....	100
3.2.6. TEST SETUP .....	100
3.2.7. PRE-TEST PREPARATION .....	103
3.2.8. TESTING PROCEDURE .....	103
3.3. MATERIALS.....	104
3.3.1. CONCRETE .....	104
3.3.2. REINFORCEMENT.....	107
3.3.2.1. FRP plate reinforcement.....	107
3.3.2.2. Steel reinforcement .....	110

### **CHAPTER 4 EXPERIMENTAL RESULTS AND DISCUSSION .....112**

4.1. INTRODUCTION .....	112
4.2. EXPERIMENTAL DATA.....	112
4.2.1. MODES OF FAILURE AND LOAD CAPACITY .....	113
4.2.2. LOAD-DEFLECTION CHARACTERISTICS .....	119
4.2.3. STRAIN MEASUREMENTS .....	121
4.2.3.1. Steel reinforcement .....	121

4.2.3.2. FRP reinforcement .....	123
4.2.3.3. Concrete .....	125
4.2.4. CRACK WIDTH .....	127
4.3. ANALYSIS OF TEST RESULTS .....	128
4.3.1. ROTATION CAPACITY .....	129
4.3.2. STIFFNESS CHARACTERISTICS .....	132
4.3.3. ENERGY ABSORPTION CHARACTERISTICS .....	132
4.3.4. ULTIMATE PUNCHING LOADS .....	133
4.3.4.1. Comparison with design codes .....	134
4.4. CONCLUSION .....	136

## **CHAPTER 5 NUMERICAL MODELLING .....**137

5.1. INTRODUCTION .....	137
5.2. FINITE ELEMENT ANALYSIS .....	137
5.3. SLAB MODELLING TECHNIQUES .....	139
5.3.1. MESHING ELEMENTS .....	140
5.3.1.1. Solid element .....	140
5.3.1.2. Truss element .....	142
5.3.1.3. Shell element .....	142
5.3.1.4. Connector (spring) element .....	143
5.3.1.5. Rigid element .....	144
5.4. MATERIAL MODELS .....	145
5.4.1. STEEL REINFORCEMENT .....	145
5.4.2. FRP REINFORCEMENT .....	145
5.4.3. CONCRETE .....	148
5.4.3.1. Failure criteria of concrete .....	151
5.4.3.1.1. Flow rule .....	153
5.4.3.2. Compressive behaviour of concrete .....	154
5.4.3.3. Post-cracking behaviour .....	155
5.4.3.3.1. Uniaxial tensile behaviour .....	155
5.4.3.3.2. Behaviour of rough cracks under mixed-mode loading .....	159
5.4.4. INTERNAL REINFORCEMENT-CONCRETE INTERACTION .....	161
5.4.4.1. Tension stiffening .....	161
5.4.4.2. Dowel action .....	164
5.4.5. FRP-CONCRETE INTERFACE .....	165
5.4.5.1. Failure Criteria .....	166
5.4.5.2. Damage evolution .....	166
5.4.6. NONLINEAR SOLUTION .....	167
5.4.6.1. Analysis procedure .....	167
5.4.6.2. Steps, increments, and iterations .....	168
5.5. INVESTIGATION OF MODEL PARAMETERS .....	170
5.5.1. DESCRIPTION OF SLAB MODEL .....	171
5.5.2. MESH SIZE .....	172
5.5.3. EFFECT OF CONCRETE TENSILE STRENGTH .....	174
5.5.4. EFFECT OF TENSION STIFFENING CURVE .....	175
5.5.5. EFFECT OF INTERFACIAL PARAMETERS .....	178
5.5.5.1. Effect of interfacial bond stiffness $K_s$ .....	180
5.5.5.2. Effect of interfacial bond strength $\tau_s$ .....	181

5.5.5.3. Effect of interfacial fracture Energy $G_s$ .....	182
5.5.6. CONCLUSION .....	184

## **CHAPTER 6 DISCUSSION ON NUMERICAL RESULTS AND CODE PROVISIONS.....185**

6.1. INTRODUCTION .....	185
6.2. NON-PRESTRESSED SLAB (RS- $F_0$ ) .....	186
6.2.1. LOAD-DEFLECTION RESPONSE .....	186
6.2.2. REINFORCEMENT STRAINS.....	187
6.2.2.1. Internal steel reinforcement .....	187
6.2.2.2. FRP reinforcement .....	189
6.2.3. CONCRETE STRAINS .....	193
6.2.4. FRP-CONCRETE INTERFACIAL BEHAVIOUR .....	194
6.2.5. CRACK PATTERN .....	197
6.2.6. CRACK OPENING DISPLACEMENT .....	198
6.2.7. ULTIMATE LOAD AND FAILURE MODE .....	199
6.2.8. CONCLUSION .....	201
6.3. PRESTRESSED SLABS .....	202
6.3.1. LOAD-DEFLECTION RESPONSE .....	202
6.3.2. REINFORCEMENT STRAINS.....	205
6.3.2.1. Internal steel reinforcement .....	205
6.3.2.2. FRP reinforcement .....	207
6.3.3. CONCRETE STRAINS .....	210
6.3.4. FRP-CONCRETE INTERFACIAL BEHAVIOUR .....	212
6.3.5. CRACK PATTERN .....	216
6.3.6. CRACK OPENING DISPLACEMENT .....	219
6.3.7. ULTIMATE LOAD AND FAILURE MODE .....	220
6.3.8. CONCLUSION .....	221

## **CHAPTER 7 CONCLUSION AND RECOMMENDATIONS.....223**

7.1. INTRODUCTION .....	223
7.2. PUNCHING SHEAR BEHAVIOUR OF FRP STRENGTHENED SLABS .....	224
7.2.1. LOAD-DEFLECTION RESPONSE .....	224
7.2.2. STEEL STRAIN .....	225
7.2.3. FRP STRAIN.....	225
7.2.4. CONCRETE STRAIN .....	226
7.2.5. CRACKING .....	226
7.2.6. MODE OF FAILURE AND ULTIMATE CAPACITY .....	227
7.3. PRACTICAL SIGNIFICANCE OF THE STUDY.....	228
7.4. RECOMMENDATIONS AND FUTURE WORK.....	228
REFERENCES .....	230
APPENDIX A .....	235
APPENDIX B .....	250

Word count is 53,309 words

## List of figures

Figure 1-1: Flat slab Structure.....	19
Figure 1-2: Schematic diagram for application of FRP in civil engineering. ....	20
Figure 2-1: Typical punching shear failure [24]. ....	25
Figure 2-2: Effect of flexural reinforcement ratio on load-deflection response; Criswell [25]. ....	26
Figure 2-3: Slab deflection during punching test; Test results of slab PG-3 by Muttoni et al. [26]. ....	27
Figure 2-4: Radial and tangential strains at surface; Test results of slab PG-3 by Muttoni et al [26]. ....	28
Figure 2-5: Vertical strains distribution at column faces according to Moe [17].	28
Figure 2-6: Interaction between shearing and flexural strength according to Moe [17]. ....	31
Figure 2-7: Dowel action effect of reinforcement; CEB-FIB [20]. ....	32
Figure 2-8: Concentration of flexural reinforcement. ....	34
Figure 2-9: Prestressed shear bolts for slab under vertical load [39]. ....	36
Figure 2-10: Strengthening mechanism used by Ebead and Marzouk [38]. ....	38
Figure 2-11: Compressive membrane action .....	40
Figure 2-12: Concrete strain on column sides of aspect ratio=3 [45]. ....	41
Figure 2-13: Influence of effective depth on nominal shear strength [44]. ....	42
Figure 2-14: Effect of span-depth ratio on punching shear strength [47]. ....	43
Figure 2-15: Strengthening patterns according to Sissakis and Sheikh [48]. ....	44
Figure 2-16: Load deformation curves of strengthened slabs according to Sissakis and Sheikh [48]. ....	45
Figure 2-17: Strengthening pattern and details (plan view) [15]. ....	46
Figure 2-18: Dimension and details of reinforced specimen [53]. ....	48
Figure 2-19: Specimen dimension and reinforcement details [55]. ....	52
Figure 2-20: Failure modes of full composite action.....	56
Figure 2-21: Debonding Failure modes.....	58
Figure 2-22: Flexural shear peeling-off failure mode.....	60
Figure 2-23: Schematic diagram of single shear lap test. ....	62

Figure 2-24: Distribution of shear stress along the bond length according to Zilch et al., cited in [11].	62
Figure 2-25: Comparison of bond–slip relations for the EBR and steel rebars.	64
Figure 2-26: Comparison of bond-slip curves available in literature; quoted from Lu et al. [63].	66
Figure 2-27: Yield line crack pattern according to Rankin and Long [43].	68
Figure 2-28: Representation of punching strength of reinforced slab [66].	71
Figure 2-29: Critical perimeter of slab reinforced by composite strip.	73
Figure 2-30: Basic control perimeter according to Eurocode 2 [21].	76
Figure 2-31: Shear perimeter according to BS 8110 [22].	77
Figure 3-1: Layout, and geometric and reinforcement details of test slabs.	82
Figure 3-2: The slab mould showing crack inducer.	85
Figure 3-3: Column-slab reinforcement paced in mould.	86
Figure 3-4: Casting and cubes' preparation process.	87
Figure 3-5: Prestress device.	89
Figure 3-6: Clamping mechanism.	90
Figure 3-7: Mises-stress plot for the clamping mechanism.	91
Figure 3-8: Plate end assembly according to Quantrill and Hollaway [5].	92
Figure 3-9: Failure pattern of FRP plate connection according to [5].	92
Figure 3-10: Section through anchor plate arrangement (part B).	93
Figure 3-11: Frame used for plate prestressing.	95
Figure 3-12: Arrangement of steel strain gauges over a specimen.	97
Figure 3-13: Arrangement of FRP strain gauges.	98
Figure 3-14: Concrete strain gauges glued to concrete surface around column. .....	99
Figure 3-15: Arrangement of pots over specimen and around induced crack.	101
Figure 3-16: Test setup	102
Figure 3-17: Concrete cub and cylinder tests.	105
Figure 3-18: Test for concrete compressive modulus of elasticity.	106
Figure 3-19: Stress strain curve for concrete.	107
Figure 3-20: Instrumentation of FRP plate in tensile test.	108
Figure 3-21: Typical FRP stress-strain curve.	109
Figure 3-22: Failure of FRP plate in tension.	110

Figure 3-23: Stress-strain curve of 12-mm steel reinforcement. ....	111
Figure 4-1: Crack pattern of slab RS <sub>0</sub> after failure .....	113
Figure 4-2: Crack pattern of slab RS-F <sub>0</sub> after failure. ....	114
Figure 4-3: Comparison of the peeling effect in non-prestressed and prestressed slabs. ....	115
Figure 4-4: Crack pattern of slab RS-F <sub>15</sub> after failure.....	116
Figure 4-5: Crack pattern of slab RS-F <sub>30</sub> after failure.....	116
Figure 4-6: Crack pattern of slab RS-F <sub>30F</sub> after failure. ....	117
Figure 4-7: Load-central deflection of the test slabs. ....	120
Figure 4-8: Load-strain relationship for the internal steel reinforcement. ....	122
Figure 4-9: Profile of steel strain at failure. ....	123
Figure 4-10: Load-strain relationship for FRP reinforcement. ....	124
Figure 4-11: Strain profile of FRP plate for slab (RS-F <sub>15</sub> ).....	125
Figure 4-12: Load-radial strain relationship for concrete at position SGV <sub>1</sub> .....	126
Figure 4-13: Load-radial and tangential strain relationships for slab (RS-F <sub>15</sub> ). ..	127
Figure 4-14: Average horizontal and vertical crack opening displacement of slab (RS <sub>0</sub> ).....	128
Figure 4-15: Deflection profile of slab RS <sub>0</sub> along the centre line. ....	129
Figure 4-16: Deflection profile of slab RS-F <sub>0</sub> along the centre line.....	130
Figure 4-17: Deflection profile of slab RS-F <sub>15</sub> along the centre line. ....	130
Figure 4-18: Deflection profile of slab RS-F <sub>30</sub> along the centre line. ....	131
Figure 4-19: Load-rotation curves of the test slabs. ....	132
Figure 4-20: Load comparison of test slabs. ....	134
Figure 5-1: First-order brick element.....	141
Figure 5-2: Truss element AB embedded in solid element; node A is constrained to edge 1-4 and node B is constrained to face 2-6-7-3. .....	142
Figure 5-3: 4-node doubly curved general-purpose shell element. ....	143
Figure 5-4: Two-node connector element (CONN3D2).....	144
Figure 5-5: Four-node, bilinear quadrilateral rigid surface element.....	144
Figure 5-6: Schematic of FRP composites.....	146
Figure 5-7: Tsai-Hill failure envelope ( $I_F = 1$ ). ....	148



Figure 5-8: Load-deflection curve for comparison of smeared cracking and damaged plasticity models. ....	150
Figure 5-9: Yield surface in deviatoric plane with different values of $K_c$ . ....	152
Figure 5-10: Flow potentials in p-q plane. ....	154
Figure 5-11: Uniaxial stress-strain curve for concrete. ....	155
Figure 5-12: Postfailure tensile behaviour: (a) stress-strain approach; (b) fracture energy approach. ....	156
Figure 5-13: Stress-displacement curve and different cracking stages. ....	157
Figure 5-14: Common tension softening curves of concrete. ....	158
Figure 5-15: Concept of tension-softening and shear-transfer relations in $(\delta_n, \delta_t)$ plane: (a) tension-softening relations; and (b) shear-transfer relations. ....	159
Figure 5-16: Feasible domain for the normal and tangential stresses in $(\delta_n, \delta_t)$ ... plane according to Bazant and Gambarova [87]. ....	160
Figure 5-17: Load transfer from steel to concrete between adjacent cracks. ....	162
Figure 5-18: Concrete tension stiffening model according to Scanlon [90]. ....	163
Figure 5-19: Idealized load-strain curve for RC tension tie according to CEB-FIP Model Code 1990 [20]. ....	164
Figure 5-20: FRP-concrete interfacial stress-slip model. ....	167
Figure 5-21: Newton-Raphson iterative solution (2 load increments). ....	170
Figure 5-22: Slab model; FRP reinforcement has been shifted down for clarity purposes. ....	171
Figure 5-23: Mesh sensitivity of slab RS <sub>0</sub> . ....	173
Figure 5-24: Mesh sensitivity of slab RS-F <sub>0</sub> . ....	174
Figure 5-25: Load-deflection curve of slab RS <sub>0</sub> for different values of concrete tensile strength. ....	175
Figure 5-26: Load-deflection curve of slab RS <sub>0</sub> with different tension stiffening models. ....	176
Figure 5-27: Stabilization energy consumed compared to the total strain energy for slab (RS <sub>0</sub> ). ....	177
Figure 5-28: Interface normal stress condition inside and outside the truncated cone; results from slab (RS-F <sub>15</sub> ). ....	179

Figure 5-29: Effect of interfacial bond stiffness on the load-deflection behaviour.	180
Figure 5-30: Effect of interfacial bond strength on the load-deflection behaviour.	181
Figure 5-31: Effect of interfacial bond strength on FRP strain distribution. ....	182
Figure 5-32: Effect of interfacial fracture energy on the load-deflection behaviour.....	183
Figure 5-33: Effect of interfacial fracture energy on FRP strain distribution. ...	183
Figure 6-1: Comparison between experimental and model prediction for non-prestressed slab (RS-F <sub>0</sub> ). ....	186
Figure 6-2: Behaviour of slabs with low reinforcement ratios; (a) deformation shape; (b) distribution of radial curvature along the radius of the slab.....	187
Figure 6-3: Steel reinforcement strain for slab (RS-F <sub>0</sub> ) at different locations. .	188
Figure 6-4: Measurement and prediction of FRP strain for Slab (RS-F <sub>0</sub> ). ....	190
Figure 6-5: Flexural shear crack induced debonding; (a) schematic diagram for crack; (b) slip field at interface element; (c) interfacial shear stress distribution at crack. ....	191
Figure 6-6: Radial and tangential concrete strains for slab (RS-F <sub>0</sub> ) at positions SGV <sub>1</sub> and SGH <sub>1</sub> , respectively.....	193
Figure 6-7: FRP-concrete interfacial behaviour of slab (RS-F <sub>0</sub> ): (a) before yielding; (b) after yielding.....	195
Figure 6-8: Crack pattern of slab (RS-F <sub>0</sub> ) at load level 372.7 kN. ....	198
Figure 6-9: Load-CMOD obtained at distance 1.5d from the column face along the centreline of the slab. ....	199
Figure 6-10: Comparison between experimental and model prediction for prestressed slab (RS-F <sub>15</sub> ). ....	203
Figure 6-11: Comparison between experimental and model prediction for prestressed slab (RS-F <sub>30</sub> ). ....	203
Figure 6-12: Comparison between experimental and model prediction for prestressed slab (RS-F <sub>30F</sub> ). ....	204
Figure 6-13: Steel reinforcement strain for prestressed slabs at different locations: (a) slab (RS-F <sub>15</sub> ); (b) slab (RS-F <sub>30</sub> ). ....	206
Figure 6-14: Measurement and prediction of FRP strain for Slab (RS-F <sub>15</sub> ). ....	208

Figure 6-15: Measurement and prediction of FRP strain for Slab (RS-F <sub>30</sub> ).....	209
Figure 6-16: Radial and tangential concrete strains for slab (RS-F <sub>15</sub> ) at positions SGCV <sub>1</sub> and SGCH <sub>4</sub> , respectively. ....	211
Figure 6-17: Radial and tangential concrete strains for slab (RS-F <sub>30</sub> ) at positions SGCV <sub>4</sub> and SGCH <sub>2</sub> , respectively. ....	211
Figure 6-18: FRP-concrete interfacial behaviour of slab (RS-F <sub>15</sub> ): (a) before cracking; (b) later stages of loading.....	214
Figure 6-19: FRP-concrete interfacial behaviour of slab (RS-F <sub>30</sub> ): (a) before cracking; (b) later stages of loading.....	215
Figure 6-20: Crack pattern of slab (RS-F <sub>15</sub> ) at load level 239.9 kN.....	217
Figure 6-21: Crack pattern of slab (RS-F <sub>30</sub> ) at load level 305.7 kN.....	218
Figure 6-22: Load-CMOD obtained at distance 1.5d from the column face along the centreline of the slab. ....	219

## List of tables

Table 3-1: Prestress system components .....	88
Table 3-2: Concrete mix proportions.....	104
Table 3-3: Concrete material properties.....	106
Table 3-4: Tensile mechanical properties of FRP plates.....	110
Table 3-5: Tensile mechanical properties of steel rebars.....	111
Table 4-1: Failure modes and load capacity results.....	118
Table 4-2: Comparison of test results with code predictions.....	135
Table 6-1: Experimental and FEM predictions of ultimate load and failure mode. .....	201
Table 6-2: Experimental and FEM predictions of ultimate load and failure mode. .....	220

## **Abstract**

The University of Manchester

AHMAD MAHMOUD ABDULLAH

Doctor of Philosophy

Analysis of Repaired/strengthened R.C. Structures Using Composite Materials:

Punching Shear

2010

Fibre reinforced plastics (FRP) have been used widely in civil engineering in order to improve the structural response (deformation and stress). Most of the current codes for the strengthening of RC structures do not provide enough provision for the design of the column-slab connections strengthened with externally bonded reinforcement (EBR) due to the lack of research covering this area. This study is to investigate, both experimentally and analytically, the effectiveness of bonding pre-stressed carbon fibre plates to the tension surface of concrete column-slab connections in both the serviceability and ultimate limit state.

The experimental programme comprises five full-scale specimens that are designed and fabricated to simulate an interior column-slab connection. The prestressing technique, application procedure and prestressing device are described in detail in this study. Different prestressing forces are applied to the FRP plates bonded to the concrete substrate. The structural response of the strengthened specimens are compared with a reference specimen in terms of punching shear strength, deflection profile, strain, crack opening displacement and failure modes.

Furthermore, a finite element model using ABAQUS is built to obtain a further insight into the punching behaviour of the test slabs. Both experimental and numerical results are compared, and a parametric study on the effect of the FRP-concrete interface on the structural integrity is conducted. Results are also compared with Eurocode 2 and ACI for the prediction of the punching strength.

It was found that bonding of prestressed FRP plates to the tensile face of the concrete slabs improved the serviceability, but was not able to enhance the ultimate behaviour as much as the non-prestressed FRP plates. The development of the critical diagonal crack (CDC) was the main reason for diminishing the ultimate strength of the strengthened slabs.

## **Declaration**

No portion of the work referred to in the thesis has been submitted in support of an application for another degree or qualification of this or any other university or other institute of learning.

## Copyright Statement

The author of this thesis (including any appendices and/or schedules to this thesis) owns any copyright in it (the “Copyright”) and s/he has given The University of Manchester the right to use such Copyright for any administrative, promotional, educational and/or teaching purposes.

Copies of this thesis, either in full or in extracts and whether in hard or electronic copy, may be made only in accordance with the Copyright, Designs and Patents Act 1988 (as amended) and regulations issued under it or, where appropriate, in accordance with licensing agreements which the University has from time to time. This page must form part of any such copies made.

The ownership of any patents, designs, trade marks and any and all other intellectual property rights except for the Copyright (the “Intellectual Property Rights”) and any reproductions of copyright works, for example graphs and tables (“Reproductions”), which may be described in this thesis, may not be owned by the author and may be owned by third parties. Such Intellectual Property Rights and Reproductions cannot and must not be made available for use without the prior written permission of the owner(s) of the relevant Intellectual Property Rights and/or Reproductions.

Further information on the conditions under which disclosure, publication and commercialisation of this thesis, the Copyright and any Intellectual Property and/or Reproductions described in it may take place is available in the University IP Policy (see <http://www.campus.manchester.ac.uk/medialibrary/policies/intellectual-property.pdf>), in any relevant Thesis restriction declarations deposited in the University Library, The University Library’s regulations (see <http://www.manchester.ac.uk/library/aboutus/regulations>) and in The University’s policy on presentation of Theses

## **Acknowledgements**

It is a pleasure to thank Egypt High Ministry of Education for financially supporting this research project.

I also owe my deepest gratitude to my supervisor Professor C.G. Bailey for his wise guidance and continuous support from the initial to the final level enabled me to develop an understanding of the subject. I am as well grateful to Dr. Jack Wu for his endless dedication in discussing and reviewing my work, and his persistence in pushing things forward.

Thanks are extend to the technical staff at the School of Mechanical, Aerospace and Civil Engineering, University of Manchester for their assistance during various stages of the project, and to Weber Building solutions for providing The FRP materials.

Last but not least, my deepest appreciation goes to my mother, father, wife and two sons, I realise that you went through a lot just for me; I love you so much.



## Notation

### Latin letters

$a$	The depth of the neutral axis
$b_0$	The perimeter length of the critical section
$b_c$	The width of the concrete substrate beneath the FRP plate
$b_f$	The width of the FRP plate
$c$	The column dimension
$d$	The effective slab depth
$d'$	The depth of the compression steel reinforcement
$d_g$	The maximum size of the aggregate
$E_c$	The concrete modulus of elasticity
$E_s$	The steel modulus of elasticity
$E_x$ , $E_y$ and $E_z$	The elastic modulus of the FRP plate in three directions
$F_{ct}$	The vertical component of the concrete tensile
$F_{dow}$	The dowel-force contribution of the flexural reinforcement
$F_p$	The vertical component of the forces in the tendons
$F_{pum}$	The punching shear capacity
$F_{sw}$	The vertical component of the shear reinforcement forces
$f'_c$	The concrete compressive strength
$f_{ck}$	The characteristic concrete strength
$f_{cm}$	The mean compressive strength of concrete
$f_{ctk}$	The characteristic tensile strength of concrete
$f_{ct,sp}$	The split tensile strength
$f_r$	The tensile strength of the FRP plate
$f_t$	The concrete tensile strength
$f_y$	The yield strength of steel
$G_f$	Fracture energy
$G_{xy}$ , $G_{yz}$ and $G_{xz}$	The Shear modulus of the FRP plate for three planes
$h$	The slab thickness
$L$	The square-slab edge length
$L_e$	The effective bond length
$M_b$	The nominal radial moment capacity of the slab
$S$	The shear strength in the $x - y$ plane of the FRP plate
$S$	The support length of the slab
$S_0$	The slip at debonding initiation
$t_f$	Thickness of FRP plate
$u_t$	The crack opening displacement
$V_{flex}$	The vertical punching shear force corresponding to the ultimate flexural capacity of the slab

$V_n$	The ultimate nominal punching shear capacity
$V_R$	The shear strength
$X_t$ and $X_c$	The tensile and compressive stress limits of the FRP plate in the $x$ direction
$Y_t$ and $Y_c$	The tensile and compressive stress limits of the FRP plate in the $y$ direction

**Greek letters**

$\beta_w$	A width factor
$\beta_l$	The bond length factor
$\xi$	A factor accounts for the influence of reinforcement ratio
$\varepsilon_0$	The terminal concrete strain at zero tensile stress
$\varepsilon_c$	The concrete strain
$\varepsilon_{ck}$	The cracking strain of concrete
$\tilde{\varepsilon}_c^{in}$	The inelastic compressive strain of concrete
$\varepsilon_{cu}$	The ultimate compressive strain of concrete
$\varepsilon_{cu1}$	The compressive strain in concrete at the peak stress $f_{cm}$
$\varepsilon_f$	The FRP strain
$\varepsilon_{fe}$	Effective strain of the FRP
$\varepsilon_{nom}$	The nominal strain
$\varepsilon_r$	The rupture strain of the FRP plate
$\varepsilon_s$	The steel strain
$\varepsilon_s^{el}$	The elastic steel strain
$\tilde{\varepsilon}_s^{pl}$	The true plastic strain
$\mu$	A factor accounting for the size effect law
$\eta$	The strengthening efficiency factor
$v_r$	The factored shear resistance
$v_c$	The factored shear resistance of concrete
$v_s$	The factored shear resistance of shear reinforcement
$\rho$	The flexural reinforcement ratio
$\rho'$	The reinforcement ratio compression steel reinforcement
$\sigma_c$	The compressive stress of concrete
$\sigma_s$	The true stress of steel reinforcement
$\sigma_t$	The tensile stress of concrete
$\sigma_{nom}$	The nominal stress of steel reinforcement
$\tau$	The interfacial shear stress
$\tau_{max}$	The maximum shear stress at debonding initiation
$\nu_{xy}$ , $\nu_{yz}$ and $\nu_{xz}$	The Major Poisson's ratio for three planes of FRP plate
$\phi_s$	The diameter of the corresponding bars

# Chapter 1

## Introduction

### 1.1. Introduction

Flat slabs shown in Figure (1-1) have been widely used since 1900 due to their economic and functional advantages. However, the resulting complex state of stress due to the high shear and moment at the column-slab connection make it one of the most critical D-regions (Discontinuity regions) in concrete structures [1]. Inadequate construction or design of such a connection makes it more vulnerable to undergo brittle punching-shear failure should it be subjected to excessive loads or earthquakes. Also, during the structure's life, it could suffer from deterioration of concrete as a result of corrosion of embedded reinforcement, freezing and thawing, or fire damage.

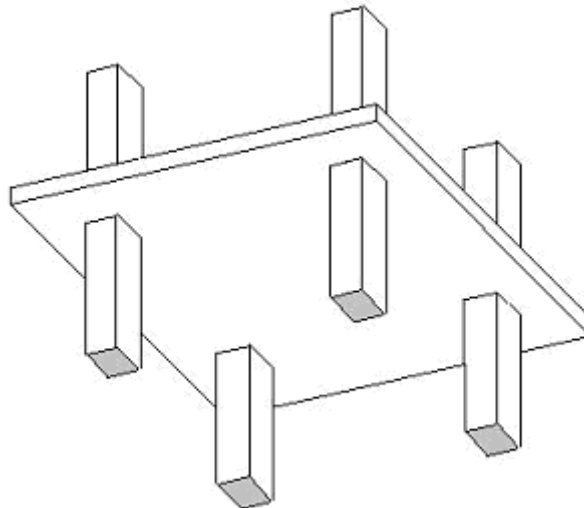


Figure 1-1: Flat slab Structure.

Before the early 1980s the technique of strengthening concrete structures by bonding steel plates with adhesives and bolts to the tensile surface was the dominant measure to repair or strengthen defected structures. After the mid-1980s, fibre reinforced polymers (FRP), due to their properties such as high strength, light weight and resistance to environmental effects, gained approval to overcome some of the shortcomings associated with steel plates in strengthening application. Therefore, corrosion resistance systems are not required, and maintenance after instillation is less laborious compared to steel [2, 3].

As a result, most previous research investigating FRP applications concentrated on the studies of reinforced concrete beams and columns. These experimental and analytical studies have demonstrated that FRP can enhance the ultimate strength and deformation capacity of concrete beams and columns [4-8]. In addition, FRP composites are not only used in the strengthening of structural elements in flexural and shear, but are also used in new construction instead of conventional steel bars in beams and slabs [9]. Results have been promising, and FRP has been used in many projects in North America, Japan and Europe [3]. A schematic diagram shown in Figure (1-1) concludes the application of FRP in civil engineering.

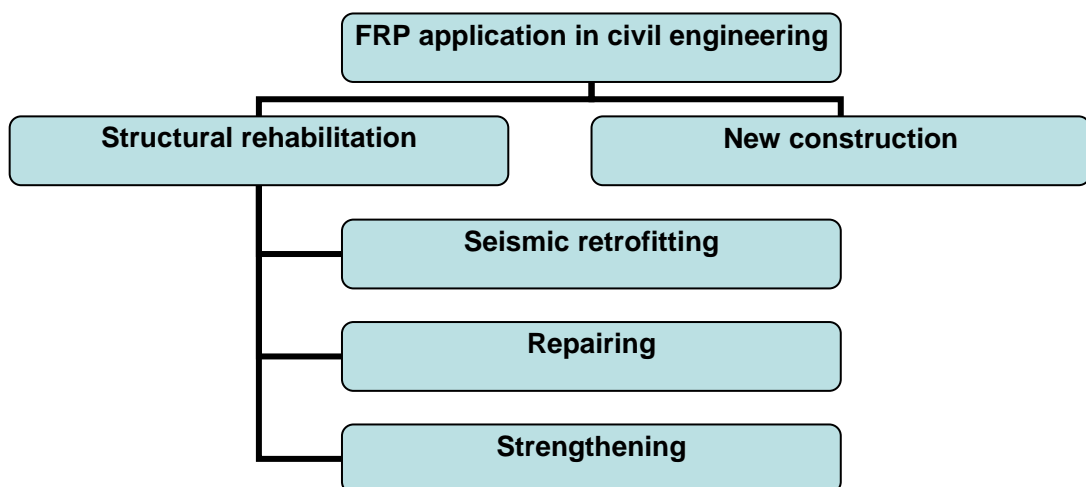


Figure 1-2: Schematic diagram for application of FRP in civil engineering.

To date there are several codes and design guidelines around the world such as, Europe/UK ISE [10], CEB-FIB Bulletin 14 [11], CSA Canadian code [12], ACI Committee 440 [3], JSCE report [13], and Technical Report 55 [14], covering strengthening techniques. However, these codes do not provide enough information about the strengthening and design of column-slab connections enhanced with FRP composites due to lack of research covering such application.

At the present time, strengthening methods to increase the ultimate shear capacity of the column-slab connections can be categorized into two main approaches; enhancing the capacity directly in shear [15] and enhancing the capacity in flexural [16]. The latter can be justified based on Moe's postulate that there is an interaction between bending and shear capacity; the punching shear capacity of slab is established from its flexural strength [17]. A common strengthening technique is to bond FRP fabrics to the tension surface of a concrete slab [18, 19]. However, no work seems to have been conducted attempting to investigate the effectiveness of two-way prestressing to concrete slabs using FRP plates, especially for those slabs constructed without adequate shear reinforcement before the 1970s.

## **1.2. Research objectives**

The aim of this study is to investigate the punching behaviour of column-slab connections strengthened with non-prestressed and prestressed Carbon Fibre plates (CFRP), using both modelling and experimental methods. The study has concentrated mainly on concrete column-slab connections without shear reinforcement and low reinforcement ratios in order to enhance their serviceability and loading capacity. So, to achieve the general aim of this research, the following more specific objectives are identified:

- (1) To investigate, through literature, the key variables and different approaches for enhancing the load bearing behaviour of flat slabs strengthened with externally bonded reinforcement (EBR) in flexural and in shear. Review of the analytical and numerical models analyzing and

identifying different modes of failure for such members is also presented.

- (2) To investigate, through experimental testing, attaching adhesively unidirectional non-prestressed/prestressed CFRP plates to the tensile surface of concrete slabs. The testing was intended to identify the main macro parameters controlling loading capacity and failure modes. The prestressing force applied, and the post-strengthening anchorage and efficiency are investigated for the design of the prestressed CFRP application in the tests.
- (3) To examine numerically the structural response of CFRP strengthened connection. Finite element modelling (FEM) has been used to predict the response of structures and materials to applied loads, and to analyse the deformation and stress state in concrete, steel and FRP plates. The interfacial behaviour between FRP and concrete is investigated selectively.
- (4) To examine and evaluate the developed models for prediction of punching capacity in literature and major codes of practice on RC structures reinforced with externally bonded FRP. Another objective is to investigate the failure modes and short-term deflection of the connections, since these are outcomes of the structural tests.

### **1.3. Outline of the thesis**

In Chapter 2, a comprehensive background and justification for this research are provided in the literature review on the punching shear behaviour of slabs strengthened by EBR. The topics included are the punching capacity, failure modes, and bond characteristics of FRP plates. Initially, the current state of knowledge of the punching behaviour of steel RC members without shear reinforcement is reviewed, and the underlying assumptions, key parameters and various approaches are identified. This is followed by a similar revision on the behaviour of slabs strengthened by FRP plates. The interfacial bond behaviour of such members is also presented. This chapter concludes by justifying the objectives and focus of this research, and by identifying the main variables that need to be considered for experimental investigation.

The experimental methodology is presented in Chapter 3. The layout and details of the test members are presented and discussed, and the experimental setup and instrumentation are illustrated. The preparation methods, quality control and test procedure are also elaborated. The concrete and reinforcement material tests are presented at the end of this chapter.

The results of the structural tests are presented in Chapter 4. Firstly, the modes of failure, crack pattern, deflection and load capacity are discussed. Then, the steel and FRP reinforcement and concrete strain are examined over the entire loading range. Subsequently, the experimental data are analysed to investigate other structural aspects that are related to serviceability and ultimate state. These involve the stiffness, energy absorption and the experimental load-curvature response. Finally, a discussion on the approaches of BSI, ACI and Eurocode 2 for evaluation of ultimate load is examined. Ultimate loads predicted by these approaches are compared with the test results.

Chapter 5 deals with numerical analysis. Finite element analysis (FEA) with smeared modelling of post-cracking behaviour and tension stiffening is presented, and its implementation in this study is elaborated. Then, investigation using FE analysis is conducted to predict the stress-displacement response of some test slabs.

In Chapter 6, a comprehensive discussion is undertaken on the punching behaviour of the FRP strengthened slabs. The predictions of steel, FRP and concrete strain and deflection, predicted by the FEA, are compared to the corresponding experimental results. The predictions of crack pattern, interfacial stresses, failure mode and ultimate load are also discussed. Conclusions are drawn regarding the parameters that control the punching behaviour of column-slab connections strengthened with FRP and the adequacy of the numerical analysis technique used.

The conclusions of this study are drawn, and recommendations for future work are made In Chapter 7.

## **Chapter 2**

### **Literature review**

#### **2.1. Introduction**

This chapter will first briefly describe the parameters which influence the behaviour and shear strength of flat slabs under concentrated loading as studied from experimental observations and theoretical models. It is followed by a review for the design of column-slab connections without shear reinforcement in codes of practice [20-23]. This is necessary because the current trend in dealing with fibre reinforced polymer (FRP) reinforced concrete member (RC) design is to make comparisons and impose modifications to the steel RC design practice. The research and current state of knowledge on punching behaviour of column-slab connection strengthened with FRP are then reviewed. The analysis trials and failure mechanisms are also presented based on experimental observations. Bond characteristics of FRP-concrete interfaces are investigated as they are important parameters governing the design of such members. Recently published state-of-the-art reports and codes of practice on RC members strengthened with EBR are also examined. Finally, justifications for the objectives of this research project are presented

#### **2.2. Punching shear behaviour of RC slabs**

When a reinforced concrete flat slab column structure is subjected to heavy gravity (vertical) load, the first crack to develop is roughly a circular flexural crack at the column vicinity due to the negative bending moments in the radial direction. From that circular crack, radial cracks then start to form due to negative bending moments in the circumferential direction; see Figure (2-1 a). After a significant increase in load, tangential cracks form around the loaded area at some distance out from the column in the slab. Also at about the same



time, punching shear cracks start to form inside the slab at the column vicinity. They propagate at a mean angle of 25 to 35 degrees through the slab thickness, starting from the mixed mode zone (flexural and shear) at the top of the slab towards the compression zone at the bottom of the slab. A truncated conical or pyramid failure surface around the column forms as shown in Figure (2-1 b).



Figure 2-1: Typical punching shear failure; Ref. [24].

In addition to vertical loads, the slab-column connections may be subjected to unbalanced moments, which are caused by unequal spans on both sides of the column or by lateral loading such as wind or earthquakes. The critical sections of such load combinations are at the perimeter of the loaded area or close to it, where the moment-shear interaction exists. This interaction adds more complexity to the classification of failure modes at the connection. The unbalanced moment is resisted by a combination of stresses in slab flexural reinforcement, shear strength of concrete, and shear reinforcement in the vicinity of column.

It was found that the characteristic of the failure mode and load-deflection curves of slabs are highly dependent on the reinforcement ratio as demonstrated by Criswell [25] in 1974, and shown in Figure (2-2). For instance,

slabs with high reinforcement ratios such as those represented by curves 1 to 3 show brittle behaviour. In these slabs the flexural punching  $V_g$  is corresponding to higher shear strength. Therefore, slabs will reach their punching strength before they reach the shear strength corresponding to the ultimate flexural capacity. On the other hand, curves 6 to 8 clearly show flexural behaviour with large ductility. The slabs represented by curves 4 and 5 reached their yield line strengths. However, they should be regarded as having failed in punching due to their lack of ductility.

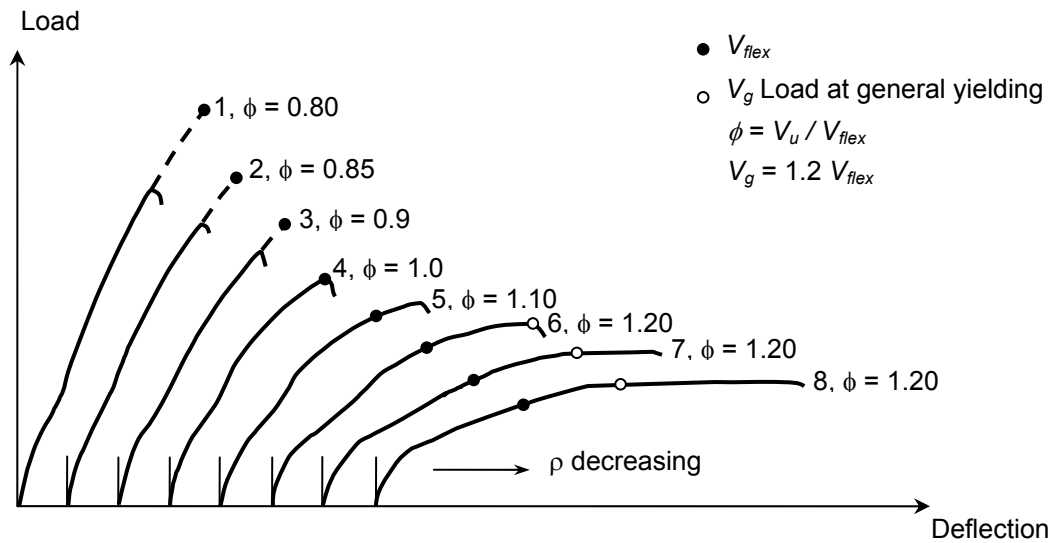


Figure 2-2: Effect of flexural reinforcement ratio on load-deflection response; Criswell [25].

Another feature of the punching behaviour is the deflected shape of the connection. As shown in Figure (2-3) the deflection profiles of the compression region can be virtually represented by a straight line rotating within a hinge adjacent to the column, while those on the tension face generally show a slight discontinuity across the shear crack region. It can be easily demonstrated from the figure that this discontinuity can be considered as a result of the rotation of the outer slab portion about its centre of rotation CR, while the crossing of flexural reinforcement through the shear crack alleviates this discontinuity [26].

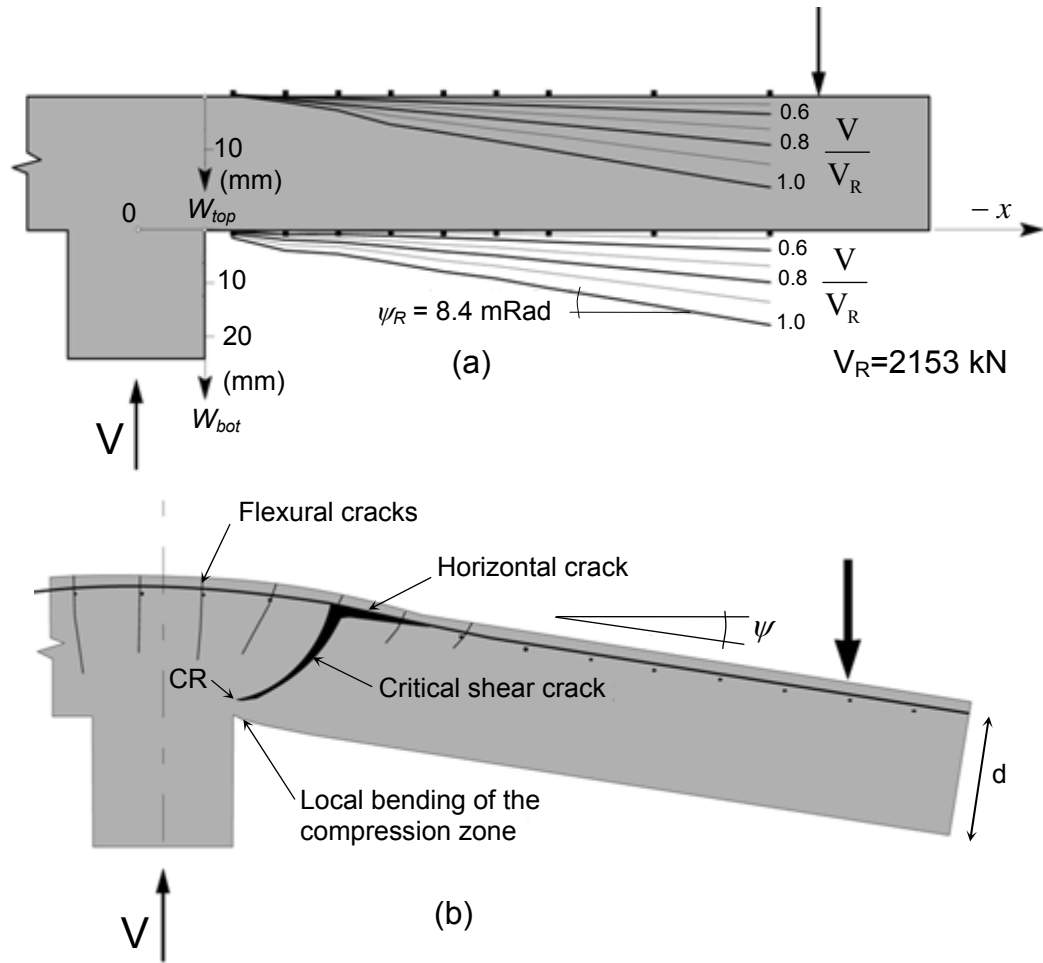


Figure 2-3: Slab deflection during punching test; Test results of slab PG-3 by Muttoni et al. [26].

The concrete strains at the compressed surface reach their highest values adjacent to the column, while the strain in the radial direction decreases very rapidly as the distance from the column increases; see Figures (2-4 a & b). The tangential strain is usually higher than the radial strain as shown in Figures (2-4 c & d), and the radial strain near the column often decreases before failure. The strain distribution on the faces of rectangular columns shows concentration of stresses at the corners, as illustrated in Figure (2-5). The concentration generally increases with larger square or rectangular columns but intuitively this concentration is absent in slabs with circular columns [17, 27].

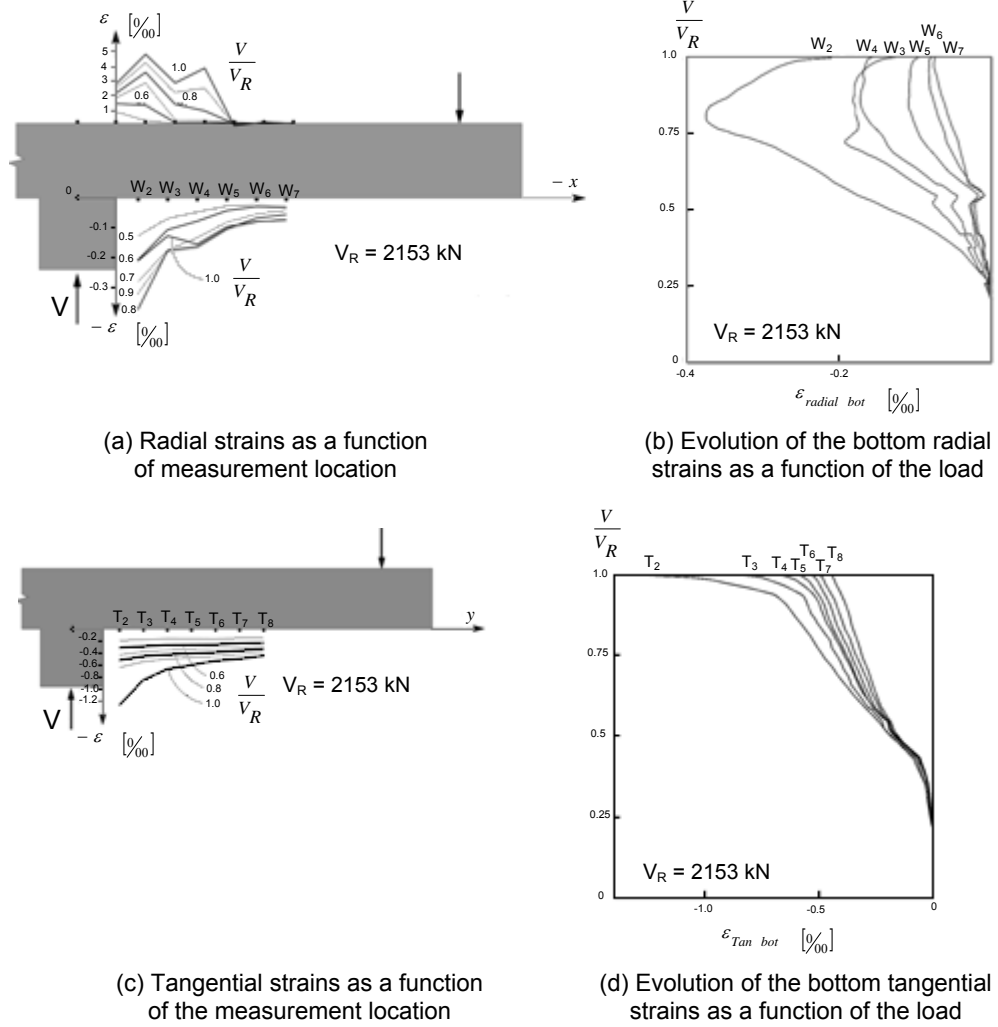


Figure 2-4: Radial and tangential strains at surface; Test results of slab PG-3 by Muttoni et al [26].

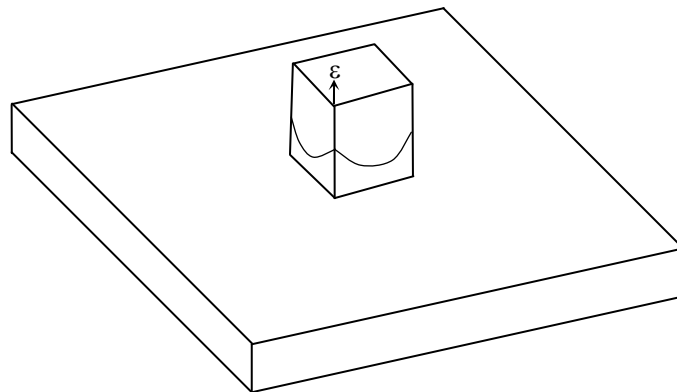


Figure 2-5: Vertical strains distribution at column faces according to Moe [17].

### **2.2.1. Parameters influencing punching shear strength of column-slab connections**

Models and theoretical methods for the design of slabs under punching shear are usually given as empirical equations based on observed failure modes or shear transfer mechanisms. The ability of the model to accurately express the failure criteria and visualize the flow of stresses depends on the number of parameters included. Consequently, to validate any model or theory, they have to be reviewed against all aspects relevant to design. Such aspects are the main parameters like concrete strength, reinforcement ratio, arrangement of reinforcement and column shape and size [1, 17, 28]. The influence of these parameters on the structural behaviour and load carrying capacity of the slab is discussed in this section.

#### **2.2.1.1. Concrete strength**

Research has been conducted to find the relation between the concrete compressive strength,  $f'_c$ , and the shear strength. Moe [17] in 1961 was the first to conclude that the shear strength relates not to  $f'_c$  but to  $\sqrt{f'_c}$ . Based on the testing results, he obtained the following equation for ultimate nominal punching shear capacity  $V_n$ :

$$V_n = \frac{1.25 \left( 1 - 0.075 \frac{c}{d} \right) \sqrt{f'_c}}{1 + \frac{0.44 b_0 d \sqrt{f'_c}}{V_{flex}}} b_0 d \quad \text{Equation 2-1}$$

Where  $c$  is the column dimension,  $d$  is the effective slab depth and  $V_{flex}$  is the vertical punching shear strength corresponding to flexural punching failure of the slab, is derived from yield line analysis according to Equation (2-15) as will be shown later in Section 2.6.1.1. Moe [17] explained that the shear strength is primarily affected by the concrete tensile splitting strength which is often assumed proportional to  $\sqrt{f'_c}$ . However, the ratio of nominal ultimate shear stress to  $\sqrt{f'_c}$  shows a significant scatter in practice due to the scatter in the tensile strength of concrete.

### **2.2.1.2. Flexural and compression reinforcement**

The strength of flexural reinforcement, reinforcement pattern and layout, and the amount of compression reinforcement has an effect on the punching shear capacity. These are explained as follows.

#### **2.2.1.2.1. Strength and ratio of flexural reinforcement**

Research indicates that shear strength can be related to flexural effects. Yitzhaki [29] in 1966 tested 14 slab-column specimens and proposed that the shear strength depends proportionally on the flexural reinforcement strength and the column size. Moe [17] in 1961 proposed a relationship between  $\frac{V_n}{V_0}$  and

$\frac{V_n}{V_{flex}}$  as follows:

$$\frac{V_n}{V_0} + C' \frac{V_n}{V_{flex}} = 1 \quad \text{Equation 2-2}$$

Where  $V_n$  is the nominal punching shear strength (vertical punching shear force of the column),  $C'$  is a constant between 0 and 1, and  $V_0$  is a fictitious reference value of shear,  $V_0 = A'b_0d\sqrt{f'_c}$ ,  $A'$  is a constant,  $b_0$  is the perimeter length of the critical section,  $d$  is the effective thickness of a slab,  $V_{flex}$  is the vertical punching shear force at the calculated ultimate flexural capacity of the slab. The magnitude of  $V_{flex}$  has no physical relation to the mechanism of failure in itself, but it reflects several other important influences, such as distribution of cracking, amount of elongation of the tensile reinforcement, magnitude of compressive stresses in the critical section and depth of the neutral axis at failure.

From Figure (2-6), it is found that if  $\frac{V_n}{V_{flex}} = 1$ ,  $\frac{V_n}{V_0}$  approaches a constant. This means that if a slab is designed to fail in flexural bending ( $V_n = V_{flex}$ , which is preferred mode of failure),  $V_n$  can be calculated using,  $V_0 = A'b_0d\sqrt{f'_c}$  which is independent of the flexural reinforcement ratio.

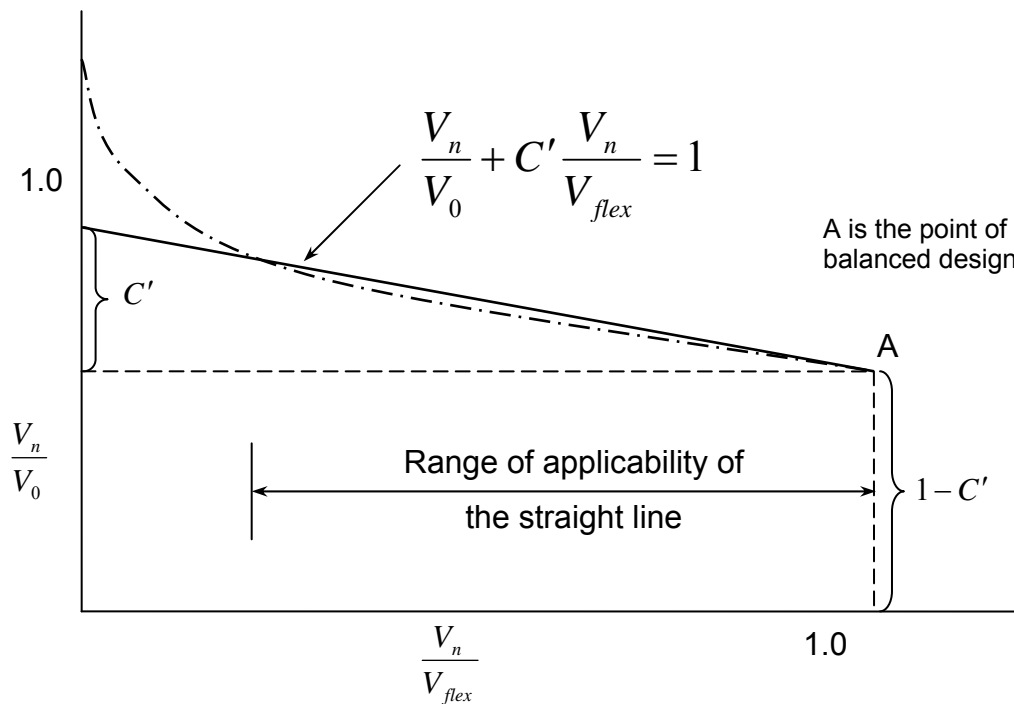
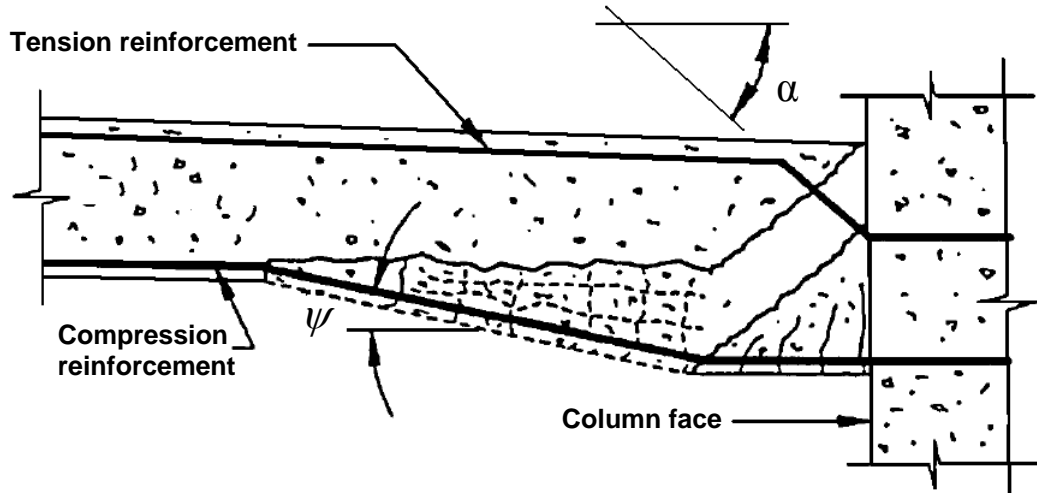


Figure 2-6: Interaction between shearing and flexural strength according to Moe [17].

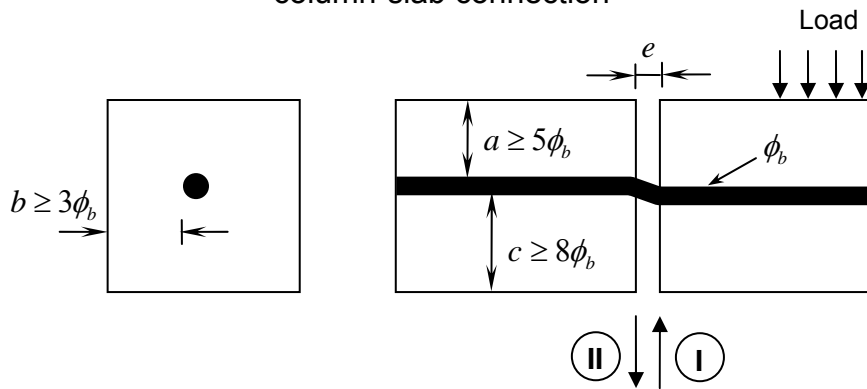
Dowel forces develop in the flexural reinforcement when they cut across the inclined shear crack. Vertical forces also develop due to the membrane effect in the flexural reinforcement mat, when the rigid parts of a slab (outside of shear cracks) rotate around the column. Kinnunen and Nylander [30], concluded that dowel forces and vertical forces from membrane effects account for 35 percent of the punching shear capacity. Therefore, according to their conclusion, slab punching shear capacity increases if the ratio and strength of flexural reinforcement increases. However, Criswell [31] in 1974, quoting Moe's [17] results, concluded that this effect is not important.

The reason for the contradiction noted above is that the concrete cover is the main parameter upon which dowel mechanism depends [20, 32]. The dowel action phenomenon is more pronounced when a single bar is embedded in a large mass of concrete. However, its effect is sometimes markedly reduced in planar elements due to the shortage of the geometrical conditions, suitable loading, or constraints. For instance, in punching shear behaviour, a shear

crack is developed in a diffusive process during the later stages before failure, with an acute angle to the reinforcement. Consequently, the skewness of the cracked plane reduces the effectiveness of mode-I mechanism. Moreover, for a small concrete cover,  $c$ , less than 8 times the bar diameter as shown in Figure (2-7 b), the mechanism is governed by the splitting of concrete which impairs the effectiveness of mode-II as well.



(a) Schematic diagram of post punching behaviour of column-slab connection



Mode I: the dowel pushes against concrete core

Mode II: the dowel pushes against concrete cover;  $c$ .

(b) Dowel action geometrical conditions, according to CEB-FIP.

Figure 2-7: Dowel action effect of reinforcement; CEB-FIB [20].

In view of the aforementioned statement, because of the small cover in slabs, concrete splitting and the lack of stirrup reinforcement decreases the dowel force which can be developed in any given bar; see Figure (2-7 a). However, if



the cover is thick enough, concrete splitting is unlikely to occur. In comparison with the situation in a beam, the width (circumference) of concrete involved in the dowel action is large resulting in a large number of bars passing through the inclined crack. This probably results in the dowel forces carrying a greater proportion of the shear in slabs than in beams. In this study, the dowel action effect was not taken in consideration, as its effect on the behaviour is nearly negligible.

#### **2.2.1.2.2. Pattern of flexural reinforcement**

Tests by Kinnunen and Nylander [30] in 1960 showed that the failure loads can be about 20%-50% higher in circular slabs reinforced with orthogonal reinforcement than that in slabs with ring bars.

#### **2.2.1.2.3. Arrangement of flexural reinforcement**

Elstner and Hognestad [28] in 1956 and Moe [17] in 1961 investigated the punching behaviour of column-slab connections with flexural reinforcement concentrated over the column region and compared them to others reinforced with uniformly spaced bars. In the Elstner and Hognestad slabs 50% of the tensile reinforcement was concentrated within a distanced  $d$  (effective depth) of the column, as shown in Figure (2-8). While in Moe's slabs the total amount of steel was held constant and the spacing varied between uniform spacing and an arrangement in which 82% of the total steel was placed within a distance  $d$  of the column. Both tests indicated that the concentration of reinforcement does not increase the ultimate load of slab. In some slabs, concentration of the reinforcement even reduced the ultimate load of the slab. This is because the concentration of reinforcement leaves a large radial sector almost unreinforced; see Figure (2-8). From these tests results, it could be concluded that concentration of reinforcement causes a slight decrease in strength and a reduction of ductility.

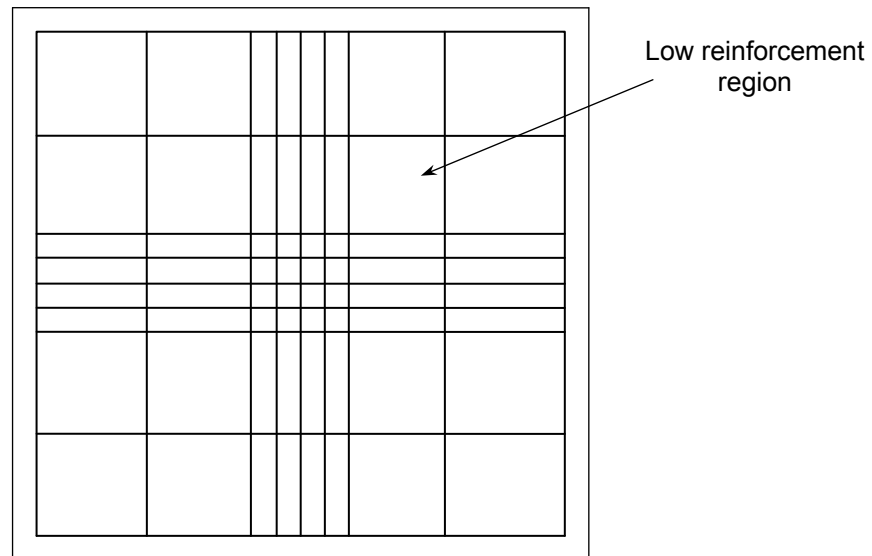


Figure 2-8: Concentration of flexural reinforcement.

Alexander and Simmonds [33] in 1992 conducted a similar study on the effect of adding extra reinforcement over the column strip. They placed a different amount of steel reinforcement over the column strip of 450mm resulting in spacings of 50mm, 75mm and 150mm at the column region. All slabs failed in punching, but they found that decreasing the spacing increases the load capacity but decreases the ductility. Also in the slab with a spacing of 50mm, the bar force profiles indicate that anchorage failure occurred in the central bars. Based on this observation, they argued that in those slabs tested by Elstner and Hognestad [28] and Moe [17] failure was actually anchorage failure. They concluded that the above observation may explain why the concentrating of reinforcement through the column region does not increase punching capacity.

However, Eurocode 2 [21] recommends 50% of flexural reinforcement needed for the negative moment should be placed in the column region at a distance equal to the sum of 0,125 times the panel width on either side of the column because it improves the behaviour of the slab in the service load range. Concentration increases the stiffness of the slab, increases the load for the first yielding of the flexural reinforcement, and consequently results in smaller maximum crack widths under the same loading condition.

#### **2.2.1.2.4. Compression reinforcement**

Elstner and Hognestad [28] in 1956 reported that, for  $\phi_0 = \frac{V_n}{V_{flex}} > 1$ , or if the tension reinforcement is small, there is negligible effect on the shear strength with the variation of the compression reinforcement, where  $V_n$ ,  $V_{flex}$  are defined, as in Equation (2-1). However, when  $\frac{V_n}{V_{flex}} \leq 1$ , or the ratio of tension reinforcement is large enough to make a doubly reinforced section, the shear strength increases if the ratio of the compression reinforcement increases. Compression reinforcement also increases the dowel force after punching failure, which can prevent progressive collapse of a structure.

#### **2.2.1.3. Shear reinforcement**

Shear reinforcement is used to enhance both the strength and ductility of the column-slab connection. It is, in general, bars (or any other shape) crossing the inclined shear cracks to prevent their propagation. It should have adequate tension strength, ductility and good anchorage to develop its strength during punching shear failure. There are many types of shear reinforcement for new or existing reinforced concrete slabs. They can be divided into three groups:

- 1) Structural steel sections such as the I-shape steel developed by Hawkins and Corley [34], or channels installed to the column side faces and the slab bottom surface that act as column heads;
- 2) Bent bars, stirrups and Shearband such as those developed by Pilakoutas and Li [35];
- 3) Headed reinforcements including shear studs and headed bars such as those developed by Ghali [36] and Ghali et al. [37] .

Only limited types of these reinforcements, such as shear bolts, can be used in post-strengthening application of existing reinforced concrete slabs, while others, such as steel sections and Shearbands, need to be applied at the time of construction.

There have been several methods proposed for punching shear retrofit of existing column-slab connections. Among the common strengthening techniques for the column-slab connection is the use of steel plates and steel bolts as vertical shear reinforcement [38]. This technique can effectively increase both the ultimate load and the ductility of the strengthened connection. Also reinforced concrete capital or a drop panel can be added to the bottom of a slab.

Ghali et al. [39] in 1974 conducted a series of tests to develop an effective method of strengthening flat plates at their connection with columns. They used transverse reinforcement pre-stressed in a direction normal to the slab surface. The technique used provided a substantial increase in both strength and ductility. They tested 10 specimens with prestressed shear bolts in three groups; see Figure (2-9).

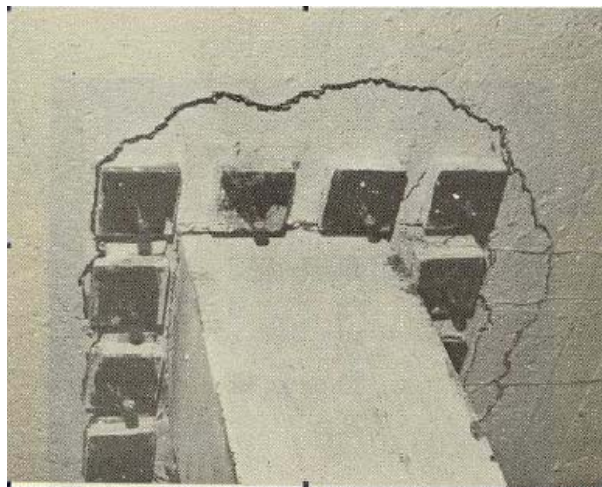


Figure 2-9: Prestressed shear bolts for slab under vertical load; Ref. [39].

The twelve bolts for each specimen were 20mm diameter high tensile strength steel bolts with a 100x100x20mm steel plate at each end. The unbonded bolts were tensioned to 75.3kN before testing. One group of specimens (Group B) were subjected to monotonically increased moments, and another group (Group C) were subjected to monotonically increasing vertical load. The results showed that the prestressed slab had much higher deflection capacity and failure load

than unreinforced slabs. In Group C, specimen No. 10 (no bolts) obtained an ultimate load of 413kN, but specimen No. 9 (prestressed bolts) obtained 690kN ultimate vertical load, an increase of 67% compared with specimens No. 10. In group C, specimen No. 5 (without bolts) reached 196kNm ultimate moment, and specimen No. 4 (with prestressed bolts) reached 241kNm moment, a 23% increase.

El-Salakawy et al. [40] in 2003 evaluated a new strengthening method for increasing the punching shear strength of edge slab–column connections. The method consisted of using shear bolts externally installed in holes drilled through the slab thickness. A full-scale edge slab–column connection was used and different configurations of the shear bolts around the column were tested. The shear bolts were post-tensioned against the surface of the slab up to about 40% of the bolt yield stress (40% of the bolt yield strain was  $700\ \mu\epsilon$ ). It was concluded that the strengthening technique increased the ductility of the column-slab connection, provided a means for changing the failure mode from punching to flexural, and increased the strength capacity of the connection. Irrespective of the configuration of shear bolts, none of the steel bolts attained yield stress and the increase in the strength of the connection ranged between 12% and 18%.

Ebead and Marzouk [38] used steel plates and steel bolts for strengthening of two-way slabs. They studied the effectiveness of two configurations of steel plates and four different arrangements of steel bolts as vertical shear reinforcement, as shown in Figure (2-10). The strengthening steel plates were extended to twice the slab depth around the column and acted as a drop panel of an equivalent concrete depth. They tested five-square specimens of 1900 mm side length and 150 mm thickness to represent a full-scale column slab connection. All slabs had a reinforcement ratio of 1.0 % to achieve a ductile punching failure mode. One specimen was used as a control specimen, and the others were strengthened specimens with different plate configurations and bolt distribution pattern.

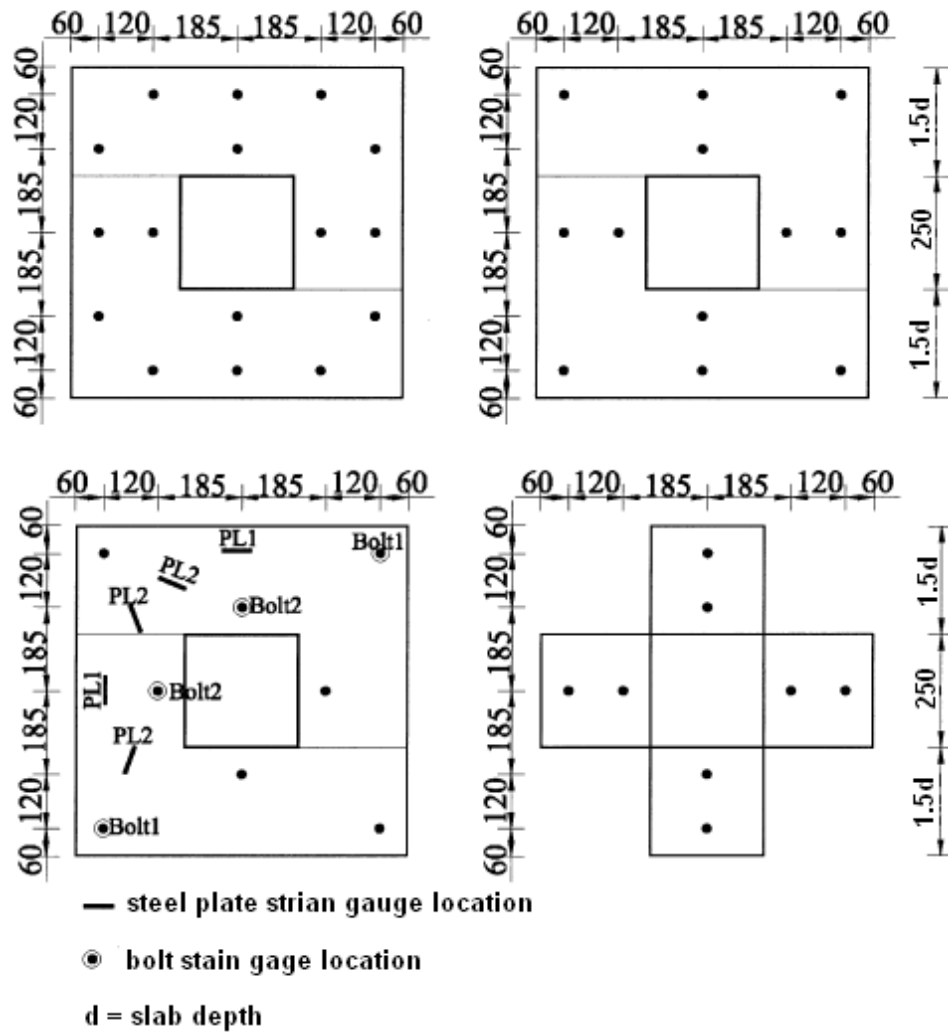


Figure 2-10: Strengthening mechanism used by Ebead and Marzouk [38].

It was found that both the yield load and the maximum load were increased due to the strengthening process. The average increase of the yield load was 50% of the yield load of the control specimen, and the average increase of the ultimate load of the strengthened specimens over that of the control specimen was 53%. The increase of the ultimate load of the specimen with separate steel plates, however, was evaluated at 36%. So they recommended the use of a L-shape steel plate instead of separate steel plates for the strengthening of two-way slabs. Also, the strengthened specimens showed stiffer behaviour than that of the un-strengthened control specimen, and the average ductility of the strengthened specimens was approximately 29% greater than the ductility of the control specimen. That was clear in the energy absorption of the

strengthened specimens which is greatly increased due to the strengthening process. The average increase of energy absorption of the strengthened specimens over that of the control specimen was approximately 100%.

#### **2.2.1.4. In plane restraints**

Taylor and Hayes [41] in 1965 carried out a series of tests on the effect of edge restraint. The slabs were divided into three groups depending on the amount of tension reinforcement which was zero, 1.57% and 3.14%. The restraint was imposed by a heavy welded steel frame which surrounded the slabs, i. e. the edges of slab were restrained against lateral movement. All slabs without reinforcement were tested in the restrained condition. For pairs of slab with reinforcement, one of each pair was tested in the simply supported condition and the other in the restrained condition.

The test results indicated that for a slab with a low percentage of reinforcement, the restraint significantly increased the ultimate load up to 60%. This group of slabs exhibited high ductility and were more likely to fail in a flexural mode. The ductile behaviour allowed compressive membrane forces, shown in Figure (2.11), to fully develop. The flexural capacity was thus significantly increased as observed by other researchers; Kuang and Morley [42] in 1992. However, for slabs with high reinforcement ratio, the enhancement by restraint was less significant and in some cases there was virtually no increase in strength. Punching shear failure is critical for this group of slabs and the slabs suddenly ruptured. It is possible that the slab fails before the membrane action has developed. Others; Rankin and Long [43] in 1987, observed that restraint will enhance the punching shear strength of slab in all cases.

Kuang and Morley [42] in 1992 tested a total of twelve slabs which were supported and restrained on all four sides by edge beams. Different degrees of edge restraint were provided by different sizes of edge beam. They observed that a restrained slab with a low percentage of steel failed in a punching shear mode when subjected to concentrated loading. This indicated that lateral restraint may also change the mode of failure because the membrane forces

developed enhances the shear and flexural capacity of the slab and at the same time reduces the ductility of the slab.

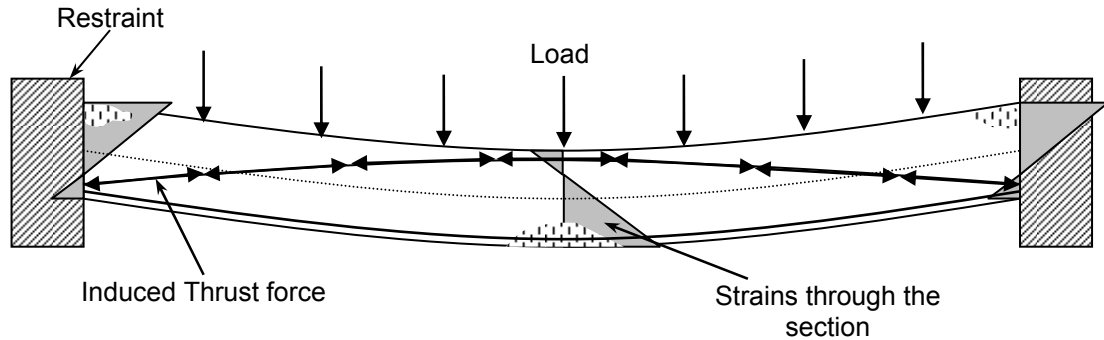


Figure 2-11: Compressive membrane action.

It is apparent that from the above test results that the restraint can considerably enhance the load carrying capacity of slab, but reduce the ductility of the slab. However, the degree of the enhancement in strength due to the membrane action is difficult to quantify since it depends on the in-plane restraint provided by the surrounding structure.

#### **2.2.1.5. Size and shape of loaded area**

Moe [17] in 1961 assumed a linear variation in shear strength with side dimension of the column based on test data when the side length of the loaded area was between  $0.75d$  and  $3.0d$ , where  $d$  is the slab thickness. Regan [44] in 1986 tested five slabs where the loaded area is the only significant variable. The shapes of loaded area were: circular with diameters of 54mm, 110mm, 150mm, 170mm and 102x102mm square. The test results confirmed the linear relationship for the loaded dimension provided that it exceeds  $0.75d$ . When the loaded area is very small (side dimension less than about  $0.75d$ ), the slab failed in local crushing and therefore the strength of slab is far below that predicted by the linear relationship.

In view of the above, if the loaded dimension is greater than  $0.75d$ , the length of the critical section becomes greater as the loaded area increases resulting in an



increase in the shear strength of slab. Therefore, it is very common in practice to provide drop panels or capitals to increase the punching shear resistance rather than increasing the column size.

Most of available test data in the literature indicates that slabs loaded through a circular area are stronger than those loaded through square areas with the same perimeter. This improvement in shear strength is attributed to the absence of stress concentrations at the corners of rectangular column [27].

Hawkins et al. [45] in 1971 carried out a series of tests on nine slabs in which the length of the perimeter was held constant but the aspect ratio was varied. He found that if the aspect ratio is increased, the shear strength of slab decreases because the behaviour of slab transforms from two-way bending to one-way bending. Therefore beam action shear tends to develop at the long faces of the loaded area. This also reflects the tendency for the shear force to be concentrated at the end of a wide column as observed in the experiment; see Figure (2-12). He concluded that when the aspect ratio for a rectangular column is greater than two, the strength can be lower than that for a square column.

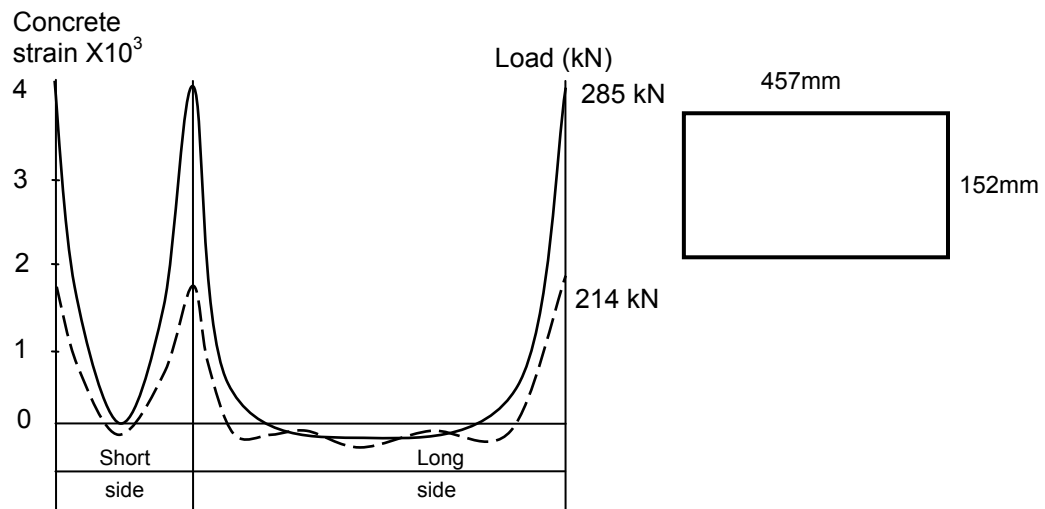


Figure 2-12: Concrete strain on column sides of aspect ratio=3; Ref. [45].

### 2.2.1.6. Size effect (span-depth ratio and aggregate size)

Regan [44] in 1986 tested six specimens where the main variable was the thickness of slab. The effective depths were 80mm, 160mm and 250mm. Test results show that nominal shear strength increased as the depth " $d$ " decreased; see Figure (2-13). These results also agree reasonably well with the size factor ( $\sqrt[4]{1/d}$ ) used in the BS8110 [22]. The same conclusion was also obtained by Bazant and Cao [46] in 1987. They add that increasing the slab thickness results in steep decline in the post-peak behaviour of the load-deflection curve showing a brittle behaviour.

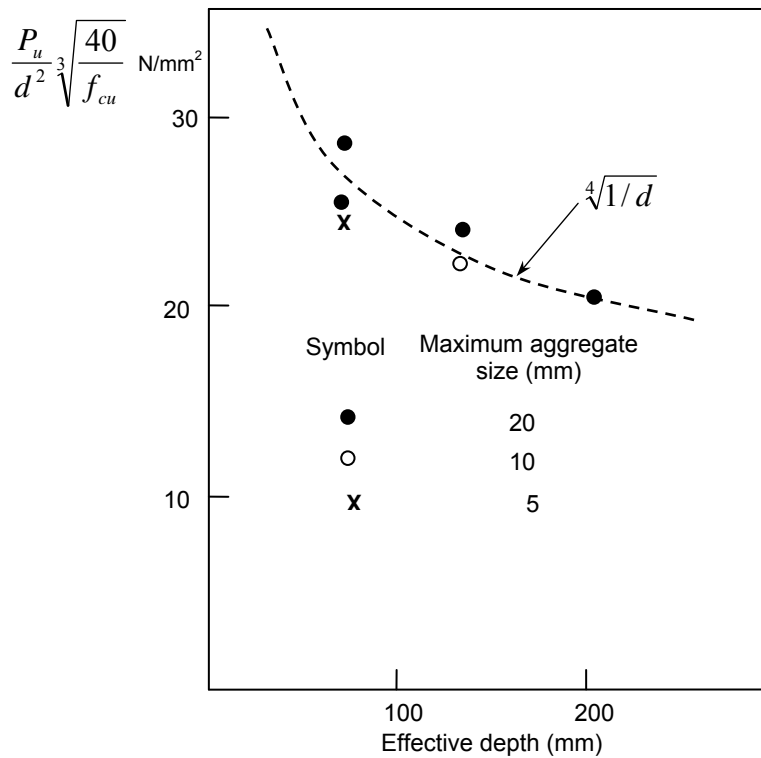


Figure 2-13: Influence of effective depth on nominal shear strength; Ref. [44].

John and David [47] in 1990 tested a series of slabs of constant thickness (100mm) with varying span-depth ratios. They concluded that the punching shear strength was significantly increased for the span-depth ratio below six; see Figure (2-14). The strength enhancement may be due to the development

of compression struts forming an arch mechanism in the slabs and in-plane compressive forces resulting from friction at the support.

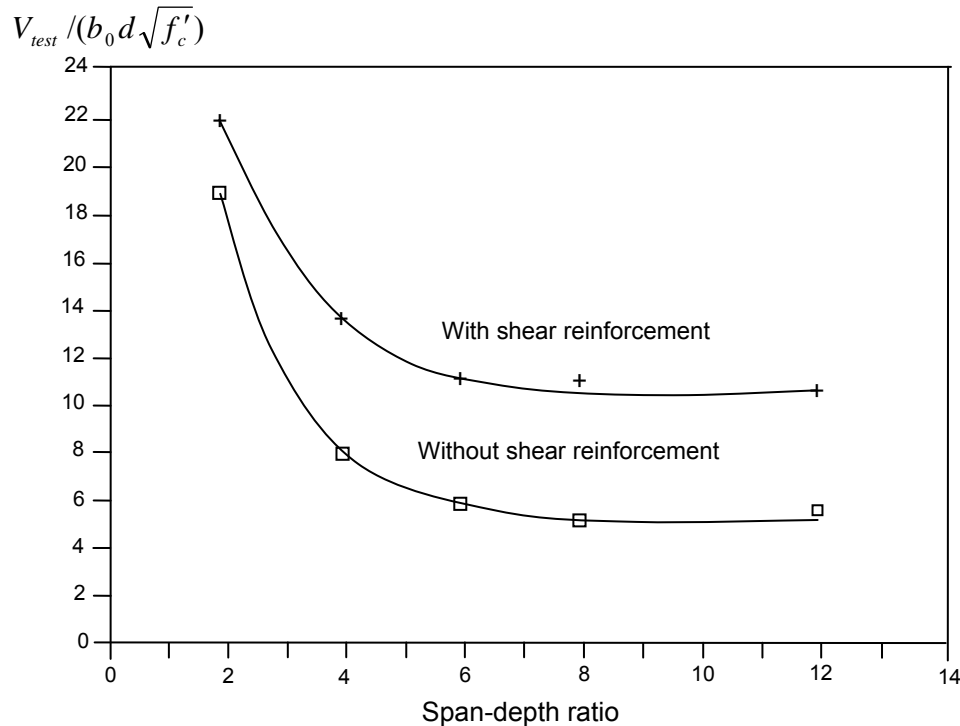


Figure 2-14: Effect of span-depth ratio on punching shear strength; Ref. [47].

### 2.3. Punching shear strengthening of slabs with FRP

As mentioned before in Chapter 1, existing concrete slabs may need to be strengthened due to insufficient punching shear capacity. This may be caused by change of the building use, new openings in a slab, design or construction errors. Thus, upgrading is a necessity. Several investigations have been conducted on strengthening the column-slab connection by different techniques since the middle of the 1970s. All investigations explored ways to delay or prevent punching shear failure. In this section, a review of the common FRP-strengthening techniques for existing structures is presented. They are categorized into two main approaches; direct shear strengthening and flexural shear strengthening.

### **2.3.1. Direct shear strengthening**

Recently, FRP fabrics have been used as shear reinforcement. In this method FRP composites are threaded through the thickness of the slab. It is similar in principle to the application of shear studs as a transverse reinforcement to carry the diagonal tension forces. Holes are drilled then FRP fabrics are woven through these holes to form shear reinforcement around the column.

Sissakis and Sheikh [48] in 2000 were the first who applied this technique. They conducted an experimental programme on punching shear strengthening of reinforced concrete slab-column connections by using CFRP strips. They studied the effectiveness of externally installed CFRP stirrups serving as shear reinforcement as a strengthening technique. They tested 32 slabs of size 1500x1500x150mm divided into four groups based on the reinforcement ratios (1.49% and 2.23%) and the strengthening pattern used. Four stitching patterns were used to investigate different alternatives of strengthening; see Figure (2-15). The strengthened slabs showed a substantial increase in shear strength, ductility, and energy dissipation capacity. The shear strength increase was over 80%, and an enhancement in ductility of over 700% was observed as shown in Figure (2-16).

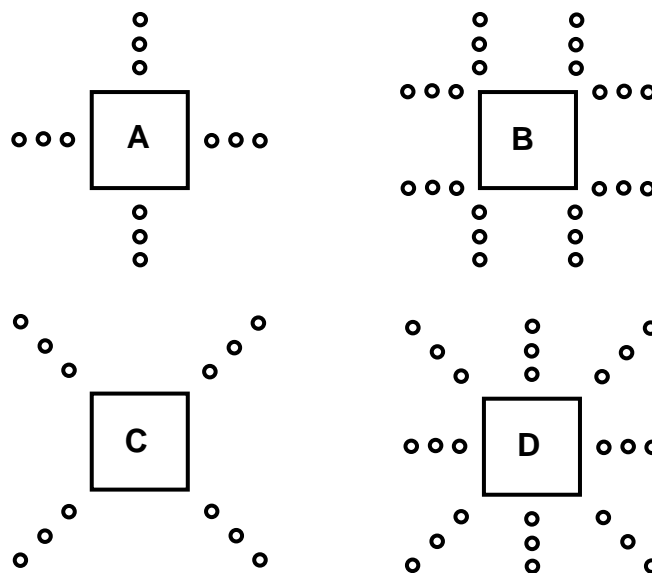


Figure 2-15: Strengthening patterns according to Sissakis and Sheikh [48].

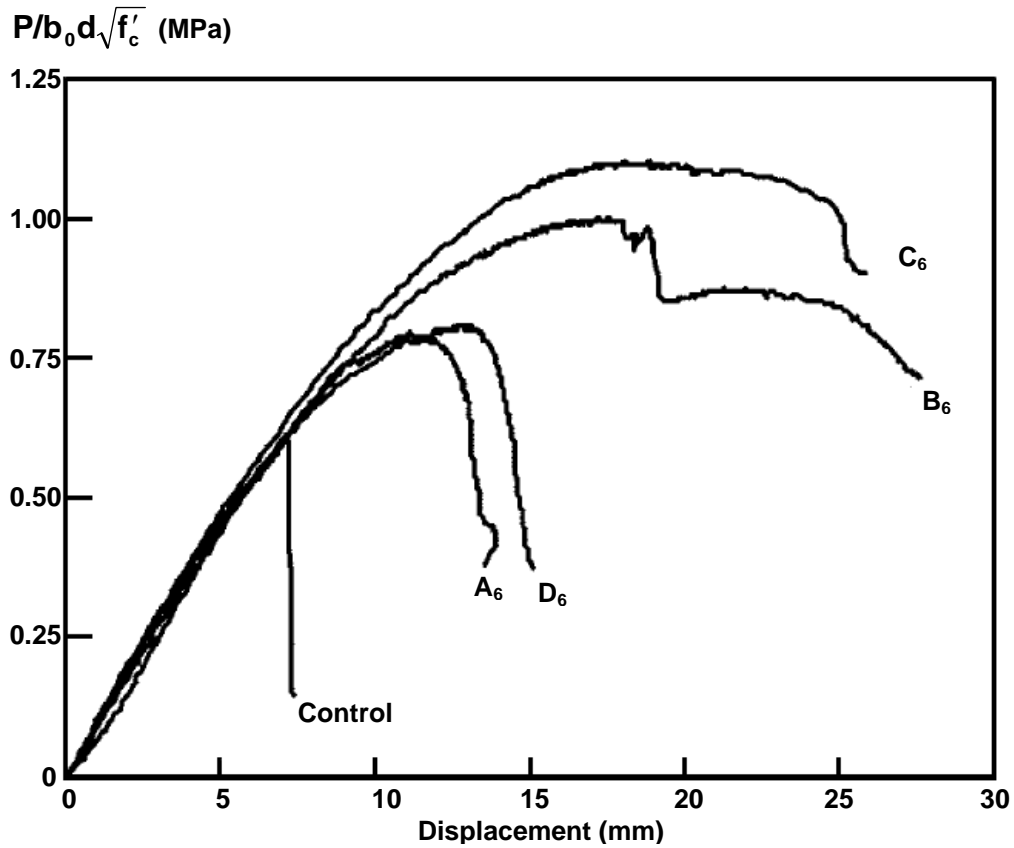


Figure 2-16: Load deformation curves of strengthened slabs according to Sissakis and Sheikh [48].

Binici and Bayrak [15, 49], adopting the same idea of using the CFRP as shear stirrups, investigated the effectiveness of different strengthening schemes. Nine slabs and two control specimens were tested in this phase of the experimental programme. The specimen size was 2135 x 2135 x 152mm. The reinforcement ratio was 1.76% for all slabs. Two stitching patterns were used to investigate different alternatives of strengthening, as shown in Figure (2-17). It was found that the use of CFRP strips as closed stirrups increased the strength and deformation capacity (ductility) of the test specimens. The increase in ultimate load-carrying capacity was between 20% and 59% depending on the pattern and number of layers used. Another remarkable improvement was the shift of punching shear failure outside the shear reinforcement region. This can be attributed to the use of CFRP strips as closed stirrups which increased the strength and deformation capacity of test specimens. That is when CFRP strips

were anchored by overlapping at the compressive side of the slab, the shear reinforced region stayed relatively undamaged with no shear cracks.

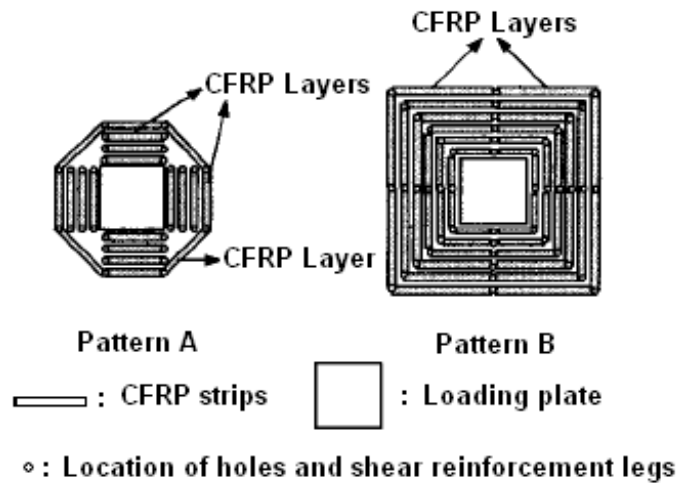


Figure 2-17: Strengthening pattern and details (plan view); Ref. [15].

The importance of anchorage of shear reinforcement has been confirmed experimentally by John and David [47] in 1990 and Broms [50] in 1990. Thus, the difficulty of achieving effective anchorage in thin slabs, if they are strengthened with shear studs, make the use of FRP fabrics as an alternative shear reinforcement highly attractive in slabs with overall thickness less than 200mm. However, this approach may have some drawbacks while it is applied in the field. Drilling such large number of holes with close spacing through the slab thickness may cut the internal steel reinforcement if there is no enough information about their distribution.

### **2.3.2. Indirect (flexural) shear strengthening**

The strengthening method mentioned in Section 2.2.1.3 does provide enough additional strength to the slab. However, strengthening slabs with FRP laminate has more advantages compared to steel plate strengthening as mentioned before, and at the same time does not change the appearance of the slab. This led researchers to divert their investigations towards the benefit of FRP used as an externally strengthening material.

Erki and Heffernan [51] in 1995 were among the early researchers that investigated the enhancement in strength of concrete structures by applying the EBR on both beams and slabs [51, 52]. They loaded eight reinforced concrete slabs ( $1000 \times 1000 \times 50 \text{ mm}^3$ ) up to failure. Six slabs were reinforced with two-way ordinary steel, and the remaining two were reinforced with one-way steel. All slabs were tested under a simply supported condition; the two-way slabs were supported on all four edges, and the one-way slabs were only supported along their short direction. One one-way and two two-way slabs were tested as controls, and the remaining five were externally reinforced on their tension face with unidirectional GRP and CFRP sheets. It should be mentioned that the specimen configuration did not have a column stub extending from the tension face of the slab where the FRP strengthening was applied. So that, a patch load was applied on the top surface of the slabs to induce two-way shear or punching shear failure. The recorded data comprised the load-deflection for key locations on the slabs and strains in both reinforcing steel and FRP sheets. These failures were initiated at flexural cracks that under increasing loads turned into shear cracks and precipitated shear failure. The additional reinforcement provided by the FRP sheets increased the flexural stiffness of the slabs, delaying the onset of flexural cracking to higher loads, and thereby increasing the punching shear strength. The efficiency of the FRP strengthened slabs was evaluated and the ultimate loads supported by the slabs were compared to those predicted by Canadian code equations [12]. They also reported that due to the use of patch load instead of the column stub, the construction limitations for strengthening the slab–column connection may not be accurately simulated.

Harajli and Soudki [53] in 2003 conducted an experimental investigation to evaluate the punching shear capacity of interior slab–column connections strengthened with flexible CFRP sheets. They tested sixteen square slab–column connections of 670mm side length and  $100 \times 100 \text{ mm}$  centre column stub to represent the interior slab-column connection, as shown in Figure (2-18). The slabs had two different thicknesses, 55mm and 75mm and reinforcement ratios of about 1 and 1.5%, respectively. Twelve specimens were strengthened with flexible CFRP sheets and the remaining four specimens were kept as controls.

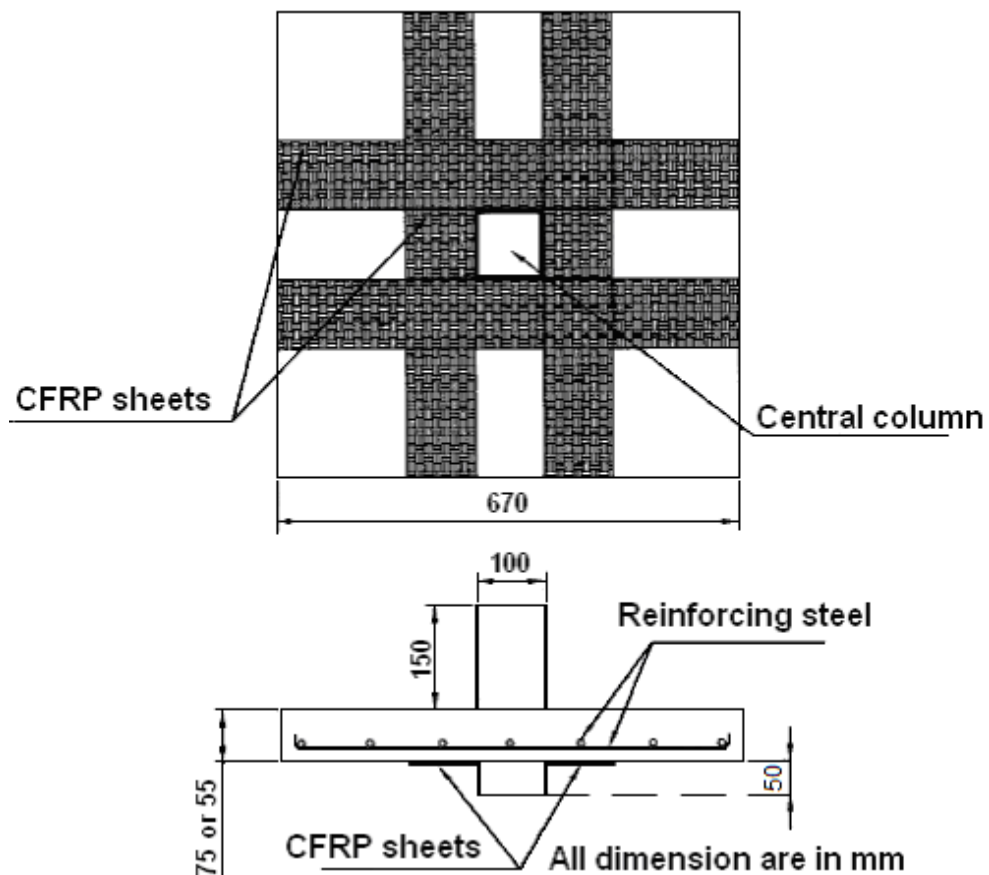


Figure 2-18: Dimension and details of reinforced specimen; Ref. [53].

The results show that the use of the CFRP sheets altered the failure mode from flexural failure to flexural shear or pure punching shear failure, thereby reducing the ductility of failure. Also, applying CFRP reinforcement increased the cracking strength, flexural stiffness of the specimens, and resulted in considerable improvement in the ultimate strength capacity. This can be explained by CFRP reinforcement improving the shear strength of slab–column connections by restricting the growth of the tensile cracks or increasing the flexural strength of the connections. The increases in the normalized shear strength capacity ranged between 17% and 45%, and the increase in the normalised flexural strength ranged between 26% and 73%. The corresponding increase depended on the area of the CFRP relative to the area of internal ordinary reinforcement and the mode of failure of the specimens and the CFRP sheets, but tended to reach the plateau with any increase in the amount of the



CFRP sheets provided. They also reported that the use of unidirectional FRP system for slab strengthening slightly increases the punching shear resistance, and the bi-directional bonded FRP system increases the punching shear strength according to the reinforcing index (the area of the CFRP relative to the area of internal ordinary reinforcement) and the mode of failure of the specimens and the CFRP sheets. Also, the use of CFRP sheets gave the highest punching shear strength for the same reinforcing index while the use of CFRP plates gave the least.

El-Salakawy et al. [54] in 2004, using different methods, tested seven full-scale reinforced concrete slab-column edge connections strengthened against punching shear. In this study, three slabs contained openings in the vicinity of the column, and the other four were without openings. The dimensions of the slabs were 1540×1020×120mm with square columns (250×250mm). The openings in the specimens were square (150×150mm) with the sides parallel to the sides of the column. The slabs were reinforced with an average reinforcement ratio of 0.75% in both directions. The test specimens were divided into three series. Series 1 included the unstrengthened control specimens without openings, and one specimen with an opening. Series II included three specimens without openings, strengthened with either glass or carbon FRP sheets using L-shaped FRP sheets scheme (one or two layers of flexible FRP sheets glued to the tension face). Series III included two specimens with openings strengthened with GRP sheets, using U-shaped GRP sheets scheme (one or two layers of flexible FRP sheets glued to both tension and compression faces of the slab). Steel bolts through holes across the slab thickness around the column were added to one GRP strengthened specimen without a hole in Series II, and another GRP strengthened specimen with hole in Series III.

Based on the test results, it was concluded that the presence of FRP reinforcement alone added flexural stiffness to the slabs, delayed the opening of flexural cracks, and, hence, increased the punching shear capacity. The increase in two-way shear resistance ranged between 2 and 23% depending on the area and configuration of FRP sheets used. Moreover, the failure of FRP

strengthened specimens was by punching shear mode, and the average distance from the punching shear crack to the face of the column was not affected after strengthening with FRP sheets. In contrast, the presence of the shear bolts increased the ductility of slab–column connections and altered the failure mode from brittle punching to a flexural one. Consequently, the use of a combination of FRP sheets and transverse steel bolts increased the ultimate strength which ranged between 23 and 30%.

Ebead and Marzouk [18] in 2004 studied the feasibility of strengthening two-way slabs in flexural and punching shear. Some of slabs were designed with low reinforcement ratios of 0.35 and 0.5 % in order to obtain a ductile flexural failure; others were designed with a high reinforcement ratio of 1.0% in order to obtain a brittle punching shear failure. The strengthening materials used were CFRP strips and GRP laminates. Among the investigated parameters were the effect of material configuration on the internal steel strain and the deflection profile of the strengthened specimens. Cross pattern was used to strengthen the flexural specimen, while an L-shape adopted before in Ebead and Marzouk [38] was used to strengthen the punching shear specimens. They concluded that using FRP composite significantly increased the stiffness and the flexural strength. However, an apparent decrease in both ductility and energy absorption was recorded. The average increase in the ultimate flexural capacity and the average energy absorption of the strengthened specimen using CFRP strips and GRP laminates were approximately 140%, 0.77 and 131%, 0.64 respectively, of the un-strengthened specimens. The dominant failure mode was the debonding between FRP materials and concrete which was the main cause of failure. With respect to the punching-shear specimens, the test results indicated that the use of CFRP strips for strengthening application resulted in a small average increase, within 9% over the unstrengthened specimens. In addition, the strengthened specimens failed under the undesirable sudden punching shear failure mode. This may be attributed to the low stiffness of the CFRP strips individually.

Chen and Li [16] in 2005 investigated the punching shear strength and failure behaviour of reinforced concrete slabs strengthened with GRP laminates

(800×800 mm square patch). Eighteen slabs were cast to study the effect of different parameters such as concrete compressive strength, reinforcement ratio, and the number of GRP reinforcement layers. The test specimens were 1000×1000×100 mm square slabs with the stub column, 150×150×150 mm, monolithically cast with the slab at its centre. It was found that the use of GRP patches changed the mode of failure from ductile flexural punching failure to brittle punching shear failure for lightly reinforced slabs. The observed behaviour and test results showed that GRP laminates significantly increased the punching shear capacity of the slab-column connection, and the lower concrete compressive strength and reinforcement ratio the more enhancement of GRP laminates to the ultimate punching shear capacity.

Not long after, Harajli and Soudki [55] in 2006, using slab specimens quite similar to the slabs used in their previous experimental work [53], conducted an experimental investigation to improve a new technique for strengthening interior slab-column connections in combined flexural and shear modes. The technique was an extension of the technique proposed by El-Salakawy et al. [54] in 2004. It comprises using a combination of shear bolts and external CFRP reinforcement. The bolts are inserted into holes and prestressed against the concrete surface for improving the punching shear capacity, while the CFRP reinforcement are bonded to the tension face of the slabs in two perpendicular directions to increase the flexural strength of the slabs, as shown in Figure (2-19). The bolt force was transmitted to the slab surface through 40 × 40mm × 5mm thick steel bearing plates by tightening the steel bolts, inserted inside the holes, against the concrete using a standard torque wrench before testing. It was found that the use of shear bolts altered the mode of failure from pure punching to flexural or to a combined shear-flexural mode, leading to the improvement in the ductility of failure. However, if a combination of shear bolts and FRP was used the slabs experience a less ductile mode of failure in comparison with the slabs strengthened using shear bolts alone.

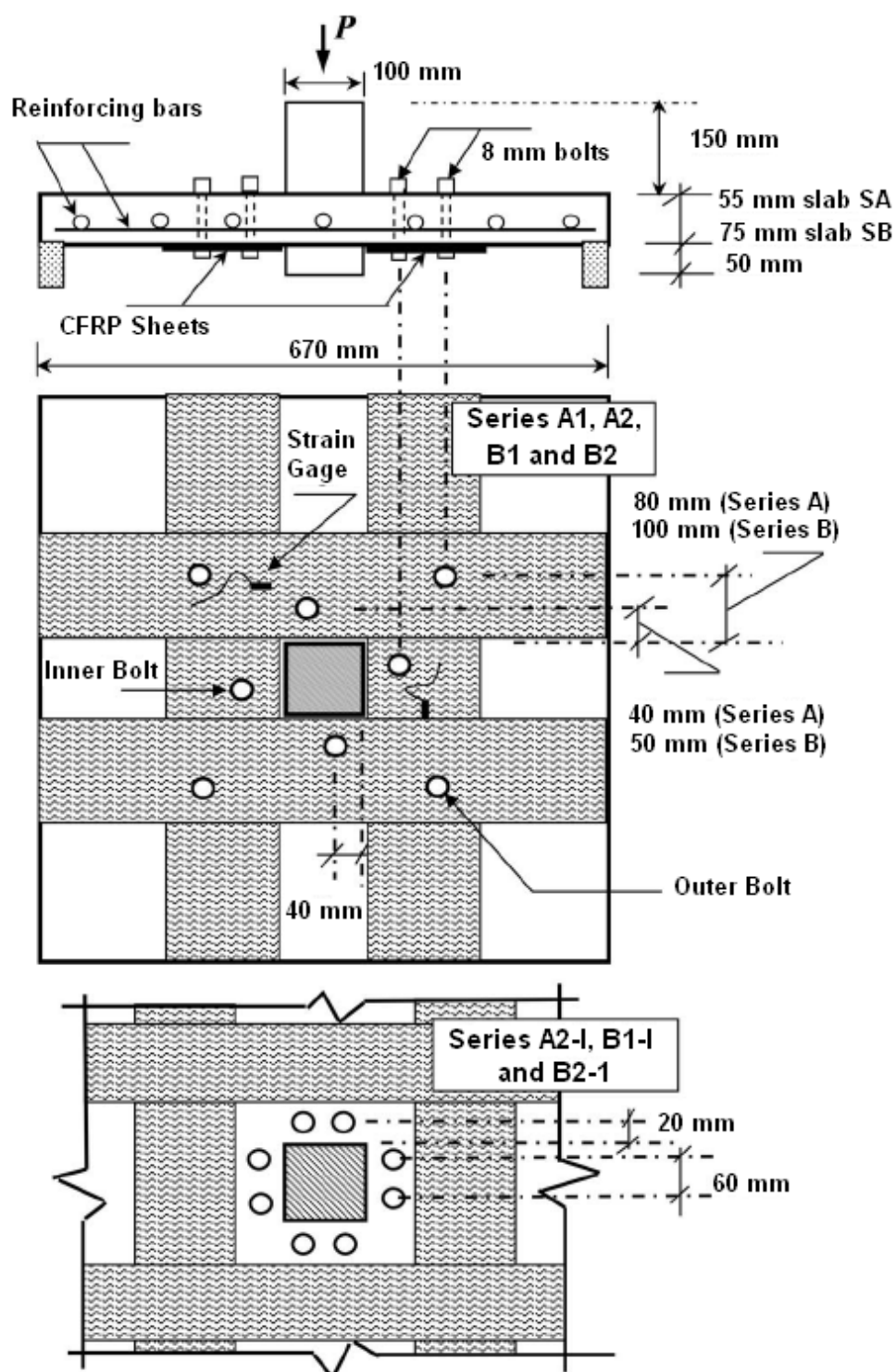


Figure 2-19: Specimen dimension and reinforcement details; Ref. [55].

Depending on the area of the CFRP relative to the area of internal ordinary reinforcement and the mode of failure of the specimens and the CFRP sheets,

the use of FRP reinforcement alone resulted in an increase of the shear capacity ranging between 16% and 32%. Using shear bolts alone resulted in an increase of the punching shear strength up to 23%. However, when a combination of shear bolts and FRP sheets were used, the increase in ultimate shear capacity ranged between 32% and 77%. It is worth mentioning that the two types of bolt configurations evaluated in this study yielded similar results for both the load–deflection response and the increase of the shear strength of the specimens.

Sharaf et al. [19] in 2006 conducted an experimental investigation to study the effect of different parameters on retrofitting interior column-slab connection against punching shear failure. The studied parameters were the amount and configuration of the FRP laminates. They tested one control and five square full-scale slabs (2000×2000×150mm) externally strengthened with CFRP strips up to failure. It was found that the strengthened specimen experienced a brittle failure mode after gaining a remarkable increase in both stiffness and ultimate strength. The measured increase in the load carrying capacity varied from 6 to 16% with corresponding deflection at the ultimate load of 83 and 70% of the control specimen. The amount and the configuration of CFRP laminates controlled the enhancement in the punching shear load.

Bonding FRP fabrics to the tension surface of concrete slabs enhances their flexural strength, which by an indirect way enhances the shear strength of the slabs up to a certain limit that the flexural shear strength of the slab is less than its ultimate shear strength. After that limit, any increase of the amount of FRP reinforcement will not increase the shear strength of the slab or the stiffness too much, but a brittle punching is expected if there is no shear reinforcement. This has been confirmed by Chen and Li [16] in 2005. The same conclusion was achieved for steel reinforced slabs by Moe [17], Elstner and Hognestad [28] and Criswell [25].

#### **2.3.2.1. Prestressed composites for external reinforcement**

Design of concrete structures strengthened with FRP is usually governed by serviceability limit states [11]. That means that only about 50% of the capacity of the FRP reinforcement is used, at best, due to its low stiffness. Consequently, using prestressed FRP reinforcement is more beneficial economically and structurally. A significant improvement in both bending stiffness and ultimate capacity can be achieved in unidirectional members (beams and one-way slabs) [5, 56-59]. Deflections and the number and width of cracks are also further reduced compared to unstressed FRP sheets. However, an apparent decrease in both ductility and energy absorption is observed.

Despite the above mentioned advantages, prestressed FRP application is still limited to unidirectional members, and has not yet been extended to two-way slabs due to its complexity in practice. Recently, Kim et al. in 2008 [60] investigated the flexural behaviour of two-way RC slabs externally strengthened with prestressed and non-prestressed CFRP sheets. They tested four slabs (3000x3000x90mm); one un-strengthened slab (SL1), one strengthened slab with non-prestressed CFRP sheets (SL2), and two slabs with prestressed CFRP sheets (SL3 and SL4). The prestress level applied to the CFRP sheets was 600MPa. They were simply supported at a span of 2700mm and loaded at the centre by 800x800mm square frame as a patch load. The use of non-prestressed CFRP sheets did not increase the first crack load of the slab. However, the prestressed sheets were able to give an increase of 97% in comparison to the control slab. That is the CFRP sheets itself has negligible flexural stiffness compared to the concrete slab, while the prestressed sheets provided an active strengthening effect. In other words, the area fraction of the CFRP sheets was very small to change the behaviour of the slab, but the application of prestressed sheets delayed the flexural cracking. At the same time, a noticeable decrease in the steel strain was observed that resulted in increasing the yield load by 10, 20 and 55% for slabs SL2, SL3 and SL4, respectively. As a result, the slab with prestressed sheets had smaller deflections and curvatures at ultimate load. The increase in the ultimate load for slabs SL2, SL3 and SL4 was 25, 18 and 72%, respectively, as compared to

slab SL1. It is noticeable that the ultimate load of slab SL3 did not increase by the same amount of slab SL4. This is due to the premature debonding failure of the CFRP sheets at the anchor plate.

## **2.4. Failure modes of slabs strengthening with FRP**

The observed modes of failure of RC slabs strengthened with EBR can be classified under the Ultimate Limit State (ULS) design criteria into two main categories as follows:

- a) Those where full composite action of concrete and FRP is maintained until the concrete reaches crushing in compression or the FRP fails in tension.
- b) Those where composite action is lost prior to class (a) failure.

The following sections give a brief description for such failure modes

### **2.4.1. Full composite action failure modes**

Within this category the following failure modes could occur [61]:

- Steel yielding followed by FRP fracture (pure flexural failure);
- Steel yielding followed by concrete crushing (flexural punching failure);
- Concrete compressive crushing (pure punching shear failure)

On the above mentioned, while full composite action of concrete and FRP is maintained, mode one is the most desirable mode. This failure mode happens in a ductile manner with large deflection developing prior to failure as a result of a low ratio of both steel and FRP. A small number of large flexural cracks develop before failure. The crack pattern might approach the full yield line pattern as shown in Figure (2.20 a). The failure starts with yielding of the tensile steel reinforcement, which usually spreads over a wide area of the slab, followed by tensile fracture of the FRP at final failure.

Next is failure mode two which is somewhere between the pure flexural failure and pure punching failure. The flexural strength may be reached with yielding of

the tensile steel reinforcement locally around the column followed by crushing of the concrete in the compression zone, whereas the FRP remains intact. In this case the yield line pattern is not fully developed, as shown in Figure (2-20 b).

For relatively high reinforcement ratios, the flexural capacity of the slab is substantially increased. Consequently, failure is more likely to take place by crushing of the concrete before the steel yields. This is attributed to the large biaxial compression resulting from bending effects plus the vertical applied load. This failure mode is characterized by a large number of fine flexural cracks (radial and tangential) that develop before failure. This mode is brittle and takes place with small deflection. Finally the slab fails in a local area around the column in the shape of a truncated cone, as shown in Figure (2-20b). For a slab with a large amount of shear reinforcement or small column size, the slab may fail in local compression failure, as shown in Figure (2-20 c).

Thus, sections with small amounts of reinforcement fail by FRP tensile rupture, while larger amounts of reinforcement result in failure by crushing of the compressive zone concrete prior to the attainment of ultimate tensile strain in the outermost layer of the FRP [62]. This behaviour is quite similar to the behaviour of steel reinforced concrete slabs observed by Criswell [25].

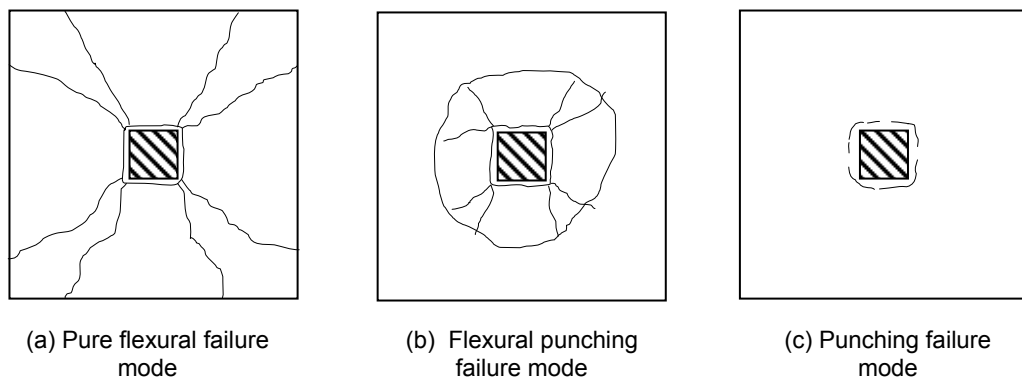


Figure 2-20: Failure modes of full composite action.



### **2.4.2. Loss of composite action failure modes**

These failure modes are so affected by the bond mechanism and to some extent related to the structural element behaviour. Since most of the research previously conducted was on beam structures, so the names of these failure modes are sometimes related to them. For instance, the possible failure modes for beam strengthened with EBR are categorized as follows [11]:

- Debonding of the FRP plate;
- Peel-off (ripping off of the concrete cover);
- FRP plate-end shear failure.

The last one is more related to beam structures. However, the other two failure modes could happen in slab structures; they are explained in the following sections.

#### **2.4.2.1. Debonding failure mode**

Generally, debonding can be localised debonding or complete loss of composite action (bond failure) between the concrete and the FRP reinforcement. The localised debonding means a local failure in the bond zone between the EBR and the concrete substrate. So, the reduction in the bond strength between the FRP and the concrete will not be affected so much. The localised debonding resulting from uneven concrete surface before bonding the FRP composite, or the loss of bond for a few millimetres near to the crack mouth of a flexural member are examples of this type of debonding. Accordingly, localised debonding is not in itself a failure mode which will definitely cause a loss of the load carrying capacity of a member with EBR.

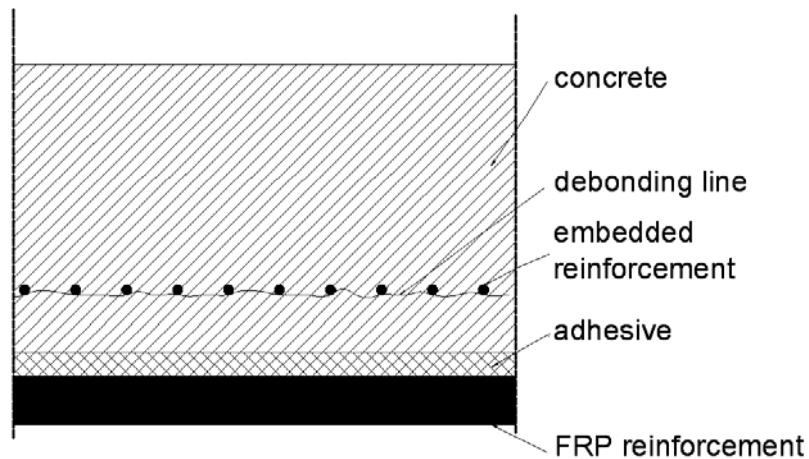
In many cases this localised bonding may propagate, and the composite action is lost in such a way that the FRP reinforcement is not able to resist loads anymore; this failure is called peeling-off. If no stress redistribution from the EBR is possible, peeling-off will be a sudden and brittle failure [11].

Bond failure may take place at different interfaces between the concrete substrate and the EBR; Figure (2-21) shows the different interfaces for bond failure, and namely as follows:

- Debonding in the adhesive (cohesion failure)
- Debonding in the concrete near the surface or along a weakened layer; e.g. along the line of embedded steel reinforcement;
- Debonding at the interface between concrete and adhesive or adhesive and FRP (adhesion failure);
- Debonding inside the FRP (interlaminar shear failure).



(a) Potential bond failure zone



(b) Debonding line along embedded reinforcement

Figure 2-21: Debonding Failure modes.

The second mode is the most common debonding failure. That is the tensile and shear strength of the adhesive material is usually higher than their

counterpart of concrete. Moreover, the new development in strengthening systems, which consists of structural adhesives made to work in harsh environment and more compatible with resin used in FRP manufacturing, reduces the possibility of the other interfacial failure modes. Consequently, failure is more predicted to occur in the concrete, consisting in a few millimetres thick of concrete remaining on the FRP surface [63]. However, in some circumstances the failure may take place in the adhesive material itself as a result of exposure to high temperature or from using a relatively high strength concrete.

#### **2.4.2.2. Peeling-off failure mode**

Peeling-off of FRP composites is a common failure mode in tests of reinforced concrete members strengthened with EBR. This failure mode takes place in the weakest point in the concrete substrate as a result of either low shear or tensile strength. The name of each mode is usually based on the starting point of the debonding process as follows:

- Peeling-off in uncracked anchorage zone; the FRP may peel-off in the anchorage zone as result of bond shear fracture through the concrete substrate. Several methods for eliminating such premature failures have been investigated. These include plate curtailment and the use of end anchorage plates.
- Peeling-off caused by unevenness of concrete surface; due to the imperfections during the surface preparation process a localized debonding of the FRP may take place. This failure may propagate causing a peeling-off failure mode.
- Flexural crack peeling-off, sometimes known as intermediate crack (IC) induced interfacial debonding; the FRP peeling-off may also occur at the tip of a flexural crack due to the horizontal propagation of such a crack.
- Shear crack peeling-off, sometimes known as critical diagonal crack (CDC) induced interfacial debonding.

This mode of failure occurs when the shear capacity of the section is exceeded prior to the load level reaching the flexural strength. Consequently, the

development of shear cracks in concrete beams and flat slabs is inclined and associated with both horizontal and vertical openings [7]. These openings are primarily due to the dowel action and aggregate interlock mechanisms as shown in Figure (2-22). For the same area fraction and spacing of shear reinforcement the crack opening is controlled by the area fractions of the longitudinal bars and the FRP sheet through the dowel mechanism. However, in elements with sufficient internal and external shear reinforcement the effect of vertical crack opening on peeling-off is negligible.

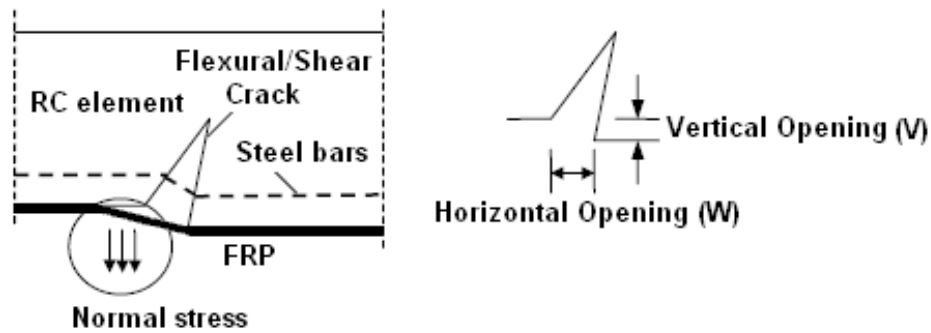


Figure 2-22: Flexural shear peeling-off failure mode.

### 2.4.2.3. Code provisions to maintain composite action

#### 2.4.2.3.1. ACI

The ACI 440-2R [3] approach in preventing debonding failure is too simple. Further, it does not differentiate between the different debonding modes mentioned earlier in Section 2.4.2. It directly limits the effective strain of the FRP to avoid debonding failures as follows:

$$\varepsilon_{fe} \leq k_m \varepsilon_{fu} \quad \text{Equation 2-3}$$

Where  $k_m$  is a factor not greater than 0.90 and calculated as follows:

$$k_m = \begin{cases} \frac{1}{60\varepsilon_{fu}} \left( 1 - \frac{nE_f t_f}{360,000} \right) \leq 0.9 & \text{for } nE_f t_f \leq 180,000 \\ \frac{1}{60\varepsilon_{fu}} \left( \frac{90,000}{nE_f t_f} \right) \leq 0.9 & \text{for } nE_f t_f > 180,000 \end{cases} \quad \text{Equation 2-4}$$

Where  $n$  is the number of FRP plies used at the location where the moment strength is being calculated.

It is worth points out that the term  $nE_f t_f$ , indicates that laminates with greater stiffnesses are more prone to delamination. Thus, as the stiffness of the laminate increases, the strain limitation becomes more severe.

#### **2.4.2.3.2. CEB-FIB Bulletin No.14**

The FIB bulletin [11] provides three alternative approaches to avoid debonding failures. The first approach is similar to the ACI 440-2R [3]. However, it limits the FRP strain in the range of 0.0065–0.0085, which is much higher than the recoded strains in this study and some of the existing tests. The second approach limits the tensile stresses that can be transferred by bond to be within the resistance envelope for tensile forces calculated between cracks. This method is too complicated and more suitable for unidirectional elements rather than planer elements. The last approach combines both the first and the second approach into two steps. However, in the second step the check is done on the maximum interfacial shear stress developed due to the change in the tensile force of the FRP along the member to a design value of,  $f_{cbd} = 1.8f_{ctk} / \gamma_c$ . Where  $f_{ctk}$  is the characteristic tensile strength of concrete. This latter method is deemed to be more appropriate for application in design in terms of simplicity. However, it also neglects important parameters such as the loading configuration and width ratio which make it unsuitable for planar elements.

### **2.5. Bond behaviour of FRP-concrete interfaces**

This mechanism is very necessary to transfer forces from the concrete substrate to the FRP composite and vice versa. Figure (2-23) shows a schematic diagram of a FRP-concrete bonded joint adopted in a single shear pull test [64] to identify the local bond–slip behaviour as well as the bond strength of the joint. The dotted lines determine a typical fracture plane of debonding failure. The fracture plane propagates from the loaded end to the free end of the FRP plate as the loading increases.

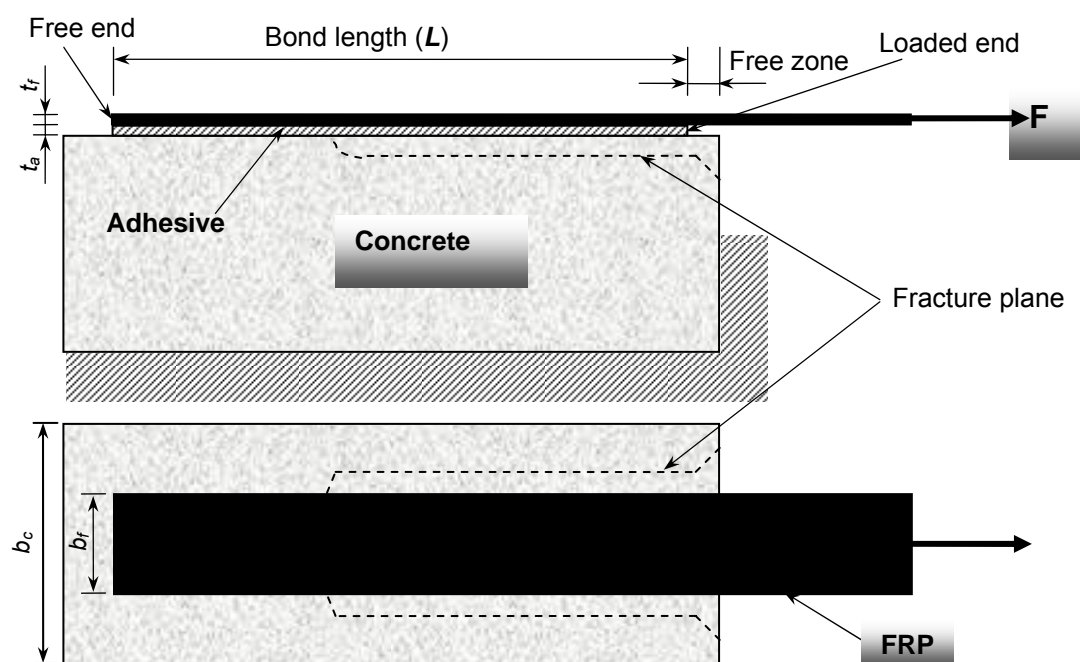


Figure 2-23: Schematic diagram of single shear lap test.

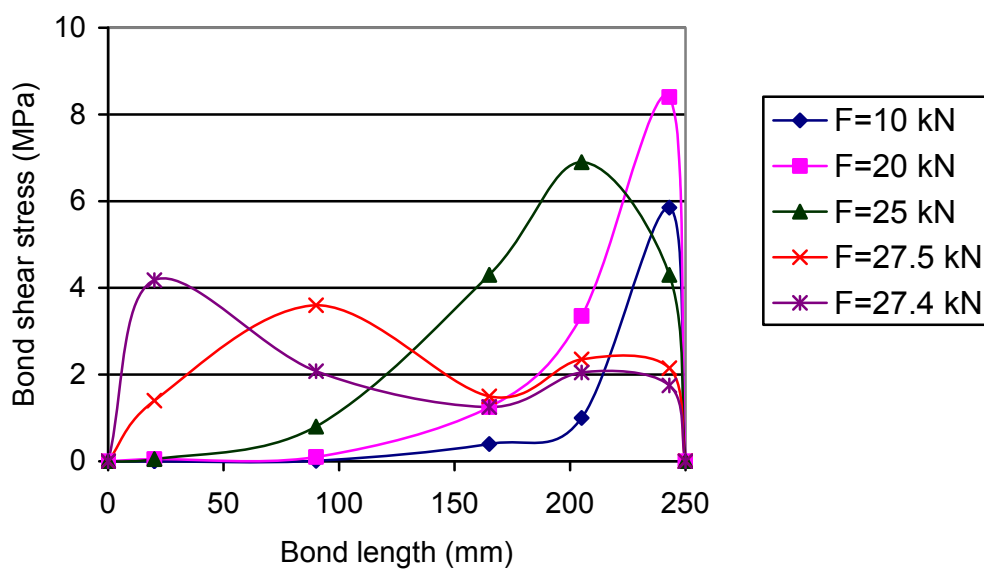


Figure 2-24: Distribution of shear stress along the bond length according to Zilch et al., cited in [11].

The bond behaviour of such joints is governed by six parameters: (a) the concrete strength, (b) the bond length  $L$ , (c) the FRP plate axial stiffness, (d) the FRP-to-concrete width ratio, (e) the adhesive stiffness, and (f) the adhesive strength. Unlike the pull-out tests of steel rebars, there is an effective bond length ( $L_e$ ) beyond which any extension of the bond length  $L$  cannot increase the ultimate load. This disadvantage is the basic reason behind not exploiting the full strength of the EBR.

Another aspect is the distribution of the shear stress along the bond length, which is influenced as well by the normal stresses resulting from the bending effects and perpendicular to the bond area. A typical distribution of the bond shear stress along the bond length for different load levels is shown in Figure (2-24); quoted from Zilch et al. [11]. The CFRP plate was 50mm wide and 1.2 mm thick, with a bond length of 250mm.

### **2.5.1. Bond-slip relationship**

The behaviour of the bond between the EBR and concrete can be described by a shear-slip relation based on strain measurements or load-slip curves. This relates the shear stress locally transferred between the concrete and reinforcement to their relative slip at the interface. The bond-slip relation of the EBR compared to embedded deformed reinforcement (quoted from Zilch et al. [11]) is shown in Figure (2-24). It is clear that the behaviour of the EBR is very stiff, and the total load capacity is much lower than deformed steel bars (the area under the curve represents the amount of energy stored in the reinforcement by bond). This is attributed to the different bond characteristics of EBR which influences the amount of tensile force that could be transferred.

Several models have been developed for design purposes of the FRP-concrete bonded joints. They are graded in complexity based on the number of parameters included in each model. Some of these models are shown in Figure (2-26). The latest model developed by Chen and Teng [63] is considered the most accurate that describes the interfacial debonding behaviour. The model was compared to 253 pull test results from the literature and got the best fit

among the models available in the literature. This model was also adopted in this study.

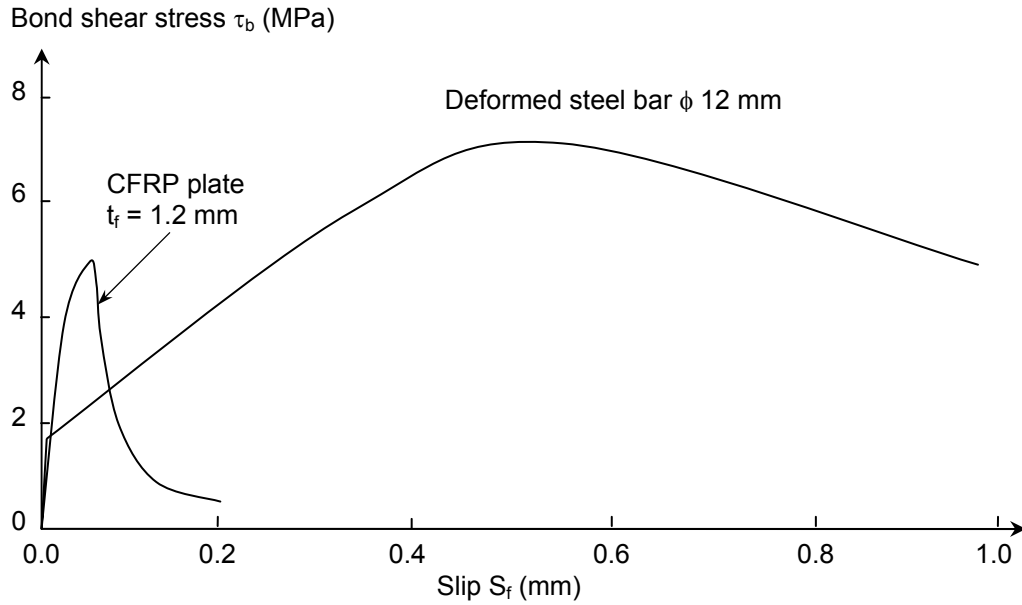


Figure 2-25: Comparison of bond–slip relations for the EBR and steel rebars.

This model accounts for the concrete material properties in terms of ultimate tensile strength and fracture energy as well as the adhesive material properties. The inclusion of the concrete material parameter into the model was based on the finding that the failure of the FRP- concrete interface usually takes place at a few millimetres layer of concrete beneath the adhesive layer. The bond-slip curve consists of nonlinear ascending and descending branches. However, here in this Thesis a linear ascending branch was adopted for the simplicity of data entry into the FE model. The model is given as follows:

$$\tau = \tau_{\max} \frac{S}{S_0} \quad \text{if } S \leq S_0 \quad \text{Equation 2-5}$$

$$\tau = \tau_{\max} \exp\left[-\alpha\left(\frac{S}{S_0} - 1\right)\right] \quad \text{if } S > S_0 \quad \text{Equation 2-6}$$

The maximum shear stress  $\tau_{\max}$  (MPa) is governed by the concrete tensile strength,  $f_t$  (MPa), and the FRP width ratio,  $\beta$ , and taken as follows:



$$\tau_{\max} = 1.5\beta_w f_t \quad \text{Equation 2-7}$$

Where  $\beta_w$  is given by

$$\beta_w = \sqrt{\left(2.25 - \frac{b_f}{b_c}\right) / \left(1.25 + \frac{b_f}{b_c}\right)} \quad \text{Equation 2-8}$$

In which  $b_f$  and  $b_c$  are the widths in mm of the FRP and concrete slab, respectively. The slip  $S_0$  is also dependent on  $f_t$  (MPa), and  $\beta_w$  as follows:

$$S_0 = 0.0195\beta_w f_t (mm), \quad f_t (MPa) \quad \text{Equation 2-9}$$

The factor  $\alpha$  in Equation (2-6) is related to the interfacial fracture energy (the energy required to introduce a unit area of interfacial-bond crack), as follows:

$$\alpha = 1/[G_f / (\tau_{\max} S_0) - 2/3] \quad \text{Equation 2-10}$$

$$G_f = 0.308\beta_w^2 \sqrt{f_t}, \quad f_t (MPa) \quad \text{Equation 2-11}$$

The bond strength of the FRP-concrete bonded joint in terms of interfacial fracture energy is given by:

$$P_u = \beta_1 b_f \sqrt{2E_f t_f G_f} \quad (\text{N}) \quad \text{Equation 2-12}$$

where,  $\beta_1$  is the bond length factor and given by:

$$\beta_1 = \begin{cases} \sin\left(\frac{\pi L}{2L_e}\right) & \text{if } L \leq L_e \\ 1 & \text{if } L > L_e \end{cases} \quad \text{Equation 2-13}$$

The analytical solution for the effective bond length  $L_e$  with the bilinear bond-slip model is given by:

$$L_e = a + \frac{1}{2\lambda_1} \ln \frac{\lambda_1 + \lambda_2 \tan(\lambda_2 a)}{\lambda_1 - \lambda_2 \tan(\lambda_2 a)} \quad (\text{mm}) \quad \text{Equation 2-14}$$

where,

$$\lambda_1 = \sqrt{\frac{\tau_{\max}}{S_0 E_f t_f}}, \quad \lambda_2 = \sqrt{\frac{\tau_{\max}}{(S_f - S_0) E_f t_f}}, \quad a = \frac{1}{\lambda_2} \arcsin \left[ 0.99 \sqrt{\frac{(S_f - S_0)}{S_f}} \right]$$

The factor of 0.99 implies that the effective bond length is the one at which 99% of bond strength of an infinitely long bonded joint is achieved.

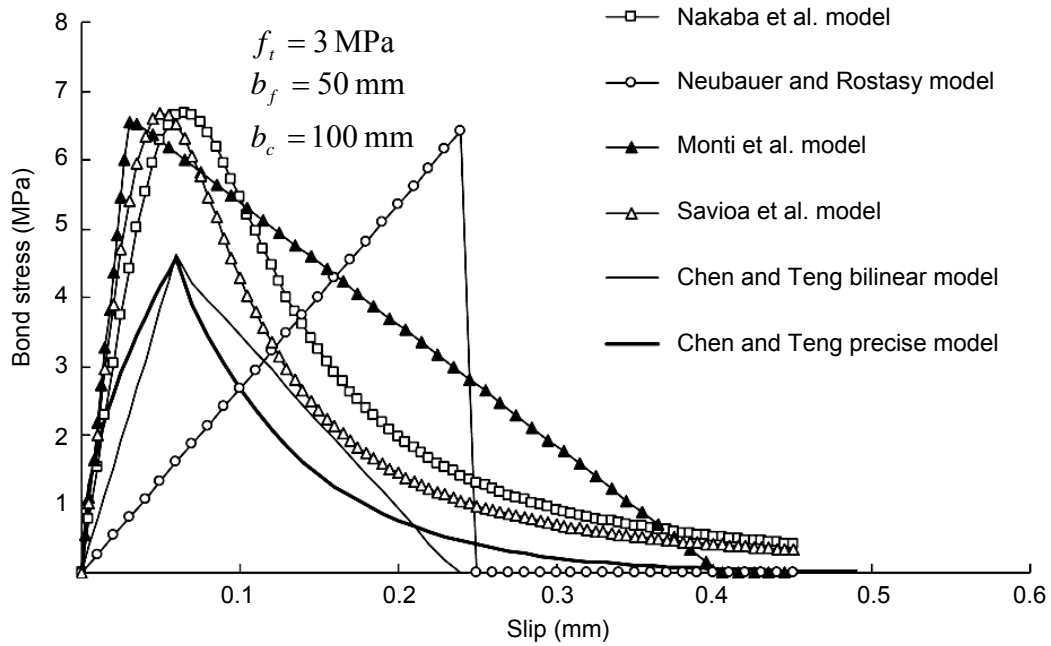


Figure 2-26: Comparison of bond-slip curves available in literature; quoted from Lu et al. [63].

## 2.6. Punching shear analysis of RC flat slabs strengthened with EBR

The punching behaviour of RC slabs strengthened with EBR during the new service life is a complicated problem because of structure complexity, material nonlinearity and the progress of both loads and cracks. Up to now, the available codes for FRP strengthening applications do not provide enough information for such applications. So, most of the research available in the literature tries to deal with the FRP-RC member design by making comparisons and imposing modifications to the steel RC design practice.

Generally, ultimate design, which is adopted in most codes, involves solutions of 'simple' design equations along with some provisions to control deflection and cracking (Serviceability Limit State). These equations are based on closed

form solutions; such as the classical beam analogy or elastic plate theory [2]. The applicability of this method is limited to certain geometries and loading configurations. Thus, it is not applicable to non-conventional slab design in some cases; for example, a slab strengthened with EBR or a slab with internal openings. The FEA may, therefore, provide a more reliable and accurate method to predict the behaviour of two-way slabs strengthened with EBR in both Serviceability and Ultimate Limit States. Hence, it can be concluded that there are two-main analysis categories to analyse the strengthened sections; the classical analysis theories and numerical analysis which is discussed in detail in Chapter 5.

### **2.6.1. Classical analysis approaches**

Classical mechanical models are basically analytical expressions of punching shear transfer mechanisms (internal forces equilibrating punching force) which include: aggregate interlock at the crack, compression and tension in the concrete, dowel force from flexural steel, and tension in transverse reinforcements if present. Several analytical models for punching shear are available in the literature. However, most of them are for slabs with uniformly distributed reinforcement. Consequently, to include the effect of adding the EBR, some modifications have to be included into these models. Only relevant models which account for the flexural reinforcement ratio are considered here. To adopt such models in the analysis of slabs strengthened with EBR, the following assumptions should be satisfied:

- No slip between the external FRP and the concrete substrate;
- Premature separation and shear failure of the FRP is not admissible;
- Tensile strength of the adhesive can be ignored (i.e. bond line is thin).

Based on these assumptions, it is clear that these models can be classified as strength ULS models which cannot account for debonding failure modes.

### 2.6.1.1. Yield line model by Rankin and Long

When a slab with low reinforcement ratio fails in punching mode, the flexural reinforcement may yield before the slab reaches the ultimate load. The failure mode is characterized by formation of cracks along the yield lines; at the maximum moment locations, as shown in Figure (2-27). Finally, the slab is divided into several elastic plates connected by plastic hinges. The ultimate load that the slab can sustain is calculated by considering the equilibrium of all these divided plates or by equating the external work of the slab loads and the internal work of the divided plates.

Assuming the yield line pattern shown in Figure (2-27), Rankin and Long in 1987 developed the following equation to calculate the ultimate vertical load  $V_{flex}$  corresponding to the yield of the flexural steel bars in the concrete slab:

$$V_{flex} = 8M_b \left( \frac{L}{S - c} - 0.172 \right) \quad \text{Equation 2-15}$$

where,  $L$  is the square slab edge length,  $S$  is the support length on four sides,  $c$  is the dimension of the square column section,  $M_b$  is nominal radial moment capacity of the slab.

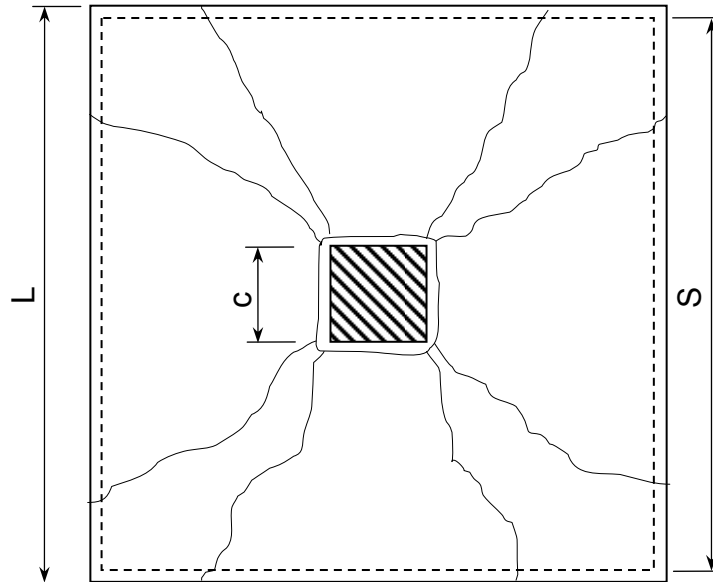


Figure 2-27: Yield line crack pattern according to Rankin and Long [43].

They also proposed an empirical formula to calculate the punching shear strength  $V_s$  of the slab when the slab is subjected to punching shear failure:

$$V_s = 1.66\sqrt{f'_c}(c + d)d(100\rho)^{0.25} \quad \text{Equation 2-16}$$

Where  $d$  is the effective slab thickness,  $\rho$  is the flexural reinforcement ratio.

### **2.6.1.2. Modified Rankin and Long model by Ebead and Marzouk**

The approach is based on calculating the contribution of the added FRP strips by superposition to the flexural capacity  $M_b$  in Equation (2-15) as follows:

$$M_b = M_{b1} + M_{b2} \quad \text{Equation 2-17}$$

where,  $M_{b1}$  is the moment capacity of the unstrengthened slab and is calculated according to ACI 318-05 [23] as follows:

$$M_{b1} = bd^2(\rho - \rho')f_y \left[ 1 - 0.59 \frac{(\rho - \rho')}{f'_c} f_y \right] + \rho'f_y d(d - d') \quad \text{Equation 2-18}$$

where,  $d$  &  $d'$ , and  $\rho$  &  $\rho'$  are the depths and reinforcement ratios for the tension and compression steel, respectively.

$M_{b2}$  is the contribution of the strengthening FRP composites and is evaluated according to the sectional analysis recommended by ACI 440.2R [3] as follows:

$$M_{b2} = E_f t_f \varepsilon_f (h - a/2) \frac{b_f}{\eta l} \quad \text{Equation 2-19}$$

where,  $a$  is the depth of the neutral axis and could be evaluated as  $0.8d\varepsilon_{cu}/(\varepsilon_{cu} + \varepsilon_y)$ ,  $h$  is the slab thickness and the term  $b_f/\eta l$  is introduced to the equation to account for the width ratio since the FRP strips do not cover the whole area of the strengthened slab. Ebead recommended a value of 0.75 for the strengthening efficiency factor  $\eta$  [18]. The FRP strain  $\varepsilon_f$  can be calculated from strain compatibility of the section as follows:

$$\varepsilon_f = \left( \frac{h}{d} - 1 \right) \varepsilon_{cu} + \frac{h}{d} \varepsilon_s \quad \text{Equation 2-20}$$

Where  $\varepsilon_{cu}$  and  $\varepsilon_s$  are the ultimate compressive strain of concrete and steel strain, correspondingly.

#### **2.6.1.3. Critical shear crack model**

Muttoni [65], adopting similar principles to Kinnunen and Nylander [30] model, developed a failure criteria for punching shear of slabs with low reinforcement ratios calling it the critical shear crack theory. It is based on the assumption that *“the shear strength of members without transverse reinforcement is governed by the width and by the roughness of an inclined shear crack that develops through the inclined compression strut carrying shear”*. He assumed that the width  $w_c$  of the critical shear crack is proportional to the slab rotation  $\psi$  times the effective depth  $d$  of the member; see Figure (2-3b). Based on these assumptions, he derived the following formula for the punching shear strength of flat slabs without stirrups:

$$\frac{V_R}{b_0 d \sqrt{f'_c}} = \frac{3/4}{1 + 15 \frac{\psi \cdot d}{d_{g0} + d_g}} \quad \text{Equation 2-21}$$

where  $V_R$  is the shear strength,  $b_0$  is a control perimeter at  $d/2$  from the edge of the column,  $d$  is the effective depth of the member,  $f'_c$  is the characteristic compressive strength of the concrete,  $d_g$  is the maximum size of the aggregate (accounting for the roughness of the lips of the cracks), and  $d_{g0}$  is a reference aggregate size equal to 16 mm.

#### **2.6.1.4. Analytical model by Menetrey**

Menetrey [66], adopting the fracture mechanics concepts of stress transfer across tensile cracks, computed the punching load of the column-slab connection by accumulating the vertical component of tensile stresses around the punching crack as shown in Figure (2-28). The model accounts for the reinforcement crossing the punching crack by adding their contribution based on the principles of superposition. The vertical components and the failure criterion determine the ultimate load. Failure is assumed to occur when the concrete tie at the column vicinity reaches its ultimate strength which is equivalent to the punching strength. Thus the punching shear capacity can be calculated as follows:

$$F_{pun} = F_{ct} + F_{dow} + F_{sw} + F_p \quad \text{Equation 2-22}$$

where  $F_{ct}$  is the vertical component of the concrete tensile force,  $F_{dow}$  is the dowel-force contribution of the flexural reinforcement,  $F_{sw}$  is the vertical components of the forces in the studs, stirrups or bent-up bars which are well anchored and  $F_p$  is the vertical components of the forces in the tendons.

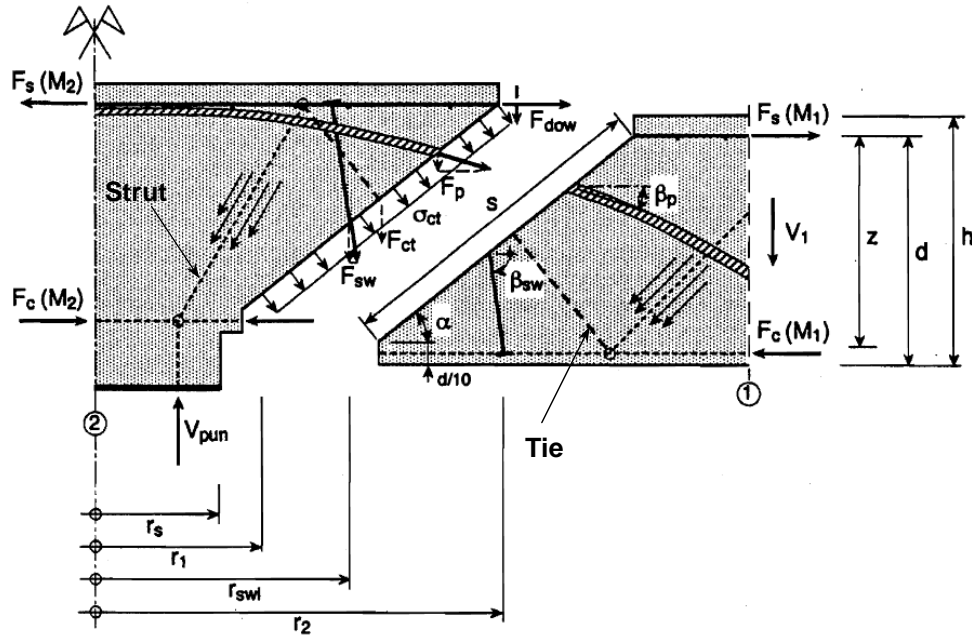


Figure 2-28: Representation of punching strength of reinforced slab; Ref. [66].

The vertical component of the concrete tensile force is calculated by neglecting of the aggregate interlocking and friction stresses as follow:

$$F_{ct} = \pi(r_1 + r_2) s f_t^{2/3} \xi \eta \mu \quad \text{Equation 2-23}$$

where  $\xi$  is a factor accounting for the influence of the reinforcement ratio  $\rho$  on the tensile stresses as follows:

$$\xi = \begin{cases} -0.1\rho^2 + 0.46\rho + 0.35 & 0 < \rho < 2\% \\ 0.87 & \rho \geq 2\% \end{cases} \quad \text{Equation 2-24}$$

$\mu$  is a factor accounting for the size effect law (aggregate size) calculated at a constant ratio  $h/r_s = 2$  and given by  $\mu = 1.6(1 + d/d_a)^{-1/2}$  with slab depth,  $d > 3d_a$  where  $d_a$  is the maximum aggregate size.

$\eta$  is a factor which accounts for the column size,  $r_s$ , which affects the size effect law and is given by:

$$\eta = \begin{cases} 0.1(r_s / h)^2 - 0.5(r_s / h) + 1.25 & 0 < r_s / h < 2.5 \\ 0.625 & r_s / h \geq 2.5 \end{cases} \quad \text{Equation 2-25}$$

Menetrey included the dowel action effect as suggested by Kinnunen and Nylander [30]. He calculated the dowel contribution, adopting the CEB-FIP [20] approach, by summing the contribution of all bars crossing the punching crack as follow:

$$F_{dow} = \frac{1}{2} \sum^{bars} \phi_s^2 \sqrt{f_c f_y (1 - \xi^2)} \sin \alpha \quad \text{Equation 2-26}$$

where  $\phi_s$  is the diameter of the corresponding bars,  $f_c$  is the concrete compressive strength,  $f_y$  is the steel yield strength and  $\xi = \sigma_s / f_y$ .  $\sigma_s$  is the tensile stress in the reinforcement and is obtained by projection of the force in the compressive strut, as shown in Figure (2-27);  $F_{pun} / \sin \alpha$ , in the horizontal reinforcement which gives  $F_{pun} / \tan \alpha$  and by dividing by the sum of the area of the reinforcing bars crossing the punching crack so that:

$$\sigma_s = \frac{F_{pun} / \tan \alpha}{\sum bars A_s}$$

It is noteworthy that the calculation of  $\sigma_s$  is done iteratively since the punching load is not known in advance.

#### **2.6.1.5. Enhancements to Menetrey's model**

Oh and Sim [67], Rochdi et al. [68] and Michel et al. [69] incorporated some modification to Menetrey's [66] model to include the effect of the strengthening material attached on the concrete surface. Oh and Sim [67] assumed that the FRP sheet enhancement could be accounted for by considering the contribution of the concrete cover, that is the strengthening material partially decreased the number of flexural cracks and confined the concrete cover making the strengthened slab resist shear stress. They divided the contribution of concrete to three components as follow:



$$F_{ct} = F_{ct1} + F_{ct2} + F_{ct3}$$

Equation 2-27

where,  $F_{ct1}$  is the vertical component of the tensile force from the compression surface to the compressive reinforcement (or to a distance  $0.1d$ ),  $F_{ct2}$  is the vertical component of the tensile force from  $0.1d$  to  $d$  and  $F_{ct3}$  is the vertical component of the tensile force from  $d$  to  $h$ .

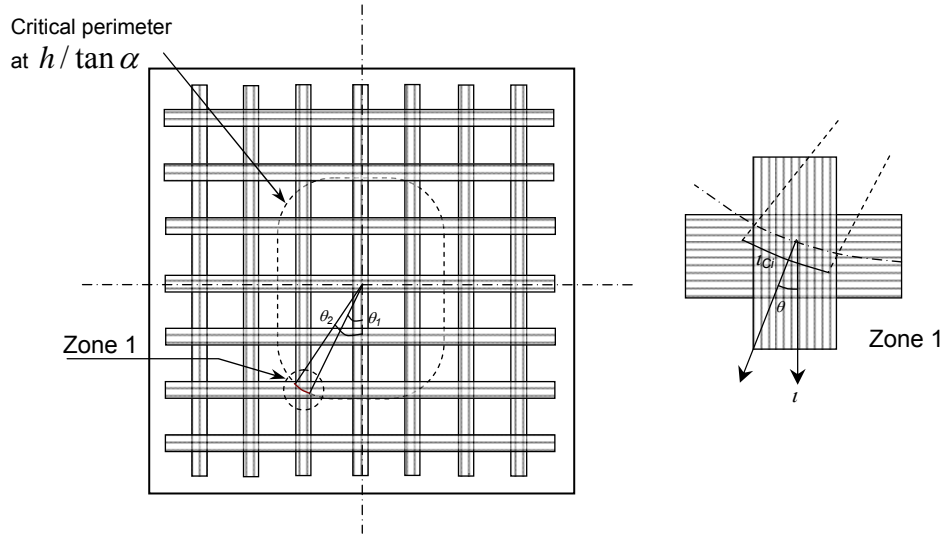


Figure 2-29: Critical perimeter of slab reinforced by composite strip.

On the other hand, Rochdi et al. [68] and Michel et al. [69] included the dowel action contribution of the FRP composites and only the first two components of the concrete contribution so that the punching load is computed for the strengthened slabs as follows:

$$F_{pun} = F_{ct1} + F_{ct2} + F_{dows} + F_{dowf}$$

Equation 2-28

where,  $F_{dowf}$  is the dowel contribution of FRP reinforcement.

The dowel contribution is calculated for the FRP reinforcement crossing the shear crack at the critical perimeter,  $u = 2(C_1 + C_2) + \frac{2\pi h}{\tan \alpha}$  as follows:

$$F_{dowf,\theta} = e_f \cdot \sqrt{f_c \cdot f_{f(\theta)} \cdot (1 - \xi_{f(\theta)}^2)} \cdot \sin \alpha \cdot l_\theta$$

Equation 2-29

where,  $\xi_{f(\theta)}$  is the composite work ratio and equals to  $\left( \frac{\sigma_{f(\theta)}}{f_{f(\theta)}} \right)$ . Where  $\sigma_{f(\theta)}$  is the composite stress in direction  $\theta$  and  $f_{f(\theta)}$  is the strength of the FRP in direction  $\theta$ . In similar way to the steel reinforcement, the FRP stress is obtained by:

$$\sigma_s = \frac{F_{ct} / \tan \alpha}{e_f \cdot 2 \cdot (l_{c,\theta})} \quad \text{Equation 2-30}$$

where  $e_f$  and  $l_{c,\theta}$  are the thickness and width of the FRP plate crossing the shear crack, respectively.

Although these models could predict numerically the shear strength of the slab, they are not able to accurately describe the flow of forces in the connection. For instance, the contribution of concrete at the compression zone by  $F_{ct1}$  and the compression reinforcement by dowel forces could not be justified as this layer of concrete experiences a compression state of stress and the propagation of shear crack towards the compression zone occurs at a later stage, which reduces the probability of the dowel action contribution [32].

## **2.7. Treatment of punching shear in codes of practice**

The provisions for evaluation of the punching shear, in different prominent codes of practice on RC slabs, are presented below. This is useful in identifying the different approaches and the key variables involved. All codes adopt an approach involving a critical section, which is at a certain distance from the column perimeter. The basic rule is that the factored shear stress on the critical section should be less than the nominal shear capacity. Eurocode 2 [21] and the CEB-FIB Model Code 90 [20] have similar provisions for punching shear. In both codes, the critical section is 2d from the column faces. In other codes such as, British Standards BS8110 [22] and the American Code (ACI 318-05) [23] the positions of the critical section are different. In all codes, shear capacity has a contribution from the concrete and the shear reinforcement. The ACI 318-05 does not account for the effect of flexural reinforcement in the calculation of the shear resistance, while the European codes consider the effect.

### 2.7.1.1. Eurocode 2 and CEB-FIB model code 1990

According to Eurocode 2 [21] and the CEB model code [20], for column-slab connection, the factored shear stress  $v_f$  at the critical section, which is located at a distance  $2d$  from the column faces, as shown in Figure (2-30), should not be more than the factored shear resistance  $v_r$ ;

$$v_f \leq v_r = v_c + v_s \quad \text{Equation 2-31}$$

where  $v_c$  is the factored shear resistance from the concrete,  $v_s$  is the factored shear resistance from the shear reinforcement.  $v_r$  will equal to only  $v_c$  in case that there is no shear reinforcement. Factored shear resistance of the critical section without shear reinforcement is;

$$v_c = (0.18/\gamma_c)k(100\rho f_{ck})^{1/3} + 0.1\sigma_{cp} \geq v_{\min} \quad \text{Equation 2-32}$$

where,  $f_{ck}$  is the characteristic concrete strength in MPa,  $\rho$  is the flexural reinforcement ratio;  $\rho = \sqrt{(\rho_z \rho_y)} \leq 0.02$ , and  $\rho_z, \rho_y$  are reinforcement ratios in the  $z$  and  $y$  direction respectively. They are calculated as a mean value taking into account a slab width equal to the column width plus  $3d$  each side,  $k = 1 + \sqrt{(200/d)} \leq 2.0$  with  $d$  in mm, where  $d$  is the mean effective depth of slab,  $v_{\min} = 0.035K^{3/2}f_{ck}^{1/2}$ , and  $\sigma_{cp} = (\sigma_{cy} + \sigma_{cz})/2$ , where  $\sigma_{cy}, \sigma_{cz}$  are the normal concrete stresses in the critical section in  $y$ - and  $z$  directions ( in MPa, positive if compression);

$$\sigma_{cy} = \frac{N_{Ed,y}}{A_{cy}} \text{ and } \sigma_{cz} = \frac{N_{Ed,z}}{A_{cz}} \quad \text{Equation 2-33}$$

$N_{Ed,y}, N_{Ed,z}$  are the longitudinal forces due to prestressing action across the full bay for internal columns and the longitudinal force across the control section for edge columns.  $A_c$  is the area of concrete according to the definition of  $N_{Ed}$ .

The shear stress  $v_f$  at the basic control section due to factored external concentric load  $V_f$  and unbalanced moment  $M_f$  is;

$$v_f = \frac{V_f}{u_1 d} \beta \quad \text{Equation 2-34}$$

where,  $\beta = 1 + \frac{\lambda M_f u_1}{V_f W_1}$  for one direction moment,

$$\beta = 1 + 1.8 \sqrt{\left(\frac{e_y}{b_z}\right)^2 + \left(\frac{e_z}{b_y}\right)^2} \quad \text{for two direction moments, Equation 2-35}$$

$$W_1 = \int_0^{u_1} |e| dl. \quad \text{Equation 2-36}$$

where,  $u_1$  is the length of the basic control section length,  $\lambda$  is the fraction factor of  $M_f$ , ( $\lambda = 0.6$  for rectangular column),  $b_y, b_z$  are the dimensions of the basic control perimeter (Figure 2-30),  $e_y, e_z$  are the eccentricities  $\frac{M_f}{V_f}$  along the  $y$  and  $z$  axes respectively.  $e$  is the distance of  $dl$  from the moment axis.

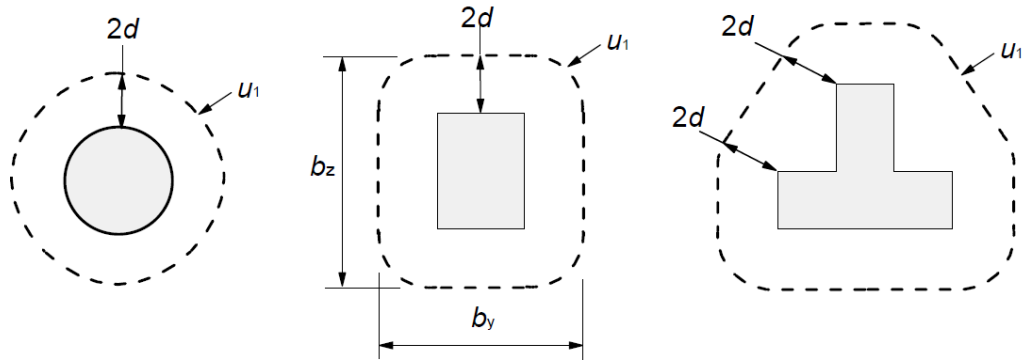


Figure 2-30: Basic control perimeter according to Eurocode 2 [21].

As shown in Figure (2-30), for rectangular columns, the basic control section includes round corners. The code also requires checks on the column face and on the control section outside the shear reinforcement area.

#### 2.7.1.2. British Standard BS 8110

Unlike Eurocode 2 [21], the British Standard BS 8110 [22] takes a critical squared perimeter  $1.5d$  from the loaded area without round corners, for both circular and rectangular loaded areas; see Figure (2-31). The factored shear resistance of concrete to punching is given as;

$$v_r = 0.79 \sqrt[3]{100 \rho \frac{f_{ck}}{25}} \sqrt[4]{400/d} \leq 0.8 \sqrt{f_{ck}} \quad \text{Equation 2-37}$$

where,  $f_{ck}$  is the characteristic concrete strength in MPa,

$\rho = (\rho_x + \rho_y)/2 < 0.03$  is the flexural reinforcement ratio calculated for a width equal to  $u$ , where  $u = 4(c + 3d)$  for circular column and  $u = 4(b + 3d)$  for square column,

$d$  is the effective depth of the slab in mm.

The British code provides two methods to account for the effect of combined shear and unbalanced moment of interior columns; either the eccentric shear expression equation, or simple shear force multipliers.

$$v_f = \frac{V_f}{A_c} \left( 1 + \frac{1.5 M_{fx}}{V_f x} \right) \quad \text{Equation 2-38}$$

Where,  $V_f$  and  $M_f$  are the factored shear force in kN and unbalanced moments in kN.m determined at the centroidal axis of the critical section,  $A_c$  is the concrete area of the assumed critical section in  $\text{mm}^2$ ,  $x$  is the length of the side of the control perimeter parallel to the axis of bending in mm.

Alternatively, the nominal shear force can be multiplied by 15% to account for unbalanced moments at an interior column.

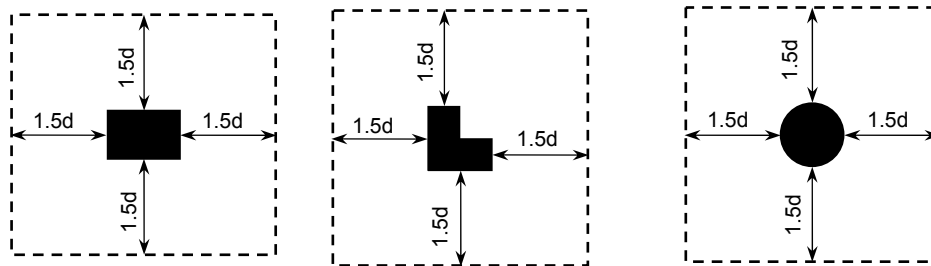


Figure 2-31: Shear perimeter according to BS 8110 [22].

### 2.7.1.3. American code ACI 318-05

The American code [23] employs a basic control section at a distance  $0.5d$  from the faces of the column or the loaded area. Similarly, the factored shear stress  $v_f$  on the control section should not be more than the product of nominal shear strength  $v_n$  times a shear strength reduction factor  $\phi = 0.75$ ;

$$v_f \leq \phi v_n = v'_r \quad \text{Equation 2-39}$$

where,  $v_n = v_c + v_s$ ,  $v_c$  is the shear resistance from concrete,  $v_s$  is the shear resistance from shear reinforcement. The strength reduction factor  $\phi$  can be assigned to  $v_c$  and  $v_s$  and Equation (2-39) can be written as:

$$v_f \leq \phi v_c + \phi v_s = v'_c + v'_s \quad \text{Equation 2-40}$$

The factored shear resistance of the critical section around columns of two way prestressed slabs without shear reinforcement is:

$$v'_c = \phi 0.083(\beta_p \sqrt{f'_c} + 0.3 f_{pc} + \frac{V_p}{b_0 d}) \quad (\text{MPa}) \quad \text{Equation 2-41}$$

where,  $\beta_p$  is the smaller of 3.5 or  $10(\frac{\alpha_s d}{b_0} + 0.15)$ ,  $b_0$  is the perimeter length of the critical section,  $V_p$  is the vertical component of all effective prestress forces crossing the critical section,  $\alpha_s = 4, 3, 2$  for interior, edge, and corner column, respectively. To apply Equation (2-41) the characteristic concrete strength  $f_{ck}$  should not be more than 35MPa, and the average value of the precompression,  $f_{pc}$  for the two directions should not be less than 0.9 MPa, or greater than 3.5 MPa. Otherwise, the following equation is applied:

$$v'_c = \min \left\{ \begin{array}{l} 0.33\phi \sqrt{f'_c} = 0.248\sqrt{f'_c} \\ 0.17\phi \sqrt{f'_c} (1 + \frac{2}{\beta_c}) = 0.128\sqrt{f'_c} (1 + \frac{2}{\beta_c}) \\ 0.83\phi \sqrt{f'_c} (0.2 + \frac{\alpha_s d}{b_0}) = 0.623\sqrt{f'_c} (0.2 + \frac{\alpha_s d}{b_0}) \end{array} \right\} \quad (\text{MPa}) \quad \text{Equation 2-42}$$

where,  $\beta_c$  is the ratio of the long side over short side of the column.

When unbalanced moments also contribute to the factored shear stress in both in the  $x$  and  $y$  direction, the factored shear stress  $v_f$  is given by:

$$v_f = \frac{V_f}{b_0 d} + \left( \frac{\gamma_v M_f e}{J} \right)_x + \left( \frac{\gamma_v M_f e}{J} \right)_y \quad \text{Equation 2-43}$$

where,  $V_f$  is the vertical shear force,  $M_f$  is the unbalanced moment in the  $x$ ,  $y$  direction.  $\gamma_v$  is the fraction of the moment  $M_f$  transferred by shear,

$$\gamma_v = 1 - \frac{1}{1 + 2/3 \sqrt{b_1/b_2}}, \quad b_1 \text{ is the width of the critical section side parallel to the}$$

axis of bending,  $b_2$  being the other side length.  $e$  is the distance from the centre of the critical section to the point where shear stress is calculated.  $J$  is the analogous polar moment of inertia of the shear critical section around the  $x$ ,  $y$  central axes, respectively. In calculations of  $V_f$  and  $M_f$ , the factors for dead loads and live loads are 1.2 and 1.6 for most load combinations.

## **2.8. Conclusion**

Strengthening and repairing of concrete column-slab connections is still an area with differing points of view. That is most of the available research is individual efforts trying to study certain cases. To date the available codes and design guidelines around the world such as, Europe/UK ISE [10], CSA Canadian code [12] and ACI Committee 440 [3] do not provide a determinate outline of how to design and apply FRP composites effectively for such a connection. This attributed to the inadequate distribution of FRP research. Most of this research has involved extensive studies on columns and beams. However, developing comprehensive design guidelines, including slab strengthening, requires an equal investigation of slab structures. Therefore, further research is required to give a full understanding of the punching behaviour of the column-slab connections strengthened with FRP.

By reviewing the existing literature, enhancing the structural response of the column-slab connections, in terms of deformation and stress, can be categorized into two main approaches; enhancing the capacity directly in shear

and enhancing the capacity in flexural. The latter, in which the FRP strips are bonded to the tension surface of a concrete slab, is more suitable for slabs with small thickness and low reinforcement ratio. This method can be developed by using prestressed FRP strips to enable better use of the FRP material. That is the FRP material usually does not develop its full strength if the design of the strengthened member is governed by serviceability limit state.

The variables that should be considered to study the punching behaviour of the column-slab connection strengthened with prestressed FRP plates can be divided into two main groups; one is related to the reinforced concrete connection such as the concrete strength, the reinforcement ratio and the geometry, while the second is related to the FRP materials such as the modulus of elasticity, interfacial bond characteristics and plate geometry. The parameters related to the reinforced concrete have been studied before by other researchers and their effect on the connection behaviour is well known, as illustrated earlier in this chapter. So, the focus of this study is to investigate the effect of the FRP parameters on the connection behaviour. For the FRP prestressed applications, carbon fibre is preferred over glass fibre because of its high modulus of elasticity. So, only CFRP plates are used in the current study which means that the effect of the FRP modulus of elasticity is overlooked.

Considering the identified parameters, this study investigates both experimentally and analytically the punching shear behaviour of the column-slab connection strengthened with prestressed FRP plates, in both serviceability and ultimate limit state.



## **Chapter 3**

# **Experimental programme**

### **3.1. Introduction**

The literature study in Chapter 2 showed different strengthening techniques for the column-slab connections. Some of them are able to increase the ultimate strength of the connection but with a considerable decrease in the ductility, whereas others are able to maintain some ductility with small increase in the ultimate load. In the current study, the experimental work comprises structural tests of a column-slab connection strengthened with pre-stressed CFRP plates externally bonded to the tension surface of the specimen. It aims to investigate the effect of the pre-stressing ratio on the deflection profile, crack pattern, steel reinforcement strain and failure mode. Moreover, material tests were carried out to determine the mechanical properties of the concrete, steel bars and CFRP plates, which were used in constructing the test specimens. This chapter presents the structural tests, including details of test specimens, experimental parameters, preparation methods, instrumentation, experimental setup, and testing procedure. The concrete, steel rebar and CFRP plate tests are also presented, together with their results.

### **3.2. Structural tests**

The focus of the structural tests was to investigate the punching shear behavior of column-slab connections strengthened with pre-stressed CFRP plates applied to the tension surface concrete substrate in the serviceability and ultimate limit state.

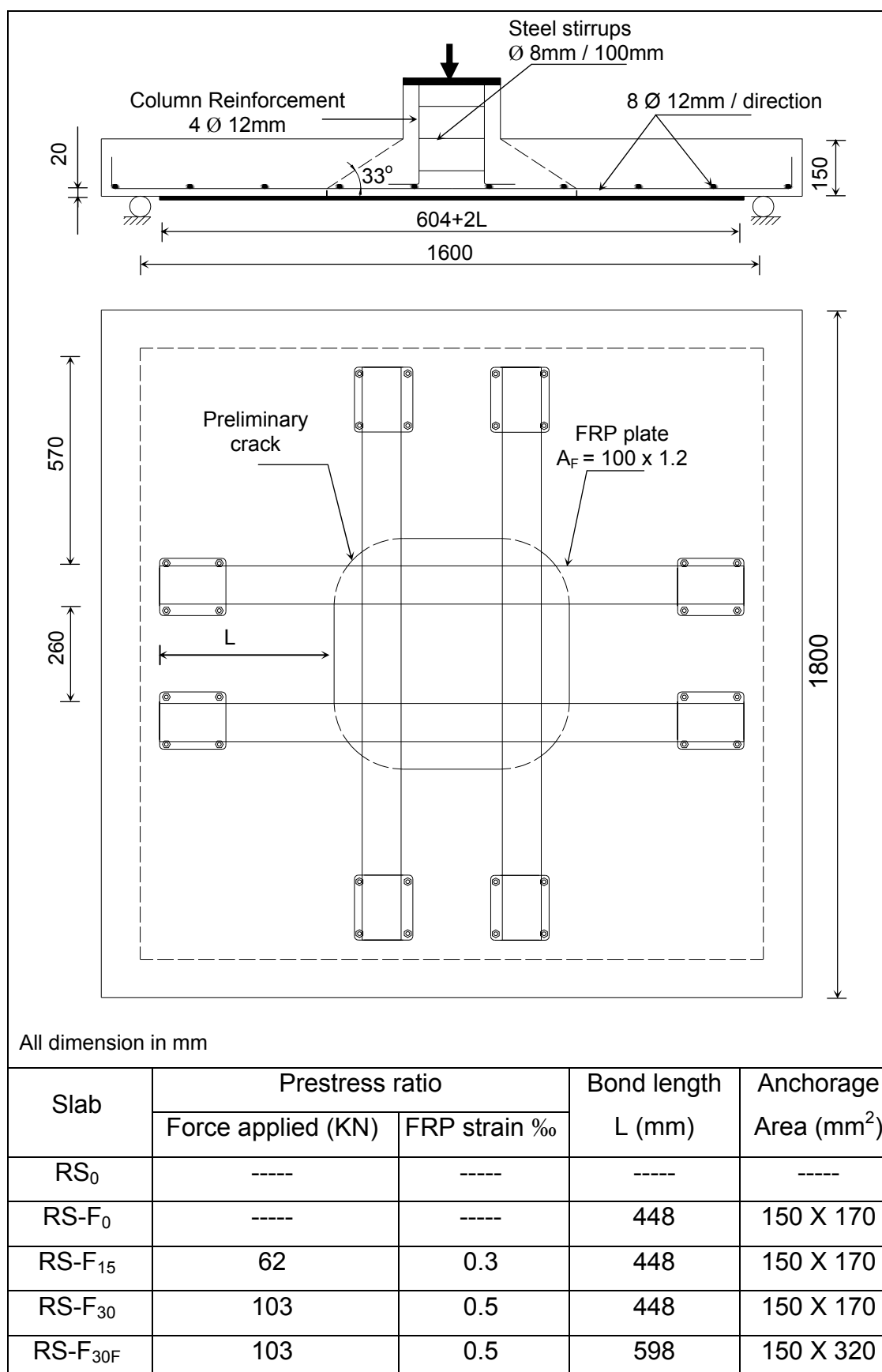


Figure 3-1: Layout, and geometric and reinforcement details of test slabs.

### **3.2.1. Details of test specimen**

The layout of the test slabs, and their geometric and reinforcement details are shown in Figure (3-1). All slabs of the present investigation were 1800×1800 mm square slabs with an overall thickness of 150mm. They were reinforced with eight 12mm diameter standard ribbed bars in each direction which gave the percentage of reinforcing ratio of 0.33%. Such reinforcement ratio may be deemed to represent those slabs represented by curve 4 or 5 in Figure (2-2) which is usually found in practice. To simulate the actual behaviour of a column-slab connection, a column stub of 250x250x150 mm was monotonically cast with the slab. The column stub was reinforced with four 12mm diameter standard ribbed bars, and three 8mm diameter steel stirrups spaced at 100mm. The specimen size was chosen to represent the region of negative bending around an interior supporting column of a medium-sized flat plate floor slab. Assuming the points of contraflexure to be about 0.20 times the span length from the supports, the span length of the prototype represented by the specimens would be 4.5 m so that 150mm would be the minimum thickness one could use for such a span length. The dimension of the slabs and the loading arrangement were similar to those slabs tested by Moe in 1961 [17] .

In all slabs the clear concrete cover to the flexural rebars was set as 20 mm. This cover was expected to be enough for applying a notch of 15mm depth to simulate a precracked slab due to ageing or overloading conditions. The locus of the notched crack was assumed to occur at the critical section for punching shear. Correspondingly, Eurocode 2 [21] suggests that the control perimeter of punching shear is normally taken at a distance of  $2d_{eff}$  from the column face; where  $d_{eff}$  is the effective depth of the slab.

### **3.2.2. Experimental parameters**

The investigation of punching shear behaviour involves three main variables; the concrete strength, the reinforcement ratio and column geometry [1]. However, in the current study, the focus was to study the effectiveness of applying prestressed FRP plates to the concrete tension surface as a new strengthening technique to enhance the punching strength. Thus, the

parameters included in this study were more related to the strengthening scheme rather than the other parameters associated with the concrete material, internal reinforcement and geometry. The main parameters were the prestressing force introduced to the FRP plate and the bond length,  $L$ , with its end anchorage. The bond length was measured from the preliminary crack up to the end of the FRP plate, as shown in Figure (3-1). All parameters were kept the same in the study except the applied prestressing force and bond length,  $L$ .

### **3.2.3. Preparation method**

#### **3.2.3.1. Mould**

The mould was made of a plywood base surrounded by a steel frame fastened with steel bolts. The steel frames were also utilized as a part of the prestressing system, and are discussed later in this chapter. The mould was cleaned and its inside edges were sealed with silicon. To act as a crack inducer, a steel strip of cross section  $18 \times 0.7$  mm was fastened with small-size sink head screws at a distance of  $2d_{eff}$  around the column to the bottom mould surface as shown in Figure (3-2). A wooden ply of cross section  $180 \times 3$  mm was glued with silicon in one direction to the bottom mould surface, as shown in Figure (3-2). This allowed lowering of the FRP plates applied in this direction from the other direction to ensure that the FRP plates were applied evenly to the concrete surface. Two lifting anchors R20mm per each side at the mid-thickness of the slab were designed and installed to enable safe lifting of the slab. Four waved anchors at each end of the FRP plate were cast within the slab to fix the end anchoring plates. In field applications, these anchors are introduced by drilling into the concrete substrate and fixing steel bolts with epoxy resin instead. To ease de-moulding, the inside surfaces of the mould were covered with a thin layer of oil.

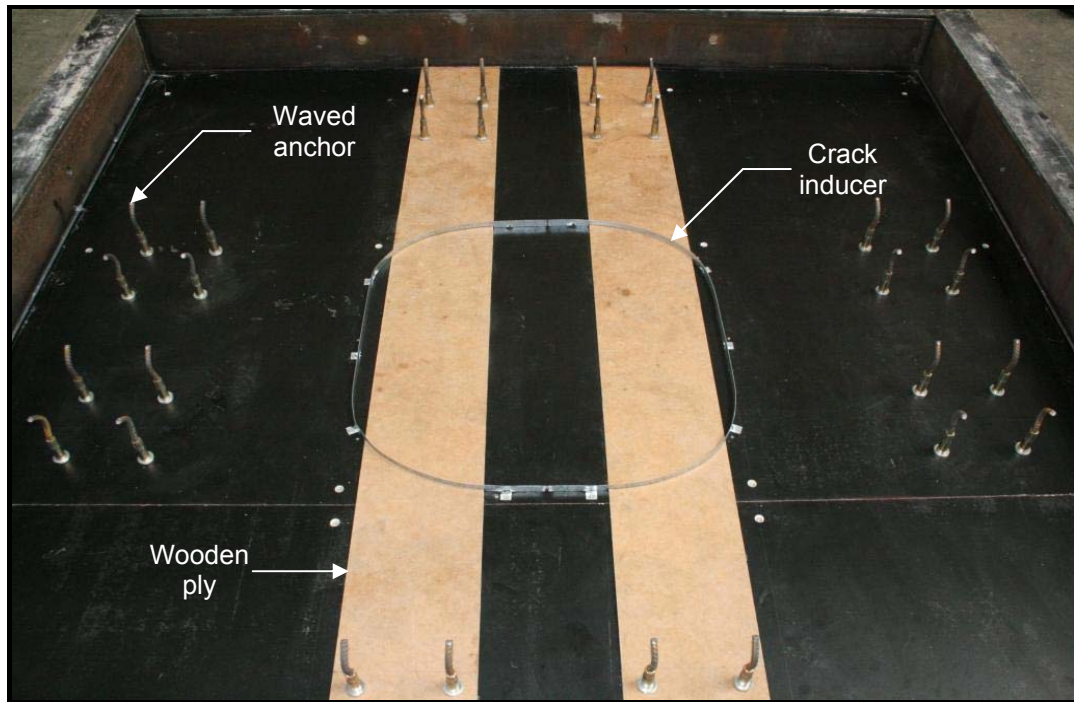


Figure 3-2: The slab mould showing crack inducer.

### **3.2.3.2. Reinforcement**

The FRP plates and steel rebars were cut to the appropriate lengths. While cutting the steel rebars required using power disc cutters or steel scissors, it was possible to cut the FRP plates with a hydraulic guillotine. The column steel stirrups were also cut and bent to the appropriate dimensions. Galvanized coated wires were used to assemble the main steel mesh and column reinforcement. The steel reinforcement was instrumented with strain gauges, as shown later in Section 3.2.5.1, and then carefully placed in the mould. Appropriate size spacers of cement cubes were used to fix the reinforcement mesh at the correct bottom and side covers. Figure (3-3) shows a completed reinforcement of a column slab-connection positioned in the mould and ready for casting.

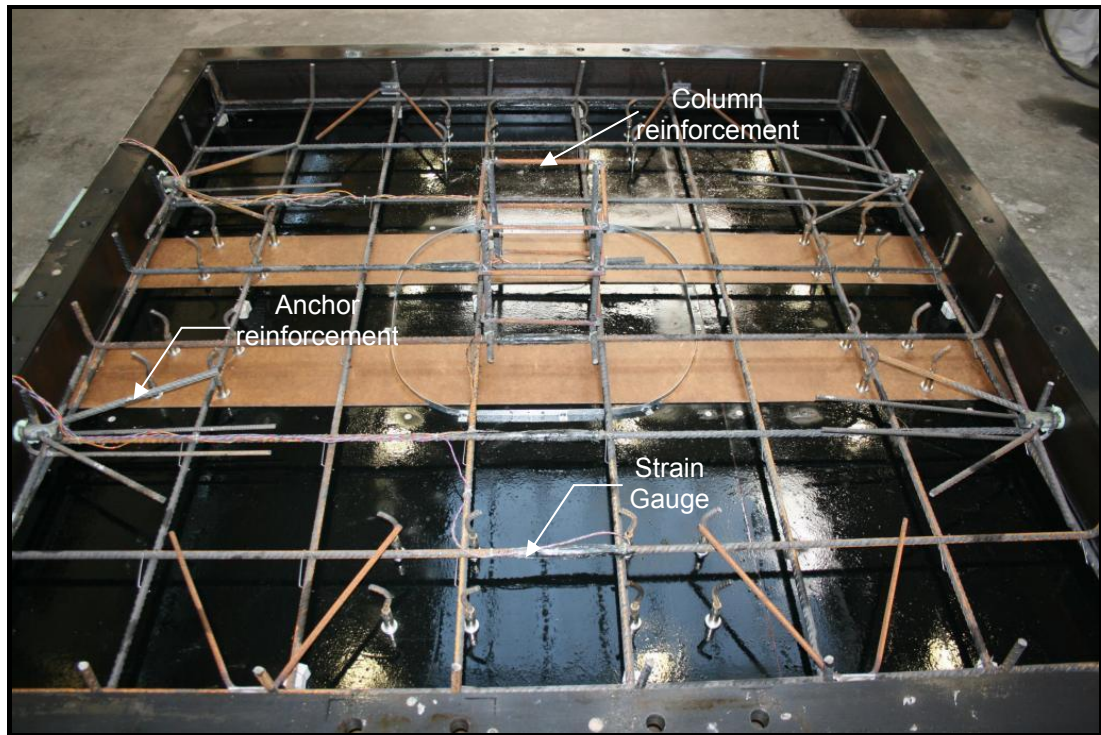


Figure 3-3: Column-slab reinforcement paced in mould.

#### **3.2.3.3. Casting and curing**

One slab was cast each time. A hand vibrator was used to place and furnish the concrete into the mould, as shown in Figure (3-4). Casting and vibration were performed in two layers. For each slab, nine control 100 mm cubes and three 100x200 mm cylinders were prepared from the same concrete batch. After casting, the top concrete surface was levelled as best as possible by using a hand trowel. One hour later, the cast specimen and control specimens were covered with nylon sheets. The next day, the cast element was labelled and covered with wet hessian and nylon sheets. The control specimens were de-moulded, labelled and covered, similar to the specimen. These curing conditions were maintained for one week. At the end of the week, concrete strength development was assessed by testing three of the control cubes. Seven days later, three cubes were tested to monitor the concrete strength at 14 days. At 28 days, the three cylinders were used to conduct split cylinder tensile strength tests. The remaining three cubes were then de-moulded and stored together with the specimen until the date of testing.



Figure 3-4: Casting and cubes' preparation process.

### **3.2.4. Application of prestressing technique**

As mentioned in Chapter 2, there are two main installation methods to achieve FRP prestressing. The prestressing technique used here can be categorized under the second category. In the current section a full description of the prestressing scheme is presented. Equally important, the prestressing frame and its peripheral devices are also given in detail.

#### **3.2.4.1. Description of prestressing Device**

Referring to Figure (3-10), the prestressing system consists mainly of three main parts; the prestress device, clamps and prestressing frame. A summary of the other main components and dimensions is also given in Table (3-1).

The prestress device, shown in Figure (3-5), is built-up of a steel box with two threaded high-tensile steel rods and two clamping heads. FRP plates are sensitive to transverse pressure. Hence, it was suitable to use steel grips similar



to that of the tension machine, while the FRP plate ends were glued with aluminium tabs to distribute the stresses resulting from the clamping force that can damage the specimen, as shown in Figure (3-6). This method is not standardized. Therefore, the clamping head had to be designed and pre-tested. It was realized that intricate analysis of a complex state of stresses was involved. So that, simplified preliminary design was made, and then checked experimentally by testing it under the design forces.

To clarify, the steel grips had to be thick enough to accommodate the transverse pressure from the clamping force  $N$ , as well as the longitudinal tensile stresses transferred to it from the dragging force  $D$  of the FRP plate. Under static equilibrium, the dragging force  $D$  equals the friction force  $F$ . This force, according to the Coulomb law of friction, could be calculated as:  $F = \mu * N$ , where  $\mu$  is the friction coefficient. The coefficient  $\mu$  was taken as one. That is the surface of the clamping blocks, which is facing the aluminium tabs, should be rough enough to prevent slippage of the FRP plate. The clamping force  $N$  was then carried by the screw bolts as shown in Figure (3-6). However, it was important to check that these steel blocks do not yield under the applied loads to prevent any losses of the prestressing force that could result from its deformation. Correspondingly, an ABAQUS model was developed, assuming the preliminary dimensions shown in Figure (3-6), to check the state of the stresses under the design forces.

Table 3-1: Prestress system components

Items description	Item ID	Serial size/dimensions (SI)
Prestress device	A	Shown in Fig. 3-5
Anchor steel plates	B	170 / 320 x 150 x 8 mm
C-channel frame border	C	300 x 90x41
Steel plate	C*	1890 x 90 x10 mm
Broad flange I beam	D	203 x 203 x 86
Supporting channel	E	230 x 75 x 26
Two equal angles	F	90 x 90 x 8 mm
Cover plates	G	300 x 100 x 10 mm



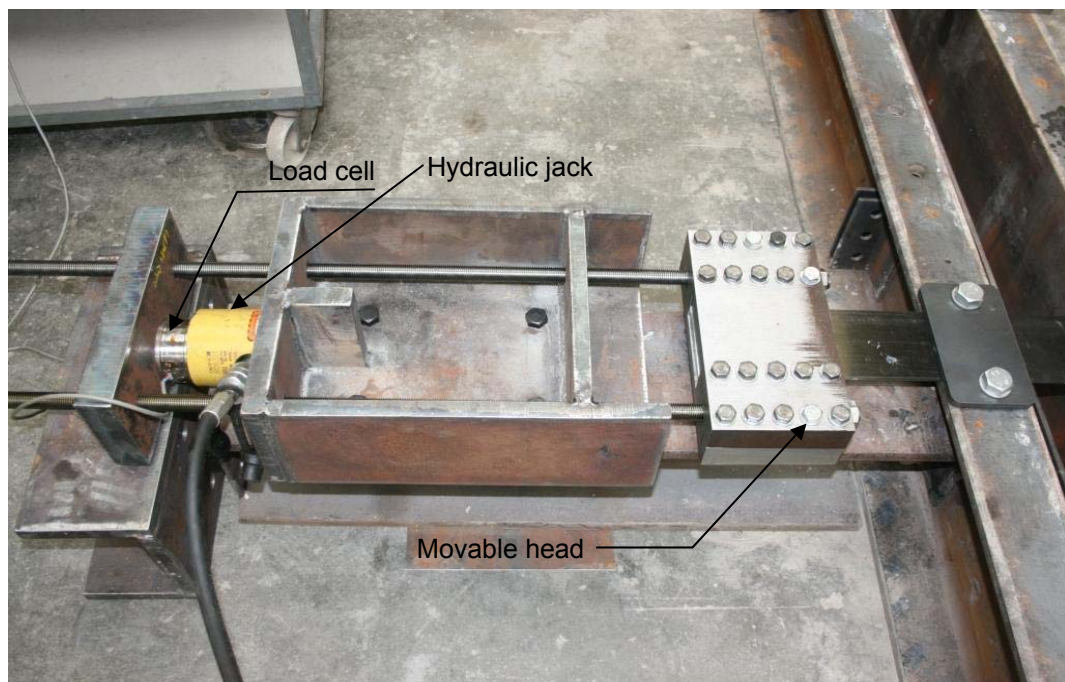
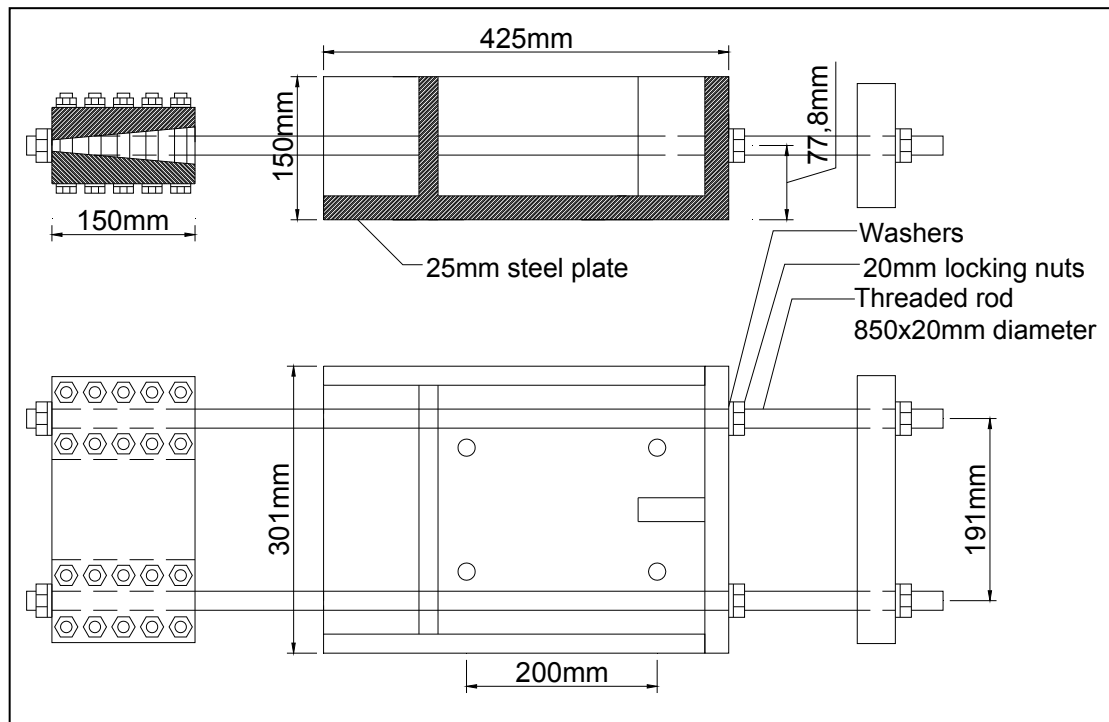


Figure 3-5: Prestress device.

The plot of the Von-Mises stresses, illustrated in Figure (3-7), shows that the clamping head did not yield, and was able to safely transfer a prestressing force up to 150 kN without experiencing too much deformation. The maximum stress recorded was 380 MPa which is less than the yield stress of the steel material

used in the manufacturing of the clamping head. It is noteworthy that the maximum prestressing force applied in this study was 103 kN which was within the limits of the design force.

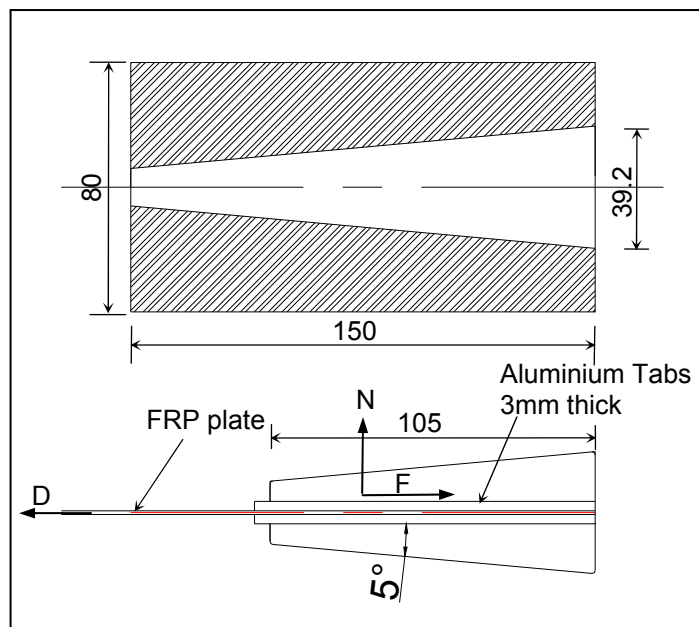


Figure 3-6: Clamping mechanism.

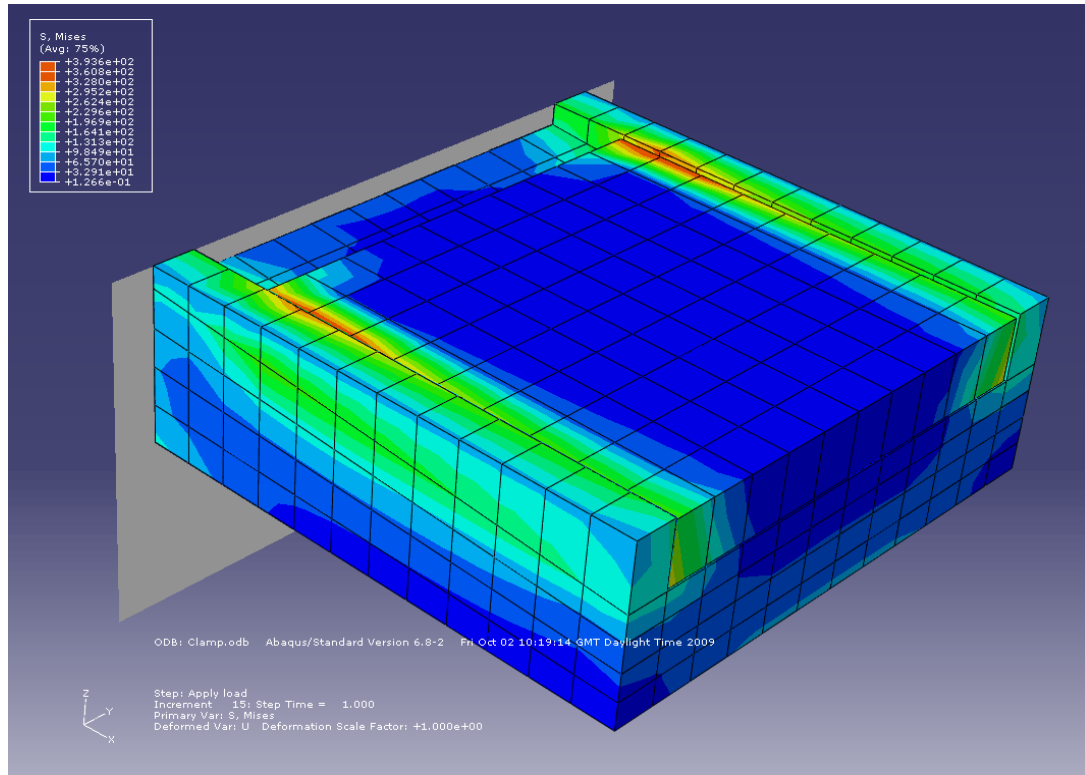


Figure 3-7: Mises-stress plot for the clamping mechanism.

This clamping mechanism has been adopted after trying the mechanism used by Quantrill and Hollaway [5] in 1998. In that mechanism, aluminium tabs were glued to the plate ends as well. However, the plate was sandwiched between two steel plates and then bolted with the configuration shown in Figure (3-8). Three specimens were prepared to test the feasibility of using the same mechanism within the current project. Unfortunately, the average failure load was 47 kN which was 15% of the plate's ultimate strength. The failure pattern comprised longitudinal cracks aligned to the bolts, as shown in Figure (3-9). This failure mechanism is attributed to the discontinuity introduced by the bolts to the longitudinal fibres which results in uneven distribution of the applied force across the section of the FRP plate and concentrates the stresses along the bolts' line of action. Such concentration of applied force triggers the shearing cracks to develop longitudinally, as shown in Figure (3-9).

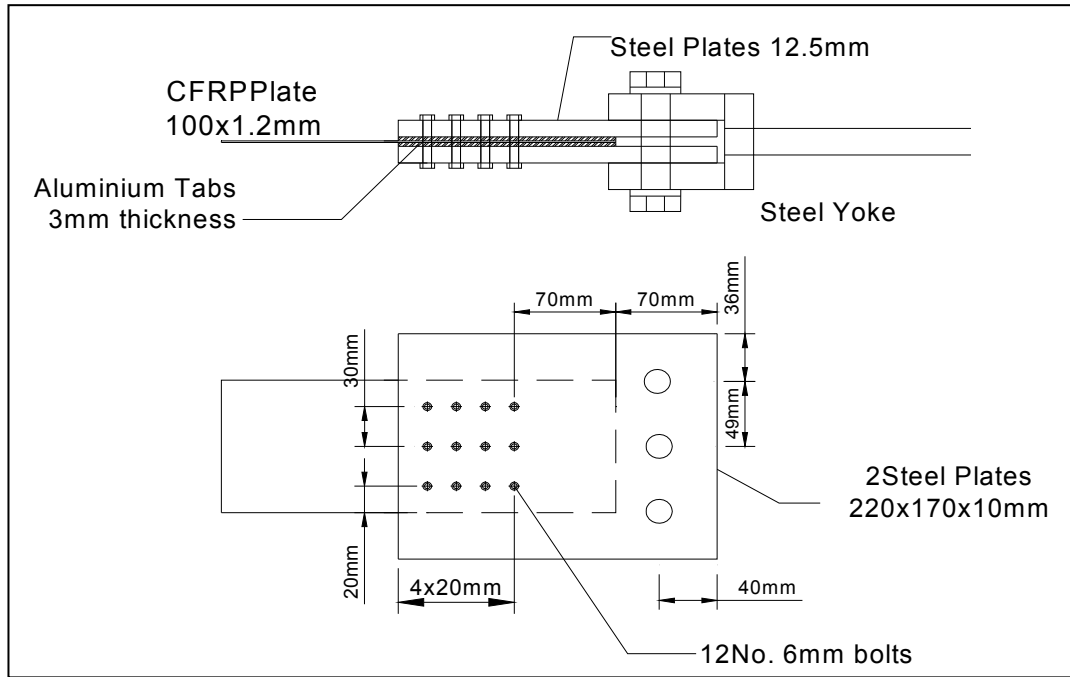


Figure 3-8: Plate end assembly according to Quantrill and Hollaway [5].

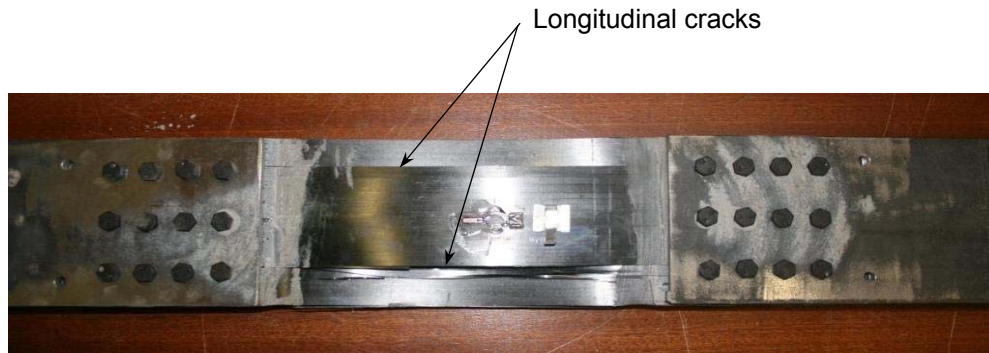


Figure 3-9: Failure pattern of FRP plate connection according to [5].

The anchorages adopted here were steel plates; designated part B, covering the full width of the FRP plate, as shown in Figure (3-10). The plates were fixed to the slab outside the cross-section of the FRP plate to not damage them. They were assumed to transfer the prestressing force from the FRP plate to the concrete substrate by bond. They were designed to carry a load limited by the creep rupture strength of the FRP plate which is 55% of its ultimate tensile strength; according to ACI Committee 440 [3]. In the field application, a non-

corrosive strengthening system could be achieved by using FRP end-plates and bolts instead of those made of steel.

The casting mould was used at the same time as a prestressing frame; designated as part C, as mentioned before in Section 3.2.3.1. It confines the slab from all four sides and was bolted to the ground with clamps, as shown in Figure (3-11). These clamps allow for the horizontal movement of the frame, but prevent the vertical movement; their job was to overcome any tendency of the frame to overturn while applying the prestress force.

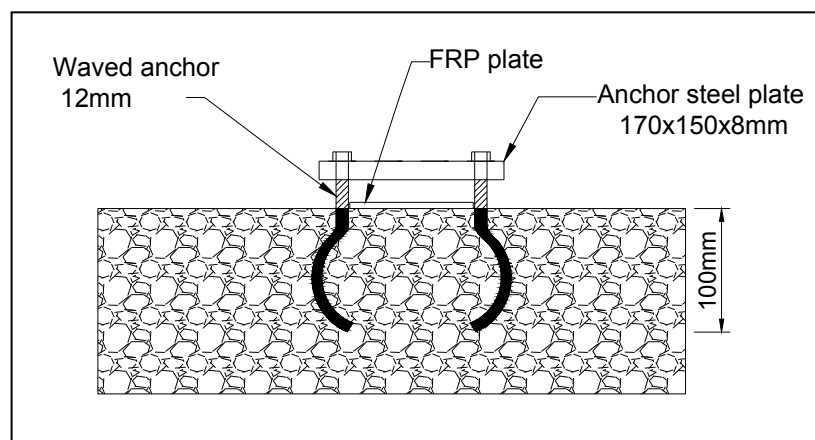


Figure 3-10: Section through anchor plate arrangement (part B).

To enable the slab to react against the prestressing force, the beam ends (part C) were kept unconnected. Some of the other components are not needed in field application such as part D, E and F, as the prestress device can be directly mounted to the concrete surface.

#### **3.2.4.2. Surface preparation and bonding process**

Surface preparation is a principal step in the strengthening procedure. Adhesive will not develop full bond adhesion strength to the surface substrate unless a mechanically sound and clean surface is carefully prepared. To achieve that, a surface grinder was passed back and forth along the aligned path until uniform exposure of aggregate was achieved. The vacuum cleaner attached to the grinder enabled achieving a clean surface from dust and loose particles

instantaneously. The CFRP surface was prepared for bonding according to BS 6270 [70] by carefully rubbing it using sand paper. Then, a degreasing solvent was used to clean its surface from any grease or dust.

The adhesive was applied to both the prepared substrate and the composite plate with a grooved trowel to ensure there was a sufficient excess which enabled the spread of the adhesive from one surface to the other. Such application process prevents the formation of air bubbles when joining the two surfaces together. The glue-line thickness was achieved by adjusting the grinder to cut a 2-mm depth in the concrete substrate. For the unstressed plates, the glued plates were pushed onto the glued substrate within the open life of the adhesive by using a hard rubber roller to squeeze the adhesive from both sides of the plate edge and ensure no air voids, while in the case of the prestressed plates this was achieved by tying the nuts of the anchor plates which pushes the FRP plate onto the glued substrate. The tendency of the stressed plate not to deform out of its plane was enough to develop a bond pressure when pushed towards the concrete substrate. Finally, the surplus adhesive was removed from the sides of the plate.

#### **3.2.4.3. Application of plate prestress**

The strengthening scheme has two FRP plates per each direction. The application of prestress to the plates was conducted in series; one after another. Every time, the adhesive was firstly applied for both the bonding surface of the FRP plate and the concrete substrate as mentioned before in Section 3.2.4.2. The ends of the FRP plate were then placed in the prestress device, while its bonding surface was facing the concrete substrate. Both the anchor plate bond surface and the opposite outer FRP surface were prepared in advance according to BS 6270 [70] and the adhesive layer was applied for both surfaces. Having the anchor plates fixed in their positions without fully tying its bolts, so that it was ready to apply the prestressing force.



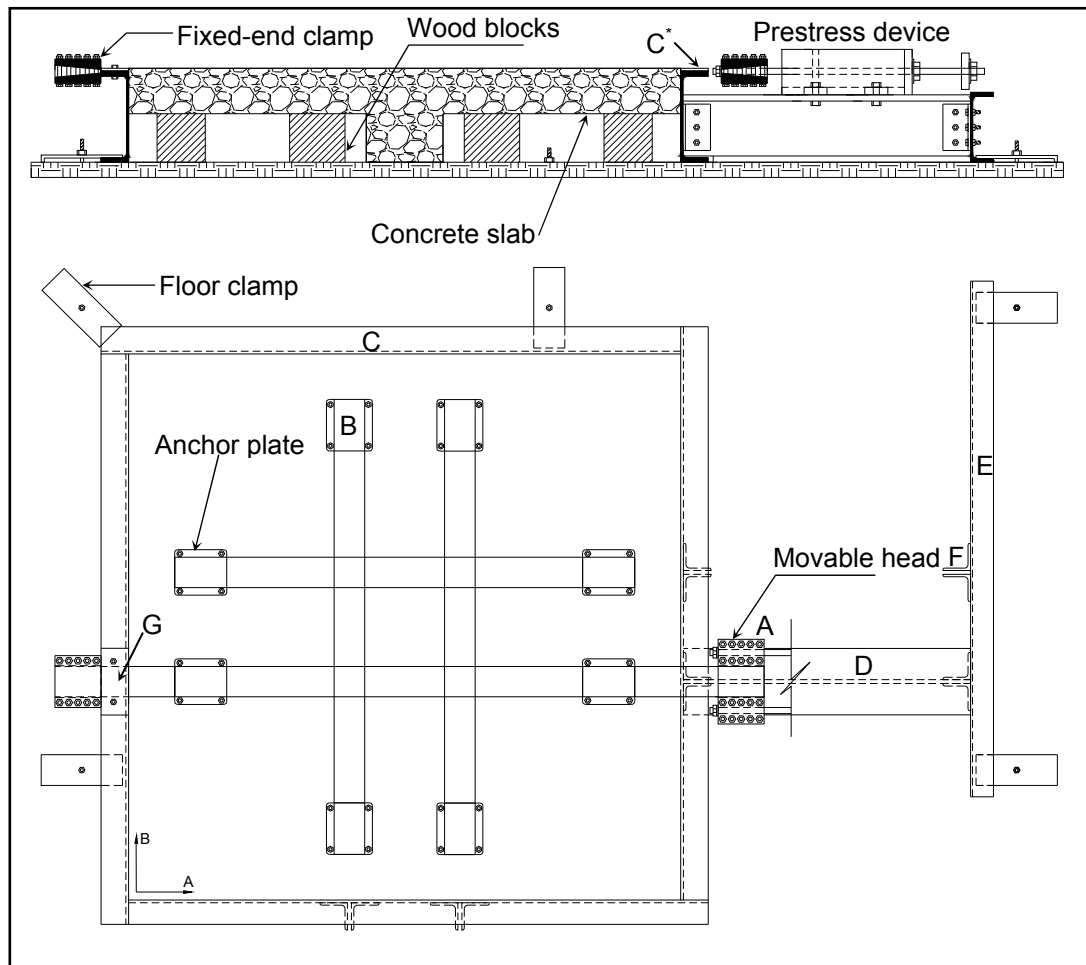


Figure 3-11: Frame used for plate prestressing.

Prestress load was monitored by using a load cell connected to the prestress device, as shown in Figure (3-5). At the same time, strain gauges were bonded to the plate on its outer-surface, as shown later in Section 3.2.5.1, to compare the prestress level with value from the load cell. The load was applied by a hydraulic jack connected to the prestress device. The tensile load to be applied to the plate in each case was achieved when the product of multiplying the nominal prestress percentage by the ultimate strength of the plate is reached. The latter was based on the material tests conducted to get its mechanical properties and is given in Section 3.3.2.1.

Once the designated prestress value is reached, the bolts of the anchor plates were tied firmly to enable curing of the adhesive under a small amount of pressure. The locking nuts were tied until the dial of the pump started to go down which meant that the load was carried by the nuts not the jack. Having the load carried by the nuts has the advantage of maintaining the same load over the adhesive setting time, as sometimes any leakage in the pump would exaggerate the prestress losses.

Finally, after completing the prestressing stage, the prestress transfer was carried out by slowly unscrewing the locking nuts. Such process ensured a mild transfer rate that could mitigate the propensity of premature debonding failure. This method was easily applied for the specimen prestressed with 15%, while for the higher prestressing ratios the transfer process was as follows:

1. The oil was pumped in the hydraulic jack till the dial reads the prestress force,
2. The locking nuts were unscrewed a complete turn,
3. The pressure was released slowly from the pump until the dial read a force less by 10% of the prestress force,
4. Repeat the previous steps until transferring all the amount of the prestress force.

Once the four FRP plates were bonded to the concrete substrate, the excess lengths of the FRP plates were cut up to the anchor plate and the slab was removed from the prestressing frame shown in Figure (3-11).



### 3.2.5. Instrumentation

Internal and external instrumentation was used for each slab. Internally, seven strain gauges were used to measure the rebar strains. Externally, four strain gauges were used to measure the concrete compressive strain. In slabs strengthened with FRP plates, eighteen strain gauges were mounted on the plates to measure the average longitudinal strain. Different ranges of linear potentiometers (pots) were used to measure deflections, support settlements, crack widths and average surface strain.

#### 3.2.5.1. Strain gauges

Three groups of strain gauges were used to monitor the strain component at the designated locations. The first group was the steel reinforcement gauges. They were well distributed over the reinforcement mesh to track the strain variation around the column area and over the slab, as shown in Figure (3-12).

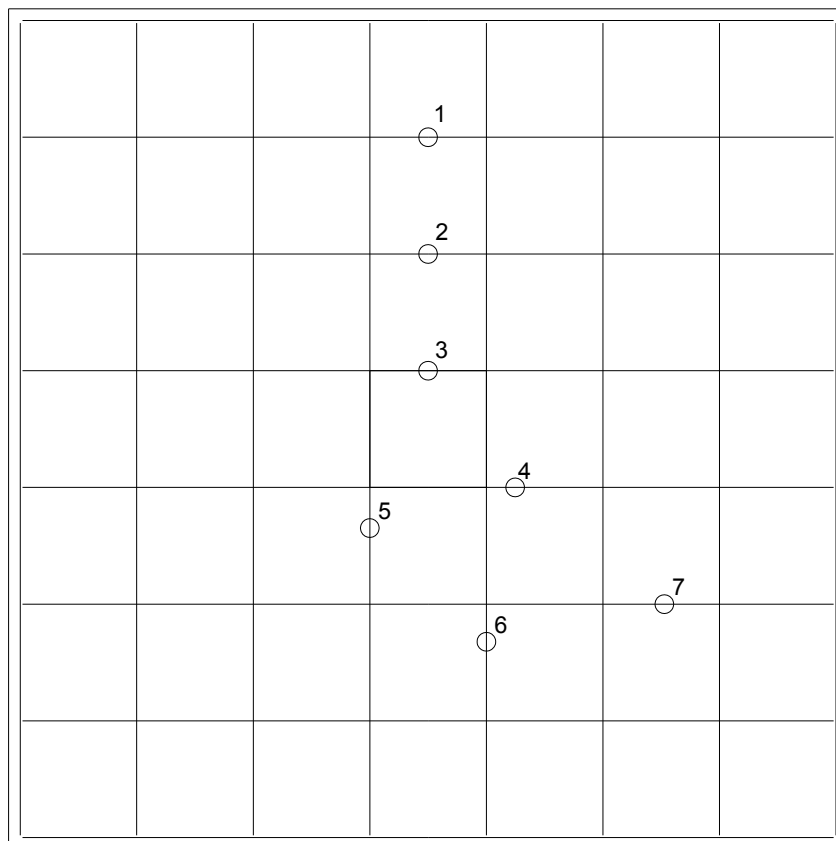


Figure 3-12: Arrangement of steel strain gauges over a specimen.

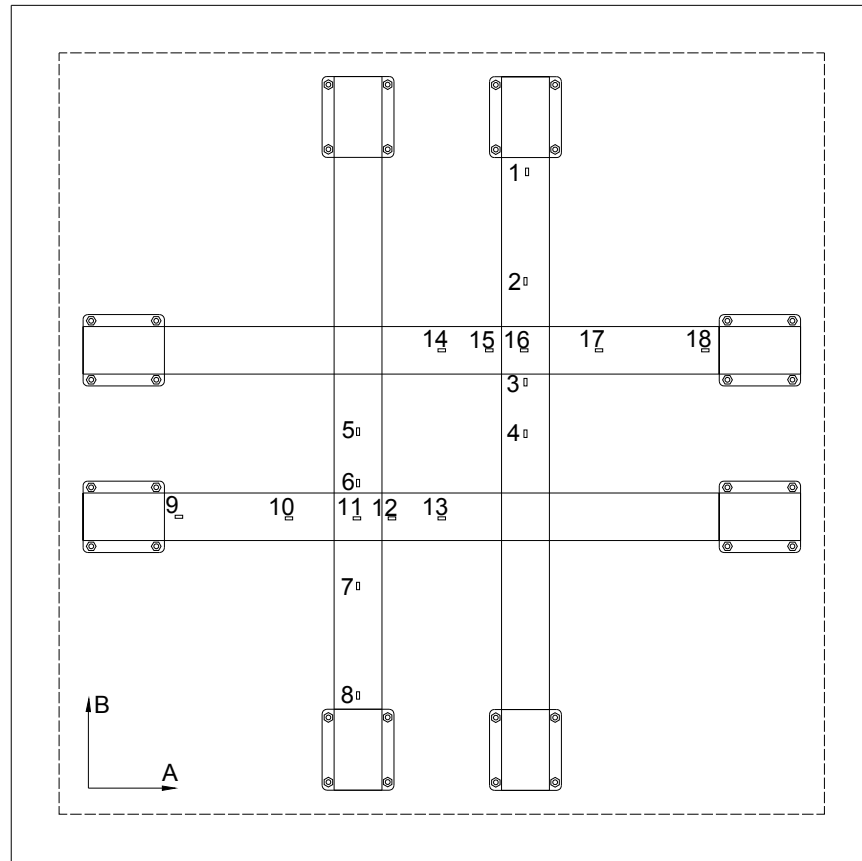


Figure 3-13: Arrangement of FRP strain gauges.

The second group; shown in Figure (3-13), was the external FRP reinforcement gauges. These gauges were used to monitor the strain levels while applying the prestressing force and to evaluate the bond status of the FRP plate during the test. Eighteen strain gauges were installed in the fibre direction and divided into four main sub-groups, as follows:

- (1) The first FRP strip included gauges number 1, 2, 3 and 4 located at distances of 200, 430, 640 and 750 mm measured from the end anchor plate towards the centre of the slab, respectively;
- (2) The second FRP strip included gauges number 8, 7, 6 and 5 located at distances of 200, 430, 640 and 750 mm measured from the end anchor plate towards the centre of the slab, respectively;
- (3) The third FRP strip included gauges number 9, 10, 11, 12 and 13 located at distances of 200, 430, 575, 640 and 750 mm measured from the end anchor plate towards the centre of the slab, respectively;

- (4) The fourth FRP strip included gauges number 18, 17, 16, 15 and 14 located at distances of 200, 430, 575, 640 and 750 mm measured from the end anchor plate towards the centre of the slab, respectively.

In the third and the fourth strip both gauge number 11 and 16 were used to evaluate the strain at the overlapping positions.

The strain gauges used for both steel and FRP plates were foil-type, three-wired temperature-compensating, with a resistance of 120 ohm, gauge length of 6 mm and base material dimensions of 3.4×10 mm. They were bonded to the surface of both reinforcements with proper adhesive. Specialized silicon was used to cover the steel strain gauges to protect them during casting, and to prevent moisture uptake.

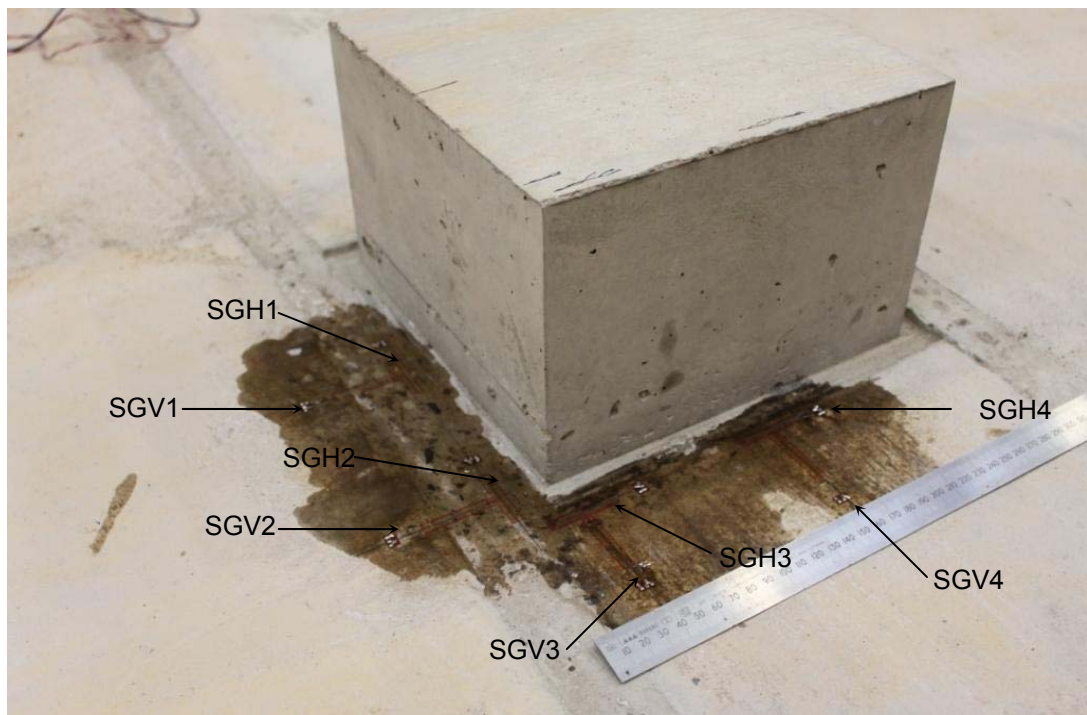


Figure 3-14: Concrete strain gauges glued to concrete surface around column.

The last group was the concrete gauges. It comprised eight strain gauges to measure the average concrete compressive strain. They were located close to the column as shown in Figure (3-14). The concrete strain gauges used were wire-type, three-wired, with a resistance of 120 ohm, gauge length of 34 mm

and base material dimensions of 6×40 mm. they were bonded to the concrete surface with adhesive. Specialized silicon was used to cover the strain gauges to prevent moisture uptake. Figure (3-14) shows the concrete strain gauge.

#### **3.2.5.2. Linear potentiometer (pots)**

Six pots were used to measure vertical deflections at mid-span and along the centreline of the slab. Another five were used to measure settlements at the supports. These pots were held by stands, which were attached to a ground-supported purpose-built frame around the test specimen. The needles of the pots were positioned on the top surface of the concrete, after smoothing it.

Additionally, eight pots were used to measure the horizontal and the vertical crack opening displacement and the average surface strains at the induced preliminary crack, over a gauge length of 100 mm. These pots were mounted on steel brackets glued to the concrete surface. Figure (3-15) shows the arrangement of pots over the test specimen and around the induced crack.

#### **3.2.6. Test setup**

All slabs were tested under concentrated loading and simply supported along all four edges with the corners free to lift, as shown in Figure (3-16). The load was applied at the specimens by means of 2500-KN capacity hydraulic ram acting against a reaction frame. The oil pressure was furnished through an Enerpac oil pumping unit with a load maintainer. A stiffened steel plate was used to distribute the actuator load over the column stub. A gypsum paste of 100 mm width was placed on the top of the supporting frame; within the override distance of the slab over the supporting beams. This pad provided an even contact between the supporting beams and the test slab. Some details of the test setup are shown in Figure (3-16).

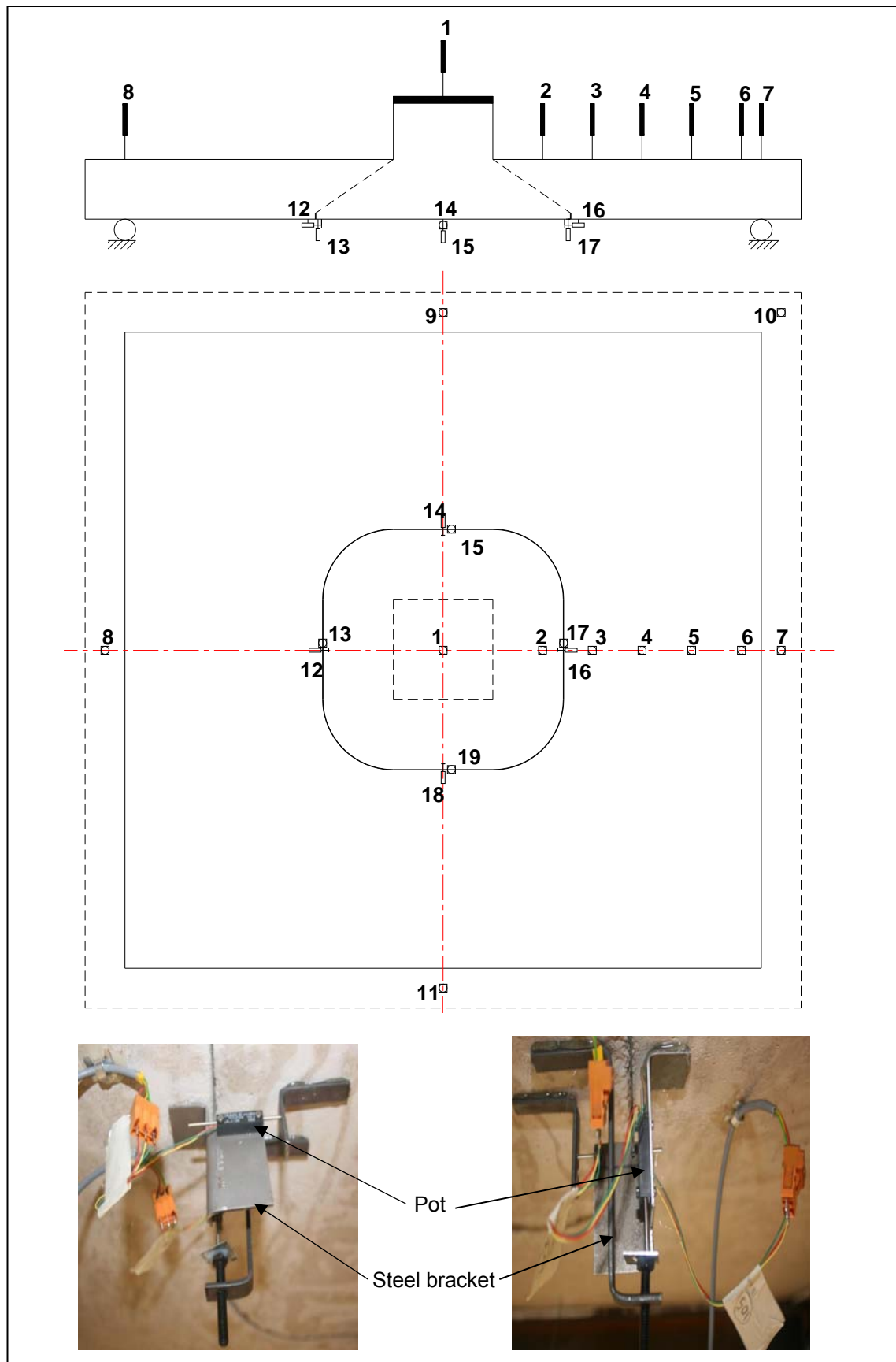


Figure 3-15: Arrangement of pots over specimen and around induced crack.

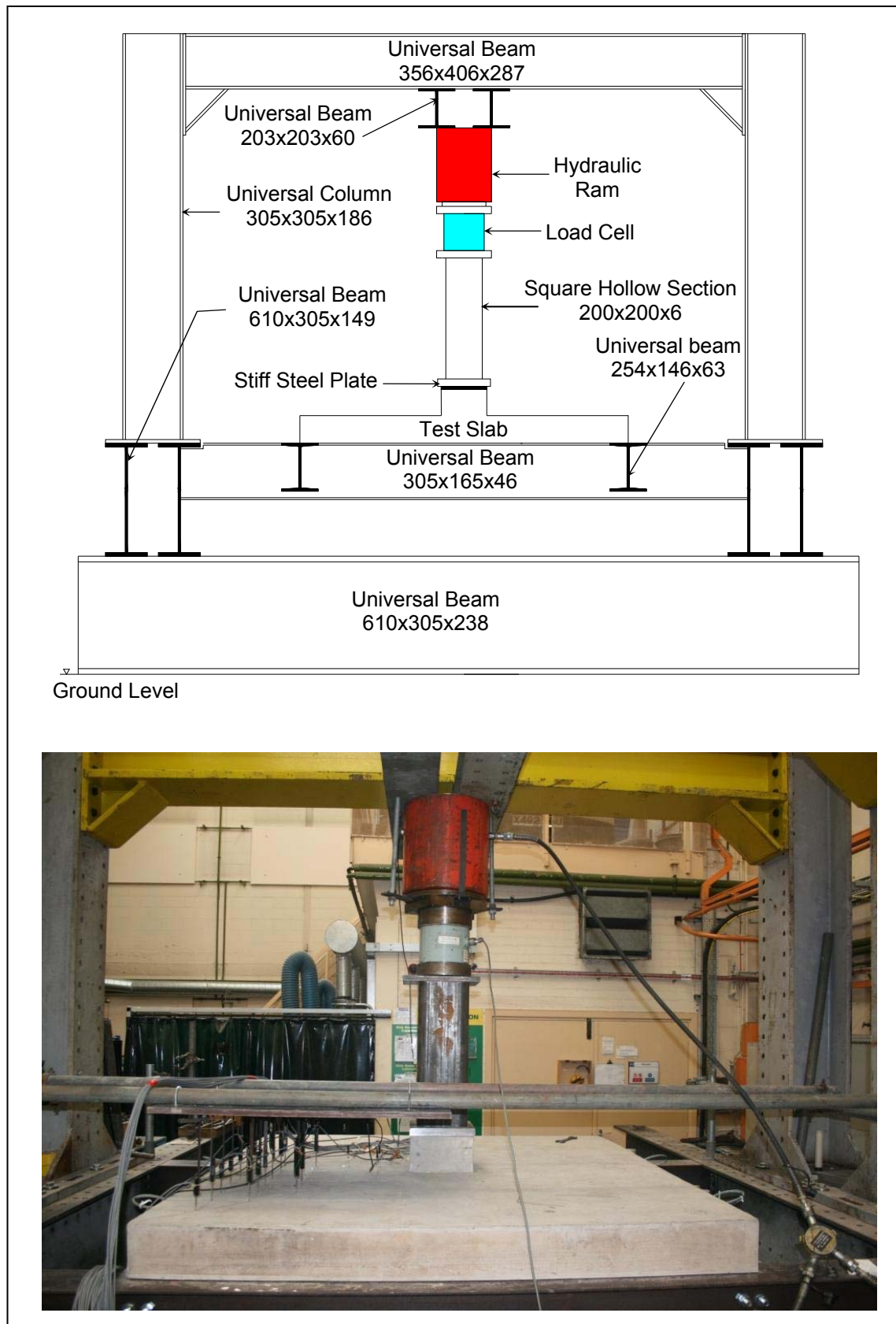


Figure 3-16: Test setup

The applied load was measured by a load cell of 3000-KN capacity. A data acquisition system connected to a personal computer was used to control the loading through a pressure transducer. All test data: load, deflections and strains, were collected by the data acquisition system and downloaded to the computer.

### **3.2.7. Pre-test preparation**

First of all, the slab was carefully placed on the testing frame. To facilitate getting accurate data from each test, the positions for measuring deflections at the top concrete surface were smoothed and clearly marked. These positions are mirrored on a wooden board supported horizontally by the steel frame. The pots were fixed to the board on the top face of the specimen, as shown in Figure (3-16). At the bottom surface of the slab, pots were glued by epoxy at the designated location, as shown in Figure (3-15). The pots for measuring the support settlements were fixed to their supporting stands, and their needles were accurately positioned while ensuring verticality. Finally, all the wires of the strain gauges and pots were connected to the data acquisition system. The beam or slab was then ready for testing.

### **3.2.8. Testing procedure**

All the instrumentation (strain gauges and pots) were automatically initialized by the data acquisition system. The data acquisition system was setup to read every 10 seconds. The test was carried out manually at an approximate rate of 10 kN/min by pumping the oil between the reading intervals. The load was paused at 20 KN intervals to take notes and photographs. Three load cycles were performed. In the first and the second cycles, the load was increased to a “service” load of not more than 10% and 20% of the ultimate design load of the reference specimen, respectively. In the third cycle, the load was increased until failure occurred, either by failure of the FRP or crushing of the concrete. All test data: force, strains and deflections were collected by the data acquisition system. The data were monitored graphically in real-time, and were downloaded digitally to the personal computer.

After test completion, the slab was removed carefully from the test-rig; a closer examination of the mode of failure was conducted. The locus of the punching cracks with the bottom surface of the slab and failure pattern were documented, and additional photographs were taken. The side crack patterns at the slab edges were investigated. The slab was then turned upside down. The concrete cover was carefully chiselled out to follow the crack path up to the reinforcement level. Then, it was possible to calculate the exact crack angle. This was necessary to study the effect of the prestressing ratio on the failure pattern.

### **3.3. Materials**

In addition to the structural tests, isolated material tests were carried out to determine the mechanical properties of the concrete, rebars and the FRP plates that were used in constructing the slabs. These tests and their results are presented below.

#### **3.3.1. Concrete**

The concrete was provided by TARMAC, UK. The concrete was designed to have a slump of 50 mm, and a 28-day cube compressive strength of 35 MPa, with 10 mm maximum aggregate size, 0.48 free water-cement ratio and 410 kg/m<sup>3</sup> cement content. The coarse aggregate used was a crushed calcareous aggregate. Table (3-2) presents the mix proportions to produce 1 m<sup>3</sup> of the concrete mix.

Table 3-2: Concrete mix proportions.

Cement (kg)	Water (kg or litres)	Fine aggregate (kg)	Coarse aggregate (kg)
410	196.8	704	1101

As explained in Section 3.2.3.3, nine control 100 mm cubes and three 100 x 200 mm cylinders were cast with each slab. Three cubes were tested on the same day of testing the slab that they represented. Another three cubes and the three cylinders were tested at 28-days. The cubes were used to determine the



compressive strength of the concrete according to BS1881-P116 [71], while the cylinders were used to determine the split cylinder tensile strength of the concrete according to ASTM C496-96 [72]. The last three cubes were tested at 7 days for purposes of quality and curing control. These concrete tests yielded an average cube compressive strength of 38.5 MPa and an average split cylinder tensile strength of 3.1 MPa at 28 days. Figure (3-17) shows the concrete cube and cylinder tests.



Figure 3-17: Concrete cub and cylinder tests.

The modulus of elasticity and Poisson's ratio were also among the important material properties that had to be evaluated accurately, as this study deals with deflection and cracking. The quality control assured by the concrete supplier was sufficient to represent all test slabs by three cylinders. This is confirmed by the cube and cylinder tests shown in Table (3-3). Then, three concrete cylinders 150 x 300 mm were tested to determine the concrete compressive modulus of elasticity, according to BS 1881-121 [73]. In these tests, the measurements of strains were duplicated by using both strain gauges and Pots, as shown in Figure (3-18). This test-determined modulus of elasticity was expected to provide a means to decide on which recognized modulus formula to be adopted for the evaluation of the modulus for all test specimens. An average experimental modulus of 28504 MPa was obtained for an average cylinder compressive strength of 31.98 MPa, as shown in Figure (3-19). The average Poisson's ratio was 0.208, which is within the common range; 0.18 to 0.25, for normal weight concrete.

Table 3-3: Concrete material properties

Slab	Cube compressive strength (MPa)		Split cylinder tensile strength (MPa)	
	Average	Standard deviation	Average	Standard deviation
RS <sub>0</sub>	41.38	0.48	3.41	0.22
RS-F <sub>0</sub>	40.86	0.86	3.24	0.21
RS-F <sub>15</sub>	40.31	0.14	3.47	0.05
RS-F <sub>30</sub>	48.56	1.04	4.53	0.04
RS-F <sub>30F</sub>	42.94	1.29	3.6	0.08

The corresponding moduli according to ACI Code [23] and Eurocode 2 [21] were 26579 MPa and 32966 MPa, respectively. The Eurocode formula, to some extent, gives a stiffer behavior, while the ACI formula was slightly closer to the experimental results. Therefore, it was decided to adopt the ACI formula to evaluate the concrete modulus of elasticity in all cases.



Figure 3-18: Test for concrete compressive modulus of elasticity.

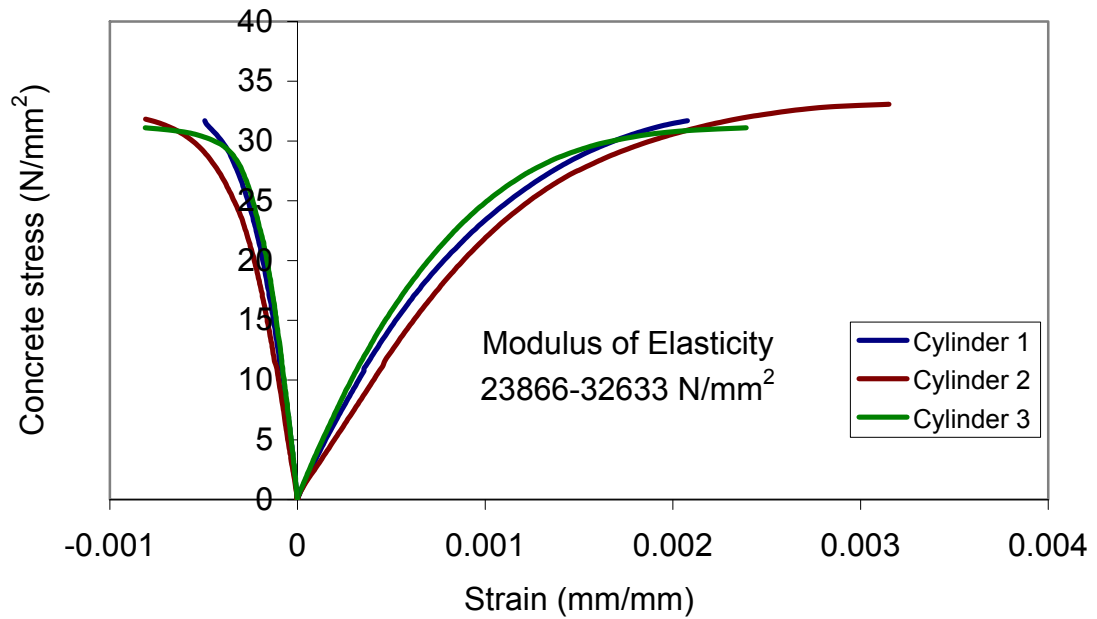


Figure 3-19: Stress strain curve for concrete.

### **3.3.2. Reinforcement**

The modulus of elasticity of the reinforcement is one of the main parameters of this research. Hence, representative FRP plate specimens were tested in uniaxial tension to determine their modulus of elasticity, as well as their ultimate stress and strain. Representative steel rebars were also tested for their yield and ultimate strength in tension.

#### **3.3.2.1. FRP plate reinforcement**

The FRP plates used were provided by Weber Building Solution, UK. Their commercial name is Weber.tec force carbon plate. It is a high-performance, corrosion-resistant carbon fibre laminate. Manufactured by S&P, Switzerland, these laminates have a fibre volumetric content up to 70% in an epoxy resin matrix. They are usually used together with Weber.tec EP structural adhesive to form the Weber.tec force composite strengthening system for use in accordance with Concrete Society Technical Report 55 [14] (Design Guidance for Strengthening Concrete Structures).

The type used in this project was S&P CFK 150/2000. The first number denotes to the characteristic modulus of elasticity, while the second number denotes to the ultimate tensile strength. It has a cross sectional area of 100 x 1.2 mm. These plates are sensitive to transverse pressure. Hence, the steel grips of the tension machine can damage the specimen. Normally, such damage would not affect the modulus of elasticity, but would undermine the tensile capacity. To overcome this problem, aluminium end-tabs were used at the grips (Figure 3-20). Low viscosity epoxy was used to adequately bond the end-tabs without entrapping air.

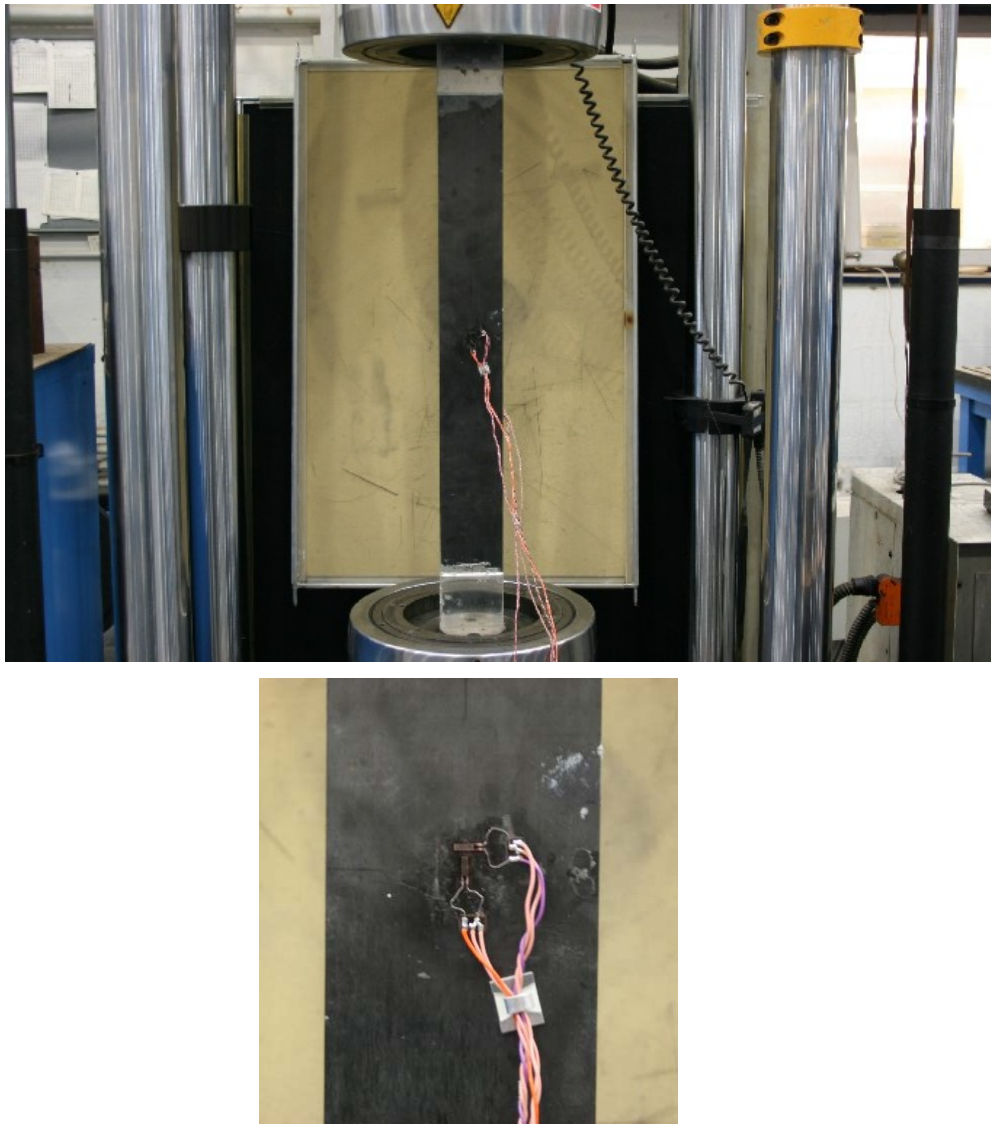


Figure 3-20: Instrumentation of FRP plate in tensile test.

Three representative specimens were tested according to ASTM D3039 / D3039M [74]. The tensile tests involved load and strain measurements to get the stress-strain curve, modulus of elasticity and poisson's ratio. All specimens were instrumented with two strain gauges; at 0° and 90°, to measure local strain at mid-length over a gauge length of 6mm. They were aligned axially along the center line. Typical instrumentation set-up for the three specimens is shown in Figure (3-20).

The tensile stress-strain diagrams were linear up to failure, as typically shown in Figure (3-21). The tensile tests of the FRP plates gave an average value of 172000 N/mm<sup>2</sup> and 2970 N/mm<sup>2</sup> for the modulus of elasticity and the ultimate tensile strength, respectively. An average value of 0.29 was obtained for Poisson's ratio. Figure (3-22) shows typical tension failure of CFRP plates. The results of the tensile tests for the FRP plates along with the mechanical properties provided by the manufacturer, at the time of the investigation, are presented in Table (3-4).

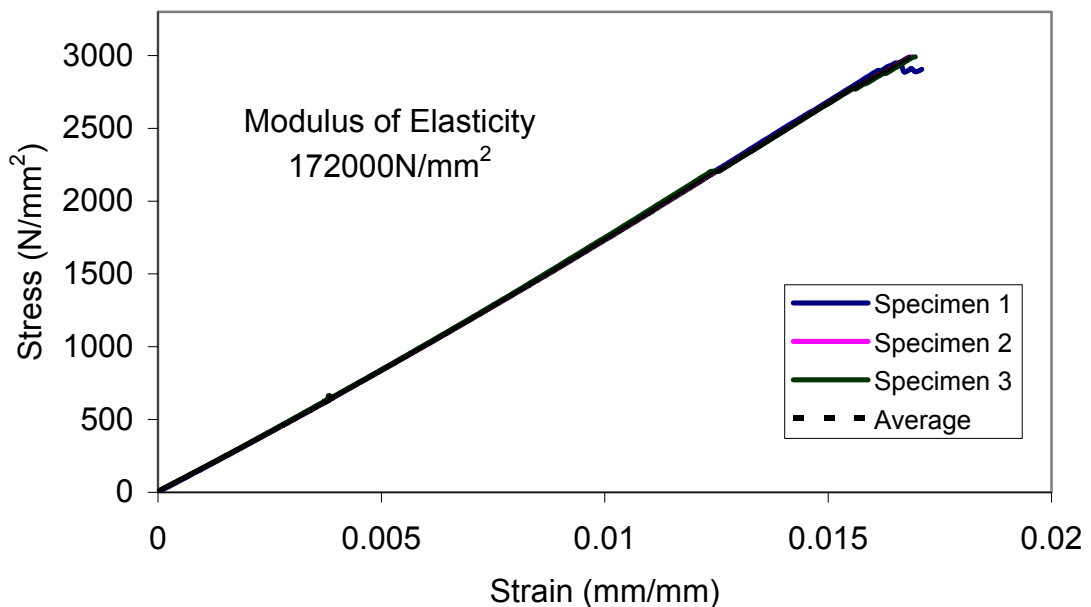


Figure 3-21: Typical FRP stress-strain curve.

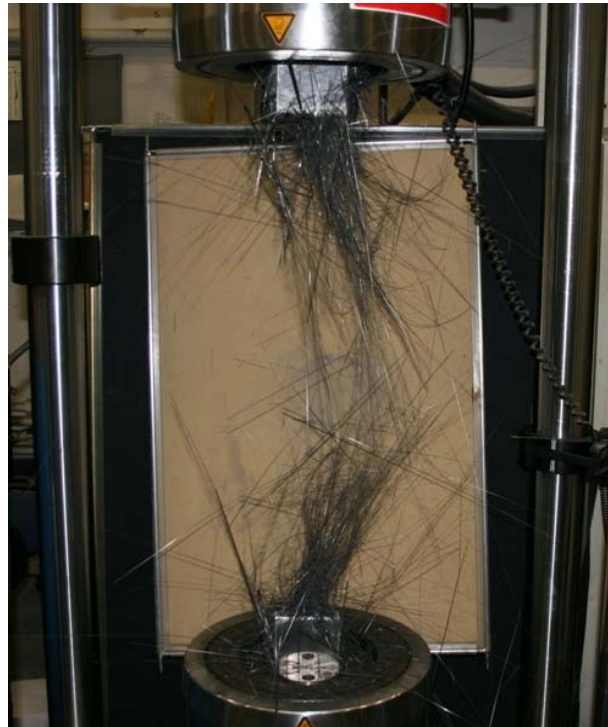


Figure 3-22: Failure of FRP plate in tension.

Table 3-4: Tensile mechanical properties of FRP plates.

Plate	Longitudinal modulus of elasticity, $E_x$ (MPa)	Rapture strain, $\varepsilon_r$	Rapture tensile stress, $f_r$ (MPa)	Coefficient of variation %		Manufacturer mechanical properties <sup>(1)</sup>	
				$E^{(2)}$	$f_r$	$E_f$	$f_r$
CFRP	172000	0.0168	2990	2.76	1.8	165000	2800

<sup>(1)</sup> Manufacturer mechanical properties as provided for the batch of the CFRP plates used at the time of the investigation.

<sup>(2)</sup> The longitudinal modulus was evaluated based on the local strains measured by strain gauges for the CFRP plates.

### 3.3.2.2. Steel reinforcement

The tensile mechanical properties of the steel rebars were also determined by testing representative samples. These tests were carried out according to ASTM A370-97a [75]. The yield strength, ultimate strength and elongation were measured, and are shown in Table (3-5).

Table 3-5: Tensile mechanical properties of steel rebars.

Material	Nominal diameter (mm)	Proportional limit (N/mm <sup>2</sup> )	Yield strength (N/mm <sup>2</sup> )	Yield strain ( $\epsilon$ )	Ultimate strength (N/mm <sup>2</sup> )
Steel	8	488	576	0.0030	655
	12	485	570	0.0034	655

To get more knowledge of the stress-strain properties of the 12mm diameter steel rebars, a uniaxial tensile test has been conducted. Both strain gauges and extensometer were use to get the strain data. The stress-strain results are shown in Figure (3-23).

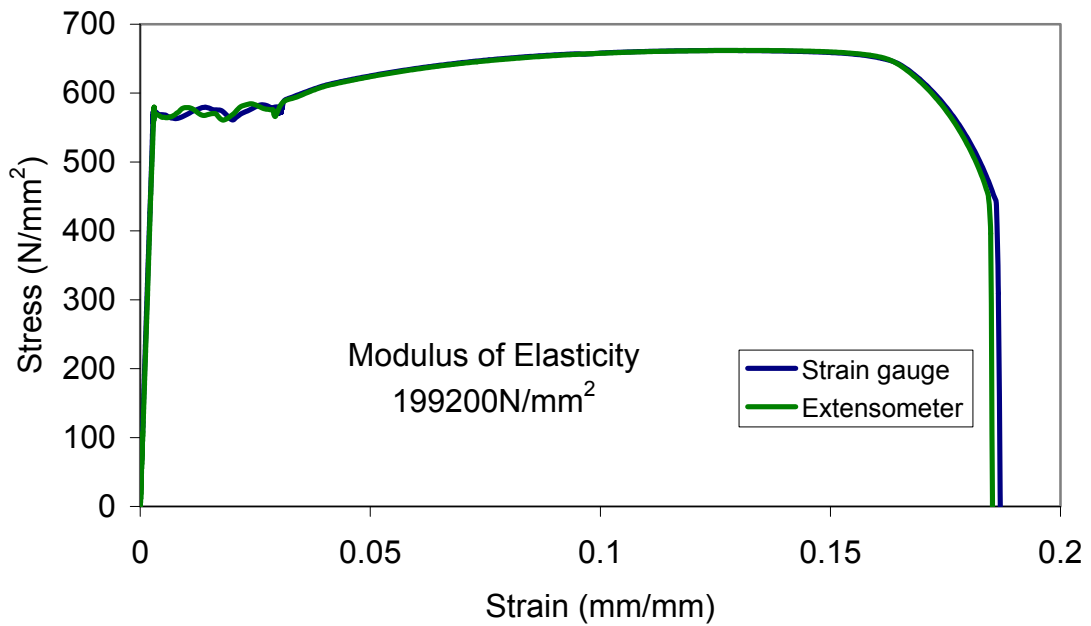


Figure 3-23: Stress-strain curve of 12-mm steel reinforcement.



## **Chapter 4**

# **Experimental results and discussion**

### **4.1. Introduction**

This chapter deals with the experimental data acquired from the slab tests discussed in Chapter 3. The various categories of data are presented and typical types of behaviour are identified instead of considering each individual test on its own. Any deviations from the general behaviour are explained. Initially, the modes of failure and load capacity are discussed. Then, the reinforcement and concrete strain, deflection, and crack width are examined. The results of the steel RC slab are always used for comparison purposes. Subsequently, some of the experimental data are analysed in order to investigate other structural aspects that are related to punching behaviour in both serviceability and ultimate limit states.

### **4.2. Experimental data**

A large amount of data was collected from the structural tests. The load is considered the most appropriate common link between the data. Therefore, the experimental load-deflection, load-rotation, load-crack width, load-reinforcement strain and load-concrete strain relationships were prepared for all tests, and are shown in Appendix B. The modes of failure and load capacity were also examined. In the following sections, only typical experimental relationships are presented and investigated to identify typical types of behaviour. Expected discrepancies and peculiarities due to the application of the FRP reinforcement are pointed out and discussed.



#### **4.2.1. Modes of failure and load capacity**

The mode of failure is usually identified based on structural responses from experimental observations such as load-deflection response, strain in flexural reinforcement, principal compressive stress and strain in concrete, and crack pattern. Accordingly, the encountered failure modes during the slab tests can be categorized into three modes, namely, flexural-punching, punching shear and premature debonding. The premature debonding failure was followed also by brittle punching failure.

The failure of the control specimen ( $RS_0$ ), which was not strengthened by the CFRP plates, was ductile. Figure (4-1) confirms that the slab reached its yield strength by the full development of the yield lines on the tension face of the specimen with wide flexural cracks. However, the slab should be regarded as having failed in flexural punching due to the sudden decrease in the load at failure, which is confirmed by the load-deflection curve shown in Figure (4-7).



Figure 4-1: Crack pattern of slab  $RS_0$  after failure

The non-prestressed FRP slab (RS-F<sub>0</sub>) failed in a punching shear failure mode, as shown in Figure (4-2). It is evident that the FRP materials contributed to the increase in the load capacity until the bond between the FRP plate and concrete failed. Localized debonding cracks appeared at a late stage of loading due to the development of the intermediate flexural cracks and the diagonal shear cracks, which resulted in a separation of the strengthening materials. These cracks were located along the edges of the FRP plate length. This indicates that end anchoring severed, to a certain extent, preventing a premature bond failure at the cut-off end of the FRP materials. After the formation of these cracks, the specimen failed due to the rapid development of the shear crack after the FRP debonded from the slabs without rupture of the FRP material. It is noteworthy that the steel reinforcement around the column area yielded and helped the rapid development of the cracks as well. Partially developed yield lines can be noticed in Figure (4-2) at the slab corners.

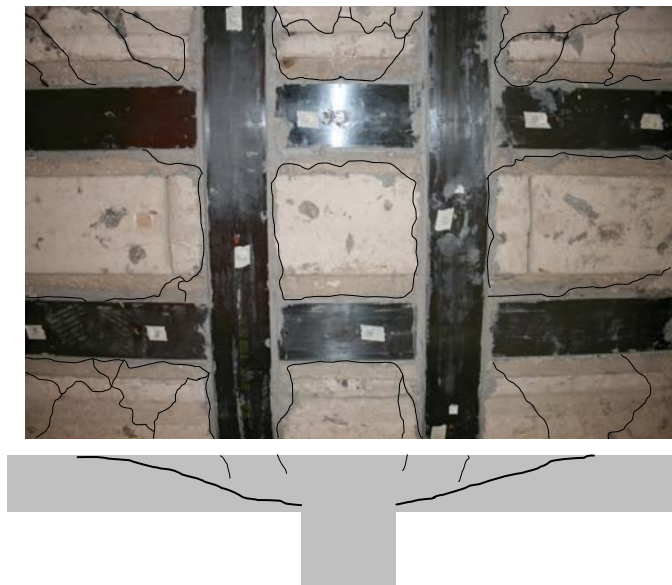


Figure 4-2: Crack pattern of slab RS-F<sub>0</sub> after failure.

For the prestressed-FRP slabs (RS-F<sub>15</sub>), (RS-F<sub>30</sub>) and (RS-F<sub>30F</sub>), the failure mode was by debonding of the FRP plates. The scenario of the crack development was similar to the non-prestressed slab (RS-F<sub>0</sub>). However, at the stage of development of the debonding cracks around the critical diagonal cracks, their growth was very fast. That is the prestressed force in the FRP

plates increased the peeling effect, by which the slabs reached their ultimate debonding load before they reach the ultimate punching load. Another factor that might speed up the debonding failure is the higher flexure stiffness of the FRP plate compared to the FRP sheets which also increase the peeling effects. This phenomenon is more explained by the schematic diagram show in Figure (4-3). By inspecting the bond surface of the FRP plates, it was found nearly smooth with very little concrete debris attached. Thus, the bond failure is believed to initiate at the layer of concrete just beneath the adhesive layer.

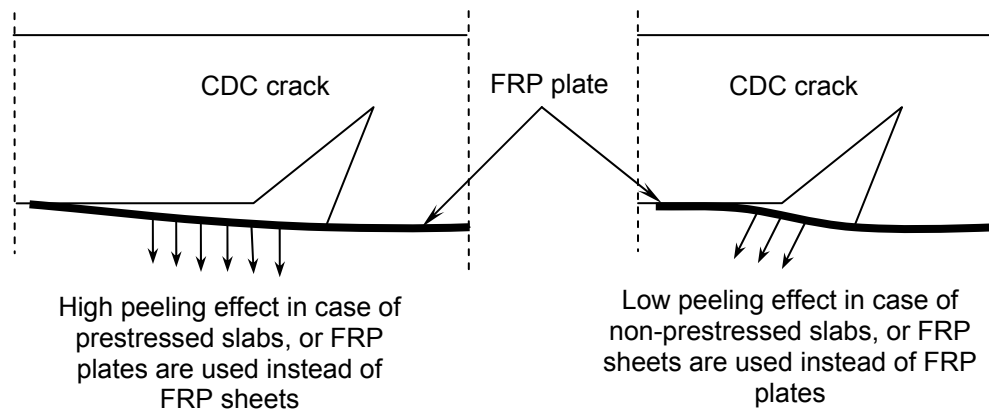


Figure 4-3: Comparison of the peeling effect in non-prestressed and prestressed slabs.

With respect to the steel reinforcement, the 30% prestressed slabs (RS-F<sub>30</sub>) and (RS-F<sub>30F</sub>) reached the yield stress, but they did not experience extensive yielding. The maximum recorded strain was around 3700 microstrain. On the other hand, the 15% prestressed slab (RS-F<sub>15</sub>) did not encounter any yielding during the loading history. The failure surface of these slabs extended up to the end anchor plates with approximate diameter of 890 to 1070 mm that represented a 25 to 20-degree cone angle, which is less than both the reference slab (RS<sub>0</sub>) and the non-prestressed slab (RS-F<sub>0</sub>). This could be attributed to the confinement effect of the prestressing, which did not allow for the tangential flexural cracks to develop in the area close to the column. The crack pattern of these slabs is shown in Figures (4-4) to (4-6).

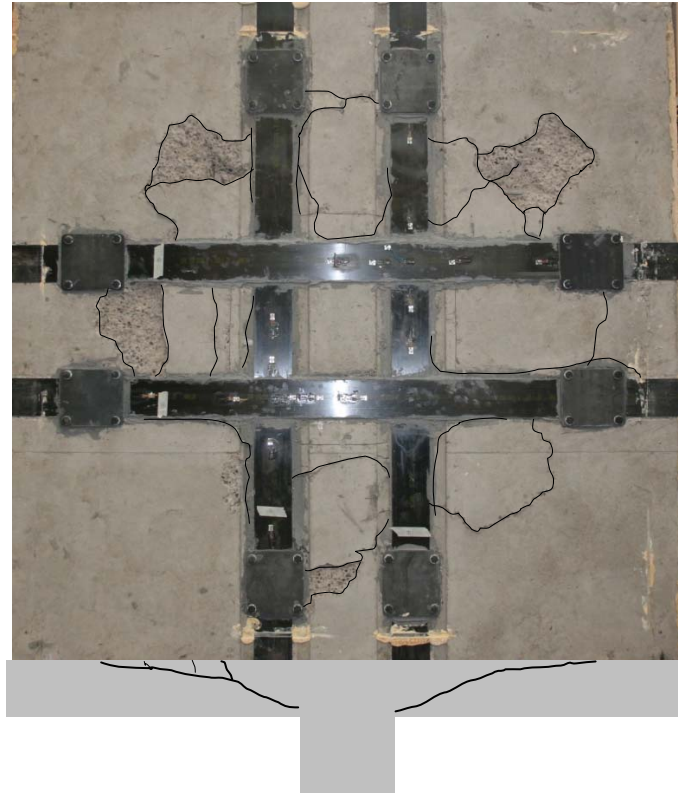


Figure 4-4: Crack pattern of slab RS-F<sub>15</sub> after failure.

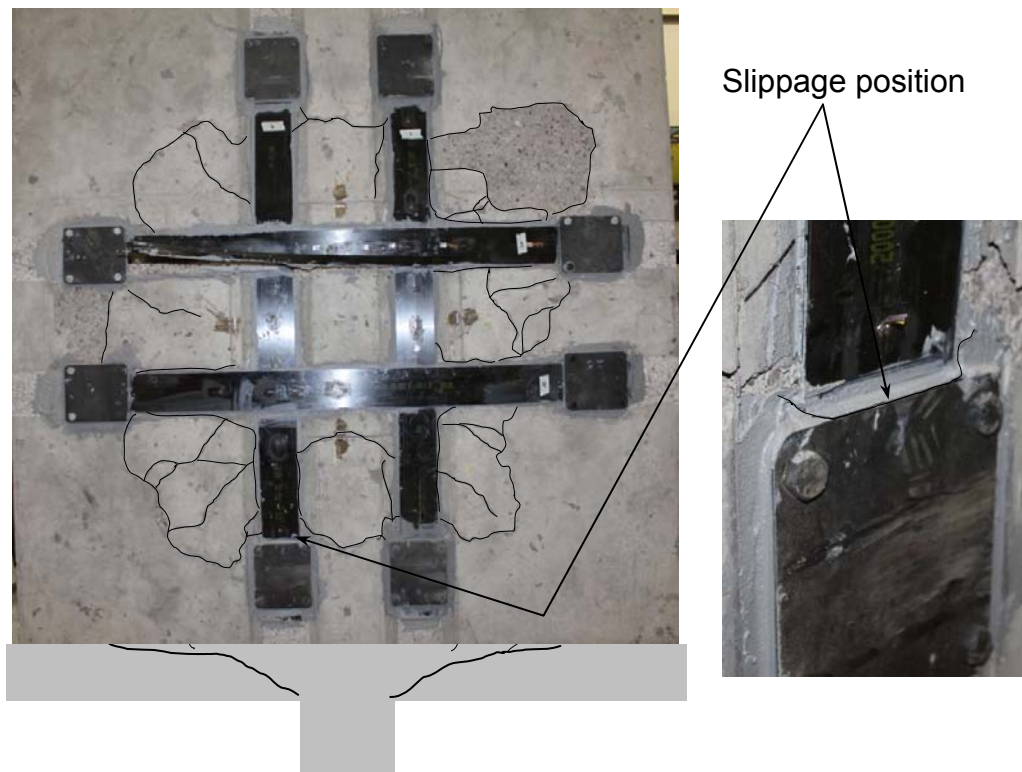


Figure 4-5: Crack pattern of slab RS-F<sub>30</sub> after failure.

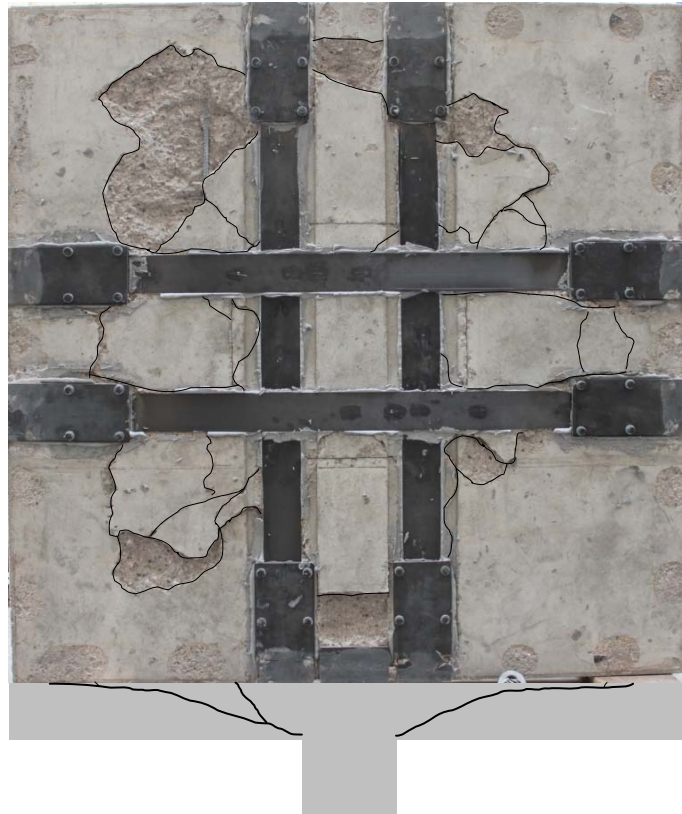


Figure 4-6: Crack pattern of slab RS-F<sub>30F</sub> after failure.

It is clear from these figures that the number of the flexural cracks in the prestressed slabs in the column vicinity has been reduced, compared to slabs (RS<sub>0</sub>) and (RS-F<sub>0</sub>). In the 30-percent prestressed FRP slab (RS-F<sub>30</sub>), one of the FRP strips experienced debonding and slippage from the end anchor plates due to the high prestressing forces; see Figure (4-5). In order to overcome the slippage problem, the end anchorage plate was extended up to the support in the slab (RS-F<sub>30F</sub>) to ensure more anchorage area.

Table 4-1: Failure modes and load capacity results.

Slab	$f_{cu}$ (Mpa)	First crack load $V_{cr}$ (kN)	Deflection at crack load $\delta_{cr}$ (mm)	Yield load $V_y$ (kN)	Deflection at yield load $\delta_{cr}$ (mm)	Ultimate Load $V_u$ (kN)	Deflection at ultimate load $\delta_{cr}$ (mm)	Energy absorption $\psi$ (kN.mm)	Stiffness $K$ (kN/mm)	Failure Mode	Estimated crack Angle ( $\alpha$ ) degrees
RS <sub>0</sub>	41.38	57.0	1.20	171.6	9.9	284	27.3	18388	47.7	Flexural punching	31
RS-F <sub>0</sub>	40.86	76.1	0.74	273.4	14.6	405	21.4	12774	98.4	Punching	29
RS-F <sub>15</sub>	40.31	148.6	1.82	240 <sup>(1)</sup>	12.0	240	15.2	2092	91.4	Debonding <sup>(2)</sup>	23
RS-F <sub>30</sub>	48.56	115.0	1.20	307 <sup>(1)</sup>	11.7	307	14.8	2498	100.0	Debonding <sup>(2)</sup>	25
RS-F <sub>30F</sub>	42.94	131.4	1.70	220 <sup>(1)</sup>	14.2	220	16.3	2105	91.1	Debonding <sup>(2)</sup>	23

(1) Ultimate load was considered as yield load for slabs that did not experience yielding of steel reinforcement.

(2) Debonding was followed by punching failure.

The modes of failure, the first crack load and load capacity results of the slabs are shown in Table (4-1). The reference specimen  $RS_0$  indicated the lowest first crack load of 57 kN, while the highest first crack load was observed for the specimen with a 15-percent prestressing ( $RS-F_{15}$ ). The first crack loads of 76.1 kN, 115 kN and 131 kN were recorded for the specimens ( $RS-F_0$ ) ( $RS-F_{30}$ ) and ( $RS-F_{30F}$ ), respectively. The use of the FRP slightly increased the equivalent reinforcement ratio compared with the reference specimen. Consequently, the associated deflection to the first crack load, for the strengthened slabs, is decreased as the reinforcement ratio is increased.

For the current strengthening scheme, the results indicate that prestressing of the FRP plate up to 15 percent, before applying it to the tension surface of slab, reduced the onset of cracking. Contrary to expectations, increasing the prestressing ratio was not able to increase the first crack any more, but reduced it. That is the high prestressing forces are more likely to trigger the debonding cracks at the early stages of loading. This explanation can be further supported by the slippage of the second FRP strip in slab ( $RS-F_{30}$ ) as mentioned earlier and is confirmed by the measurement of strains mounted on the FRP plate, as shown later in this chapter. Moreover, the concentration of the prestressing forces around the column area, leaving a large area of the slab corners without strengthening, makes that area more potential to tangential tensile cracks, which is quite clear from the above figures.

#### **4.2.2. Load-deflection characteristics**

Typical experimental load-deflection diagrams, measured at the centre of the slab, are shown in Figure (4-7). All data were recorded using the data acquisition system, and then corrected against the support settlement and the test-rig deformation. In all slabs, before any cracking occurs, the load-deflection relationship was nearly linear, and the deflection was almost negligible as the slab possesses a relatively high stiffness that is associated with the uncracked concrete section. After the first crack, the characteristic of the load-deflection was largely dependent on the reinforcement and prestressing ratio.



For the reference specimen ( $RS_0$ ), a rapid reduction in the slab stiffness occurred with the formation of the first circular crack around the column. A subsequent considerable reduction in stiffness (represented by almost a short horizontal plateau in the load-deflection curve) was associated with the formation of several other radial and tangential flexural cracks within the zone of negative bending moment. Thereafter, the deflection followed an almost linear relationship with load up to the yield load. The load-deflection curve then arched reaching the plateau at the ultimate load, while the existing cracks widened and propagate towards the compression zone.

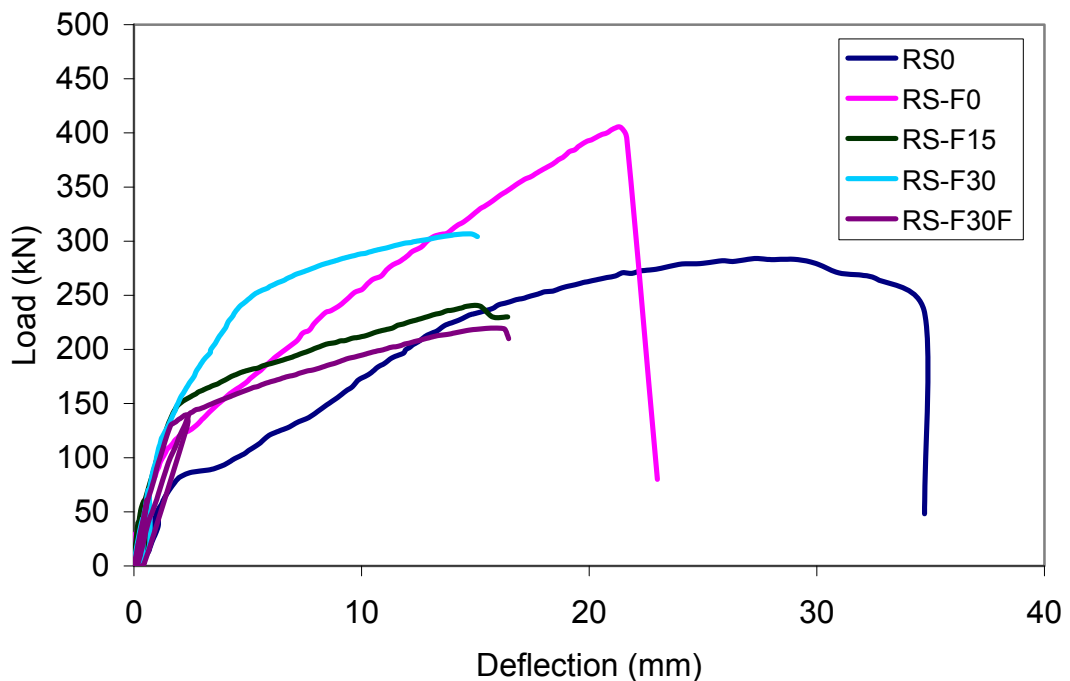


Figure 4-7: Load-central deflection of the test slabs.

The non-prestressed specimen ( $RS-F_0$ ) showed similar behaviour to the reference slab ( $RS_0$ ), except that the crack formation zone was shorter than that of the reference slab, and the behaviour following the crack stabilisation point was nearly linear up to the failure load. This linear behaviour is attributed to the linear material properties of the FRP reinforcement. Correspondingly, the deflection at the ultimate load decreased from 27.3 mm of the reference slab to 21.4 mm.



The prestressed specimens (RS-F<sub>15</sub>), (RS-F<sub>30</sub>) and (RS-F<sub>30F</sub>) exhibited brittle behaviour. The average deflection at the ultimate load was approximately 0.57 and 0.72 that of the reference specimen (RS<sub>0</sub>) and non-prestressed specimen (RS-F<sub>0</sub>), respectively. Moreover, the slope of the load-deflection curves was lower than that of the reference and non-prestressed specimens. Once the FRP began debonding from the concrete substrate, the stiffness of the slab was markedly reduced. After the onset of debonding, the load-deflection curves were linear up to failure and similar in shape to the constitutive law of a linear elastic material, which reflects that the prestressed slabs reached their debonding or punching strength before they reach the shear strength corresponding to the ultimate flexural capacity. In general, prestressed specimens experienced smaller deformation compared to the reference and non-prestressed specimens due to the effect of prestressing, which enhanced the serviceability of the slabs.

For slab (RS-F<sub>30F</sub>), a small leakage problem in the pump connection was noticed at a load level of 130 kN. The slab was intentionally unloaded to zero kN to repair the connection leakage. So that, an additional cycle is shown in the load-deflection curve of the slab at that load level, see Figure (4-7).

### **4.2.3. Strain measurements**

#### **4.2.3.1. Steel reinforcement**

A typical experimental load-strain relationship for the internal steel reinforcement is shown in Figure (4-8). The figure combines the steel strain distribution for all test specimens at the location of strain gauge 5 in Figure (3-12), which is 100 mm from the column face. They are in general following the same trend of the load-deflection curves shown in Figure (4-7). A stiffer behaviour was noticed for the prestressed and non-prestressed specimens compared with the reference specimen (RS<sub>0</sub>). In addition, specimens (RS-F<sub>15</sub>) and (RS-F<sub>30</sub>) showed stiffer behaviour compared with the non-prestressed specimen (RS-F<sub>0</sub>) for the same range of loading. The prestressed specimen (RS-F<sub>30F</sub>) showed lower stiffness compared with the strengthened specimens.

The lower stiffness can be explained as result of the early debonding of the FRP strips. So, there was not enough confinement to enhance the behaviour of this specimen.

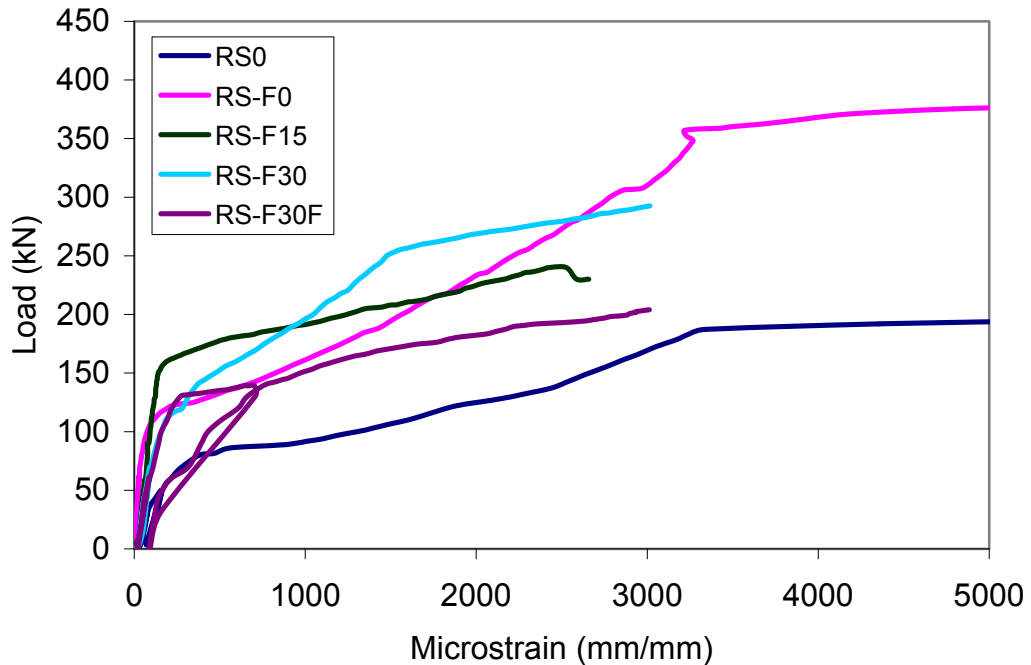


Figure 4-8: Load-strain relationship for the internal steel reinforcement.

The recorded steel strains also indicated that for the reference specimen ( $RS_0$ ) and non-prestressed specimen ( $RS-F_0$ ), the steel strain at the failure load was approximately 4.3 times the yield strain. However, for the prestressed specimens ( $RS-F_{15}$ ) and ( $RS-F_{30}$ ), the steel reinforcements did not yield. Only the steel reinforcements in the area close to the column ( $SG_{S4}$ ,  $SG_{S5}$ ) for specimen ( $RS-F_{30F}$ ) reached the yield strain at failure, but they did not experience extensive yielding. Moreover, the radius of the yielding area decreased as the strain level at failure reduced due to the effect of prestressing, see Figure (4-9). During the prestressing process, the recorded steel strains for these specimens were nearly negligible and they did not exceed 75 microstrain in compression.

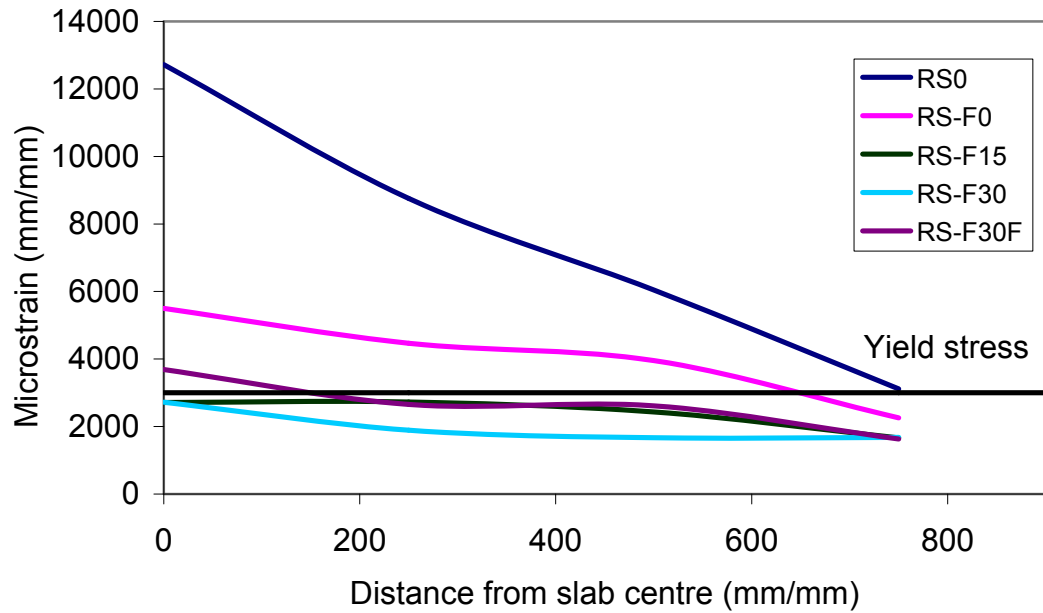


Figure 4-9: Profile of steel strain at failure.

#### 4.2.3.2. FRP reinforcement

Figure (4-10) shows a typical experimental load-strain relationship for the FRP reinforcement. The figure combines the FRP strain distribution for the strengthened specimens (RS-F<sub>0</sub>), (RS-F<sub>15</sub>), (RS-F<sub>30</sub>) and (RS-F<sub>30F</sub>) at the location of strain gauge 7 in Figure (3-13). For clarity purposes, the strain levels of the prestressed specimens (RS-F<sub>15</sub>), and (RS-F<sub>30</sub>) and (RS-F<sub>30F</sub>), were reduced by the amount of prestressing; 2000 and 4500 microstrain, respectively, which are the strain levels after the immediate losses. Before cracking, the strains in the plates are compatible with the strains in the concrete substrate, and are therefore of negligible magnitude. It is noticeable also that the strain levels of the FRP are comparable to the steel strains shown in Figure (4-8), which implies the strain compatibility in the slab cross section is maintained. After the formation of the first crack, the rate of strain increase for the prestressed specimens (RS-F<sub>15</sub>), (RS-F<sub>30</sub>) and (RS-F<sub>30F</sub>) is higher than that of the none-prestressed slab (RS-F<sub>0</sub>). This higher rate is attributed to the sudden transfer of forces to the FRP plates at the onset of debonding. As a

result, some strips such as the second strip in slab (RS-F<sub>30</sub>) experienced slippage from the anchor plate at the later stage of loading, as mentioned before in Section 4.2.1, and confirmed by the strain readings shown in Figure (4-10).

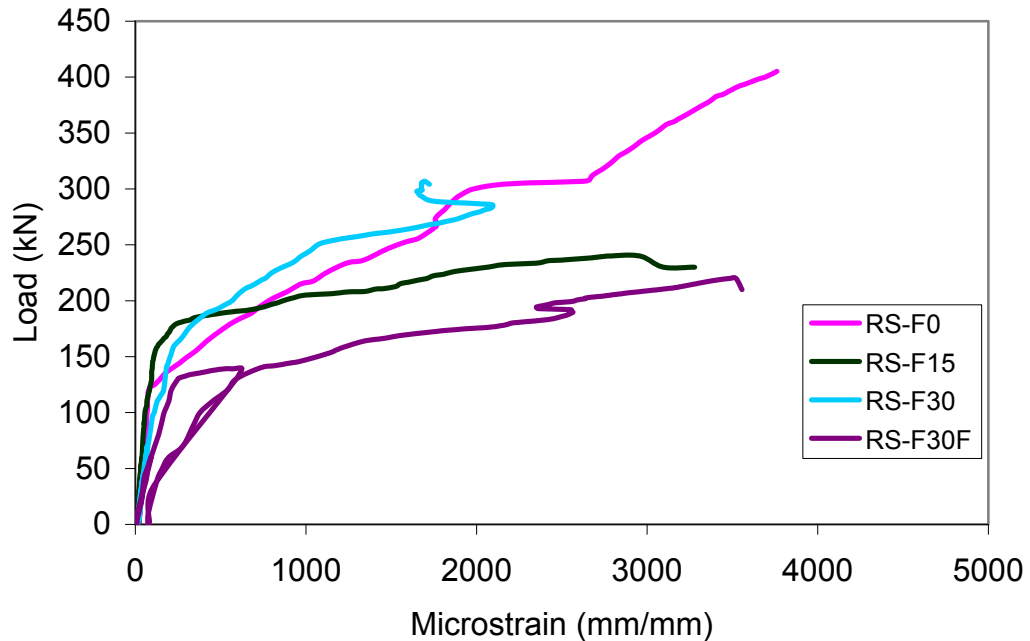


Figure 4-10: Load-strain relationship for FRP reinforcement.

Figure (4-11) shows the strain profile development of the FRP plates in slab (RS-F<sub>15</sub>) at different load levels. This strain behaviour indicates that the average bond between the plate and the concrete, in the negative moment zone, continues to increase when debonding cracks have formed. The magnitude of the increase in strain is highest at debonding cracks, and gradually reduces away from debonding cracks as the tension carried by the intact concrete increases. The negligible strains near the anchor plate indicate that the FRP plate is adequately anchored, with effectively no slip at its end. However, some times when the shear crack extends near the anchor plate resulting in peeling-off debonding cracks, the strains increase considerably; see strain of A-direction at 240 kN load level shown in Figure (4-11). Another noticeable feature is the strain drop of direction A at the overlap with direction B. This is attributed the fact that any lateral tension strain would result in compression strain in the fibre direction due to the Poisson's ratio effect.

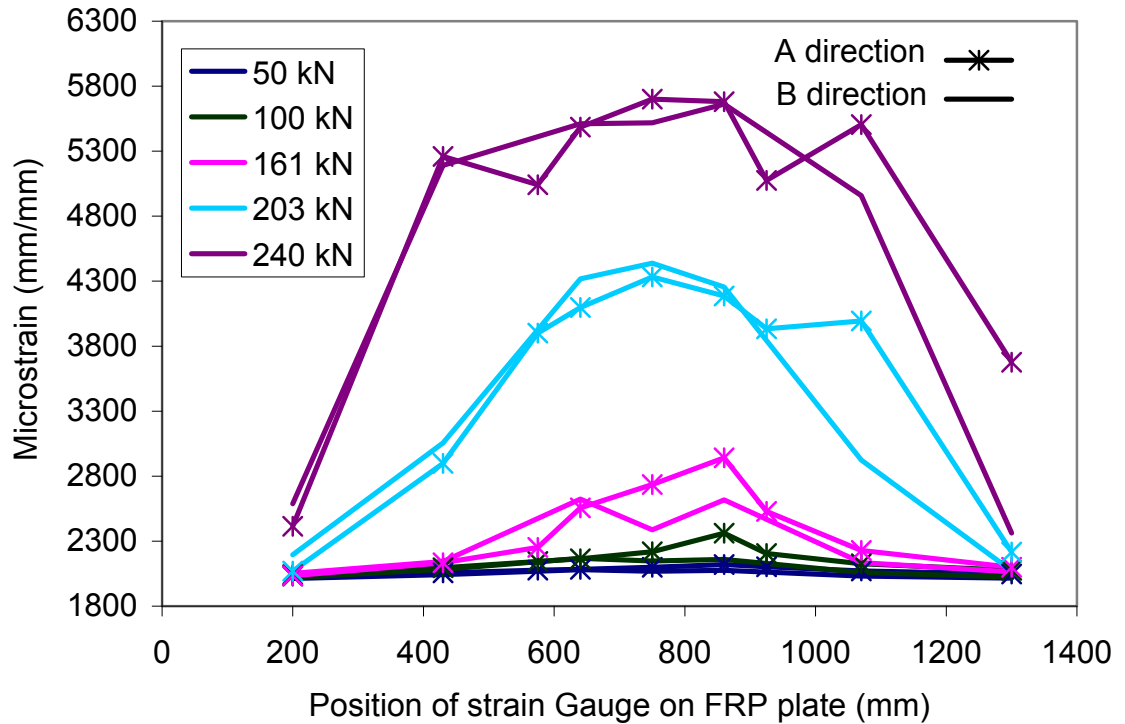


Figure 4-11: Strain profile of FRP plate for slab (RS-F<sub>15</sub>) at different load levels.

The recorded strains also indicated that the FRP plates did not develop their full strength in the non-prestressed specimen (RS-F<sub>0</sub>) because the strains of the FRP plates corresponding to the ultimate load ranged from 2500 to 5000 microstrain, which represent only 15 to 30% of their ultimate strengths. However, strain levels more than 10000 microstrain were recorded for the prestressed specimens, which points to the advantages of using prestressed FRP plates.

#### 4.2.3.3. Concrete

Figure (4-12) shows a typical experimental load-concrete strain relationship. The concrete strain shown was measured in the radial direction at position SGV<sub>1</sub> at the top concrete surface, as shown in Figure (3-14). Before cracking, the concrete strain is negligible. With the formation of the first crack, the concrete strain increases noticeably. A stiffer behaviour was noticed for the prestressed and non-prestressed specimens compared with the reference

specimen (RS<sub>0</sub>). In addition, specimens (RS-F<sub>15</sub>) and (RS-F<sub>30</sub>) showed stiffer behaviour compared with the non-prestressed specimen (RS-F<sub>0</sub>) for the same range of loading. The prestressed specimen (RS-F<sub>30F</sub>) showed lower stiffness compared with the strengthened specimens as a result of the early debonding of the FRP strips.

Another feature was noticed for the reference slab (RS<sub>0</sub>) and non-prestressed slab (RS-F<sub>0</sub>) that the strain reached its ultimate strain then decreased before failure. This phenomenon has also been reported by other researchers [26, 30]. However, for the prestressed slabs, the failure occurred at low strain levels as these slabs reached their debonding strength, which is function of the concrete tensile strength, before they reached the flexural punching strength. This confirms that the tensile strength controls the punching load [76].

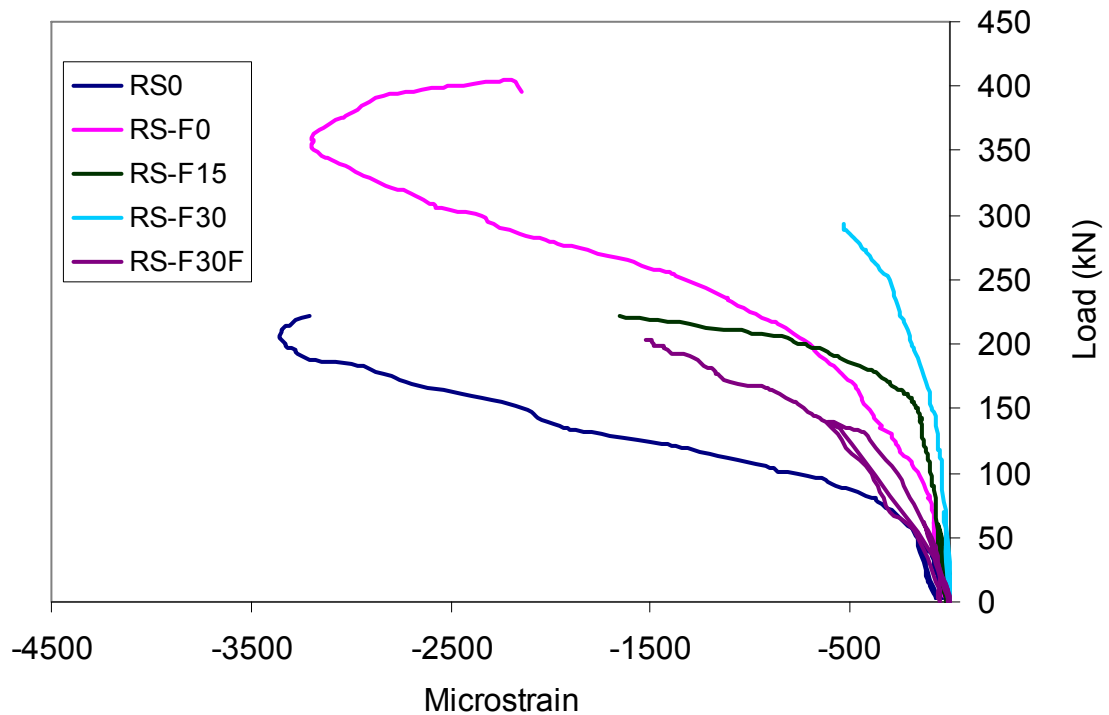


Figure 4-12: Load-radial strain relationship for concrete at position SGV<sub>1</sub>.

Figure (4-13) shows the load-strain relationship at positions SGV<sub>1</sub> and SGH<sub>1</sub> in the radial and tangential directions, respectively, for slab (RS-F<sub>15</sub>). The figure

confirms the fact that the strain level in the tangential direction is usually higher than that of the radial direction at the same load level.

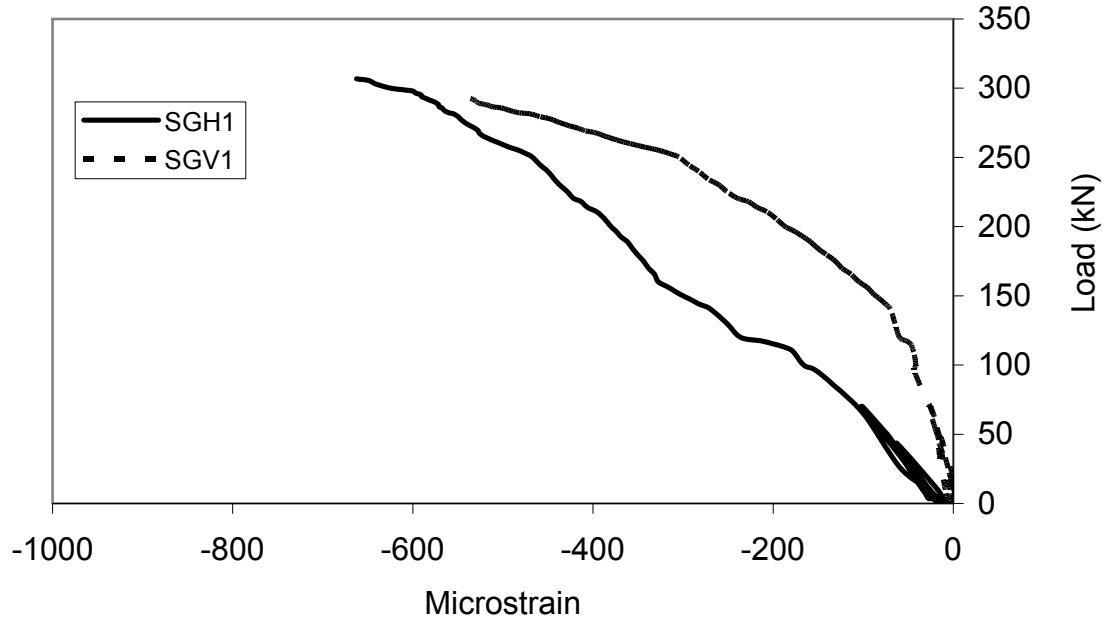


Figure 4-13: Load-radial and tangential strain relationships for slab (RS-F<sub>15</sub>).

#### 4.2.4. Crack width

A typical load-crack opening displacement relationship is shown in Figure (4-14). The crack widths shown for slab (RS<sub>0</sub>) were measured by linear potentiometers (pot), at the crack inducer positioned at the critical section for punching shear, on the tension surface of the slab. As the slab experience mixed mode behaviour, the crack opening has both a horizontal (CMOD) and vertical component (CMVD). The horizontal component was measured over a gauge length of 500 mm. The pot measurement has actually two components: the crack width and the elongation in the concrete at the surface. However, the elongation in the concrete is negligible. For instance, at a concrete strain of 100 microstrain, which approximately corresponds to the concrete tensile strength, the elongation would be only 0.05 mm. The load-crack mouth horizontal displacement behaviour is somewhat similar to that of the load-steel strain perpendicular to the crack surface. On the other hand, the vertical component

showed stiffer behaviour compared to the horizontal component behaviour. This can be attributed to the aggregate interlocking and dowel effects caused by steel reinforcement, which restrain the crack sliding.

For the strengthened specimens, the crack location has been shifted away towards the anchor plates, as mentioned earlier. This was confirmed by the pot readings at the crack inducer, which fluctuated around zero. So the use of prestressed plates reduces the onset of cracking, resulting in an enhanced serviceability.

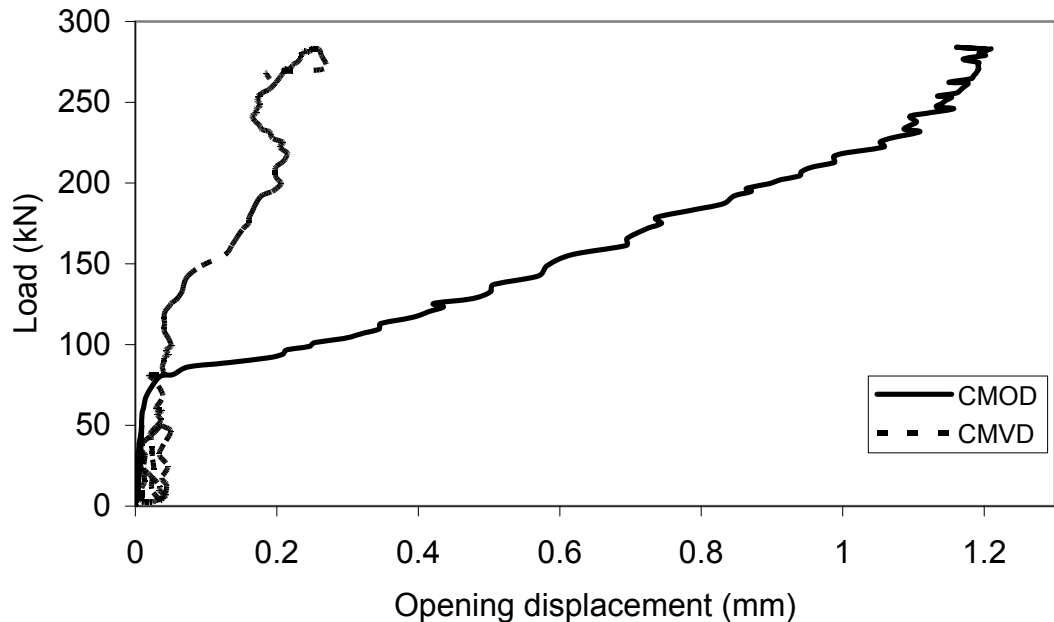


Figure 4-14: Average horizontal and vertical crack opening displacement of slab (RS<sub>0</sub>).

### 4.3. Analysis of test results

The focus of this research is on the punching behaviour of slabs strengthened with EBR. Therefore, the load and deflection data are analyzed and used to investigate other structural aspects that are related to the punching behaviour in both serviceability and ultimate limit states. The load-rotation diagrams are constructed from the deflection profile along the centre line. Moreover, the



deformation capacity in terms of the stiffness and energy absorption is evaluated.

#### **4.3.1. Rotation capacity**

The deflection profiles of the test slabs along the centreline are shown in Figures (4-15) to (4-18). For the reference slab ( $RS_0$ ), it is quite clear that the low reinforcement ratio resulted in a flaccid behaviour. The deflection values around the column area are nearly similar to the central deflection, which was translated in the high value of absorbed strain energy. However, for the strengthened slabs, only columns experienced high deflection values. The contribution of the strengthening effect was investigated by comparing the deflection of each slab at an arbitrarily service load of 90 kN. The measured deflections of the strengthened slabs were 30%, 25% and 26% for the non-prestressed slab ( $RS-F_0$ ) and the prestressed slabs ( $RS-F_{30}$ ) and ( $RS-F_{30}$ ), respectively, relative to the reference slab ( $RS_0$ ).

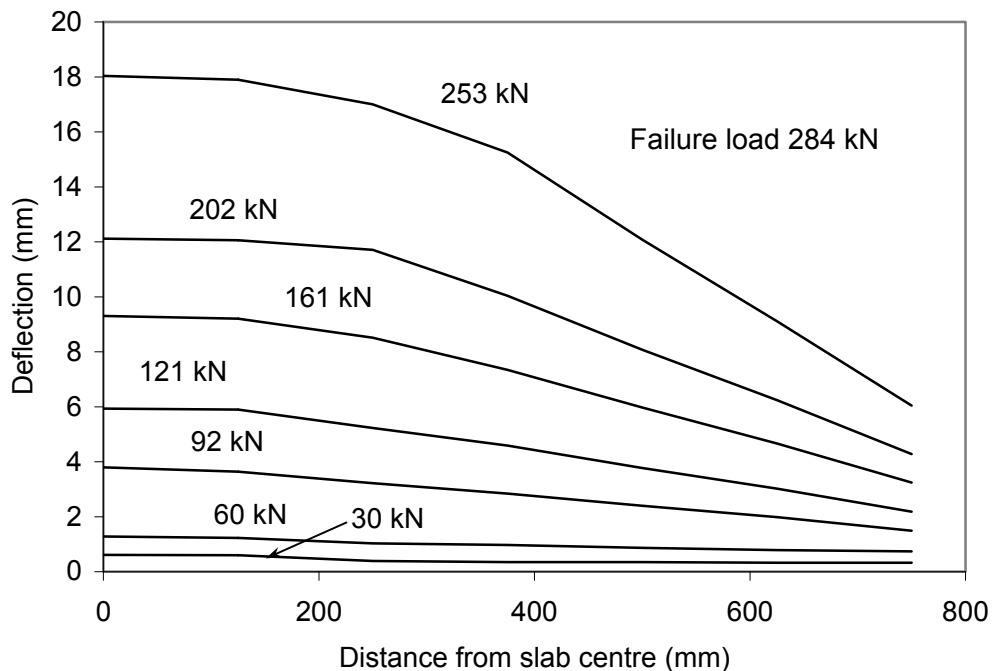


Figure 4-15: Deflection profile of slab  $RS_0$  along the centre line.

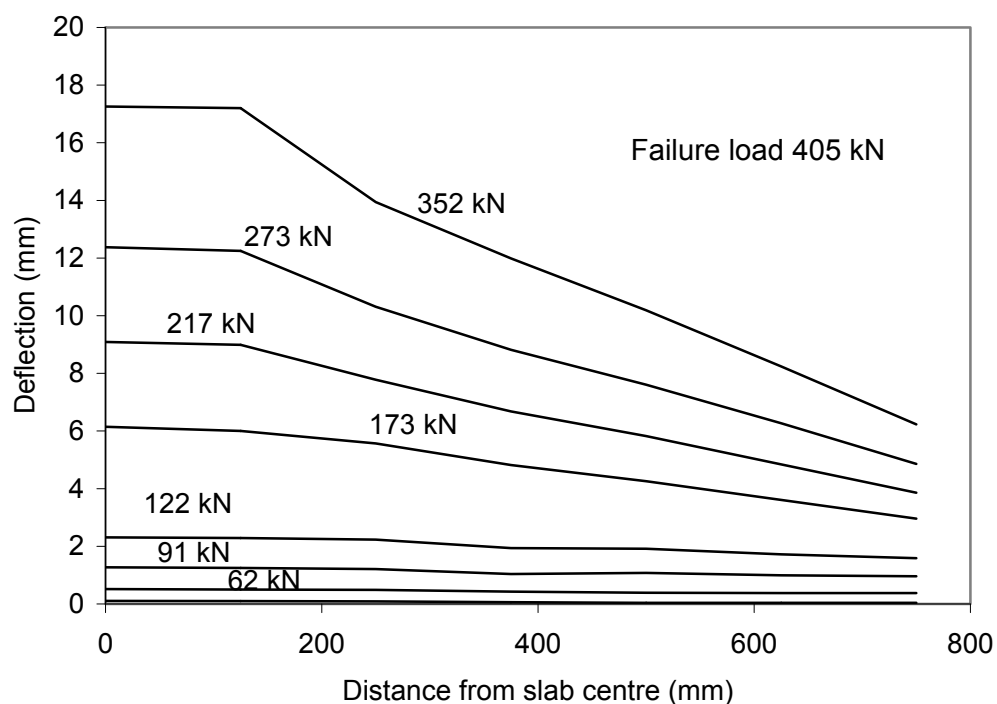


Figure 4-16: Deflection profile of slab RS-F<sub>0</sub> along the centre line.

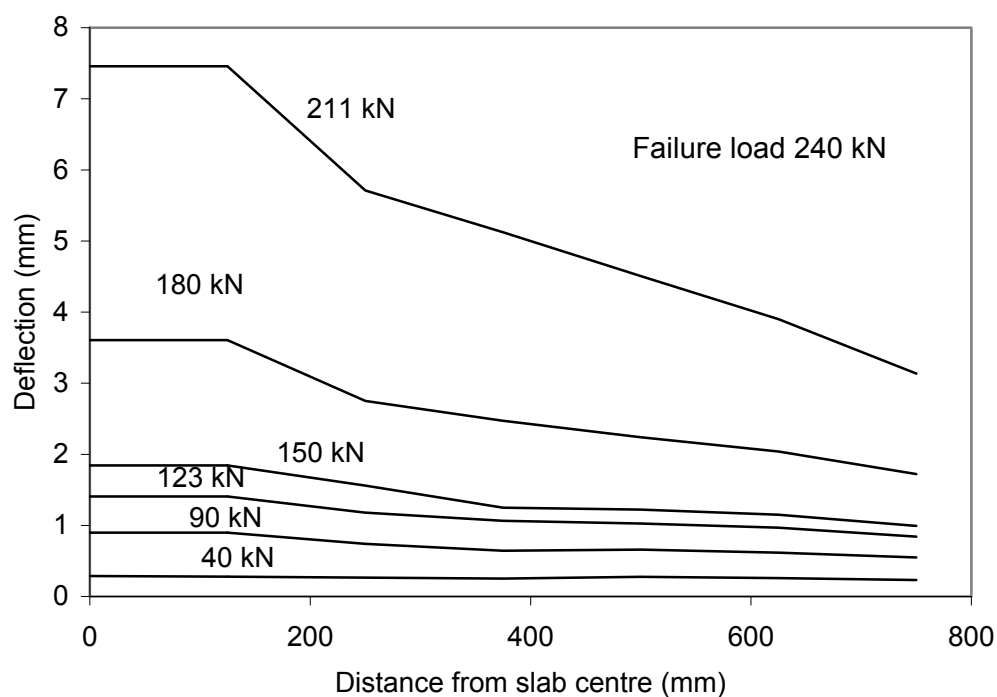


Figure 4-17: Deflection profile of slab RS-F<sub>15</sub> along the centre line.

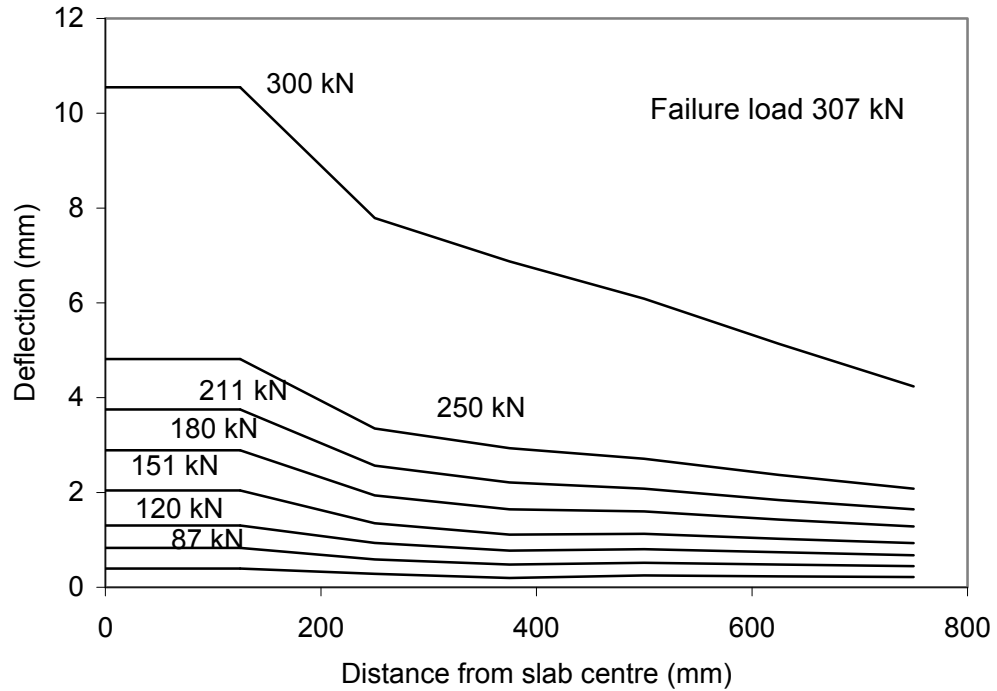


Figure 4-18: Deflection profile of slab RS-F<sub>30</sub> along the centre line.

The load-rotation curves can also be constructed from the deflection profiles, as shown in Figure (4-19), assuming a conical shape for the deflection profile outside the critical shear crack. The load rotation curves are shown with the Muttoni [65] failure criteria for slabs with low reinforcement ratio. The effect of FRP reinforcement is shown by increasing the punching capacity of the slab (RS-F<sub>0</sub>) compared to the reference slab (RS<sub>0</sub>), but simultaneously decreased the ratio of the punching load to the flexural load, which is translate into smaller rotation at failure. For the prestressed slabs (RS-F<sub>15</sub>), (RS-F<sub>30</sub>) and (RS-F<sub>30F</sub>), a considerable reduction in the rotation capacity was encountered by applying the prestressing to the FRP reinforcement, but a large bonding area is required to make the ultimate punching load within that range predicted by the failure criteria shown in the figure if full bond is assumed for the FRP reinforcement. This emphasizes that the design of FRP RC can be controlled by the serviceability limit state.

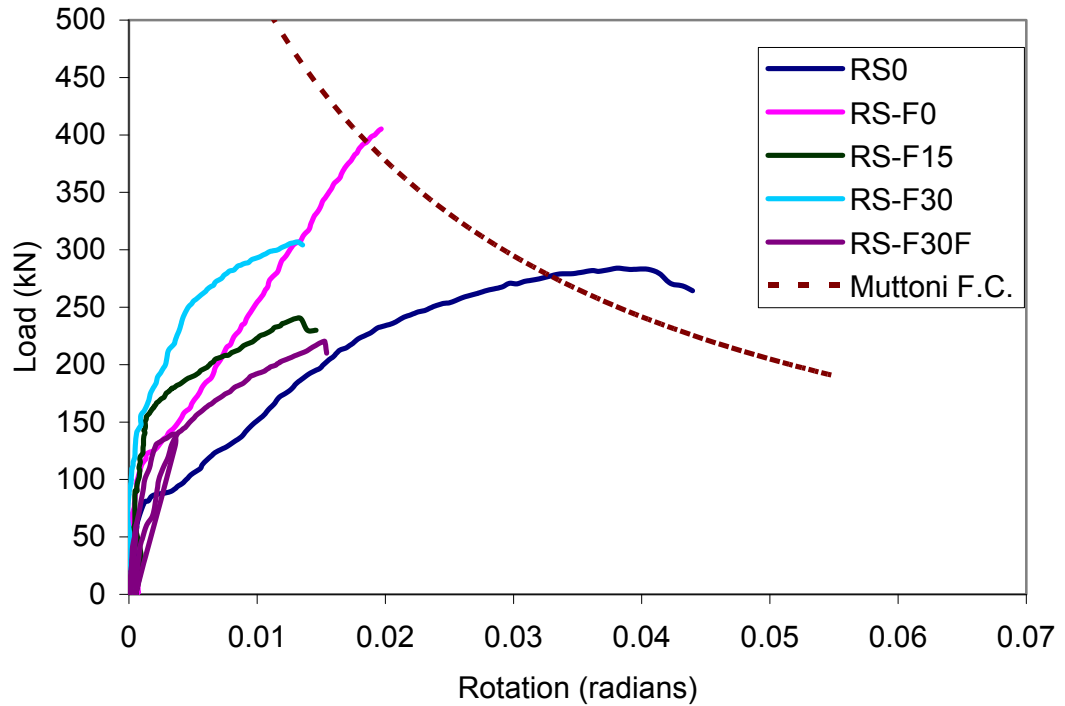


Figure 4-19: Load-rotation curves of the test slabs.

#### 4.3.2. Stiffness characteristics

The slope of the load-deflection curve at a point is known as the member stiffness at that loading point. Here in this study, the initial stiffness  $K$  of the test slabs was evaluated analytically as the slope of the load-deflection curve within the first crack load. The results show that the use of the FRP reinforcement nearly doubled the initial stiffness of the strengthened specimens. No significant difference between the non-prestressed and prestressed specimen could be recognized. The initial stiffness  $K$  values of all specimens are given in Table (4-1).

#### 4.3.3. Energy absorption characteristics

The energy absorbed is the area under the load-deflection curve for a tested specimen. This area was calculated by numerical integration up to the ultimate load and corresponding displacement. It was clearly noticed that the non-prestressed specimen (RS-F<sub>0</sub>) encountered a considerable decrease in the

energy absorbed by nearly 38.5% of the reference specimen ( $RS_0$ ), whereas the average absorbed energy of the prestressed specimens ( $RS-F_{15}$ ), ( $RS-F_{30}$ ) and ( $RS-F_{30F}$ ) was only 20% of the of the reference specimen ( $RS_0$ ). The reason for this massive reduction in the prestressed specimens is attributed to the prestressing effect and debonding, which reduced the deformation capacity of the slab. Values of the absorbed energy  $\Psi$  for each slab are summarized in Table (4-1).

#### **4.3.4. Ultimate punching loads**

Referring to the ultimate load as the load capacity without exceptions is not practical from the serviceability point of view. For instance, slabs with low reinforcement ratios experience large deflections before they reach their ultimate load. So that, referring to the yield load as the load capacity could be more realistic. That is these members can store more strain energy after the yielding of the internal steel as a result of the strain hardening of the internal steel reinforcement, membrane action and tension stiffening, which appears as an increase in the load capacity. Nevertheless, this increase does not enhance the serviceability as mentioned earlier. Therefore, in this study the load capacities of the strengthened slabs were compared to both the yield and ultimate loads to obtain a conclusive comparison.

Figure (4-20) presents the normalized increase/decrease of the punching capacity for the strengthened specimens compared with both the yield and ultimate loads of the control specimen ( $RS_0$ ). The diagram shows that the non-prestressed FRP strips were able to enhance both the yield and ultimate load of slab ( $RS-F_0$ ) by 59.3% and 42.7%, respectively, over that of the control specimen ( $RS_0$ ). On the other hand, the prestressed FRP strips were only able to enhance the first crack load and to prevent yielding of steel reinforcement. The percentage increase in the yield load of slabs ( $RS-F_{15}$ ), ( $RS-F_{30}$ ) and ( $RS-F_{30F}$ ) were 39.9%, 78.8% and 28.2%, correspondingly, over that of the control specimen ( $RS_0$ ). The reduction in the ultimate load of the prestressed slabs was between 15 and 22%. It is observed that the strengthening is more effective for the specimen with non-prestressed FRP strips, whereas the early debonding

was the main reason for the reduced ultimate strength of the prestressed slabs. This supports what Alexander and Simmonds [33] argued that the anchorage failure of the reinforcement was the reason for the reduced strength of the slabs with flexural reinforcement concentrated over the column region, and tested by Elstner and Hognestad [28] in 1956 and Moe [17] in 1961.

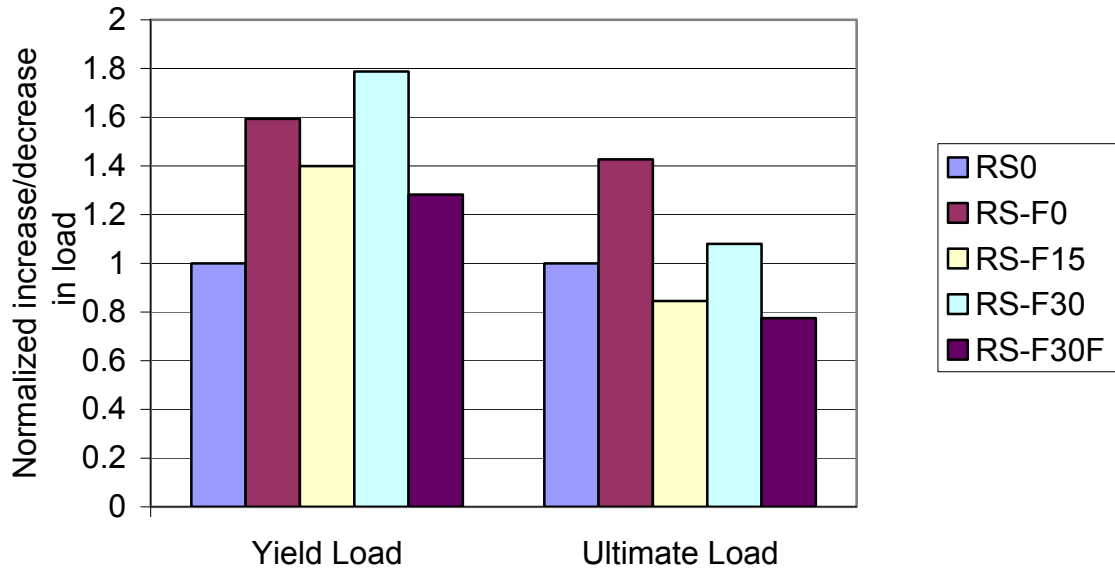


Figure 4-20: Load comparison of test slabs.

#### 4.3.4.1. Comparison with design codes

Since the British standard BS 8110 [22] does not have any provision to estimate the punching shear capacity of prestressed concrete flat slabs, so the test results were only compared with the values predicted by the punching shear formulae of ACI 318 [23], Eurocode 2 [21] and Ebead and Marzouk modified model [18] explained in Chapter 2. It can be seen from the data in Table (4-2) that only the reference slab (RS<sub>0</sub>) and non-prestressed slab (RS-F<sub>0</sub>) reached the flexural capacity  $V_{flex}$ , while the punching shear strength of the prestressed slabs is overestimated as they early failed by debonding.

The ACI formulae are, in general, conservative with average value of 1.164. This is because they only consider the effect of column geometry and slab size

but they do not account for the reinforcement ratio, which significantly affects the punching capacity. This is quite clear in specimen (RS-F<sub>0</sub>) where the punching shear strength is underestimated by nearly 60%. However, for the prestressed slabs, the ACI code was able to give predictions, to some extent, consistent with the test results, for the same reason. That is in this case when the FRP reinforcement debonds from the concrete substrate, only the concrete controls the slab behaviour.

Table 4-2: Comparison of test results with code predictions

Specimen	$V_{u,test}$ kN	$V_{u,predicted}$ kN			$V_{u,test} / V_{u,predicted}$		
		ACI	EC2 <sup>(3)</sup>	$V_{flex}^{(4)}$	ACI	EC2	$V_{flex}$
RS <sub>0</sub>	284	248.6 <sup>(1)</sup>	231.4	299	1.142	1.227	0.95
RS-F <sub>0</sub>	405.2	248.6	359	376.1	1.63	1.129	1.077
RS-F <sub>15</sub>	240	248.6	374	381.86	0.965	0.631	0.629
RS-F <sub>30</sub>	307	253 <sup>(2)</sup>	396.2	449.7	1.213	0.775	0.683
RS-F <sub>30F</sub>	220	253	396.2	449.7	0.87	0.534	0.49
Mean value					1.164	0.866	0.766
Coefficient of variation					0.253	0.344	0.315

(1) Values calculated according to Equation (2-34)

(2) Values calculated according to Equation (2-35)

(3)  $V_R$  is calculated using equivalent reinforcement ratio as shown in Appendix A

(4)  $V_{flex}$  is calculated using sectional analysis as shown in Appendix A.

On the other hand, both the Eurocode 2 and Ebead model significantly overestimate the punching shear strength of the prestressed slabs, as they reflect the effect of prestressing and reinforcement ratio, with the full bond assumption. They overestimate the punching shear strength by almost 30 to 50%, as shown in Table (4-2). This could be clarified more by the level of the strains predicted by the sectional analysis, with reference to Table (A-1) in the appendixes. It is noticeable that the level of strains for the prestressed slabs exceeded the limits provided by ACI 440.2R [3] for debonding failure which confirms the debonding failure of these slabs. However, for the reference slab

(RS<sub>0</sub>) and the non-prestressed slab (RS-F<sub>0</sub>), the predictions of Eurocode 2 and Ebead modified model are much closer to measured value than those of ACI. In conclusion, this comparison shows that the code formulae are suitable for cases in which the bond between the reinforcement and the concrete is maintained, but they could give misleading prediction in cases where the debonding is the governing failure mode.

#### **4.4. Conclusion**

Bonding non-prestressed FRP plates to the tension face of RC slabs with low reinforcement ratio, both strength and stiffness of the slabs can be increased. However, bonding prestressed FRP plates was only able to enhance the stiffness but did not significantly contribute to the ultimate punching load, since the high prestressing forces can easily trigger the debonding failure modes. The variation of the bond length outside the truncated cone has no effect on increasing the ultimate load. This is based on the fact that there is an effective bond length ( $L_e$ ) beyond which any extension of the bond length  $L$  cannot increase the ultimate load. This disadvantage is the basic reason behind not exploiting the full strength of the EBR. Therefore, the longer bond length does not show better strengthening effect

The interfacial debonding is progressively activated with the increase of the external load. Once it is initiated at the critical shear crack location, it propagates quickly to a FRP plate end. The time between the initiation of debonding propagation and the attainment of the ultimate load is too short, and the two loads are usually very close to each other.

The design of RC structures strengthened by FRP reinforcement is governed by the serviceability limit state. This was quite clear in the comparison study conducted in this chapter using classical analysis approaches. At the time these formulae were able to predict the ultimate strength of the cases where the full bond assumption was maintained, they failed to deal with cases more susceptible to bond failure. So that, a more advanced approach, such as FEA, is needed to deal with these cases which are conducted in the next chapter.



## **Chapter 5**

### **Numerical modelling**

#### **5.1. Introduction**

In addition to the experimental work, numerical analysis was carried out to investigate deflections of the punching shear specimens, together with the associated tension stiffening, dowel action and interfacial debonding, and steel, FRP reinforcements and concrete strains. The objectives were to provide further insight into the experimental results, to evaluate the adequacy of the corresponding theoretical predictions, and to carry out parametric studies. As a numerical tool, the Finite Element Method (FEM) is considered the most powerful approach to deal with such cases when the simple analytical models cannot account for reinforcement-concrete interactions, rather than their adoption to linear-elastic assumptions of the constituent materials. This chapter presents the background to the approach used and elaborates on its implementation in this study. Sample analytical results are presented and briefly discussed, while a comprehensive comparison of the experimental and theoretical results is undertaken in the next chapter.

#### **5.2. Finite element analysis**

At the micro-scale level, plain concrete is considered a heterogeneous material; that is a composite of aggregate and cement paste. Not so, however when it is modelled at the macro-scale level as a homogeneous representative volume, several times the aggregate size, with effective or equivalent properties [77]. This principle could be extended to the reinforced concrete if only the reinforcement is uniformly distributed in that volume. So, a homogeneous description of reinforced concrete is rarely used. Instead, the two materials are usually modelled individually, and then the assumption that the sum of the two

constituent materials, but not simply by superposition, describes reliably the behaviour of the actual composite behaviour. Such representation fits very well with numerical simulation.

Due to adopting this type of modelling, the high nonlinearity becomes a salient aspect in the stress-displacement analysis of reinforced concrete members, other than the nonlinearity in the plain concrete itself. In compression, the concrete behaviour is nonlinear. In tension, concrete has a very limited tensile strength and then it cracks. Cracking creates complex bond conditions between the reinforcement and the surrounding concrete, which involves invisible micro and secondary cracks, relative slip between the concrete and reinforcement, as well as splitting transverse stresses in the concrete. The problem is further complicated in the presence of high shear forces when other mechanisms are activated, such as dowel action and aggregate interlock. These phenomena are discussed later in this chapter.

Extensive testing is a very expensive and time-consuming process. Therefore, more interest has been given recently to numerical simulation to complement testing. FE analysis is currently the most reliable numerical analysis tool available. One of these available commercial codes is ABAQUS version 6.8 [78]. It is a renowned FE package that is based on state-of-the-art theoretical methods. Among numerous capabilities, ABAQUS can deal with a wide range of stress-displacement analysis problems allowing for almost any structural material. For reinforced concrete, ABAQUS has two measures to deal with concrete post-cracking behaviour; the oriented damaged elasticity concept (smeared cracking), and the isotropic tensile and compressive plasticity. These models account implicitly for the effect of the bond-slip on the average stresses and strains in the steel and the concrete, or to the concrete only, by modifying the properties of these two materials. These modifications are effected through appropriate incorporation of the tension stiffening effect in the constitutive models of steel and concrete [32]. ABAQUS also offers nonlinear analysis techniques designed for unstable local or global collapse situations but may be appropriate to deal with the sudden release of strain energy due to cracking of concrete. The following sections present the geometric and material models and

nonlinear analysis techniques in ABAQUS. Model parameters are then investigated, and ABAQUS is used to analyse representative punching shear tests. The detailed discussion of the analytical results in comparison to the corresponding test results is undertaken in the next chapter.

### **5.3. Slab modelling techniques**

Two techniques exist for modelling reinforced concrete slabs [79]: layered and discrete modelling. In layered formulation, the concrete section is divided into a set of layers, while the reinforcement is smeared into a layer between the concrete layers. Since real reinforcement is discrete, only highly and uniformly distributed reinforced slabs can be appropriately modelled by this approach such that each element contains reinforcement. Moreover, the incorporation of bond slip can only be achieved artificially, and the calculated strain for concrete and reinforcement is the average strain.

In discrete modelling, which is adopted in this study, concrete is modelled by three-dimensional solid elements while the reinforcements is modelled by bar, truss or shell elements (bar or truss element is used in case of modelling internal steel reinforcements, while shell element is used in case of planner reinforcement such as FRP). The connectivity between a concrete node and a reinforcement node can be achieved by two methods. In the first method, a bond element is inserted at the interface to connect the corresponding degrees of freedom for both the concrete and the reinforcement nodes; hence, the interaction response can be modelled. In the second method, concrete and reinforcement share the same node, and perfect bond is therefore assumed. This later method is computationally more efficient when used with smeared cracking. This can be justified as the smeared cracking approach and is not designated for predicting the localization of fracture. Alternatively, it can produce proper strain localization in different cases; such as mixed mode cracking, if the general behaviour is of interest [32]. So, discrete modelling of RC slabs provides a more realistic representation of steel than the layered approach. In the past, it was more expensive in terms of analysis time, since a large number of degrees of freedom are required. But now, the super fast

computers effectively reduced the analysis time and make this approach more viable.

Both methods are used to model the reinforcement of the test slabs; shell elements are used to represent the external FRP reinforcement along with an interface element to connect the corresponding nodes of concrete and FRP reinforcement, while the truss element has been chosen to represent the internal steel reinforcement assuming perfect bond. The following sections present the approach used for modelling and analysing the test specimens. Topics covered include the different meshing elements and their characteristics, reinforcement and concrete models and solution procedure for nonlinear analysis.

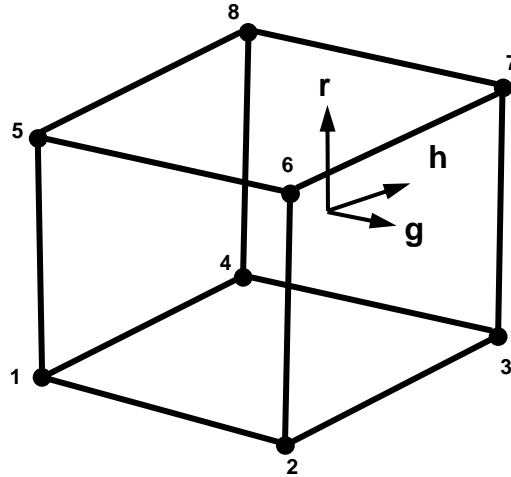
### **5.3.1. Meshing elements**

#### **5.3.1.1. Solid element**

A wide range of three-dimensional (3D) continuum elements is available in ABAQUS. For instance, the ABAQUS/Standard solid element library includes first-order (linear) interpolation elements and second-order (quadratic) interpolation elements in one, two, or three dimensions. They can be used in almost any linear/nonlinear stress-displacement analysis and to model nearly any shape. They are more accurate, provided they are not distorted, particularly for hexahedral elements.

Among these is the eight-node isoparametric brick element (C3D8) illustrated in Figure (5-1), which is adopted here to model the concrete slabs. Each node has three dimensional translational degrees of freedom. They can predict the same behaviour of the second-order element if a fairly detailed mesh is used. Furthermore, it is generally better to use first-order elements for those parts of a model that will form a slave surface (the slab surface in this case) in a contact problem. Second-order elements can sometimes cause problems with contact because of the way these elements calculate consistent nodal loads for a constant pressure. In this way, ABAQUS adds a mid-face node to any face of a

second-order brick element that defines a slave surface to consistently distribute the contact pressure over the slave surface, which increases the analysis time.



Interpolation function for translation:

$$u_i(g, h, r) = a_0 + a_1g + a_2h + a_3r + a_4gh + a_5hr + a_6rg + a_7ghr$$

Figure 5-1: First-order brick element.

Shear locking is a problem with all fully integrated, first-order, solid elements subjected to bending loads. It is the inability of elements to reproduce a zero transverse shear strain energy state in pure bending. This spurious shear stress arises because the edges of the element are unable to curve to maintain the initial angle between them, but these elements function perfectly well in direct or shear loads. Obviously, the behaviour of the column-slab connection is shear dominated, and the loading condition produces minimal bending deformations. Consequently, the problem of shear locking is less of concern in the current study.

Finally, in these elements, the strain operator provides constant volumetric strain throughout the element. This constant strain prevents mesh locking when the material response is approximately incompressible.

### **5.3.1.2. Truss element**

In ABAQUS, both the truss and rebar element could model the main steel reinforcement and yield the same results as will be shown later in this chapter. The truss element was preferred to the rebar element as ABAQUS/CAE does not support visualization of element-based rebar or rebar results. A two-node linear displacement (T3D2) truss element was adopted to represent the internal steel reinforcements. These truss elements are embedded into “host” continuum elements as shown in Figure (5-2). Embedding means that the translational degrees of freedom at the nodes of the embedded element are eliminated and become constrained to the corresponding interpolated values in the host continuum element. The reinforcement-concrete interaction is not accounted for, but is indirectly considered in the concrete model by modifying some aspects of the plain concrete behaviour as mentioned before in Section 5.2.2.

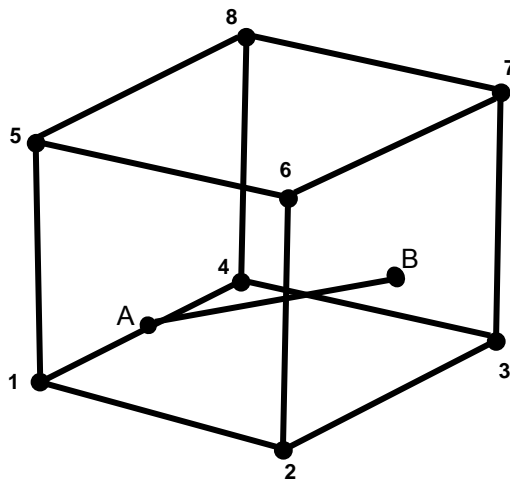


Figure 5-2: Truss element AB embedded in solid element; node A is constrained to edge 1-4 and node B is constrained to face 2-6-7-3.

### **5.3.1.3. Shell element**

If the material response is linear like FRP, the more economic approach in terms of computational efficiency is to use a general shell section. Therefore, a conventional layered shell element (S4) with five degrees of freedom; three

displacement components and two in-surface rotation components at each node, was chosen to model the FRP reinforcement; illustrated in Figure (5-3). This is based on the assumption that the loading configuration is most likely to produce in-plane stresses in FRP, so that the out of plane normal stress component is zero. Consequently, FRP could be modelled as an anisotropic homogeneous material under plane stress. The assumptions of using this element are as follows:

1. The shell thickness is less than about 1/15 of the characteristic length of the shell surface, such as the distance between supports or the breadth of the plate in this study. However, the thickness may be larger than 1/15 of the element length.
2. Kirchhoff constraint is applicable so that the shell normal remains orthogonal to the shell reference surface.
3. Only small strain is allowed, so the change in thickness with deformation is ignored during the analysis time. However, the element could sustain large rotation.
4. The stress component perpendicular to the plane surface of the element is zero.

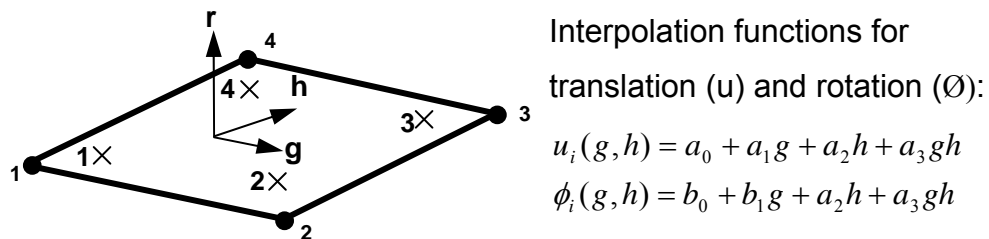


Figure 5-3: 4-node doubly curved general-purpose shell element.

#### 5.3.1.4. Connector (spring) element

As discussed in Chapter 2, and has been proved by the test results in Chapter 4, the debonding failure in concrete structures strengthened with EBR usually takes place in the near-surface layer of the concrete substrate. Thus, the connector element used here is to represent that interface not the adhesive material (epoxy). The connectivity of this element could be simplified as if it

combines three springs working orthogonally. As shown in Figure (5-4), the element provides a Cartesian connection between the two nodes where the response in three local connection directions is specified. These three local directions  $\{e_1^a, e_2^a, e_3^a\}$  are defined at the first node  $a$ , while the change in position of the second node  $b$ , along these local coordinate directions, is measured.

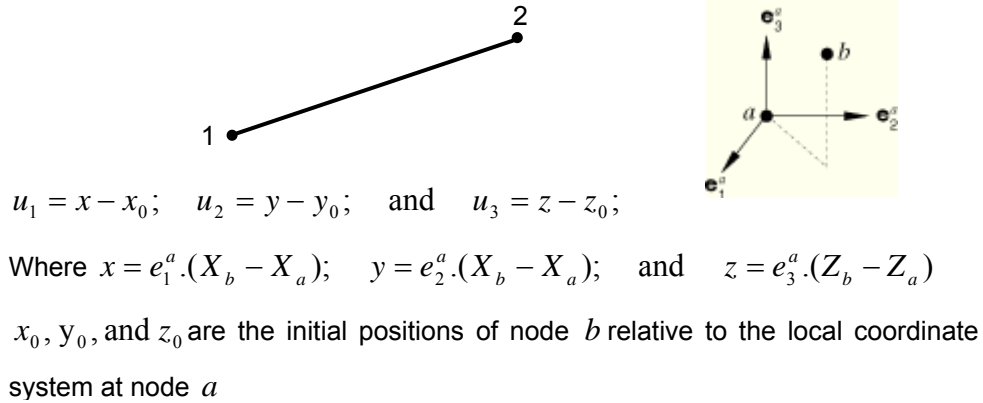


Figure 5-4: Two-node connector element (CONN3D2).

#### 5.3.1.5. Rigid element

Figure (5-5) shows the three dimensional, four-node rigid surface element (R3D4) with its normal ( $n$ ) given according to the right-hand rule. Each node has three degrees of freedom. This element was chosen to model the supports as will be illustrated later in Section 5.5.1. All elements were connected to a reference point where the boundary conditions were applied.

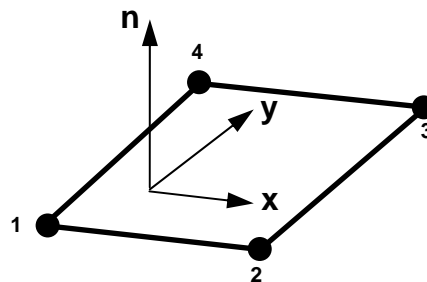


Figure 5-5: Four-node, bilinear quadrilateral rigid surface element.



## 5.4. Material models

### 5.4.1. Steel reinforcement

The steel reinforcement was defined based on the stress-strain results of the uniaxial tensile tests given in Chapter 3. The behaviour was defined as a bi-linear curve (linear elastic with strain hardening). The elastic part of the behaviour was defined by the longitudinal elastic modulus and Poisson's ratio of 0.3, while the plastic part was defined by true stress,  $\sigma_s$ , and true plastic strain,  $\tilde{\varepsilon}_s^{pl}$ , data pairs as follow.

$$\sigma_s = \sigma_{nom} (1 + \varepsilon_{nom}) \quad \text{Equation 5-1}$$

$$\tilde{\varepsilon}_s^{pl} = \varepsilon_s - \varepsilon_s^{el} \quad \text{Equation 5-2}$$

Where  $\varepsilon_s = \ln(1 + \varepsilon_{nom})$ ;

$$\varepsilon_s^{el} = \sigma_s / E_s.$$

And  $\sigma_{nom}$ ,  $\varepsilon_{nom}$  and  $E_s$  are the nominal stress, the nominal strain and the modulus of elasticity, respectively

A linear descending branch was then specified when the strain exceeded the limiting strain of the ultimate tensile strength.

### 5.4.2. FRP reinforcement

FRP composites are materials that consist of two constituents. The constituents are combined at a macroscopic level and are not soluble in each other. One constituent is the reinforcement fibre, which is embedded in the second constituent, a continuous polymer called the matrix [2]. The reinforcing fibres, which are typically stiffer and stronger than the matrix, take up to 70% of the compound volume. The FRP composites are anisotropic materials; that is, their properties are not the same in all directions. Figure (5-6) shows a schematic of FRP composites.

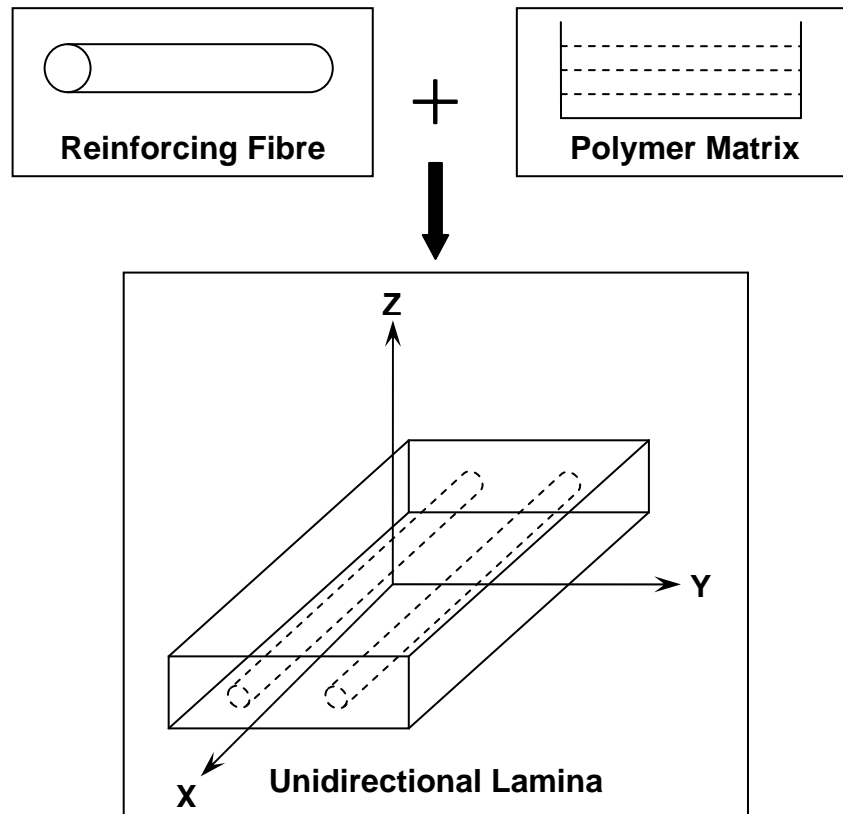


Figure 5-6: Schematic of FRP composites.

As shown in Figure (5-6), the unidirectional lamina has three mutually orthogonal planes of material properties ( $xy$ ,  $xz$ , and  $yz$  planes). The  $xyz$  coordinate axes are referred to as the principal material coordinates where the  $x$  direction is in the same direction of the fibres, and the  $y$  and  $z$  directions are perpendicular to the  $x$  direction. Therefore, it is considered as an orthotropic material. This orthotropic material is also transversely isotropic, where the properties of the FRP composites are nearly the same in any direction perpendicular to the fibres. Thus, the properties in the  $y$  direction are the same as those in the  $z$  direction. So, this material is so-called a specially orthotropic material [80].

The FRP plate reinforcement was defined in the FE model based on the uniaxial tensile test results given in Chapter 3. This plate typically consists of a big number of laminas stacked together, but practically it could be modelled at

the macro-scale level as a plate with equivalent material properties. The input data needed for the model are as follows:

- The overall thickness of the plate.
- Orientation of the fibre direction of the plate.
- Elastic modulus of the FRP composite in three directions ( $E_x$ ,  $E_y$  and  $E_z$ ).
- Shear modulus of the FRP composite for three planes ( $G_{xy}$ ,  $G_{yz}$  and  $G_{xz}$ ).
- Major Poisson's ratio for three planes ( $\nu_{xy}$ ,  $\nu_{yz}$  and  $\nu_{xz}$ ).

Assuming the  $x$  direction is the same as the fibre direction, while the  $y$  and  $z$  directions are perpendicular to the  $x$  direction.

The properties of isotropic materials, such as elastic modulus and Poisson's ratio, are identical in all directions. This is not the case with specially orthotropic materials. For example,  $E_x \neq E_y$  and  $\nu_{yx} \neq \nu_{xy}$ .  $E_x$  is the elastic modulus in the fibre direction, and  $E_y$  is the elastic modulus in the  $y$  direction perpendicular to the fibre direction. The values of  $E_x$  and  $\nu_{xy}$  were given by the manufacturer and checked experimentally in Chapter 3, while the Poisson's ratio  $\nu_{yx}$  was implicitly given with the following equation [80].

$$\nu_{yx} = \left( \frac{E_y}{E_x} \right) \nu_{xy} \quad \text{Equation 5-3}$$

The shear moduli  $G_{xz}$  and  $G_{yz}$  were included because they might be required for modelling potential transverse shear deformation in the FRP plate. In this case the stress-strain relations for the in-plane components of the stress and strain are of the form;

$$\begin{Bmatrix} \varepsilon_x \\ \varepsilon_y \\ \gamma_{xy} \end{Bmatrix} = \begin{bmatrix} 1/E_x & -\nu_{xy}/E_x & 0 \\ -\nu_{xy}/E_x & 1/E_y & 0 \\ 0 & 0 & 1/G_{xy} \end{bmatrix} \begin{Bmatrix} \sigma_{xx} \\ \sigma_{yy} \\ \tau_{xy} \end{Bmatrix} \quad \text{Equation 5-4}$$

The rupture of the FRP reinforcement was defined by specifying a stress based failure criterion; Tsai-Hill failure theory [80]. The input data required for this failure envelop are tensile and compressive stress limits,  $X_t$  and  $X_c$ , in the  $x$  direction; tensile and compressive stress limits,  $Y_t$  and  $Y_c$ , in the  $y$  direction; and shear strength (maximum shear stress),  $S$ , in the  $X - Y$  plane. The Tsai-Hill failure criterion requires that:

$$I_F = \frac{\sigma_{xx}^2}{X^2} - \frac{\sigma_{xx}\sigma_{yy}}{X^2} + \frac{\sigma_{yy}^2}{Y^2} + \frac{\sigma_{xy}^2}{S^2} < 1 \quad \text{Equation 5-5}$$

If  $\sigma_{xx} > 0$ , then  $X = X_t$ ; otherwise,  $X = X_c$ . If  $\sigma_{yy} > 0$ , then  $Y = Y_t$ ; otherwise,  $Y = Y_c$ . A summary of material properties used for the modelling of all four slabs is given in Appendix A. Figure (5-7) shows the failure envelope (i.e.,  $I_F = 1$ ) in  $(\sigma_{xx} - \sigma_{yy})$  stress space.

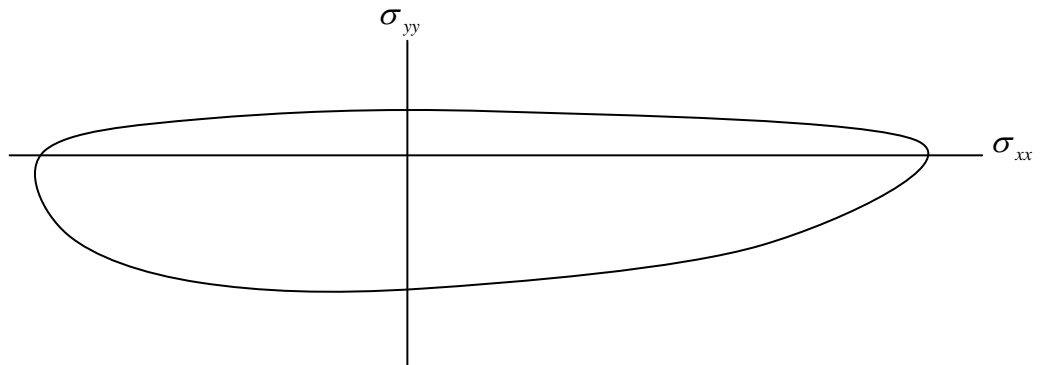


Figure 5-7: Tsai-Hill failure envelope ( $I_F = 1$ ).

### 5.4.3. Concrete

As mentioned before in Section 5.2, the concrete material library in ABAQUS has two approaches for concrete modelling; smeared cracking and damaged plasticity [78]. A comparison between the two models was carried out to identify their capabilities in modelling the test slabs. The reference slab (RS<sub>0</sub>) was chosen to perform this comparison. Two identical models were created in

ABAQUS/standard adopting the same analysis procedure and material definition for both concrete and steel reinforcement. C3D8 solid elements and T3D2 truss elements were adopted to represent the concrete matrix and the internal steel reinforcements, respectively, as shown in Figure (5-22). The average characteristic length of the mesh was 48.7mm based on the convergence study presented later in this chapter. It was concluded that the smeared cracking model has two main disadvantages making the model inappropriate in 3D applications.

Firstly, is the yield function adopted which consists of independent surfaces; an isotropic-hardening yield surface that is active when the stress is dominantly compressive, while a “crack detection surface” that determines if a point fails by cracking. Both surfaces are linear relationship between the equivalent pressure stress,  $P$ , and the Mises equivalent deviatoric stress,  $q$ , which means associated flow assumption is used. So, the model significantly simplifies the compressive behaviour as the associate flow assumption over estimates the volumetric plastic strain. As a result, applying such yield surface in 3D stress states gives an inaccurate prediction due to the omission of the 3rd stress invariant dependence. In addition, the model uses a fixed angle crack model (FACM) to detect subsequent cracks, which results in a shear stress locking problem. This problem is attributed to the increase of shear stress on the crack plane due to restricting subsequent cracking to be orthogonal to the first crack since stress components associated with an open crack are not included in the definition of the failure surface used for detecting the additional cracks [78].

Since the smeared crack approach was developed, three methods have been proposed as remedies for the shear stress locking phenomenon [81, 82]: (1) mesh refinement; (2) inclusion of an explicit shear softening law; and (3) use of a multi-directional or rotating crack model. The mesh refinement method could relieve the finite element model of the shear stress locking problem as the number of elements employed is so large that cracking in any orientation can be captured, but its disadvantage is obviously the large increase in the required computational effort. The second method is available in ABAQUS. However, it

allows for the simulation of shear softening by the inclusion of linear-descending shear softening law without considering the shear lag phenomenon. Consequently, the model is unable to accurately follow the development of cracks [82]. The last method is not supported by ABAQUS.

Secondly, no attempt is made to include the prediction of cyclic/unloading response or the damage in the elastic stiffness caused by inelastic straining. The aforementioned simplifications for the sake of the computational cost result in convergence problems; early upon crack detection, makes the analysis stop due to numerical stability after a very small deflection. On the other hand, the damaged plasticity model, which is described later in this section, could predict the behaviour of the test slab (RS<sub>0</sub>) up to failure as illustrated in Figure (5-8).

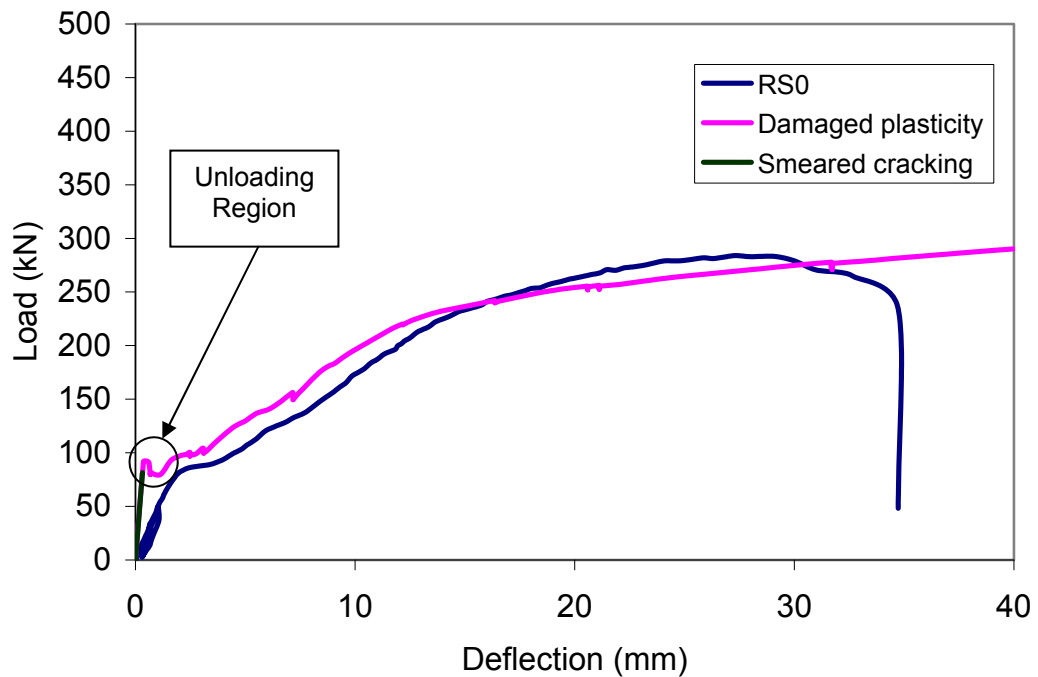


Figure 5-8: Load-deflection curve for comparison of smeared cracking and damaged plasticity models.

The concrete damaged plasticity model is intended for the analysis of plain or reinforced concrete subjected to monotonic or cyclic loading under low confining pressures. At the material point, the model allows for either tensile cracking or concrete crushing. Structural aspects of the rebar-concrete interaction, like

bond-slip and dowel action, are indirectly considered by introducing some "tension stiffening" into the concrete softening behaviour to simulate load transfer across cracks through the rebar. As the model provides a general capability for the analysis of concrete structures under cyclic and/or dynamic loading, only the relevant aspects of the concrete model under monotonic loading are presented in the following, while the input data for the FEM are given in Appendix A.

#### 5.4.3.1. Failure criteria of concrete

Cracking and post-cracking behaviour are the most important aspects of the concrete model. Cracking is assumed to occur when the triaxial state of stress reaches a failure surface determined in terms of effective stresses by the following Equation [78].

$$F(\bar{\sigma}, \tilde{\varepsilon}^{pl}) = \frac{1}{1-\alpha} \left( \bar{q} - 3\alpha\bar{p} + \beta(\tilde{\varepsilon}^{pl}) \langle \hat{\sigma}_{\max} \rangle - \gamma \langle -\hat{\sigma}_{\max} \rangle \right) - \bar{\sigma}_c(\tilde{\varepsilon}_c^{pl}) \leq 0$$

Equation 5-6

Where,

$$\alpha = \frac{(\sigma_{b0} / \sigma_{c0}) - 1}{2(\sigma_{b0} / \sigma_{c0}) - 1}; 0 \leq \alpha \leq 0.5,$$

$$\beta = \frac{\bar{\sigma}_c(\tilde{\varepsilon}_c^{pl})}{\bar{\sigma}_t(\tilde{\varepsilon}_t^{pl})} (1 - \alpha) - (1 + \alpha),$$

$$\gamma = \frac{3(1 - K_c)}{2K_c - 1}.$$

And,

$$\bar{p} = -\frac{1}{3} \bar{\sigma} : \mathbf{I} \quad \text{is the effective hydrostatic stress;}$$

$$\bar{q} = \sqrt{\frac{3}{2} (\bar{S} : \bar{S})} \quad \text{is the Mises equivalent effective stress;}$$

$$\hat{\sigma}_{\max} \quad \text{is the maximum principal effective stress;}$$

$$\sigma_{b0} / \sigma_{c0} \quad \text{is the ratio of initial equibiaxial compressive yield stress to initial uniaxial compressive yield stress (the default value is 1.16);}$$

$K_c$  is the ratio of the second stress invariant on the tensile meridian,  $q(TM)$ , to that on the compressive meridian,  $q(CM)$ , at initial yield for any given value of the pressure invariant  $p$  such that the maximum principal stress is negative,  $\hat{\sigma}_{\max} < 0$ , as shown in Figure (5-9); it must satisfy the condition  $0.5 < K_c \leq 1.0$  (the default value is 2/3);

$\bar{\sigma}_c(\tilde{\epsilon}_c^{pl})$  is the effective compressive cohesion stress; and

$\bar{\sigma}_t(\tilde{\epsilon}_t^{pl})$  is the effective tensile cohesion stress.

While  $\tilde{\epsilon}_t^{pl}, \tilde{\epsilon}_c^{pl}$  are the hardening parameters that control the evolution of the yield surface.

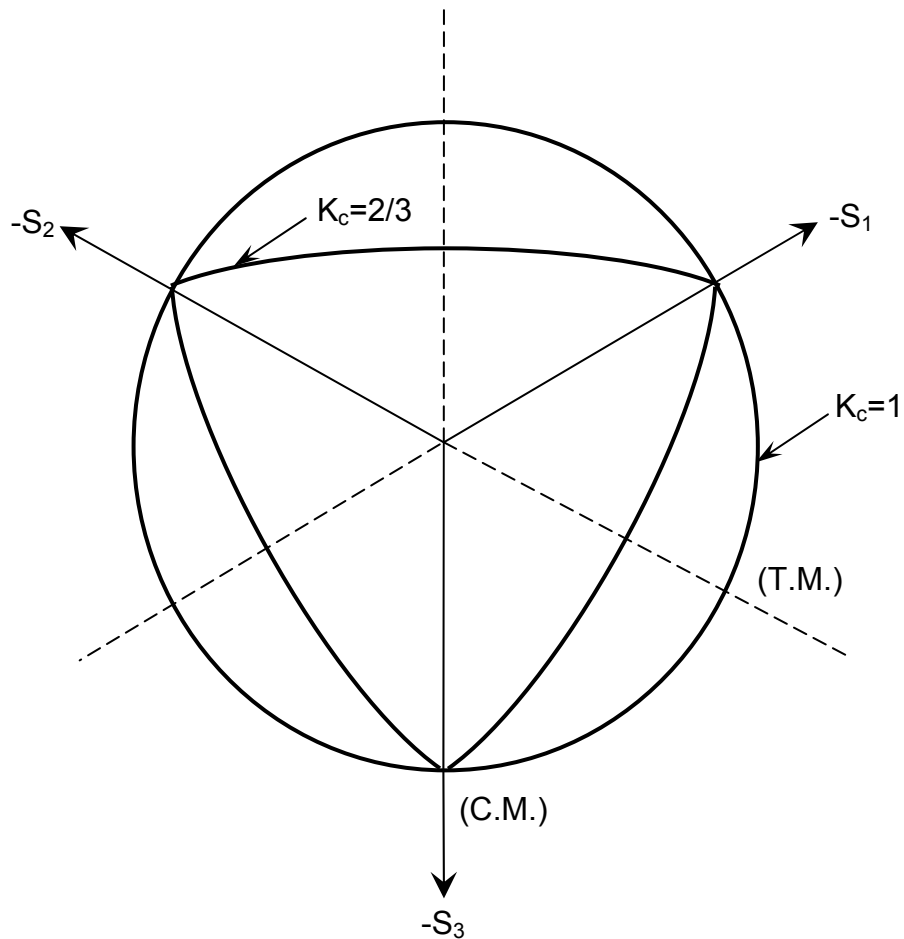


Figure 5-9: Yield surface in deviatoric plane with different values of  $K_c$ .



The concrete cracking is treated by a smeared method, meaning that the model does not physically generate individual macro cracks. Cracks are indirectly accounted for by the way their presence not only affects the stress and material stiffness perpendicular to their surfaces, but the damage in the stiffness is experienced in all three principal axis. Therefore, the model is referred to as isotropic damaged plasticity model.

#### **5.4.3.1.1. Flow rule**

The damaged plasticity assumes a non-associated flow rule to determine the flow potential which is based on the Drucker- Prager hyperbolic function, cited in [78]. The flow potential  $G$  is defined in the  $\bar{p} - \bar{q}$  plane as follows:

$$G = \sqrt{(\epsilon \sigma_{t0} \tan \psi)^2 + \bar{q}^2} - \bar{p} \tan \psi \quad \text{Equation 5-7}$$

Where,

- $\psi(\theta, f_i)$  is the dilation angle measured in the  $p-q$  plane at high confining pressure;
- $\sigma_{t0}(\theta, f_i)$  is the ultimate tensile strength, taken from the user-specified tension stiffening data; and
- $\epsilon(\theta, f_i)$  is a parameter called eccentricity that define the rate at which the function approaches the asymptote (the default value is 0.1)

It is noteworthy that using values of  $\epsilon$  that is significantly less than the default value may result in convergence problems as the flow potential tends to a straight line at low confining pressures, shown in Figure (5-10).

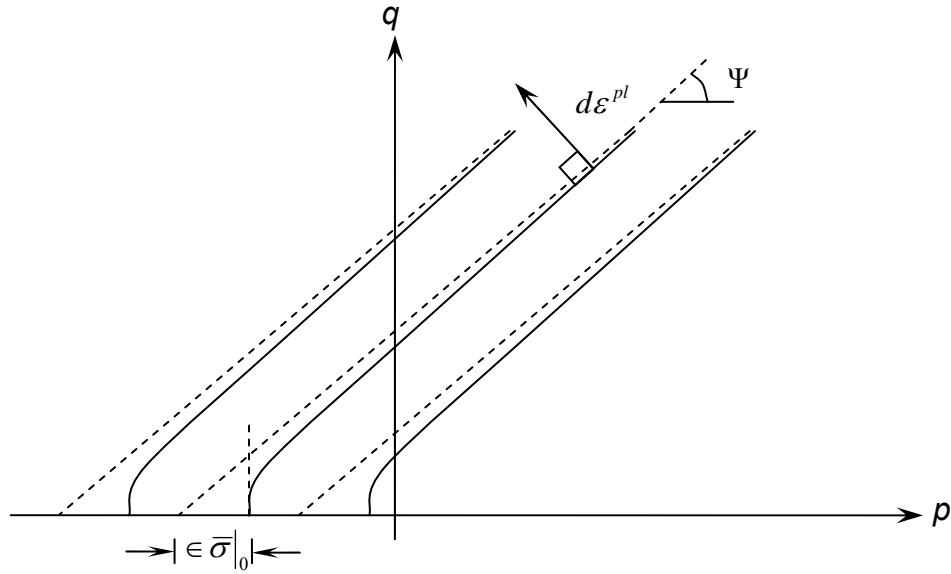


Figure 5-10: Flow potentials in p-q plane.

#### 5.4.3.2. Compressive behaviour of concrete

In compression, an equivalent uniaxial compressive stress-strain relationship for plain concrete outside the elastic range is defined. Both hardening and strain-softening regimes are given in terms of compressive stress,  $\sigma_c$ , and inelastic strain,  $\tilde{\varepsilon}_c^{in}$ , which is given as follows:

$$\tilde{\varepsilon}_c^{in} = \varepsilon_c - \varepsilon_{0c}^{el} \quad \text{Equation 5-8}$$

Where  $\varepsilon_{0c}^{el} = \sigma_c / E_0$ , and  $E_0$  is the initial modulus of elasticity.

Both uniaxial compressive and tensile models are used along with concepts of isotropic hardening and non-associated flow to determine the failure surface and control its evolution, as shown in Figure (5-10). The FE analyses were carried out based on the uniaxial compressive concrete model of Eurocode 2 [21]; shown in Figure (5-11).

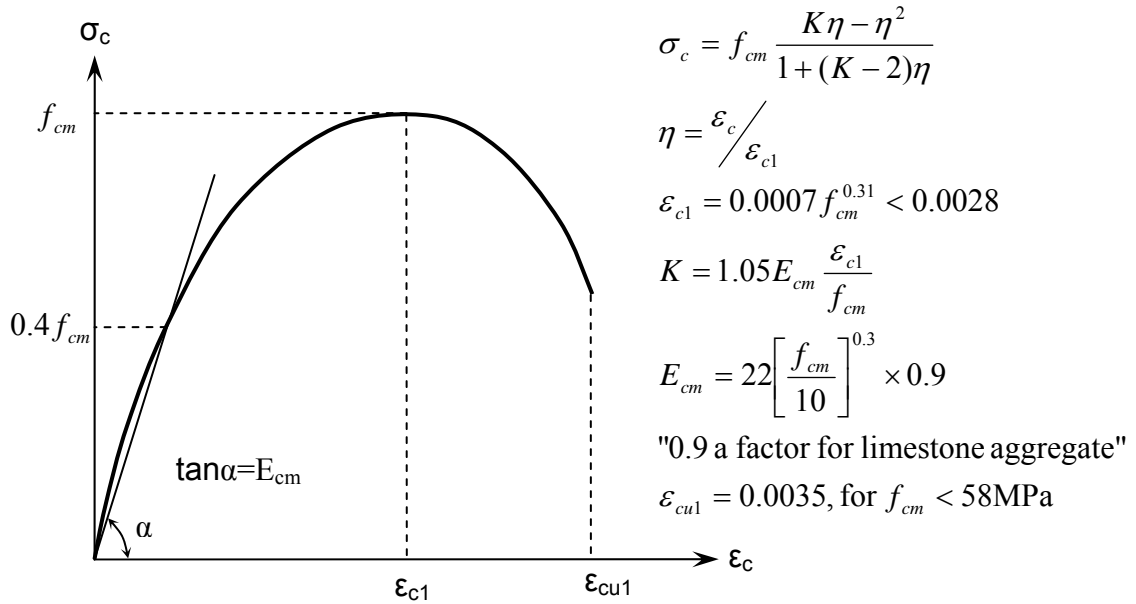


Figure 5-11: Uniaxial stress-strain curve for concrete.

### 5.4.3.3. Post-cracking behaviour

#### 5.4.3.3.1. Uniaxial tensile behaviour

Two approaches to describe the softening behaviour of cracked concrete are available in ABAQUS, as shown in Figure (5-12). The first method uses a strength criterion, while the other adopts a fracture energy cracking criterion. Stress-strain softening, based on strength criterion, may lead to mesh sensitivity, meaning that the analysis does not converge to a unique solution as the mesh is refined, because mesh refinement results in narrower crack bands rather than formation of additional cracks [78]. This is usually the case when the failure occurs only at localized regions in the structure due to the lack of reinforcement or such as the slabs under investigation where the cracking region is determined by the punching cone. The softening data are defined in a similar way to the compressive behaviour in terms of true stress,  $\sigma_t$ , and cracking strain,  $\tilde{\epsilon}_t^{ck}$ , as shown in Figure (5-12 a).

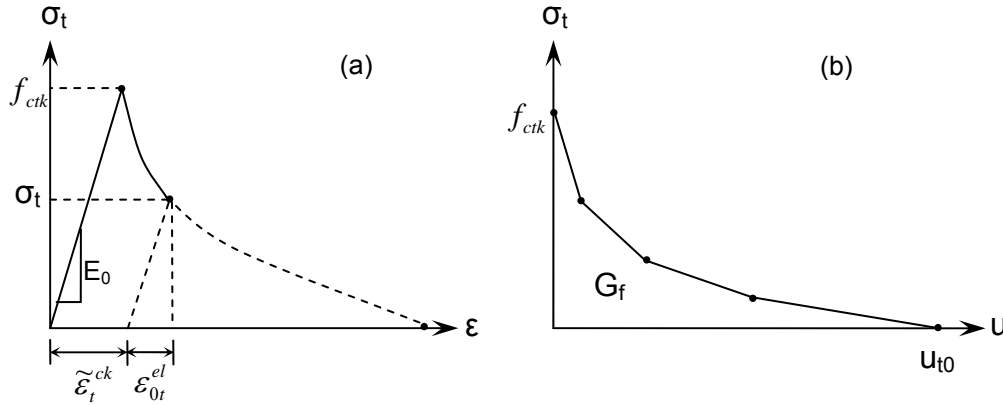


Figure 5-12: Postfailure tensile behaviour: (a) stress-strain approach; (b) fracture energy approach.

On the other hand, the fracture criterion approach, developed by Hillerborg [83], overcomes the shortcomings of the former approach. He described the brittle behaviour of concrete by a stress-displacement response rather than a stress-strain response as shown in Figure (5-12 b). Based on the brittle fracture concepts, he defined the energy required to open a unit area of crack as a material parameter,  $G_f$ , called the fracture energy. The fracture energy equals numerically the area under the stress-displacement curve which represents the work done by the tensile stress and its conjugate opening displacement. Like any quasi-brittle material, concrete specimen under tension cracks across some section due to the coalescence of micro-cracks at that section, as shown in Figure (5-13); point C. So its length will be determined by the opening at the crack. Intuitively, this opening does not depend on the specimen's length [84].

Later on, Bazant [77] developed the crack band theory claiming that the area under the stress-strain tensile softening branch of concrete is equal to the fracture energy per crack band width ( $h$ ). If the area under different tensile softening branches is the same, the post-crack behaviour of concrete should be similar. He assumed that the minimum value for the crack band width could be taken as three times the aggregate size, while the maximum value of crack band width is mesh dependent in analysing large structures if the ultimate tensile strength,  $f_{ctk}$ , is kept constant, but does not depend on the element size.

Here in this Thesis, the crack band width adopted is based on the recommendation of CEB [32]. It is assumed that the crack band width is within the tributary region of an integration point (IP) at which cracking occurs. So, as the direction in which cracking occurs is not known in advance, this characteristic length is taken as the cubic root of the volume of each IP for a three dimensional element.

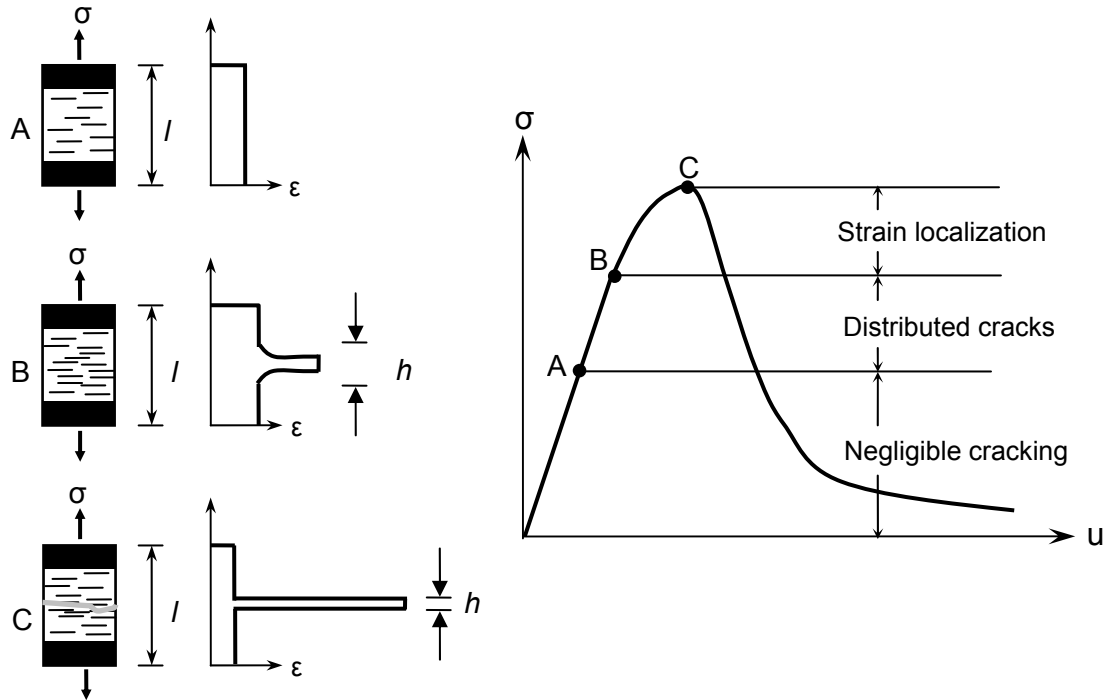


Figure 5-13: Stress-displacement curve and different cracking stages.

Currently, numerous models for tension softening are found in the literature. They are based on analytical expressions derived from curve-fitting of experimental test data. Their shapes are usually predetermined to be exponential, linear, or bilinear, with the latter including drop-constant, drop-sloped, and sloped-constant shapes [85, 86]. The linear and bilinear models have been widely used in modelling of plain concrete. However, the exponential shape such as Hordjik's model [85] is considered the most realistic one that could describe the tensile behaviour of plain concrete. Figure (5-14) shows the different shapes of softening curves adopted in this study. Assuming the area under the different curves remains constant to represent constant fracture

energy within the crack-band width, the ultimate strains accordingly are defined as follows:

1. Hordijk:  $\varepsilon_{ult,h} = 5.136G_f / f_{ctk}h$ ;
2. Linear:  $\varepsilon_{ult,l} = 2G_f / f_{ctk}h$ ;
3. Bi-linear:  $\varepsilon_{ult,b} = 25\varepsilon_{ck}$ .

Where

$\varepsilon_{ult,h}$ , is the ultimate strain of concrete in tension according to Hordijk [85];

$\varepsilon_{ult,l}$ , is the ultimate strain of concrete in tension assuming a linear softening curve;

$\varepsilon_{ult,b}$ , is the ultimate strain of concrete in tension according to the Peterson bilinear formula [32];

$\varepsilon_{ck}$ , is the cracking strain of concrete;

$G_f$ , is the fracture energy of concrete;

$f_{ctk}$ , is the characteristic tensile strength of concrete;

$h$ , is the crack band width.

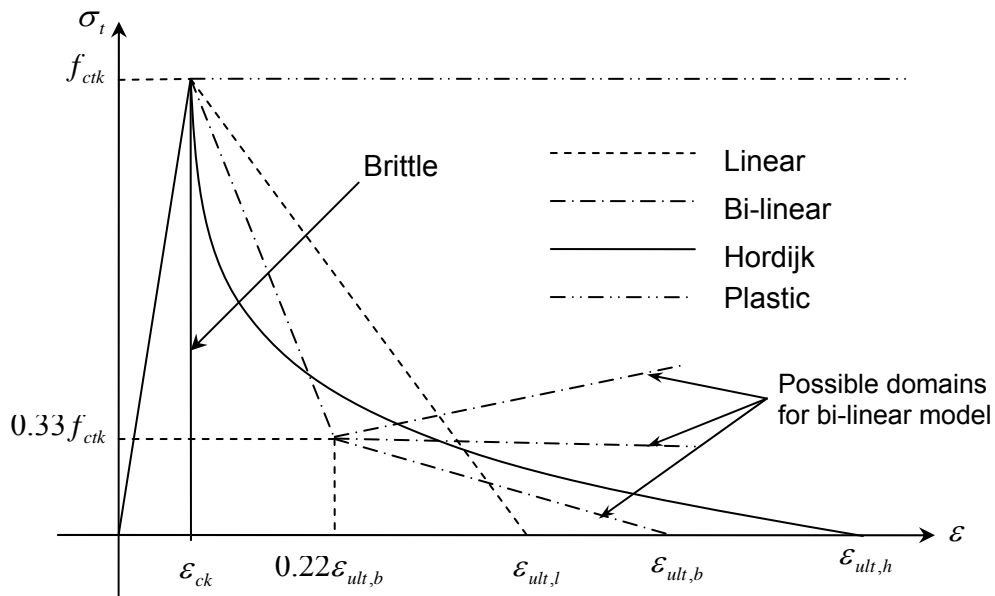


Figure 5-14: Common tension softening curves of concrete.

#### 5.4.3.3.2. Behaviour of rough cracks under mixed-mode loading

While crack initiation is based only on Mode I fracture (a tensile stresses acting normal to the plane of the crack), post-cracking behaviour in a mixed mode fracture includes Mode II (a shear stresses acting parallel to the plane of the crack and perpendicular to the crack front) as well as Mode I. However, the Mode II shear behaviour can only take place after some finite opening,  $\delta_n^*$ , has already been achieved. This delay of the shear-stress component contribution in force transfer across the crack surface is known as shear lag phenomenon [82, 87], as shown in Figure (5-15).

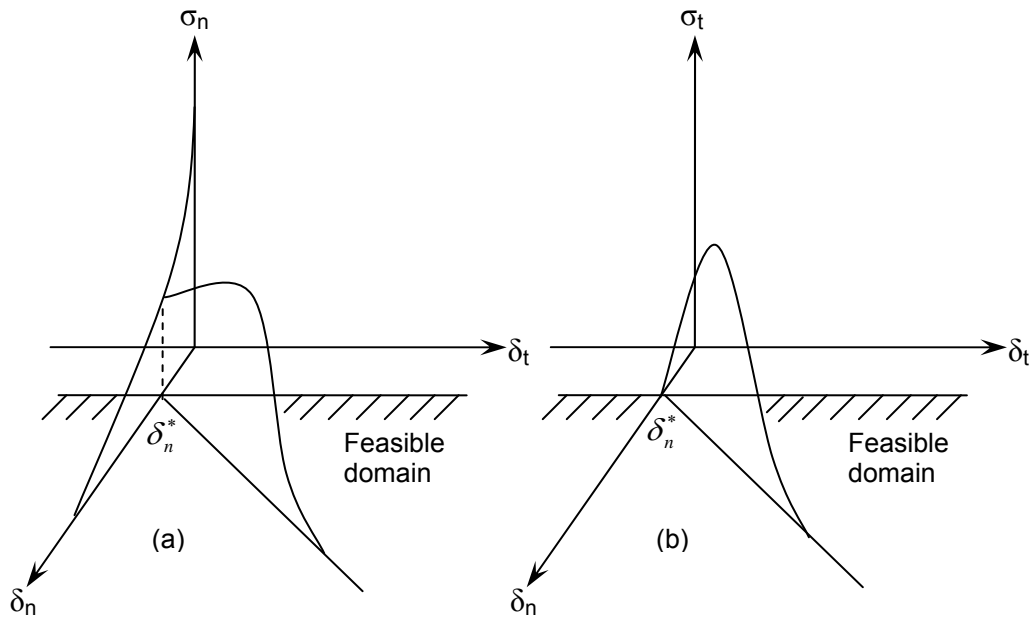


Figure 5-15: Concept of tension-softening and shear-transfer relations in  $(\delta_n, \delta_t)$  plane: (a) tension-softening relations; and (b) shear-transfer relations.

This finding had been presented by Bazant and Gambarova [87] in 1980. They introduced empirical stress-displacement relations that describe the stress transfer on rough-crack surfaces under mixed-mode fracture in reinforced concrete. The cohesive forces in the fracture process zone (FPZ) contain two components; the normal stress,  $\sigma_n$ , and the shear stress,  $\sigma_t$ , given as a

function of,  $\delta_n$ , the crack opening displacement (COD) and,  $\delta_t$ , the crack sliding displacement (CSD) is given as follows:

$$\sigma_n = f(\delta_n, \delta_t) \quad \text{Equation 5-9}$$

$$\sigma_t = f(\delta_n, \delta_t) \quad \text{Equation 5-10}$$

Based on these equations for  $\delta_n = 0$ , there is full continuity in the material which means that there is no crack. Thus, the states where  $\delta_n = 0$  and  $\delta_t \neq 0$  cannot exist. This restriction for the load path in the  $(\delta_n, \delta_t)$  plane is shown in Figure (5-16), and could be expressed in the feasible domain near the origin ( $\delta_n = \delta_t = 0$ ) by the following smoothing formula:

$$\delta_t = c\delta_n^a \quad \text{Equation 5-11}$$

Where  $c$  and  $a$  are constants.

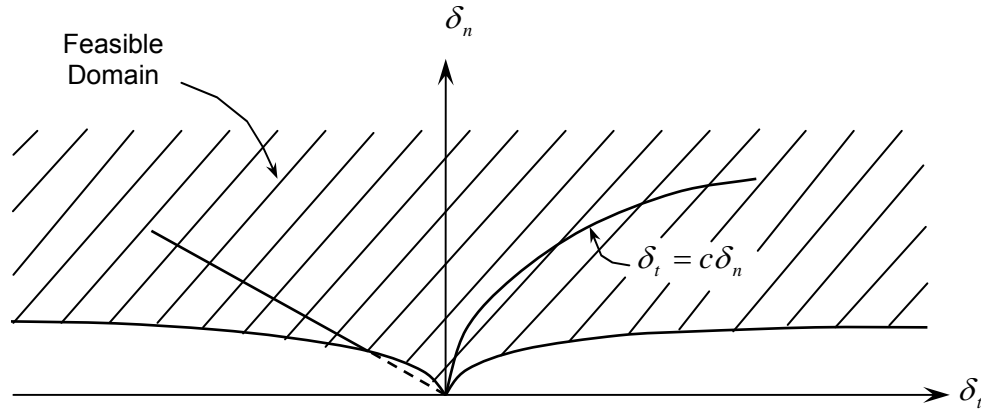


Figure 5-16: Feasible domain for the normal and tangential stresses in  $(\delta_n, \delta_t)$  plane according to Bazant and Gambarova [87].

Equation (5-11) shows that the shear slip and the crack opening are correlated. It means that a shear slip on the crack surface is always accompanied by crack opening; known as crack dilatation [87]. So, if the crack is restrained from opening; by means of internal reinforcement or steel fibres, that will result in growth of normal stresses on the crack surface. This could be justified that the



crack asperities tend to reinterlock as the crack surfaces slide, resulting in toughening mechanism. This toughness should appear in the postpeak softening behaviour, as shown in Figure (5-15 a). It is worth mentioning that dealing with mixed-mode fracture problems as if it experiences only mode I fracture will yield roughly that same ultimate load, but will not track the same crack trajectories. This is attributed to neglecting the shear stress component which affects the postpeak behaviour [82].

#### **5.4.4. Internal reinforcement-concrete interaction**

The abovementioned concrete softening models, in general, apply to cracking of plain concrete. As mentioned earlier, structural effects associated with reinforcement-concrete interaction around cracks, such as tension stiffening, bond-slip and dowel action, are indirectly considered in ABAQUS by modifying some aspects of the plain concrete behaviour to mimic them. It is stipulated that the concrete softening branch can be modified to account for these effects; depending on the reinforcement ratio, bond characteristics, aggregate size, as well as the mesh size. Very little guidance is provided in ABAQUS for that purpose, so that a detailed study is introduced later in this chapter to investigate the effect of tension stiffening and dowel action on the model results. The basic principles of these phenomena are introduced below.

##### **5.4.4.1. Tension stiffening**

After concrete cracking in reinforced concrete elements, all tensile forces are balanced by the steel only. However, between adjacent cracks, concrete contributes in transmission of tensile forces through bonding mechanisms as shown in Figure (5-17). This contribution of concrete to the stiffness of concrete member is the reason for calling the phenomena “Tension Stiffening Effect” [32].

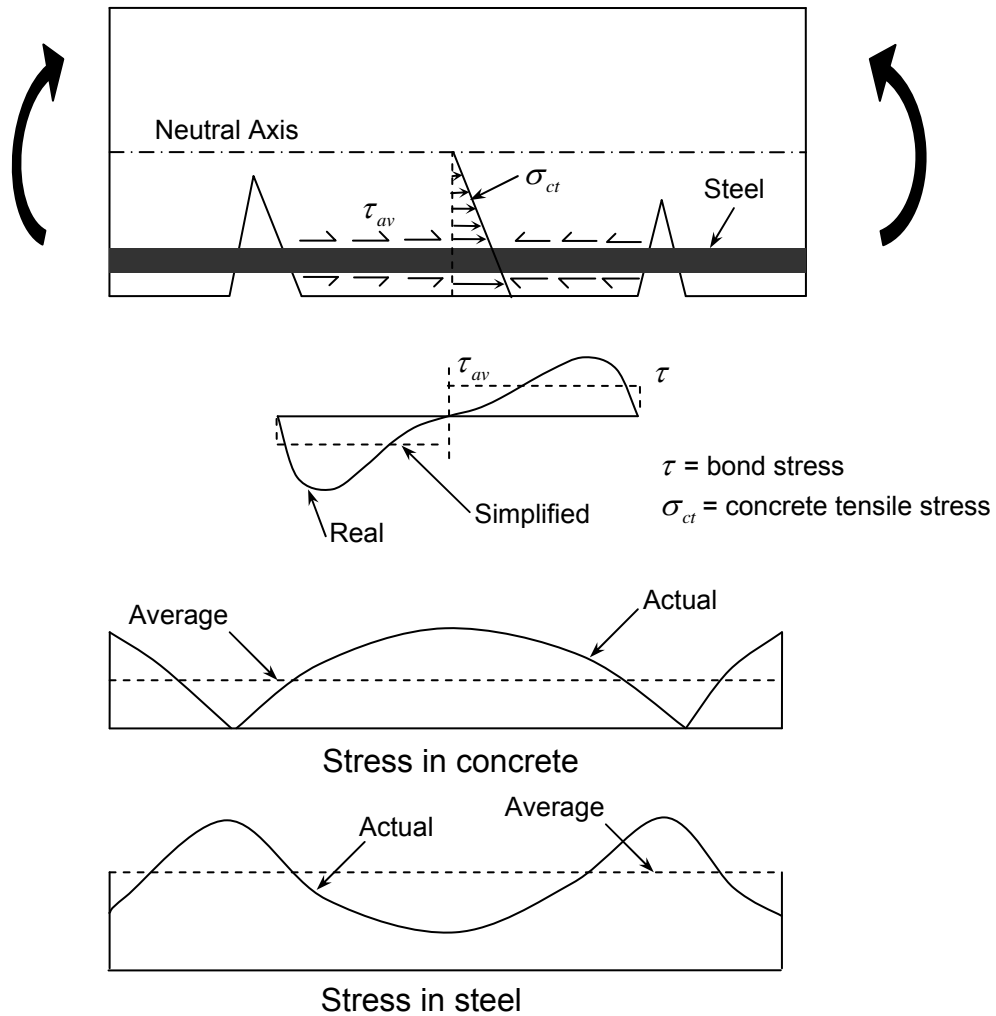


Figure 5-17: Load transfer from steel to concrete between adjacent cracks.

There are two approaches to account for the tension stiffening effect in modelling of reinforced concrete structures. The first approach is to modify the concrete softening curve into a long-tailed average concrete stress-smeared strain curve, whereas an average steel stress-smeared strain is used for steel. This method was firstly applied by Scanlon in 1971, cited in [88, 89]. Scanlon's approximation for the tension stiffening curve of concrete is shown in Figure (5-18). He assumed that the tension stiffening effect vanishes at a strain level,  $\varepsilon_0 = \alpha \varepsilon_{ck}$ . The selection of the factor,  $\alpha$ , in most cases depends on the problem studied in terms of the reinforcement ratio, bond characteristics, dimensionality of such a problem and whether the ultimate load is reached before or through

the yielding of reinforcement. For instance, selection of a very small value of,  $\varepsilon_0$ , means that the tension stiffening is underestimated. Hence, the post-cracking stiffness is underestimated as well. However, if the ultimate load is reached during the yield of reinforcement, an appropriate value for,  $\varepsilon_0$ , should be selected, otherwise the ultimate capacity is overestimated.

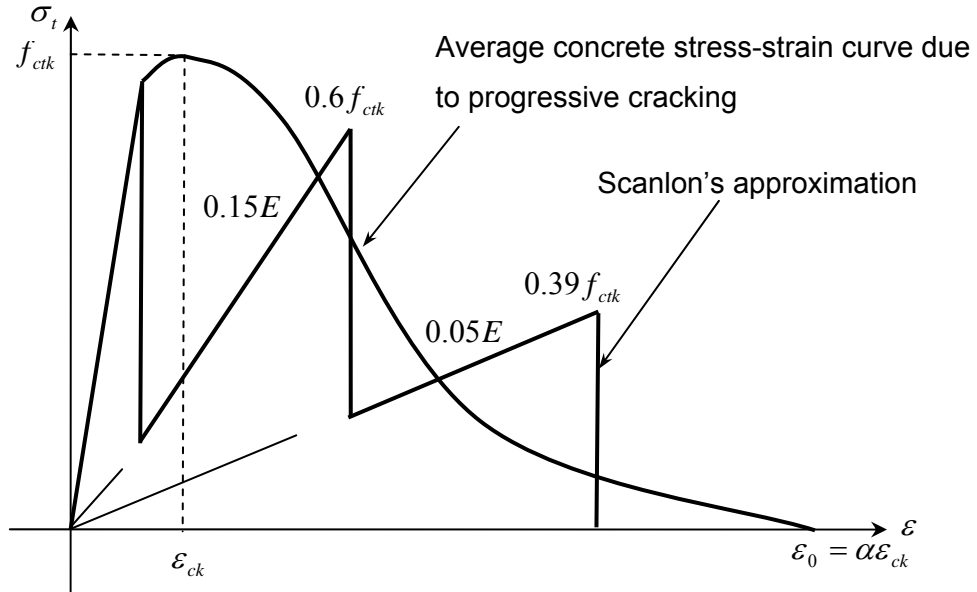


Figure 5-18: Concrete tension stiffening model according to Scanlon [90].

When the structural element is over reinforced, usually the ultimate capacity is reached before yielding of reinforcement, in such cases, the ultimate load capacity prediction is not affect too much by the selection of,  $\varepsilon_0$ . Recommendation for,  $\alpha$ , ranges from 10-25 according to Abdel-Rahman, cited in [88]. However, if a linear descending branch is assumed for the average stress strain curve, the range for,  $\alpha$ , could be taken as high as 20 to 80 times the cracking strain,  $\varepsilon_{ck}$ , with the higher values corresponding to high reinforcement ratios, according to CEB-FIP [32]. It is noteworthy that the CEB-FIP [32] recommendations conflicts with Barzegar's [88] findings. That is for high reinforcement ratios, the presence of such stabilizing elastic material would alleviate the effect of tension stiffening. Hence, selecting a small value for,  $\varepsilon_0$ , would achieve the analysis without experiencing too much numerical problems.

On the other hand, the second approach lumps the strain energy stored in the system due to the tension stiffening effect at the level of reinforcement and orients it into its direction, which means that the stiffness of the reinforcement is artificially increased to account for the tension stiffening [91], as shown in Figure (5-19). This method was deemed inappropriate if it is applied for slabs with orthogonal reinforcement [88]. However, it yields the same results as the first method if the RC element studied is a one-dimensional element under pure tension [32]. Therefore, the first approach was adopted in the current study along with Scanlon's approach.

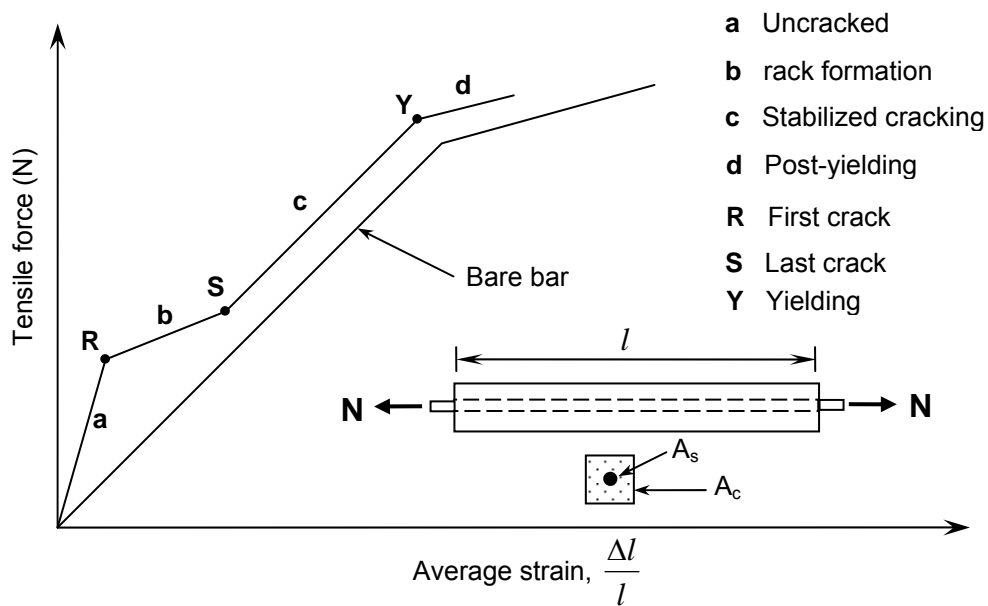


Figure 5-19: Idealized load-strain curve for RC tension tie according to CEB-FIP Model Code 1990 [20].

#### 5.4.4.2. Dowel action

As mentioned before in Section 2.2.1.2, “Dowel action” is a well known shear-transfer mechanism. It is similar, in principle, to the aggregate-interlocking effect mentioned in Section 5.5.3.3. However, dowel action is considered as a structural property rather than a material property, as its effectiveness depends strongly on the detailing of the reinforcement, to the shape of the section and even to the load configuration or the boundary conditions [20, 32].

The dowel effect can be incorporated in a continuum model by using an equivalent shear stiffness and shear strength for cracked concrete, just as proposed previously for the aggregate-interlocking effect, but since its effect is not pronounced in the current study, as explained before in Section 2.2.1.2, it was not considered in the FE modelling of the test slabs. One of the shortcomings of the damaged plasticity model is that it does not include a shear retention model to account for shear-transfer mechanisms. This is because the model adopts the isotropic damaged concepts for the post-cracking behaviour.

#### **5.4.5. FRP-concrete interface**

The common failure mode in reinforced concrete structures strengthened by EBR usually takes place at a few millimetres from the adhesive layer [63]. So, the interface material properties depend strongly on the strength of concrete rather than the epoxy adhesive.

To model this interface, a traction-separation model was used to simulate this behaviour [78]. This model assumes linear elastic behaviour followed by the initiation and evolution of damage. The elastic behaviour is written in terms of an elastic constitutive matrix that relates the nominal stresses to the nominal strains across the interface. The nominal stresses are the force components divided by the original area at each integration point, while the nominal strains are the separations divided by the original thickness at each integration point. The nominal traction stress vector,  $t$ , consists of three components:  $t_n$ ,  $t_s$ , and  $t_t$ , which represent the normal (along the local  $z$ -direction) and the two shear tractions (along the local  $x$ - and  $y$ -directions), respectively. The corresponding separations are denoted by  $\delta_n$ ,  $\delta_s$ , and  $\delta_t$ . Denoting  $T_0$  as the original thickness of the interface element, the nominal strains can be defined as;

$$\varepsilon_n = \frac{\delta_n}{T_0}, \varepsilon_s = \frac{\delta_s}{T_0}, \varepsilon_t = \frac{\delta_t}{T_0} \quad \text{Equation 5-12}$$

Due to the lack of information about the interaction between the normal and shear stress at the interface, uncoupled behaviour was assumed between the all components of the traction vector and separation vector. In other words, no interaction was considered between mode I and mode II cracking. Thus, the elastic behaviour can be written as follows:

$$\mathbf{t} = \begin{Bmatrix} t_n \\ t_s \\ t_t \end{Bmatrix} = \begin{bmatrix} k_{nn} & 0 & 0 \\ 0 & k_{ss} & 0 \\ 0 & 0 & k_{tt} \end{bmatrix} \begin{Bmatrix} \varepsilon_n \\ \varepsilon_s \\ \varepsilon_t \end{Bmatrix} = \mathbf{K} \boldsymbol{\varepsilon} \quad \text{Equation 5-13}$$

#### 5.4.5.1. Failure Criteria

Damage of the interface layer was assumed to initiate when the maximum nominal stress ratio reaches a value of one in any direction. This criterion is defined as follows.

$$\text{Max} \left\{ \frac{t_n}{t_n^0}, \frac{t_s}{t_s^0}, \frac{t_t}{t_t^0} \right\} = 1 \quad \text{Equation 5-14}$$

Where  $t_n^0$ ,  $t_s^0$  and  $t_t^0$  represent the peak values of the nominal stress when the deformation is either purely normal to the interface or purely in the first or the second shear direction, respectively.

#### 5.4.5.2. Damage evolution

Once the damage initiation criterion was met, an exponential damage evolution law was applied according to Chen and Teng's [63] simplified model. Figure (5-20) shows the traction-separation curve for the bond interface assuming  $f_t = 0.5 f_{ct,sp}$  (MPa) for the concrete used in this study, where  $f_{ct,sp}$  is the split tensile strength of concrete according to the CEB-FIP model code 1990 [20]. A detailed method for the calculation of the damage parameters corresponding to the stress-displacement curve is shown in Appendix A.

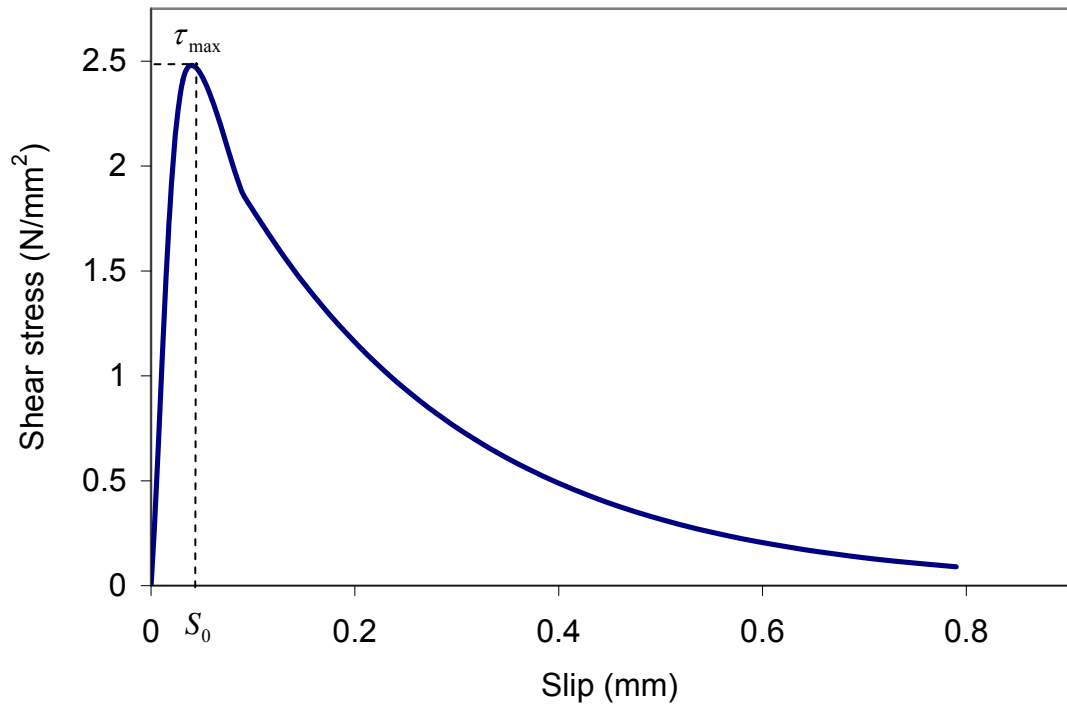


Figure 5-20: FRP-concrete interfacial stress-slip model.

#### **5.4.6. Nonlinear solution**

##### **5.4.6.1. Analysis procedure**

Due to material nonlinearity, solving RC problems requires nonlinear analysis. Furthermore, when cracks develop, strain energy is suddenly released, meaning that kinetic effects are generated and the analysis becomes highly unstable. ABAQUS offers two specialized algorithms to deal with unstable nonlinear problems: the modified RIKS algorithm and the STABILIZE algorithm which is used along with general static analysis procedure.

The RIKS method is designed for geometrically nonlinear collapse and global post-buckling analysis, but can include nonlinear materials. The load is treated as an unknown, and the solution is carried out for the load and displacement simultaneously. The progress and increment of the solution is measured by an arc length over the static equilibrium path [78]. The “STABILIZE” algorithm is suitable for cases where the instabilities are local, in which case global load

control becomes inappropriate. Stabilization is effected by applying damping (dashpots) throughout the model such that the viscous forces are sufficiently large to prevent instantaneous buckling or collapse, but small enough so as not to affect stable behaviour[78]. Both methods were compared in the FE analyses carried out. They nearly yield the same results, so it was decided to use the STABILIZE algorithm for the whole study.

#### **5.4.6.2. Steps, increments, and iterations**

The load history for this model comprised three main steps for the non-prestressed slabs, while an additional Forth step was needed for prestressed slabs, as follows.

- Establish contact: the supports were modelled as a rigid surface to distribute the load over the supporting area and to allow the slab corners to lift up. Therefore a contact definition was needed before applying the loads;
- Release constraints: this step is a consequence of the previous step;
- Prestressing step: is a step where the prestressing force is applied;
- Loading: load increments are applied until failure in this step.

Each step load (or displacement) is broken into smaller increments so that the nonlinear solution path can be followed. One only needs to suggest the size of the first increment in each step, which is usually taken as a small percent of the load applied through the step to make sure that the elastic limit has not been exceeded. In the loading step for instance, the initial increment size was 5% of the ultimate load applied. Thereafter, ABAQUS/Standard automatically adjusts the size of the increments. In each increment ABAQUS iterates attempting to find an equilibrium solution for the increment. By default, if the solution has not converged within 16 iterations or if the solution appears to diverge, ABAQUS abandons the increment and starts again with the increment size set to 25% of its previous value. An attempt is then made to find a converged solution with this smaller load increment. If the increment still fails to converge, ABAQUS reduces the increment size again. By default, ABAQUS/Standard allows a



maximum of five cutbacks of increment size in an increment before stopping the analysis [78].

ABAQUS uses the Newton-Raphson equilibrium iterations for updating the model stiffness. These equilibrium iterations provide convergence at the end of each load increment within force and displacement tolerance limits. Prior to each solution, the Newton-Raphson approach assesses the out-of-balance load vector,  $R_a$ , which is the difference between the restoring forces (the loads corresponding to the element stresses,  $I_a$ ) and the applied loads,  $P$ . Subsequently, the program carries out a linear solution, using the out-of-balance loads, and checks firstly for convergence within the force tolerance limit, which is set by default to 0.5% of the average force in the structure, averaged over time. If the convergence criteria are not satisfied, the out-of-balance load vector is re-evaluated, the stiffness matrix is updated, and a new solution is attained. This iterative procedure continues until the problem converges.

Before considering the current configuration is in equilibrium and continuing to the next time increment, ABAQUS also makes checks that the last displacement correction  $c_a$  (the load increment times the initial stiffness,  $K_0$ ) is smaller than a fraction of 1%; by default, of the total incremental displacement,  $\Delta u_a = u_a - u_0$ . If  $c_a$  is greater than the displacement tolerance limit, ABAQUS performs another iteration based on the new stiffness,  $K_a$ , for the structure's updated configuration,  $u_a$ . This stiffness, together with the residual,  $R_a$ , determines another displacement correction,  $c_b$ , that brings the system closer to equilibrium at point  $b$ , as shown in Figure (5-21). A new force residual,  $R_b$ , is then calculated using the internal forces from the structure's new configuration,  $u_b$ . Again, both  $R_b$  and  $c_b$  are compared to their new tolerance limits. Both force and displacement convergence checks must be satisfied before a solution is said to have converged for that time increment. If necessary, ABAQUS performs further iterations till convergence criteria are met [78]. These default tolerance limits were found suitable to conduct the analysis of the tested slabs

and there was no need to modify them. Figure (5-21) shows the use of the Newton-Raphson approach in a single degree of freedom nonlinear analysis.

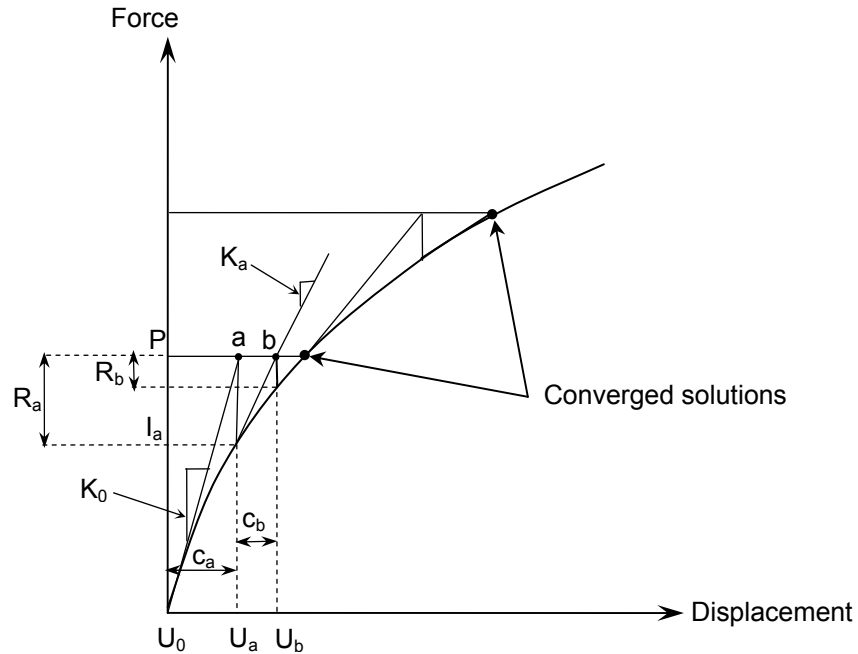


Figure 5-21: Newton-Raphson iterative solution (2 load increments).

### 5.5. Investigation of model parameters

The second step in FE analysis, after deciding on a suitable meshing element and identifying the material models and analysis techniques, is to investigate the various modelling parameters. Firstly, the density of the mesh that would diminish mesh sensitivity was determined. Then, the effect of tension stiffening was investigated in some detail to enable proper prediction of the behaviour of test slabs. Furthermore, for the strengthened slabs the interfacial material properties, such as bond strength and interfacial fracture energy, were also investigated as these parameters could affect the prediction of the ultimate load and slab stiffness.

### 5.5.1. Description of slab model

Due to double symmetry of the support and loading conditions, only a quarter of the slab was modelled. The perimeter of the slab was simply supported, without any horizontal restraint, and the corners are free to lift as shown in Figure (3-16). In order to represent these boundary conditions in the slab model, the planes of symmetry; X-Z and Y-Z, were assumed to be horizontally restrained in the Y and X directions respectively, and a rigid surface supports the slab perimeter over a distance of 1600 mm into the slab.

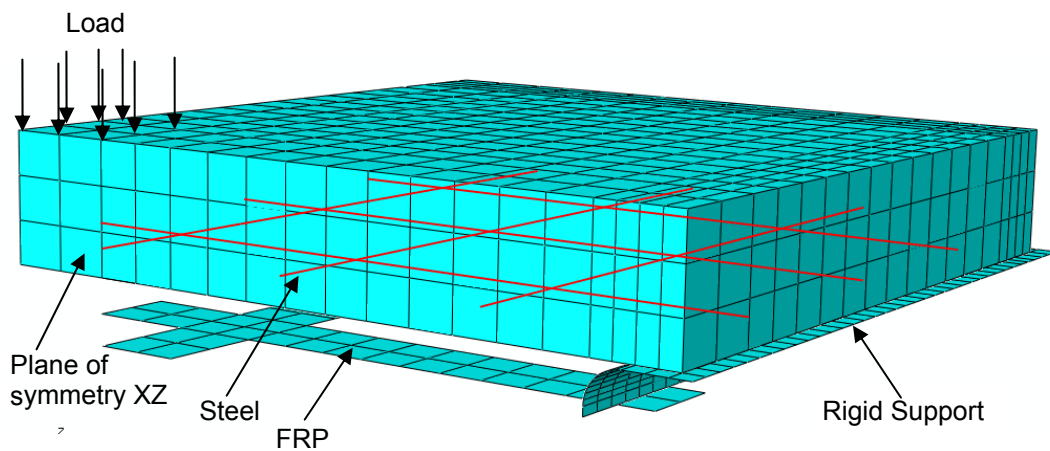


Figure 5-22: Slab model; FRP reinforcement has been shifted down for clarity purposes.

To simulate the contact between the slab surface and the rigid surface, a simple contact algorithm is defined by specifying the interaction between the contacting surfaces. This interaction consists of two components: one tangential to the surfaces and one normal to the surfaces. The tangential component, which consists of the relative motion of the surfaces, was assumed frictionless, since this is the common assumption in simply supported members. The normal behaviour applies the contact constraints only when the clearance between two surfaces becomes zero. In such case, the accumulation of the contact pressure transmitted from the slab element to the rigid surface is equal to the applied load (reaction). The surfaces separate when the contact pressure between them becomes zero or negative, and the constraint is removed.

This method is more appropriate than the method of releasing predetermined nodes near the slab corners, as the latter method requires iterative process to identify these nodes. Moreover, these nodes are in contact with the supporting frame at the beginning of the analysis, and are released during the analysis. So, neglecting such phenomenon could affect the state of stress near that area.

### **5.5.2. Mesh size**

As mentioned before in Section 5.5.3.3, reinforced concrete elements with reasonably distributed cracks may not be considered mesh sensitive if the element aspect ratio is close to unity. On the other hand, if the failure mode of the structural element is characterized by crack localization in certain areas, as in the slabs under investigation, mesh density is still a crucial problem. Therefore, mesh sensitivity was investigated. For this purpose, both reference slabs (RS<sub>0</sub>) and strengthened slab (RS-F<sub>0</sub>) were considered in order to cover the range of reinforcement ratio.

At this stage, a linear tension stiffening curve for concrete was considered. The tensile strength was taken as the lower bound defined in Eurocode 2 [21];  $f_{ctk,min} = 0.21f_{ck}^{(2/3)}$ , where  $f_{ck}$  is the characteristic compressive strength of concrete. A fracture energy cracking criterion, which is suited for lightly reinforced elements, was adopted since all tested slabs nearly underlie such category. The terminal crack opening displacement,  $u_{t0}$ , in the concrete softening model was chosen at the lowest values that would enable a numerical solution. This curve is not necessarily able to predict a closer behaviour to the experimental tests. However, mesh sensitivity was confirmed to follow similar trends as those obtained herein for the realistic tension stiffening levels that were identified later.

Different mesh sizes were considered in the sensitivity analysis so that the tension stiffening overshadows softening of concrete. This was achieved by keeping the crack band width,  $h$ , for each mesh size less than the characteristic length of concrete,  $\lambda = 2G_f E / f_{ctk}^2$ , which prevents the snap-through behaviour

[32, 77]. The individual elements were kept as close to a cube, as possible, in every case. The nominal mesh sizes considered were 75 mm, 50 mm, 30 mm and 25 mm. The mesh was said to be converged when an increase in the mesh density had a negligible effect on the results obtained, while the load-midspan deflection response was the reference parameter in determining the appropriate mesh size. The convergence of the response parameter for slabs  $RS_0$  and  $RS-F_0$  are shown in Figures (5-23) and (5-24), respectively.

Based on the results shown in Figure (5-23) for slab  $RS_0$ , the convergence study implies that the 50 mm mesh size converges to both the 30 mm and 25 mm mesh sizes. On the other hand the 75 mm mesh appears to have unstable behaviour after cracking and to experience numerical problems. Therefore, it was decided to adopt the 50 mm mesh size for the rest of the analysis. Similar results were obtained for slab ( $RS-F_0$ ), as shown in Figure (5-24). It can thus be seen that regardless of the external FRP reinforcement, the results start to converge with a model having the same mesh element size of 50 mm.

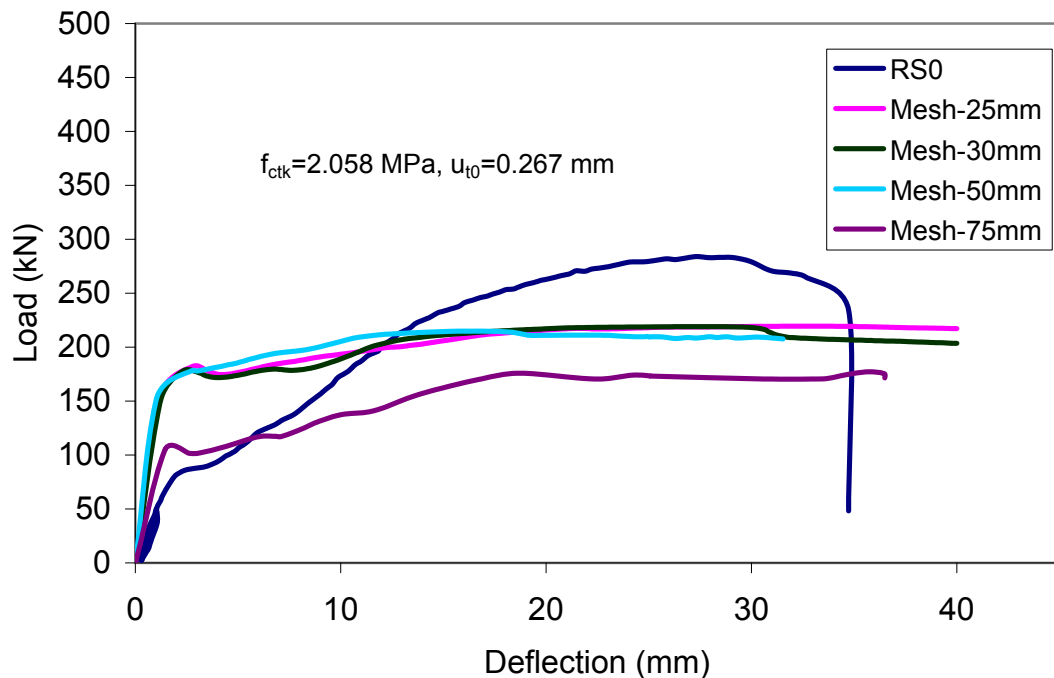


Figure 5-23: Mesh sensitivity of slab  $RS_0$ .

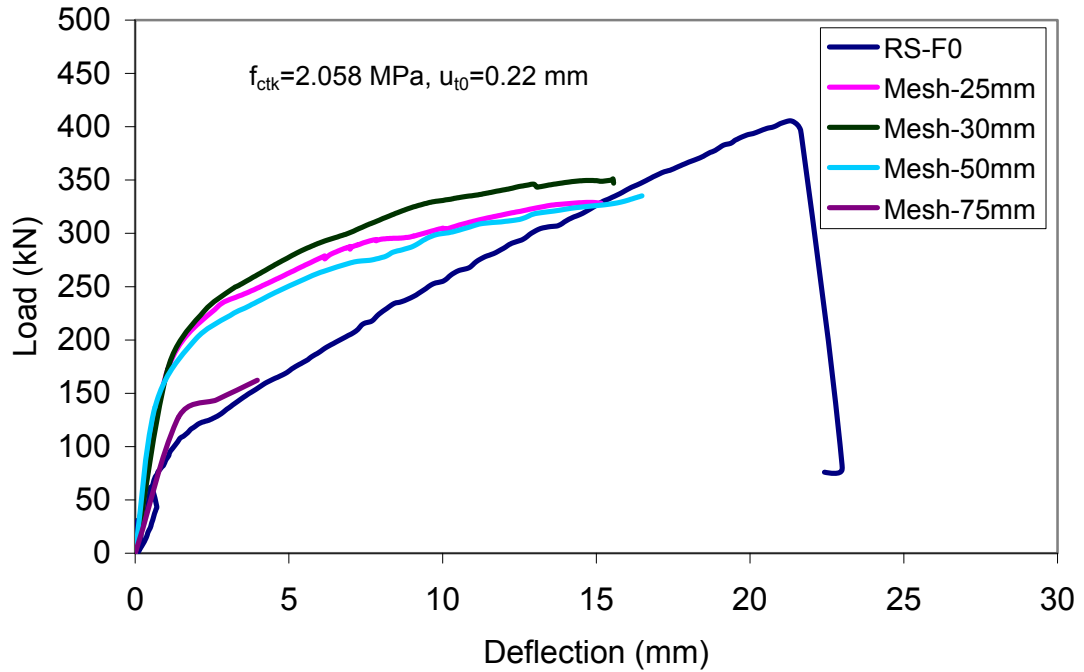


Figure 5-24: Mesh sensitivity of slab RS-F<sub>0</sub>.

### 5.5.3. Effect of concrete tensile strength

The tensile strength of concrete has a visible effect on the first crack load as shown in Figure (5-25). The predicted load-deflection relationship is nearly similar after the first crack if the tensile strength is within the range of the lower bound and upper bound limit defined in Eurocode 2 [21]. Also noticeable is that the model underestimates the applied load of the slab at a given displacement if the tensile strength is lowered. The lower levels of the tensile strength are characterized by a continuous response without drop in the load levels after the first crack. This is because the low tensile strength results in earlier microcracking causing lower stiffness behaviour up to failure.

In this study, a reduced tensile concrete strength was used in the FE analyses of beams and slabs;  $f_{ct} = 0.5f_{ct,sp}$ , where  $f_{ct,sp}$  is the split tensile strength of concrete and equals to 1.11 times the mean tensile strength of concrete;  $f_{ct,sp} = 1.11f_{ctm}$  [20]. This could be justified based on the size effect phenomenon “The nominal strength of structural element decreases as its size increases”

[46]. Moreover, the modulus of rupture of two-way slabs is greatly dependent upon the reinforcement ratio as it affects too much the drying shrinkage of the surrounding concrete. A low reinforcement ratio could easily allow for shrinkage cracks to develop between the reinforcing bars. Correspondingly, such slabs may experience a much lower cracking load than beam members do. Therefore, the Canadian standard (CSA) [92] recommends one half of the mean tensile splitting strength to account for the shrinkage effects in the two-way slabs.

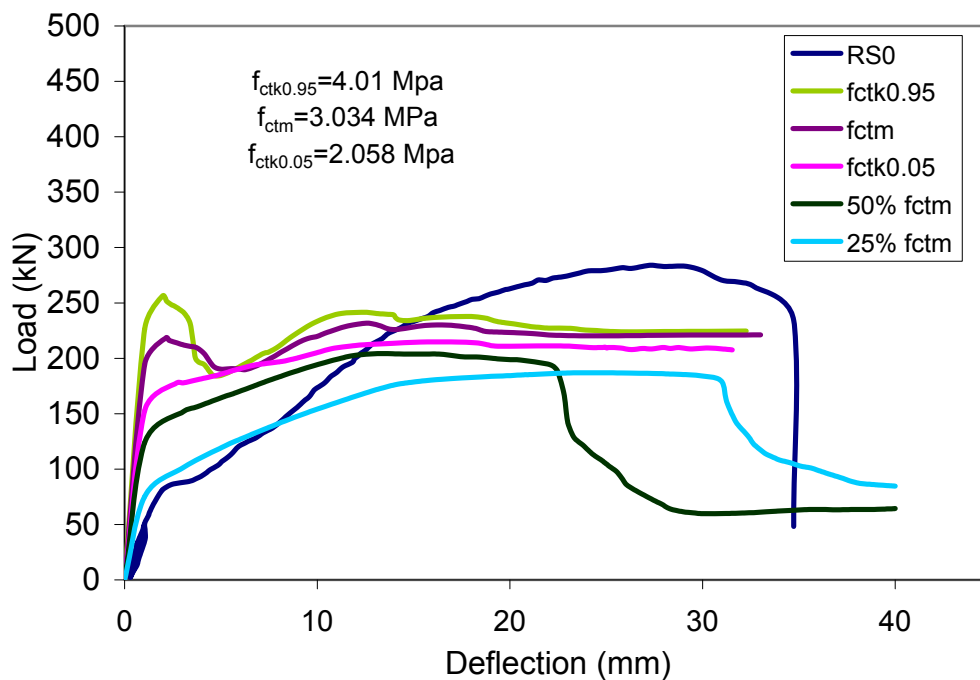


Figure 5-25: Load-deflection curve of slab RS<sub>0</sub> for different values of concrete tensile strength.

#### 5.5.4. Effect of tension stiffening curve

For lightly reinforced members, such as floor slabs, the flexural stiffness of a fully cracked section is many times smaller than that of an uncracked section, and tension stiffening contributes greatly to the post-cracking stiffness. In other words, the behaviour of such members, directly after cracking, is similar to the behaviour of plane concrete in tension, which is characterized by a steep decline in the tensile strength followed by a gentle loss of the remainder

strength. However, in lightly reinforced members the bond interaction contributes to the stiffening in the post-cracking behaviour. This phenomenon is well described by Scanlon's model as shown in Figure (5-18). The model lumps the tension stiffening effects to later stages in the post-cracking region, so it enhances the element stiffness after cracking up to the ultimate load. On the other hand, the other models consume the tension stiffening effects directly after cracking; as shown in zone A of Figure (5-26), so the predicted first crack load is effectively increased and the ultimate load is underestimated. Consequently, Scanlon's model was adopted for conducting the analysis of the test slabs.

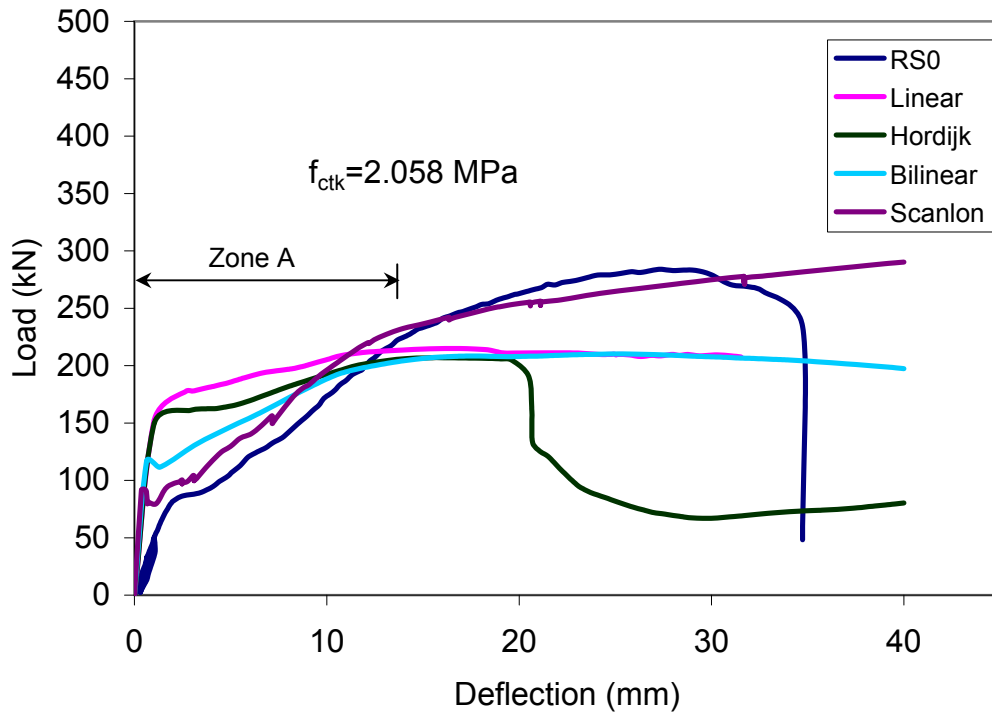


Figure 5-26: Load-deflection curve of slab  $RS_0$  with different tension stiffening models.

Referring to Section 5.4.6.1, the STABILIZE algorithm was adopted in all the previous FE analyses. It was investigated at this point to find how much it affects the accuracy of the predicted numerical results. As shown in Figure (5-27) for slab ( $RS_0$ ), the amount of the strain energy imposed, due to applying of



damping, was nearly negligible compared to the total strain energy consumed in the model. The amount of stabilization energy was 127330N.mm which was less than 5% of the strain energy consumed during the loading step. Consequently, it could be concluded that the applied damping was small enough so as not to affect the stable behaviour. Moreover, this amount of stabilization energy was significantly reduced for the strengthened slabs due to the effect of the FRP reinforcement which reduced cracking.

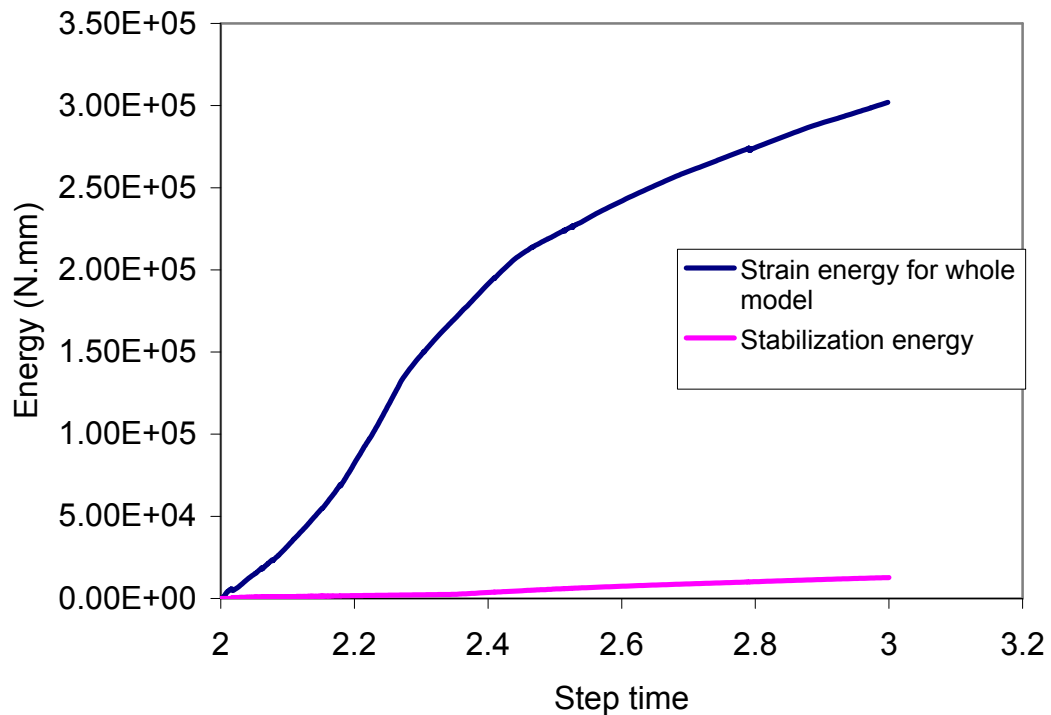


Figure 5-27: Stabilization energy consumed compared to the total strain energy for slab (RS<sub>0</sub>).

In conclusion, the approach of tension stiffening with reduced tensile concrete strength was used in the FE analyses of the test slabs. Scanlon's approach was used with appropriate terminal strain  $\varepsilon_0$ . This terminal strain was "calibrated" based on the load deflection response of each test. This difference in the tension stiffening curves is attributed to the different failure mechanisms of the test slabs. For instance, the reference slab (RS<sub>0</sub>) failed in flexural punching mode so the effect of bond interaction between the internal steel reinforcement

and the surrounding concrete is quite prominent in the tension stiffening curve by a higher value for  $\varepsilon_0$ . However, for example, for the prestressed slab (RS-F<sub>30F</sub>) failed in a brittle mode which should be reflected in the tension stiffening curve by a small value of the terminal strain  $\varepsilon_0$ . This implies that a theoretical tension stiffening model based on physical variables could be developed if such tension stiffening is compared between different tests. However, this is outside the scope of this study as the number of the test specimens is not enough to conduct such analysis.

#### **5.5.5. Effect of interfacial parameters**

As illustrated before in Section 2.4.2.2, the debonding propagation in structural members failing in a diagonal shear crack experiences mixed mode behaviour. In other words, the debonding behaviour is not only related to mode II component but also the mode I component. So, in general both components should be taken into account in debonding analysis, otherwise a misleading prediction for the strengthened behaviour is obtained. Lately, Pan and Leung [93] developed a theoretical model for the bond interface under pulling/peeling effect. However, their model overestimates both the normal and shear strength at the interface which makes their model inapplicable from a practical point of view. This points out that further research is needed to study the interface under shear-normal interaction.

Also, to study such interfacial behaviour a detailed mesh with discrete crack approach is needed [94, 95], which makes such a method quite expensive in three dimensional modelling. The smeared crack model is still able to pick up such mixed mode behaviour, but it lessens the effect of the normal stress components around the shear crack, as shown in Figure (5-28). This is because the smeared crack model can only pick up the area of strain localization but does not allow for displacement discontinuity in the element nodes around the crack. Such displacement discontinuity has a significant contribution in producing the peeling effect.

In the current study, a smeared cracking approach is used. This method smoothes the peeling angle around the shear crack as mentioned above. In such cases, Niu and Wu [94] argue that the overall debonding behaviour can be treated as a mode II fracture. This is based on the fact that the mode II shear behaviour can only take place after some finite opening has already been achieved under mode I. So, for a given shearing fracture energy introduced on the crack surface, the effect of mode I fracture energy is already included. This assumption could be accepted since the time between the initiation of debonding and final failure is too short. Consequently, since the shear-normal interaction is a point under investigation and most of the available interface bond models do not account for this interaction only three interfacial parameters can then be studied; the interfacial bond stiffness  $K_s$ , bond strength  $\tau_s$  and the interfacial fracture energy  $G_s$ .

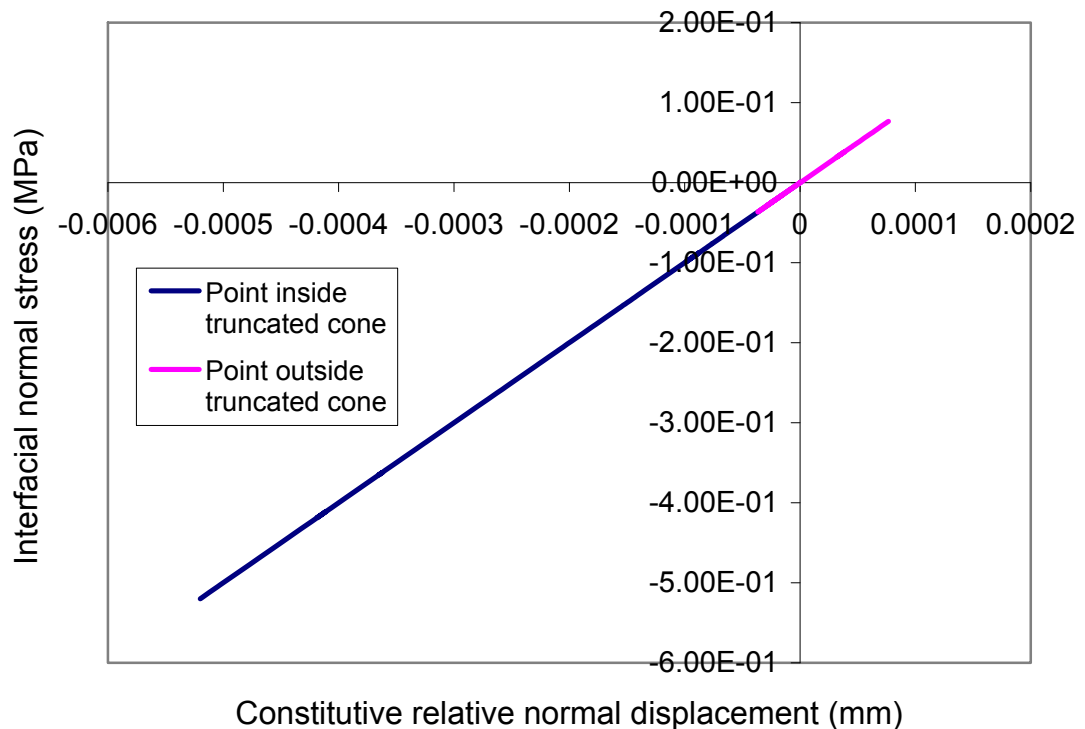


Figure 5-28: Interface normal stress condition inside and outside the truncated cone; results from slab (RS-F<sub>15</sub>).

#### 5.5.5.1. Effect of interfacial bond stiffness $K_s$

Interfacial stiffness is related to properties of the layer resulting from penetration of adhesive into the concrete substrate [63, 93, 95]. It usually ranges between 30 and 300 MPa/mm, depending on the type of adhesive used and the concrete substrate. As shown in Figure (5-29), the interfacial stiffness has negligible effect on the load-deflection behaviour and ultimate capacity, but it only influences the load transfer efficiency between the concrete substrate and the FRP plate. These results are consistent with those of Niu and Wu [94]. This is based on the fact that the ultimate capacity of a structural member is more affected by mode I related material properties ( $f_{ctk}$ ,  $G_f$ ) as demonstrated earlier in Section 5.4.3.3.2.

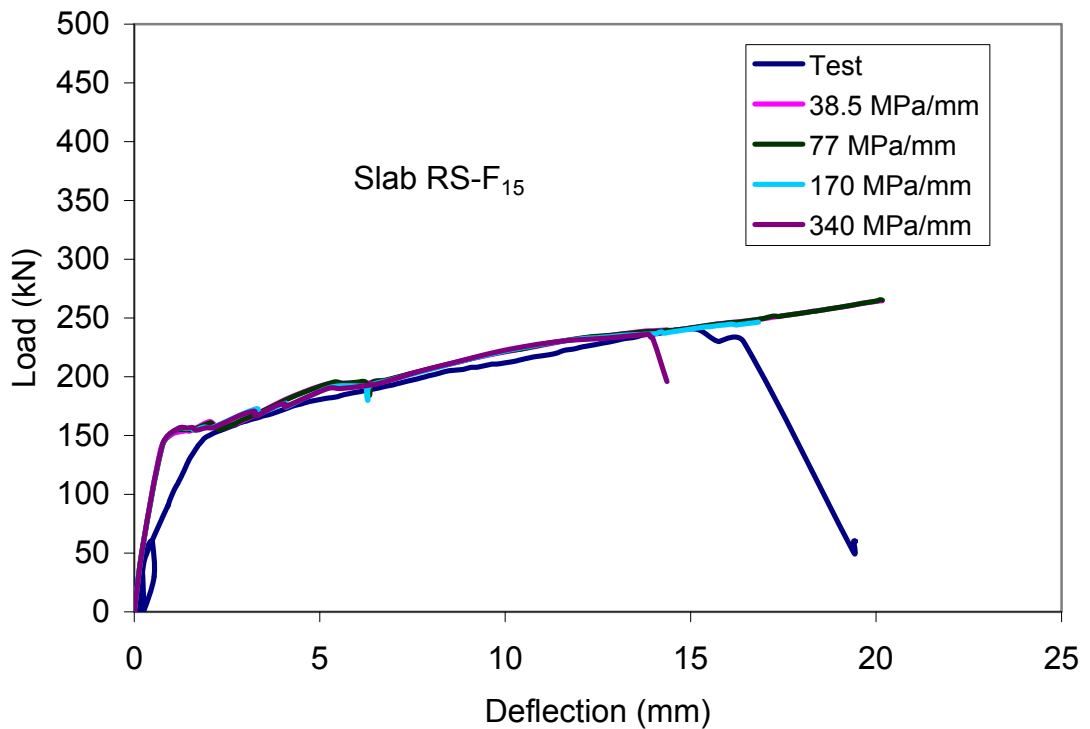


Figure 5-29: Effect of interfacial bond stiffness on the load-deflection behaviour.

### 5.5.5.2. Effect of interfacial bond strength $\tau_s$

By fixing  $K_s = 77$  MPa/mm and  $G_s = 0.67$  N/mm, the effect of interfacial bond strength  $\tau_s$  on structural performance was investigated. As shown in Figure (5-30), the effect of the bond strength is nearly negligible up to a value of 1.5 MPa. However, a value of bond strength as low as 0.5 MPa could affect the structural stiffness at the early stage of loading, resulting in lower ultimate load. That is the low bond strength value leads to early debonding cracks, which lowers the level of strengthening. Consequently, the FRP strain distribution is flattened and markedly lowered, as shown in Figure (5-31), meaning very low efficiency of use of the FRP.

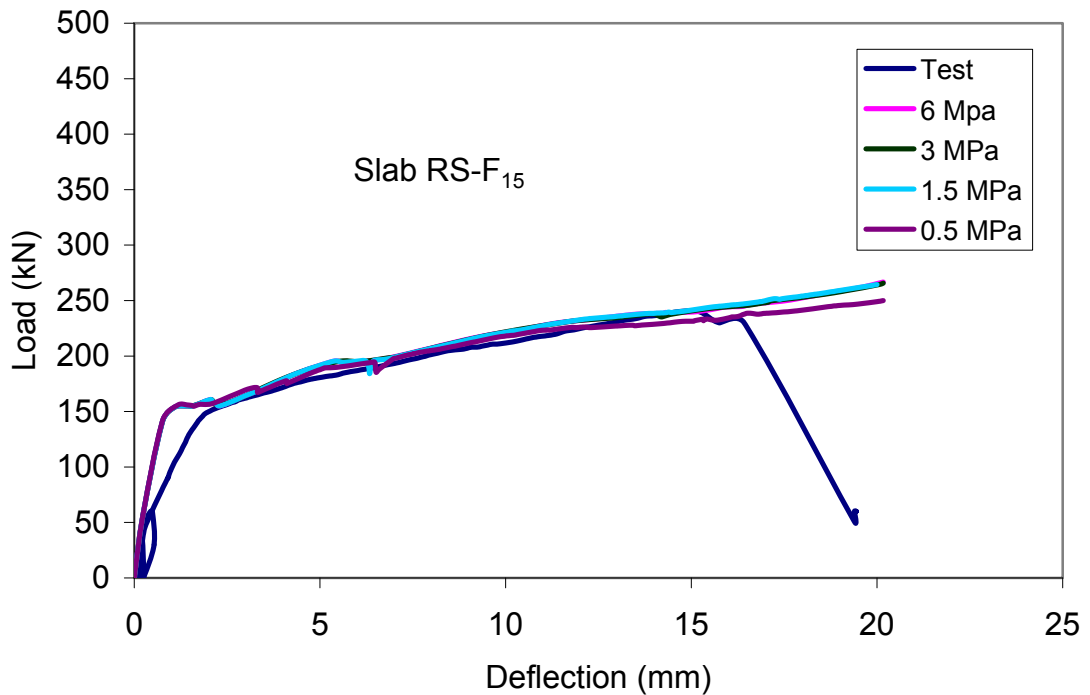


Figure 5-30: Effect of interfacial bond strength on the load-deflection behaviour.

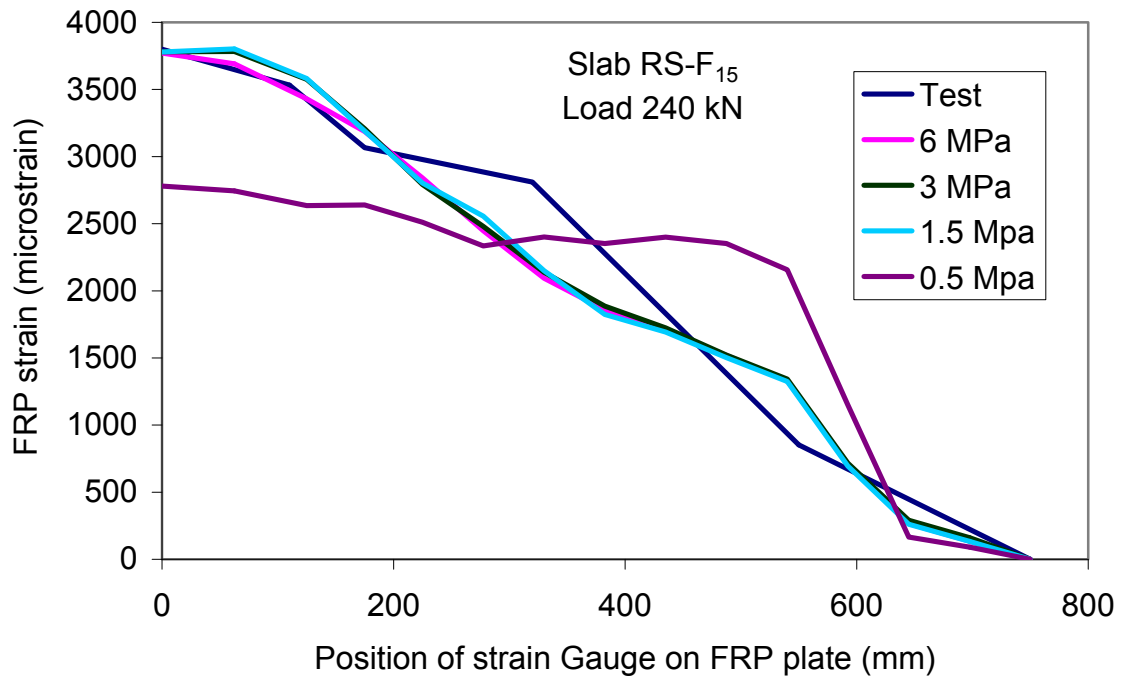


Figure 5-31: Effect of interfacial bond strength on FRP strain distribution.

#### 5.5.5.3. Effect of interfacial fracture Energy $G_s$

The effect of the interfacial fracture energy  $G_s$  on the structural response is expected to be similar to the effect of bond strength, as they are directly related. Hence, an increase in the fracture energy is supposed to increase the loading capacity of the strengthened member. As shown in Figure (5-32), the effect of changing the fracture energy, while all other parameters were kept constant, is apparent to some extent. The low interfacial fracture energy can ease debonding propagation, starting from the maximum moment region (the centre of the slab) towards the end of the FRP plate. This is because the low interfacial fracture energy is rapidly consumed in a short shear transfer length. Thus, the structure integrity is rapidly lost. This effect is quite clear in Figure (5-33), in which the FRP strain related to the low fracture energy is smaller than those of the high interfacial fracture energies implying inefficient use of the FRP material.

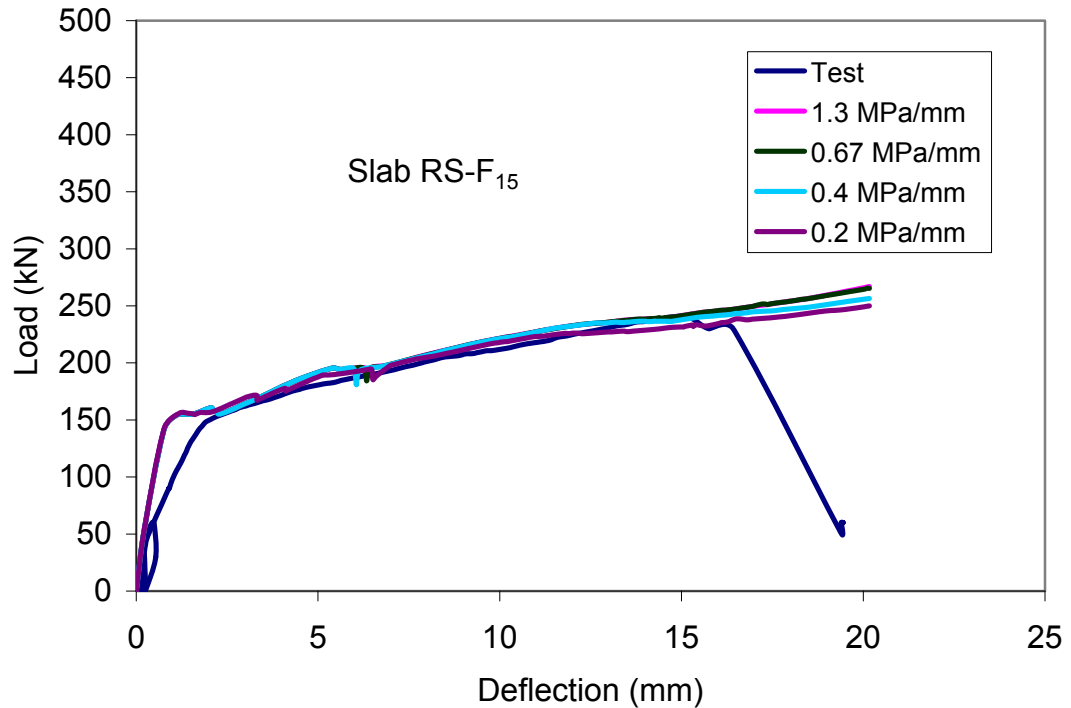


Figure 5-32: Effect of interfacial fracture energy on the load-deflection behaviour.

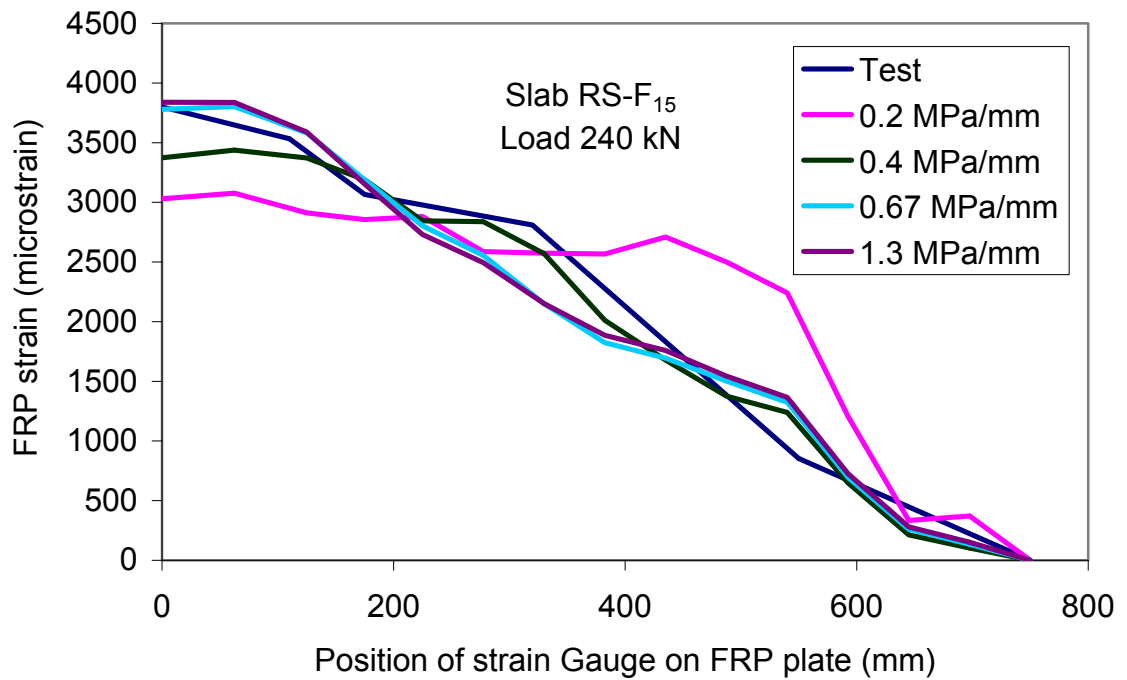


Figure 5-33: Effect of interfacial fracture energy on FRP strain distribution.

### **5.5.6. Conclusion**

The deflection of slabs strengthened with EBR could be properly evaluated by the FE analysis. Most importantly, such analyses require proper evaluation of tension stiffening, which may be better achieved by a concrete softening model rather than a rebar tension stiffening relationship. In cases where the structure under study has low reinforcement ratio and is characterized by a localised failure, a proper estimation for the tension stiffening should be made, as in such members the ultimate load is usually reached during the yield of reinforcement. An underestimation of the tension stiffening means that the post-cracking stiffness is underestimated as well. So, an appropriate value for the terminal strain  $\varepsilon_0$  should be selected, otherwise the ultimate capacity is underestimated.

Equally important is the shape of the tension stiffening curve used. Since the lightly reinforced structures, in their behaviour, resemble the plane concrete, so the tension stiffening curve should take into consideration that the energy required to open unite are of crack is not too much at the beginning of the loading history. Nevertheless, more energy may be needed later in the analysis to increase the crack area due to the effect of bond interaction and some toughening mechanisms. This phenomenon is well described by the Scanlon approach and some bilinear models.

Another noticeable aspect for the strengthened slabs is that their behaviour is more governed by concrete, rather than the reinforcement or interface. This is attributed to the strengthening area of a two-way slab is usually less than that of one dimensional elements like a beam or a column. Moreover, the end anchor plates have a significant role in diminishing the relative displacement field in the interface layer. Thus, a little effect for the bond strength and fracture energy on the structural performance is encountered. However, they affect the distribution of forces between the internal steel reinforcement and the external FRP reinforcement; low interfacial properties underestimate the FRP strain and, at the same time, increase the internal steel strain.



## **Chapter 6**

# **Discussion on numerical results and code provisions**

### **6.1. Introduction**

This chapter discusses the punching behaviour of the tested slabs strengthened with FRP. The behaviour predicted by FE analysis is also investigated and compared to the experimental results. All through the discussion, the recognised behavioural aspects and practice of slab ( $RS_0$ ) are used as a reference. The comparison between the experiments and predicted values was based on the following aspects of structural behaviour:-

- The load-deflection response;
- Strains in the FRP and internal steel reinforcement;
- Distribution of concrete strains and stresses within the column area;
- FRP/concrete interfacial behaviour;
- The ultimate load capacity of the slab;
- Crack pattern;
- The mode of failure.

The prestressed slabs are dealt with separately, because they showed some unexpected behaviour that needs to be addressed on its own. So, additional FE analyses were undertaken in connection with the bond interface of the prestressed members.

The discussion on punching behaviour concludes with a summary of the factors that affect the serviceability and ultimate state of the strengthened member, as well as the adequacy of the numerical analysis technique used.

## 6.2. Non-prestressed slab (RS-F<sub>0</sub>)

### 6.2.1. Load-deflection response

Based on the sensitivity analysis carried out in the previous chapter it was found that a mesh with 50-mm nominal size was adequate. In that analysis, the level of tension stiffening was calibrated to obtain the best possible fit to the experimental deflection. As shown in Figure (6-1), it can be seen that the model provided good correlation, up to the failure load predicted in the test, for the load-deflection relationship for the non-prestressed slab (RS-F<sub>0</sub>).

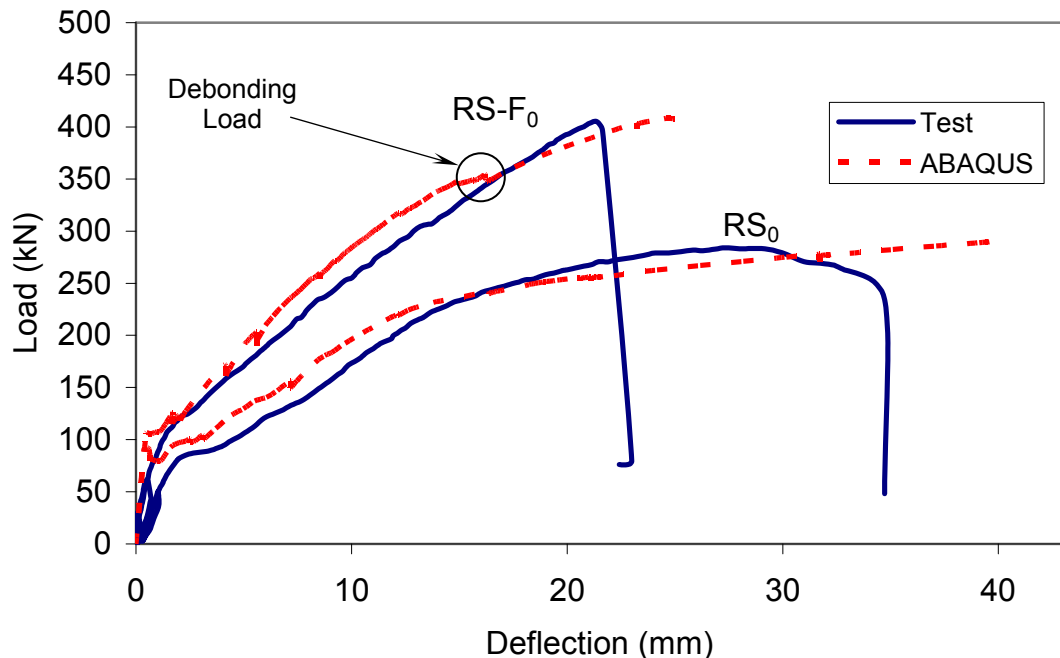


Figure 6-1: Comparison between experimental and model prediction for non-prestressed slab (RS-F<sub>0</sub>).

However, a stiffer behaviour was noticed for the FE model of slab (RS<sub>0</sub>) up to a deflection of 15mm. A probable explanation for this behaviour is that the deflection predicted by the FE analysis is based on a smeared cracking approach which usually adopts the assumption of full bond between concrete and steel reinforcement. Such a model underestimates the deflection predicted as any slip is not allowed between the concrete and steel reinforcement. Also, this model cannot account for the additional deflection resulting from rotation of

the slab about CR, as shown in Figure (6-2). That is flexural deflection is a result of curvature within the member. Nevertheless, for the strengthened slab (RS-F<sub>0</sub>) the additional FRP reinforcement alleviated the discontinuity in the member rotation at the critical shear crack region which in turn reduced the amount of deflection resulting from slab rotation.

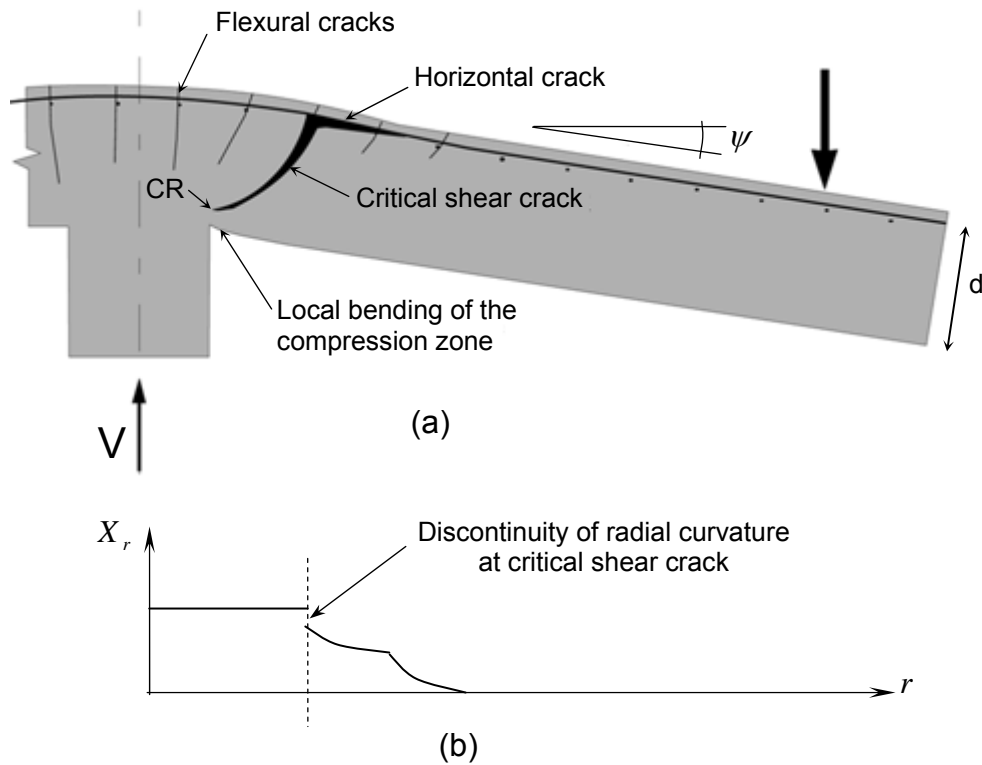


Figure 6-2: Behaviour of slabs with low reinforcement ratios; (a) deformation shape; (b) distribution of radial curvature along the radius of the slab.

## 6.2.2. Reinforcement strains

### 6.2.2.1. Internal steel reinforcement

As mentioned in the previous section that FE analysis smears the effect of cracks and, in itself, does not differentiate between cracked and uncracked sections. The level of tension stiffening in FE analysis was chosen to obtain the best possible prediction of the experimental deflection. Therefore, FE analysis is

expected to predict the average rebar strain between cracks. This strain is usually less than that of an individual rebar, as shown before in Figure (5-17).

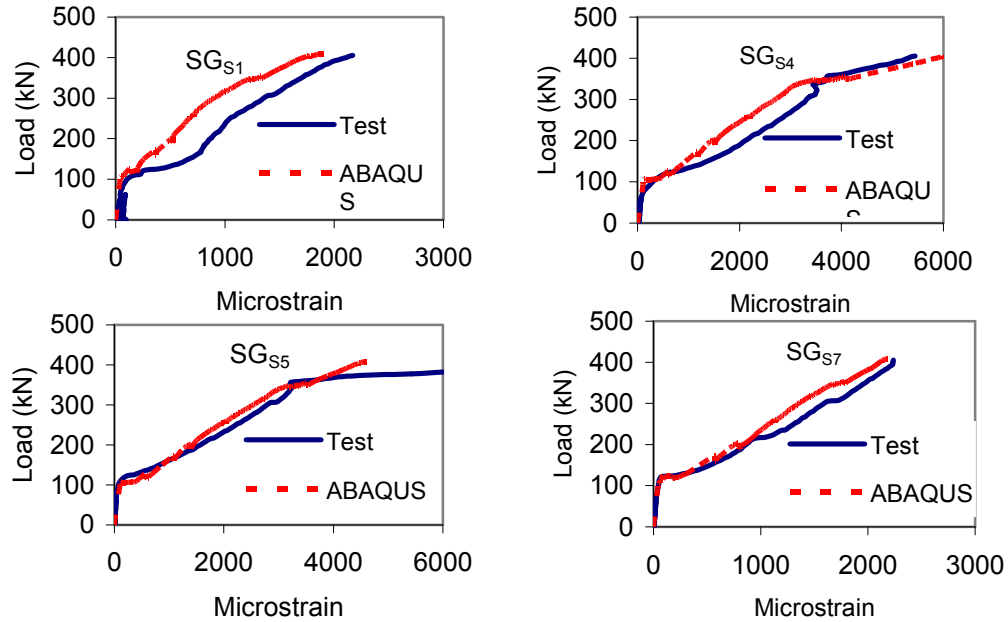


Figure 6-3: Steel reinforcement strain for slab (RS-F<sub>0</sub>) at different locations.

Thus, from the data shown in Figure (6-3), it is apparent that the FE model predicts reasonably well the average rebar strain between cracks. However, in some cases, such as SG<sub>S4</sub>, the rebar strain predicted by the model, to some extent, is less than the actual average rebar strain. Only after a level of 337 kN does the model follow the actual behaviour measured from the test. On the other hand, for strain gauge SG<sub>S7</sub> the strain predicted by the model compares very well with the measured strain up to a load of about 218 kN. Beyond that load, the model underestimates the predicted strain. A probable reason for such discrepancy might be the amount of tension stiffening added to the concrete model. As it is well known, the punching behaviour is characterised by localization of strains near to the loading area, in contrary to the flexural behaviour in which cracking is nearly distributed all over the member. So, the model may overestimate the strains in some regions while underestimating them in other regions. Also, as mentioned before in Section 5.4.3.3, the

damaged plasticity model adopted in this FE analysis only predicts flexural effects and does not account for shear modelling in the post-cracking behaviour. As a result the model is not able to predict the correct crack trajectories. Hence, the FE model shifts the position of critical shear crack towards the centre of the slab. In such cases, the radius of the constant curvature; shown in Figure (6-2b), is reduced. This reduction results in an underestimation of the rebar strain outside the truncated cone; such as strain gauge SG<sub>s1</sub>, and overestimation of the rebar strain inside the cone; such as strain gauge SG<sub>s4</sub>. Another possible explanation, in the light of what has been mentioned in Section 5.4.4.1, is the probability of crack development near these strain gauges. So, the measured strains will be higher than the average rebar strain. At the time the developed model is based on smeared cracking, so it predicts the average rebar strain between cracks as mentioned earlier; see for example the load-strain curve of strain gauge SG<sub>s1</sub>.

Another feature characterizing the steel strain readings is that shown in the load-strain curve of strain gauge SG<sub>5</sub> (Figure 6-3). The strain predicted by the model compares very well with the measured strain up to a load of about 350 kN. After that, the measured strain increases at a faster rate which implies a dramatic transfer of forces to the steel reinforcement. This dramatic transfer of forces results from the debonding of the FRP reinforcement from the concrete substrate. So, the section to remain in balance under the applied loads, the steel reinforcement compensates the contribution of the FRP, resulting in such behaviour by reaching the yield limit. At failure, the measured strain is about two times the predicted strain.

#### **6.2.2.2. FRP reinforcement**

Figure (6-4) shows the FRP strains predicted by the FE model compared to the measured strains. It is clear from the figure that the level of the strains is slightly higher than the steel strains discussed in the previous section. This is due to the strain compatibility in the slab cross section. So, their level should be in the

range of;  $\varepsilon_f = \frac{h-c}{d-c} \varepsilon_s$ , where  $h$  is the overall thickness of the slab,  $d$  is the

depth of the steel reinforcement,  $c$  is the depth of the neutral axis and  $\varepsilon_s$  is the steel strain.

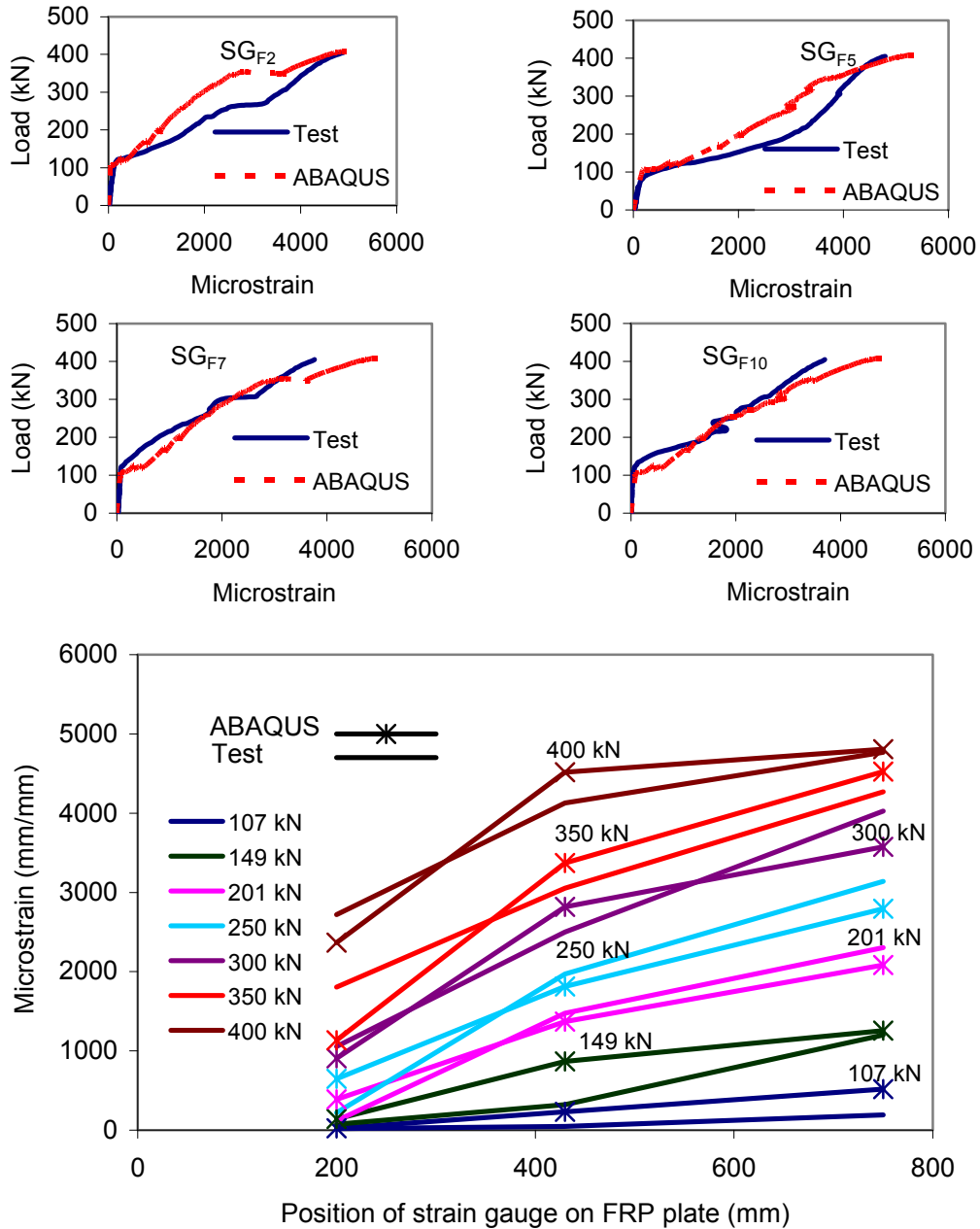


Figure 6-4: Measurement and prediction of FRP strain for Slab (RS-F<sub>0</sub>).

As shown in the previous figure, some measured load-strain curves, such as that of strain gauge SG<sub>F2</sub> and strain gauge SG<sub>F7</sub>, have a horizontal shift at load levels of 260 and 305 kN, respectively, at which the shear crack is expected to

develop. The position of these strain gauges is located near the zone where the critical shear crack is developed. Such a crack usually results in a peeling-off of the FRP reinforcement, as mentioned before in Section 2.4.2.2. So, this deviation can be then explained as a consequence of debonding initiation at the crack mouth, which is characterized by a change in the displacement field at the interface around the crack. This phenomenon is further explained in Figure (6-5) [93, 96].

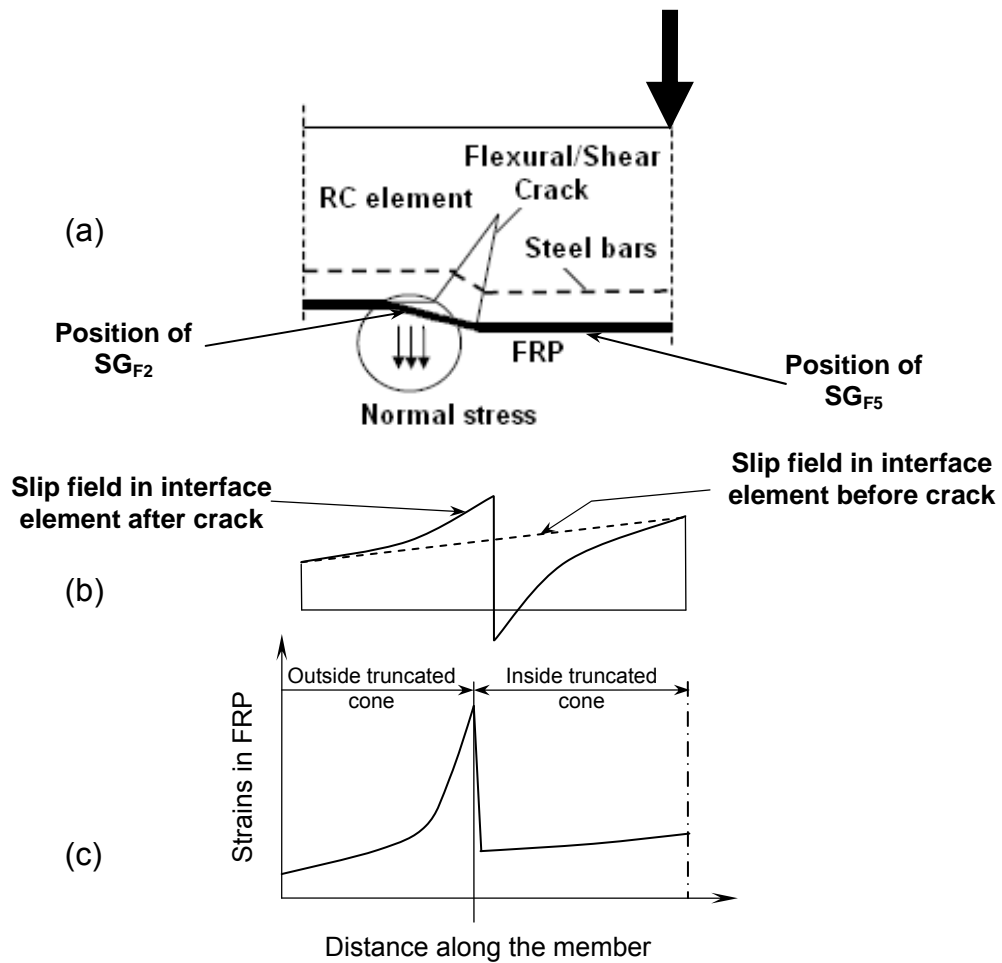


Figure 6-5: Flexural shear crack induced debonding; (a) schematic diagram for crack; (b) slip field at interface element; (c) interfacial shear stress distribution at crack.

As it is well known that the conical shear crack in flat slabs propagates in a mixed mode. When loading is increased, the crack tends to propagate upwards

but the crack opening at the bottom is resisted by the FRP plate. A high shear stress level at the concrete-adhesive interface is then developed due to the change in the displacement field in the interface layer. As shown in Figure (6-5), the displacement field after cracking for the interface layer outside the truncated cone suddenly increases, while on the other side of the crack the displacement field decreases. Intuitively, this slip concentration should appear as a high shear stress in the interface layer which results in a crack parallel to the FRP plate at the interface level.

With further loading, the combined opening and shearing of the major crack will result in both horizontal and vertical displacements between the two sides of the crack. So, the FRP plate is subjected to a combined pulling and peeling effect. In such case, the peeling force generates tensile stresses acting perpendicular to the interface, as shown in Figure (6-5). These stresses make it easier for initial debonding to occur in the area outside the truncated cone. Moreover, the opening displacement (in the direction normal to the interface) along the debonded part of the interface reduces the interlocking effect and accelerates debonding. Correspondingly, a strain gauge near an area such as (SG<sub>F2</sub>) will experience high strain levels after debonding, as shown in Figure (6-4). However, such displacements will increase the interlocking effect on the other side of the crack. So, any strain gauge located inside the truncated cone, such as a strain gauge (SG<sub>F5</sub>), will have a mild increase rate after debonding as shown in Figure (6-4).

Accordingly, it is apparent from Figure (6-4) and Appendix B that the FE model was able to simulate such behaviour reasonably. However, it delays the debonding phenomenon, as shown from the curves of strain gauge SG<sub>F2</sub> and strain gauge SG<sub>F7</sub>. For instance, the predicted load-strain curve for strain gauge SG<sub>F7</sub> shows such debonding failure at high load level of 350 kN instead of 305 kN. This delay could be explained as a result of using an average value for the bond strength in the model, but in reality this bond strength is not constant over the member. Another possible reason is the adoption of the smeared cracking approach. As mention before in Section 5.5.5, the smeared crack model reduces the effect of Mode I component as it does not allow for displacement



discontinuity in the element node around the crack. Therefore, to overcome such a problem, a reduced value for the bond strength and interfacial fracture energy should be used to compensate the contribution of Mode I parameters (Normal strength and fracture energy). Otherwise, the model overestimates the debonding load.

Figure (6-4) shows also the predicted strain profile of a representative length of the FRP plate compared to the measured strains at discrete load levels. It is clear that the FE model, to some extent, overestimates the average FRP strain at a position of 400 mm, but at the same time, the strains within at the central area of the slab are underestimated at higher load levels. That is the profile reflects the same behaviour of the individual load-strain curves at the strain gauges positions.

### 6.2.3. Concrete strains

As shown in Figure (6-6), the concrete strains predicted by the FE model are close to those measured concrete strains, since the model was able to obtain a representative prediction for the slab deflection, as discussed before in Section 6.2.1. That is the response of the compressive concrete zone is related to the deflection of the slab or in another way related to curvature of the slab which may be defined as the slab rotation divided by the effective depth of the slab [65].

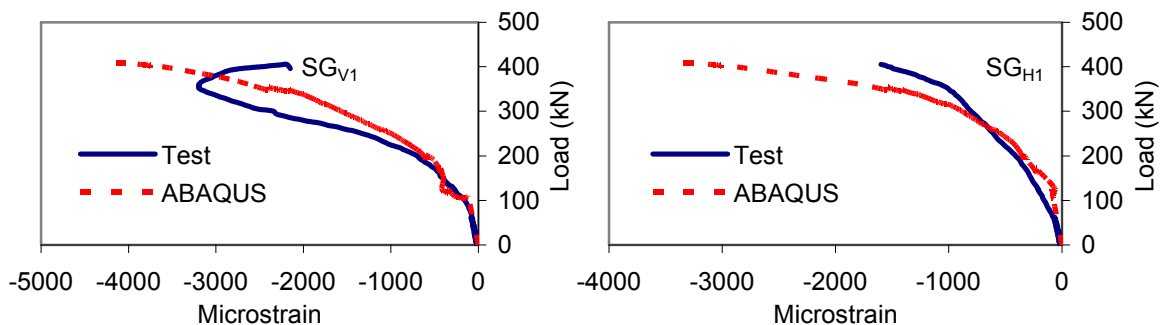


Figure 6-6: Radial and tangential concrete strains for slab (RS-F<sub>0</sub>) at positions SGV<sub>1</sub> and SGH<sub>1</sub>, respectively.

However, the decompression phenomenon in the radial stresses near failure could not be simulated for the same reason of adopting the smeared crack modelling approach. In this phenomenon a local positive curvature develops close to the column due to the local bending of the compression zone, as shown before in Figure (2-3). So, to model such behaviour a discrete modelling approach with very fine mesh near the column area may be needed.

#### **6.2.4. FRP-concrete interfacial behaviour**

The interfacial stress distribution and bond development between the FRP plate and the concrete substrate can be calculated from the strain readings of the FRP plate. However, the number of the strain gauges spaced over the FRP plate in the experimental tests was not enough to conduct such analysis. Therefore, the FE model was used to predict the interface behaviour. Figure (6-7) shows the interfacial shear stress distribution for the non-prestressed slab (RS-F<sub>0</sub>) at the plate centreline at different load levels. The behaviour can be easily simplified as a half sine-wave travelling from the slab centre towards the end of the FRP plate. This can be easily identified at the early stages of loading before cracking (106.3 kN). The crest denotes the location of the maximum shear stress which begins near the slab centre where the maximum radial moment occurs. The change in the slope of the interfacial shear stress distribution at the overlapping area, as shown in the circled area on the figure, is a well-known phenomenon. It indicates a decrease in the slope rate due to the overlapping of the FRP plates which results in lower slip values. The interfacial shear stress values then decrease gradually towards the plate end.

After cracking, the interfacial shear stress near the maximum radial moment area increases significantly. It is nearly eight times the value in the previous step as shown by the second lowest curve (149.8 kN) in Figure (6-7a). The drastic increase is undoubtedly caused by localized concrete cracking. At this stage of loading, the stress concentration starts to appear near the plate end as well, but with less concentration due to the presence of the anchor plates. It increases 0.36 MPa from 0.02 to 0.38 MPa. The shear stress distribution still has a gradual descending trend towards the plate end, but with some fluctuation.

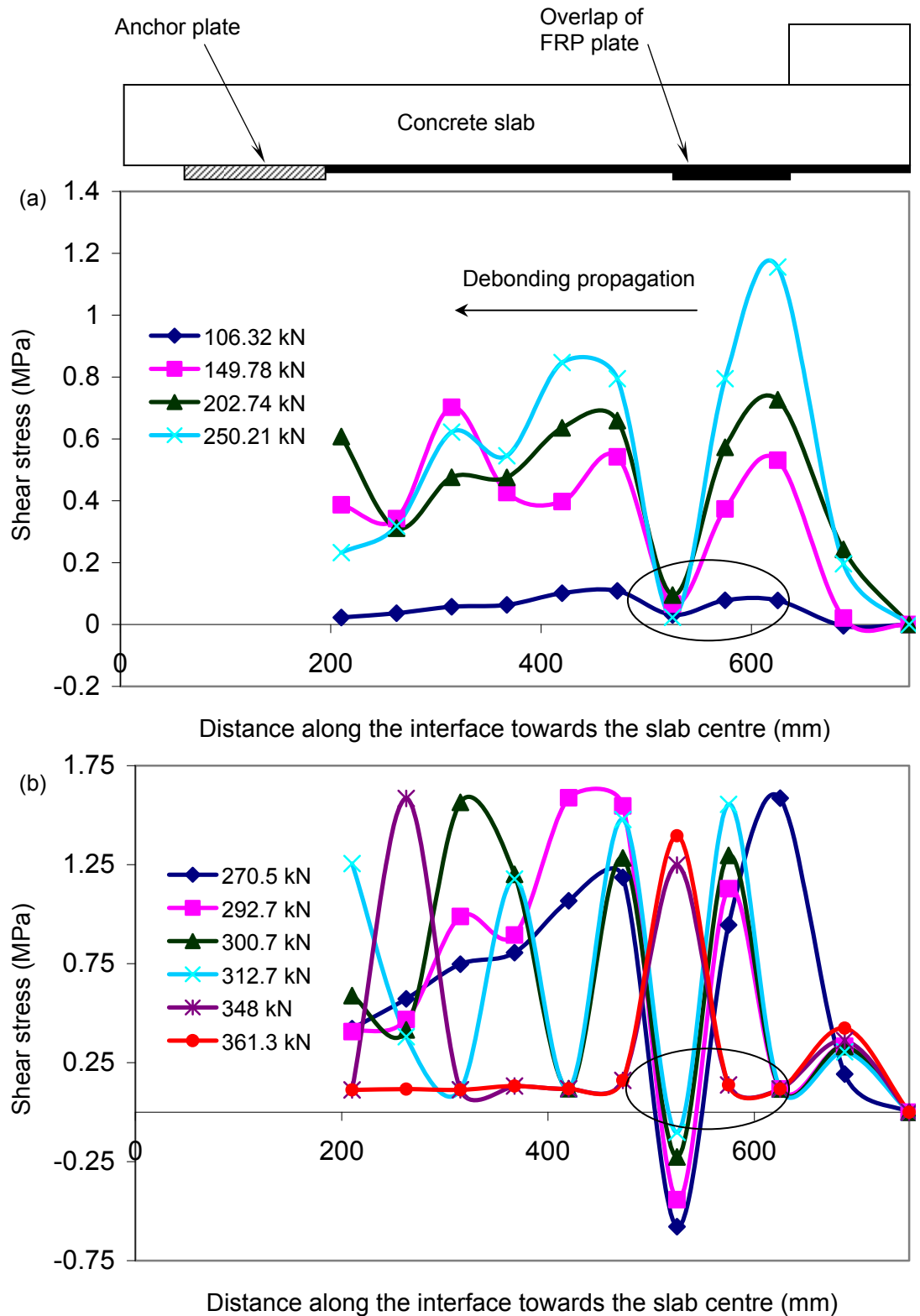


Figure 6-7: FRP-concrete interfacial behaviour of slab (RS-F<sub>0</sub>): (a) before yielding; (b) after yielding.

This fluctuation is attributed to the unsymmetrical position of the FRP plate around the column, by which uneven distribution of the stresses across the plate width occurs. As a result, the outer edges of the FRP plate start to debond before the inner edges. In this case, some stress concentration appears at discrete adjacent locations on the centre line of the plate resulting in such behaviour. This can be easily identified from the crack pattern of the slab which is discussed in the next section.

As the load is further increased (270.5 kN), the shear stress reaches a peak value after which the stress values descend progressively, as shown in Figure (6-7b). At the overlapping of the FRP plate, the interfacial shear stress progresses negatively, allowing the damage to occur in subsequent locations. At load level of 292.7 kN, the interfacial shear stress just after the overlapping position reaches the debonding strength, while the shear stress near the plate end is still at low level of 0.4 MPa. After yielding of the tension reinforcement, the interfacial shear stress keeps increasing with the increase of load. The full debonding of the FRP plate occurs at load level of 361.3 kN at the overlapping position when the interfacial shear stress reaches 1.6 MPa. It may seem that this value of shear stress is too low. However, this value was able to give good prediction for the FRP and steel strains as shown before. Moreover, a value much lower such as 0.2 MPa has been reported in the literature [95], as the bond strength is highly dependent on the plate geometry and stiffness [94].

It should be noted that this debonding behaviour shows that the debonding failure initiates near the slab centre and propagates towards the end of the FRP plate. Therefore, the debonding mode of failure can be classified as intermediate crack induced debonding (IC). However, the experimental results show that the position of the critical shear cracking has been shifted outside the area implying critical diagonal crack induced debonding (CDC). This raised a question of how representative these numerical results are. As discussed before, the damage plasticity model does not reflect exactly the shear effect in its prediction. So, whatever the mesh size or shape the model will give the same position of the first crack directly under the load, which of course triggers the debonding at this position. Nonetheless, it should be remembered as well

that the model was able to give a prediction of strains and deflection that compares very well with the experimental measurements, as demonstrated before, at the time the slab did show some features of the flexural behaviour such as the formation of the yield lines and the yield of the strain reinforcement around the column. Therefore, the interfacial shear stress prediction is believed to be reasonably representative.

#### **6.2.5. Crack pattern**

The damage plasticity model adopts different criteria to show the crack direction. It does not show the crack direction itself. However, it assumes that the direction of the vector normal to the crack plane is parallel to the direction of the maximum principal plastic strain [78]. Consequently, Figure (6-8) shows the tensile equivalent plastic strain,  $\tilde{\varepsilon}_t^{pl}$ , of the bottom surface and central cross section of slab (RS-F<sub>0</sub>) at the predicted failure load of 372.7 kN.

Firstly, the crack strains started to occur tangentially at the area of the maximum bending moment near the column then spread radial towards the slab edges as the predicted load increases. A noticeable large crack strain occurs at the inner and outer edges of the FRP plates, while relatively small strains occur at the area just beneath the plates where they are bonded to the concrete substrate. The changes of crack pattern during the loading history are shown in Appendix B. The figures also show a perfect prediction for the position of the yield lines extending between the slab centre and near the slab corner. They are comparable to those shown in Figures (2-27) and (4-2).

Also by comparing the cracking patterns and their corresponding loads of the non-prestressed slab (RS-F<sub>0</sub>) and the reference slab (RS<sub>0</sub>), one can see that the non-prestressed slab (RS<sub>0</sub>) achieved a noticeable cracking resistance by bonding the FRP plates. This is based on the fact that the increase of the reinforcement ratio enhances the crack resisting capability of the structural member.

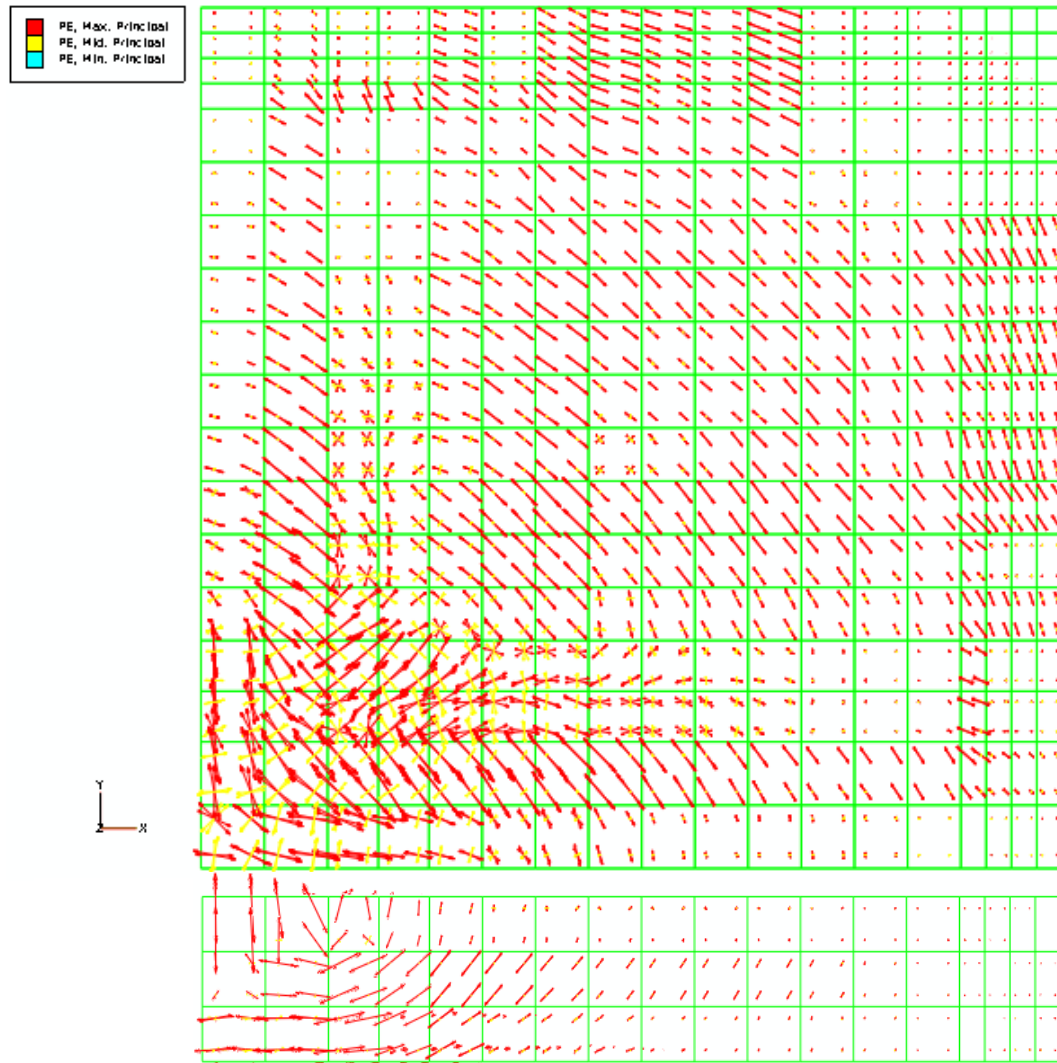


Figure 6-8: Crack pattern of slab (RS-F<sub>0</sub>) at load level 372.7 kN.

### 6.2.6. Crack opening displacement

Large deflections and excessive cracking significantly influence the serviceability of structural members. It has been demonstrated before in Section 4.2.4 that bonding FRP plates to the tension surface of concrete slabs does not only reduce the crack widths, but also shifts the shear crack positions away from the loading region. This was confirmed by the reading of the pots positioned at the notched crack, which gave zero measurements. This can be further supported by drawing the load versus crack mouth opening displacement (CMOD) obtained at the strain localization area within a distance of  $1.5d$  from the column face, based on FEA. In this case, the CMOD can be

assumed equal to the tensile equivalent plastic strain,  $\tilde{\varepsilon}_t^{pl}$ , at the tension face of the slab multiplied by the characteristic length of the FE mesh. As shown in Figure (6-9), there exists clear evidence that the application of the FRP reinforcement reduced the crack opening displacement. For example, at a load level of 250 kN the percentage reduction in the CMOD is about 40% of the reference slab. That implies an enhanced serviceability of the strengthened member.

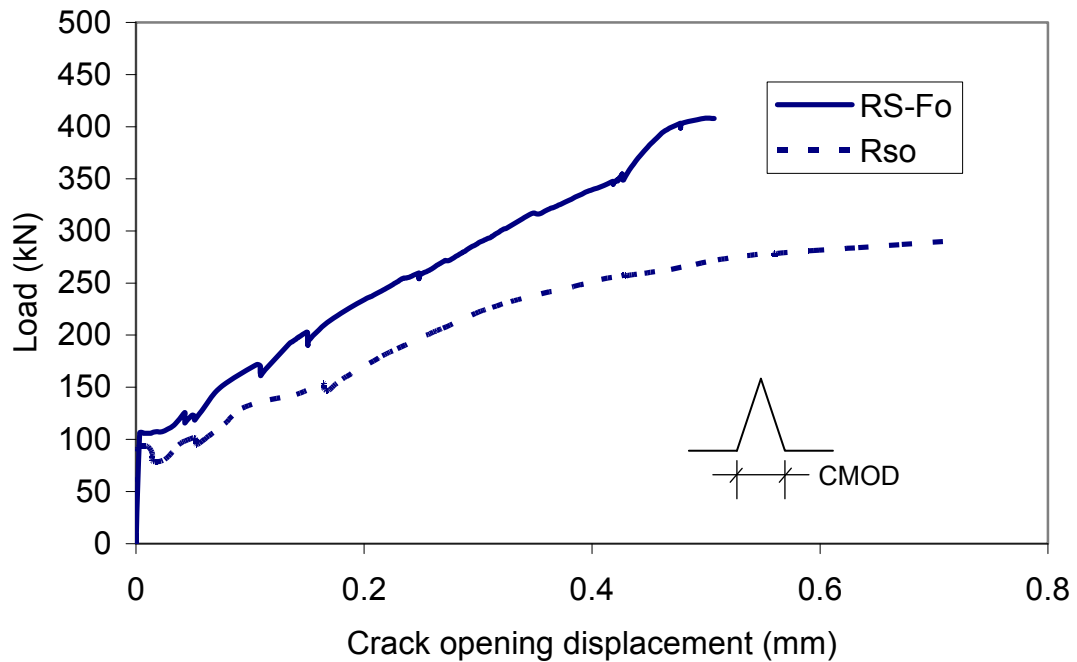


Figure 6-9: Load-CMOD obtained at distance 1.5d from the column face along the centreline of the slab.

### 6.2.7. Ultimate load and failure mode

Referring back to Section 2.4, if full composite action is maintained up to failure for the slabs strengthened by FRP reinforcement, the ultimate concrete compressive strain or the reinforcement yield strain can be taken as margins for the punching and flexural capacity of the slab, respectively. Correspondingly, the ACI Committee 440 [3] follows the steel RC practice taking  $\varepsilon_{cu1}$  equals to 0.003. For the concrete grade used in this study, Eurocode 2 [21] adopts a

higher value of 0.0035 for  $\varepsilon_{cu1}$ . However, such full composite action rarely happens. So, another parameter, which is the slip at the FRP-concrete interface, should be included in the limits that determine the ultimate load of these members. In the current study, concrete crushing is assumed to occur when the maximum compressive strain exceeds 0.0035. Therefore, when either the principal compressive stress is greater than  $f'_c$  or the principal compressive strain reaches a value of 0.0035, the slab is said to fail in punching. Whereas, for the strengthened slabs, the slab is said to fail in debonding if the damage parameter at the interface reaches a value of 0.99 of the interface strength (see Appendix A), at which the interface element is removed from the overall stiffness of the member and the slab starts to restore the reference behaviour without FRP reinforcement. Denoting to the debonding load as the ultimate load is based on the fact that the load increase between the two instances (i.e, the initiation of debonding propagation and the attainment of the ultimate load) is usually very small [96]. However, in some cases where the FRP plate end is anchored to the concrete substrate, like the slabs in this study, the debonding may start in some areas but does not lead to failure unless there is high force in the FRP plate that could spread the debonding process over the whole member, such as the case of the prestressed slabs shown later in this chapter.

Table 6-1 shows the FEM predictions compared to the test results. The failure load predicted by the FE model is within 11% of the actual failure load. The failure mode predicted is based on checking both the principal compressive strain and steel yielding. For the reference slab (RS<sub>0</sub>), the slab is said to have failed in flexure punching mode because the flexural steel yields at failure and the yielding of reinforcement spreads over a large area of the slab. Moreover, the predicted strains are more than two times the yield strain; see Appendix B for results of slab (RS<sub>0</sub>). However, for the strengthened slab (RS-F<sub>0</sub>) the slab is said to have failed in debonding since the composite action is totally lost at the strain localization area around the column. At this corresponding load level; 361.3 kN, the interface elements are removed and the slab starts to restore to the reference behaviour, as shown in Figure (6-1). It is noticeable that this load level is lower than the load corresponding to the concrete crushing; 372.7 kN.



This may be attributed to the use of low tensile strength for the concrete to match the slab deflection as mentioned before in Section 6.2.1. Such low tensile strength lessens the calculated strength and stiffness of the interface layer. Also at this load level, the predicted steel strains have just reached the yield strain and they are confined to a small area locally around the column.

Table 6-1: Experimental and FEM predictions of ultimate load and failure mode.

Specimen	Test		FEM		Ultimate Load ratio FEM/Test
	Ultimate load (kN)	Failure mode	Ultimate load (kN)	Failure mode	
RS <sub>0</sub>	284	Flexural punching	253.7	Flexural punching	0.89
RS-F <sub>0</sub>	405.2	Punching	361.3	Debonding	0.89

#### **6.2.8. Conclusion**

The results produced above corroborate the findings of a great deal of the previous work in this field. Bonding FRP reinforcement to the tension face of concrete column-slab connections provides a good performance in both serviceability and ultimate limit states. In this study, the percentage increase in the ultimate load was more than 40% of the reference slab. The onset of cracking has been delayed and the crack widths diminished as well.

The FE model enabled detailed investigation of the interfacial behaviour, and was able to capture the onset of debonding and macro-debonding which is very difficult to identify in the physical tests. As a result, the model gave a conservative prediction of the ultimate load. Also, it provided an accurate prediction of the crack patterns which agree to the experimental results. This is attributed to the approach used in modelling the support. So the slab corners were able to lift.

## **6.3. Prestressed slabs**

### **6.3.1. Load-deflection response**

In this section, the deflection behaviour of prestressed FRP slabs is examined. Figure (6-10) shows the load-deflection curve of slab (RS-F<sub>15</sub>) compared to the reference slab (RS<sub>0</sub>), along with the predictions of the FE analysis. It is clear that the deflection predicted by the FE model compares very well with the measured deflection up to failure, but with a stiffer behaviour in the elastic region at the beginning. As mentioned before, the additional deflection due to the slip between concrete and steel reinforcement could not have been predicted by FE model adopting a smeared cracking approach with full bond assumption unless low tension stiffening is used. However, such low tension stiffening underestimates the ultimate load and corresponding deflection. Moreover, the idealization of concrete behaviour by elastic behaviour up to nearly 40% of the ultimate strength exaggerates that difference, particularly when the structural member is confined by prestressing forces. As such confinement prolongs the elasticity behaviour of the member in the concrete model. At failure, the measured deflection is about 5% higher than predicted.

The behaviour of the 30%-prestressed slab (RS-F<sub>30</sub>) resembles, to some extent, the behaviour of the 15%-prestressed slab (RS-F<sub>15</sub>). It can be simplified by a bilinear trend, as shown in Figure (6-11). Nevertheless, the FE model prediction for the linear part shows more stiff behaviour. It should be remembered that the second FRP strip experienced early debonding, as mentioned before in Chapter 4. This made the slab to deviate from the predicted linear behaviour at an early load level of 115 kN. Interestingly, the FE model was able to simulate the debonding progression process; the circled location in Figures (6-10) and (6-11), and the full debonding after which the slab restores the reference behaviour. Again, the predicted deflection at failure was safer than that obtained experimentally. The measured deflection is about 7% higher than predicted. Also noticeable is that the deflection at failure of slab (RS-F<sub>30</sub>) is lower than that of slab (RS-F<sub>15</sub>), implying that the more prestressing force applied the more reduction in slab deformability is achieved. Intuitively, such behaviour is similar to increasing the reinforcement ratio of the structural member.

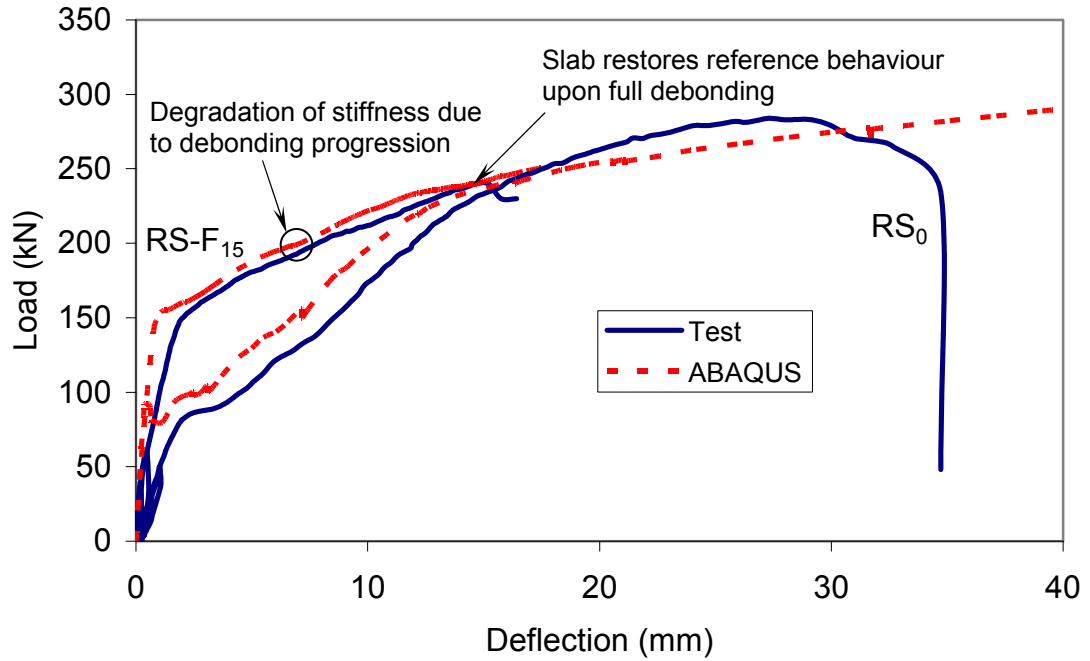


Figure 6-10: Comparison between experimental and model prediction for prestressed slab (RS-F<sub>15</sub>).

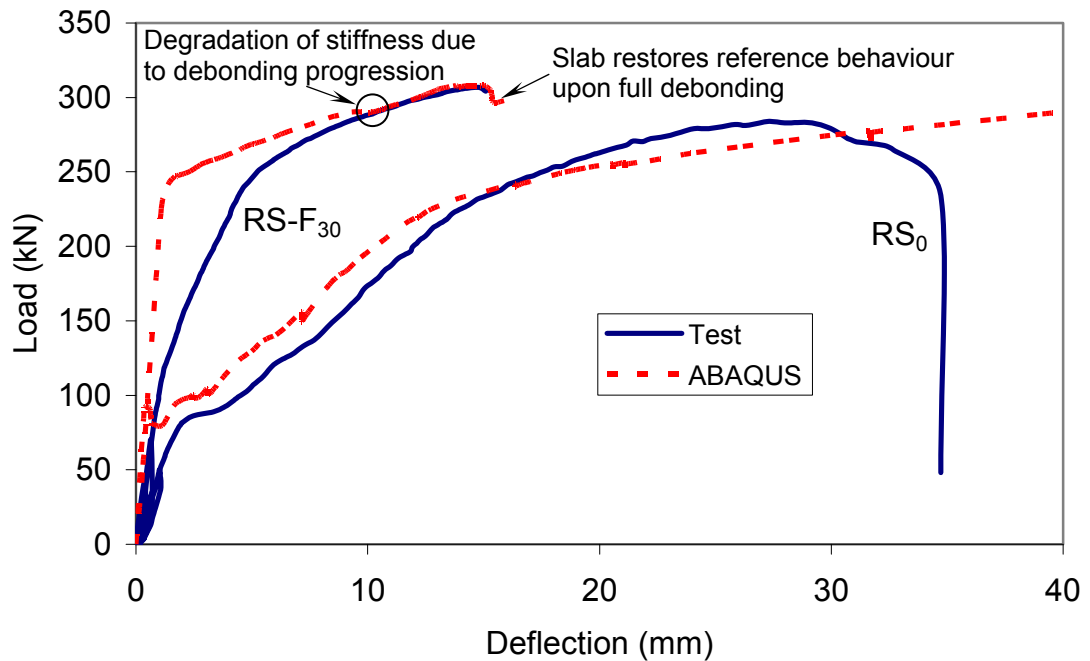


Figure 6-11: Comparison between experimental and model prediction for prestressed slab (RS-F<sub>30</sub>).

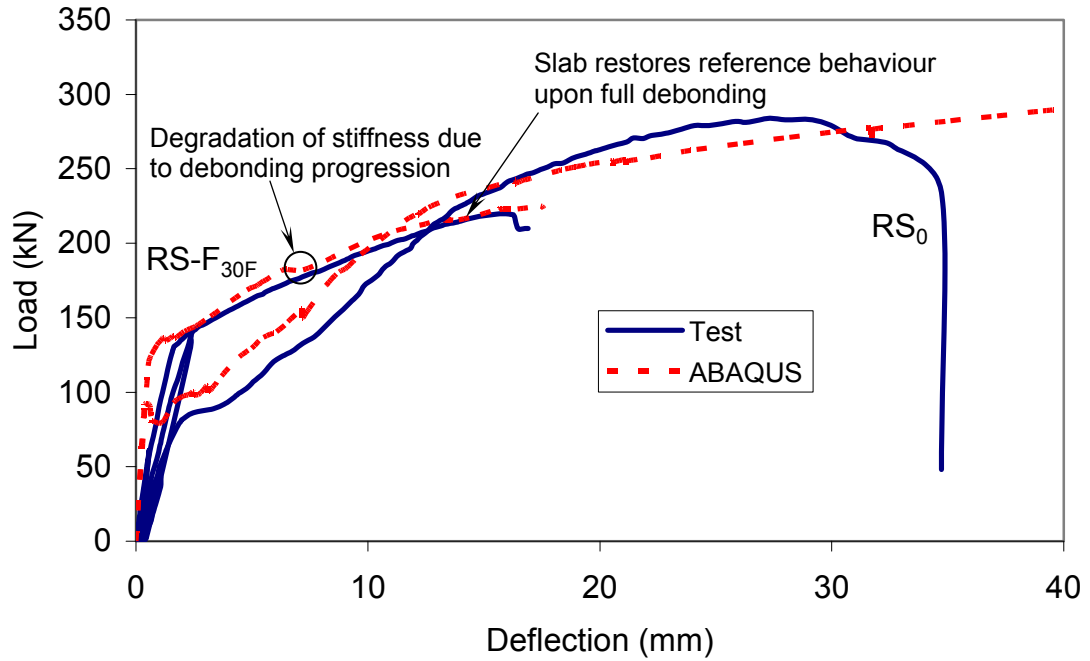


Figure 6-12: Comparison between experimental and model prediction for prestressed slab (RS-F<sub>30F</sub>).

With respect to specimen (RS-F<sub>30F</sub>), the low load level at corresponding displacement compared to slab (RS-F<sub>30</sub>), was the most surprising result. It is even lower than the load level of slab (RS-F<sub>15</sub>), as shown before in Figure (4-7). It looks as if the prestressing force has not been actually transferred to the concrete slab. This could be possible as the prestressing force was being transferred through the frame resting on the ground, by which the force was then transferred to the concrete substrate. Moreover, the use of large anchors extending up to the slab edges could adversely affect the transfer efficiency of the prestressing force as it prevents the FRP plates from deforming with the concrete substrate. The aforementioned reasons, together, increase the potential of such high loss in the prestressing force. This problem is not faced in the field application, as the prestressing devices are usually mounted on the concrete surface directly which allows only for immediate losses due to concrete deformation.

Another explanation that may cross someone's mind is that the concrete patch of this slab (RS-F<sub>30F</sub>) had a lower tensile strength which could result in a lower

first crack load. However, interpretation of the results based on such an assumption was disregarded for the following reasons. The split tensile tests did show that the tensile strength of this specimen was in the normal range of such concrete strength, and as it is well known the tensile strength may reduce in the member, but no more than about 10%, depending on the concrete grade. Moreover, the low tensile strength would result in early debonding, as the bond strength is related to the tensile strength of the concrete substrate. Nevertheless, the FRP plates were in contact with the concrete substrate up to the later stages of loading. This was confirmed by the FRP strain measurements shown in Appendix B.

Thus, the concrete tensile strength may not be responsible for the low load levels of slab (RS-F<sub>30F</sub>) during the load history, and the difference is attributed to the high loss of the prestressing force. So, to numerically validate the response of this slab a lower prestressing force of 7.5% was used.

### **6.3.2. Reinforcement strains**

#### **6.3.2.1. Internal steel reinforcement**

Figure (6-13) shows the FE prediction of the internal steel strains compared to the measured strains of the prestressed slabs (RS-F<sub>15</sub>) and (RS-F<sub>30</sub>). For the prestressed slab (RS-F<sub>15</sub>), the figure shows perfect agreement up to a load level of 200 kN which is about 85% of the ultimate load. After that the predicted strain increases with a mild rate leaving the trend of the measured strains. At the load level of 200 kN debonding of the FRP plates is expected to develop, and as a result cracks start to widen. Again, it has been mentioned before that the deflection resulting from crack widening could not be accounted for in a model adopting smeared cracking approach. So, the strain resulting from such deflection could not be accounted for as well. Moreover, the debonding propagation results in a higher proportion of stresses to be carried by the internal steel reinforcement, and hence the strains in these reinforcements would grow with a faster rate, as shown in Figure (6-13 a).

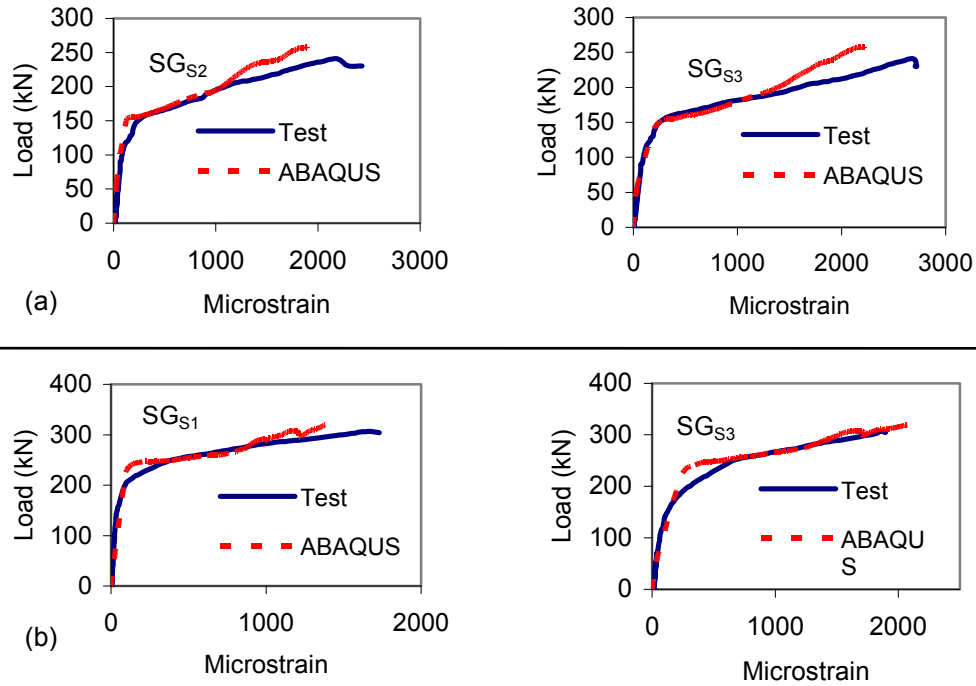


Figure 6-13: Steel reinforcement strain for prestressed slabs at different locations: (a) slab (RS-F<sub>15</sub>); (b) slab (RS-F<sub>30</sub>).

Also, neglecting the shear modelling on the crack surface has some disadvantages in predicting the strains of both the reinforcement and concrete; it imbalances to some degree their relative contribution to the curvature. So, it may be possible that reinforcement strains are underestimated while the concrete strains are overestimated. This explanation will be further discussed later in the following sections while discussing the concrete strains.

On the other hand, the predicted strains of slab (RS-F<sub>30</sub>) compare very well with the measured strains up to failure, as shown in Figure (6-13 b) and Appendix B. Only, strain gauge SG<sub>S7</sub>, which is located far outside the loading area, was underestimated by the FE analysis for the same abovementioned reasons. In general the predicted steel strains are considered to be in a good agreement with the measured strains.

#### **6.3.2.2. FRP reinforcement**

The FRP plate strains were not far from the internal steel strains. For instance, in slab (RS-F<sub>15</sub>) the load-strain curve of strain gauge SG<sub>F6</sub> has a similar trend to the behaviour of the internal steel reinforcement, as shown in Figure (6-14). The position of this strain gauge is located inside the truncated cone. As mentioned before in Section 6.2.2.2, such strain gauge experiences a mild increase rate upon debonding initiation due to the effect of the aggregate interlocking. It is clear that the model reflects this behaviour, but with some exaggeration compared to the experimental measurement.

Also shown in Figure (6-14) is the load-strain curve measured at strain gauge SG<sub>F9</sub>. This strain gauge is located near the plate end and just before the anchor plate, as shown in Figure (3-14). It is clear that the model was able to simulate the behaviour reasonably well. The model was able to identify the unloading phenomenon near the anchor plate. As it is well known, during the early stage of loading the anchors start to accommodate with the surrounding concrete. During this process the stress and strain levels at the portion of the prestressing plate, near to the anchors, increase with a mild rates, and sometimes decrease resulting in some losses in the prestressing force. After this stage, the strains start to increase, but with a faster rate compared to the previous stage. Just a few kNs before failure, the strain dramatically increases due to the development of the interfacial and shear cracks near the anchor plate. This has been confirmed by the failure mode discussed before in Section 4.2.1.

Also shown in Figure (6-14), the predicted strain distributions along a representative length of the bonded FRP plate compared to the measured strains at different load levels. The circled zone in the figure indicates a change in the curve slope at the end of the overlapped FRP location. It should be remembered that this phenomenon has been discussed before in Section 6.2.4. That is the FRP-concrete interfacial behaviour is directly related to the strain of the FRP plate. Intuitively, such change in the slope is a result of lower strains at the FRP overlapped locations. This reduction in the strain level at the overlapping is due to the effect of the lateral Poisson's ratio  $\nu_{21}$ , which transfers

the effect of the prestressing force in the second direction into a compressive force in the first direction and vice versa. By comparing the predicted strains to the measured strains, it can be noticed that the FE model is in good agreement with the measured strains over most of the loading history. Moreover, the model was able to simulate the overlapping phenomenon before failure.

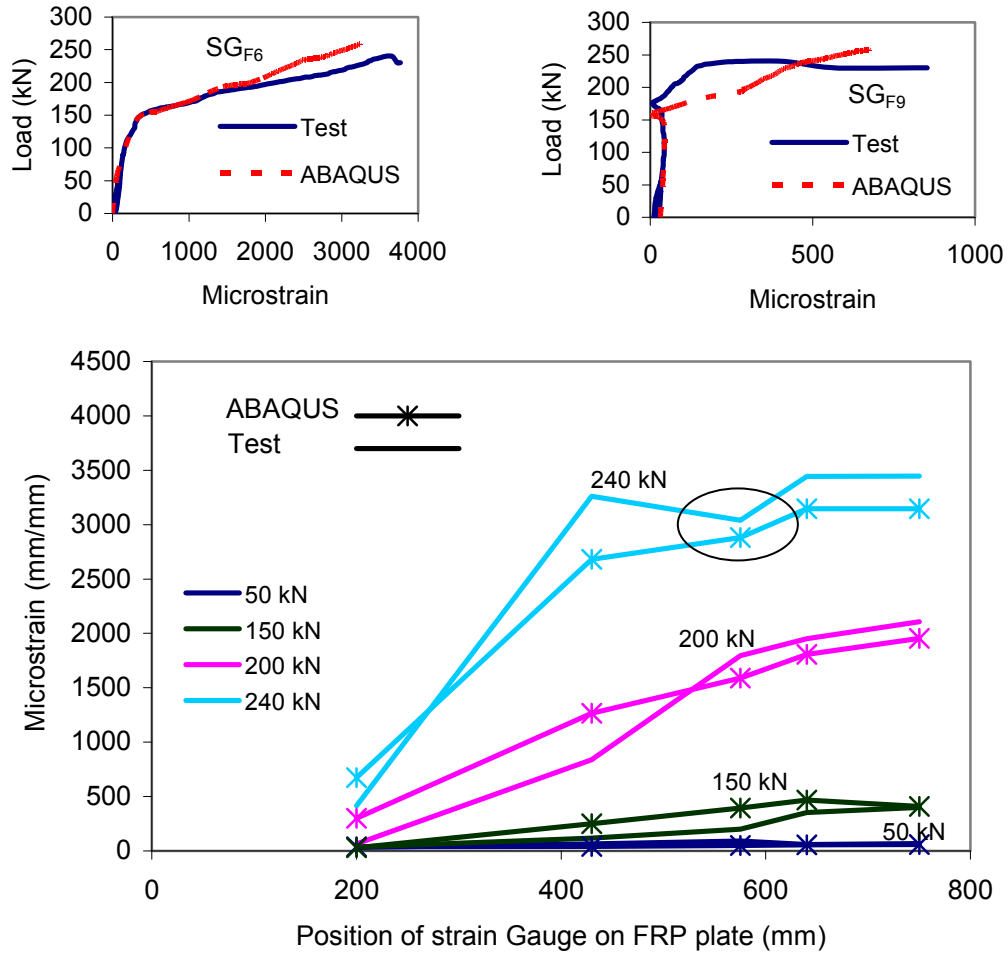


Figure 6-14: Measurement and prediction of FRP strain for Slab (RS-F<sub>15</sub>).

Similar to slab (RS-F<sub>15</sub>), Figure (6-15) shows the predicted strains of slab (RS-F<sub>30</sub>) compared to the measured strains. It can be seen that the FE analysis compares very well with measured strains, see for example SG<sub>F14</sub> and Appendix B. However, for the strain gauges near the anchor plate such as SG<sub>F1</sub>, the dramatic increase in the strain at failure could not be validated. As



mentioned before, the shear cracks extended near the end plates resulted in a sudden increase in the FRP strain at failure, as shown in the figure, which can not be modelled using a smeared model. Also, the strain gauges mounted on the second FRP strip, such as SG<sub>F5</sub> and SG<sub>F6</sub>, could not be validated as well, see Appendix B. That is these locations might have lower bond strength than the average value used in the model. Moreover, the FRP plates were modelled firmly connected to the end anchor plates, without allowing any slip between them. This was based on the experimental finding that all the FRP plates were in good contact to the anchor plate at failure, except the second plate of slab (RS-F<sub>30</sub>).

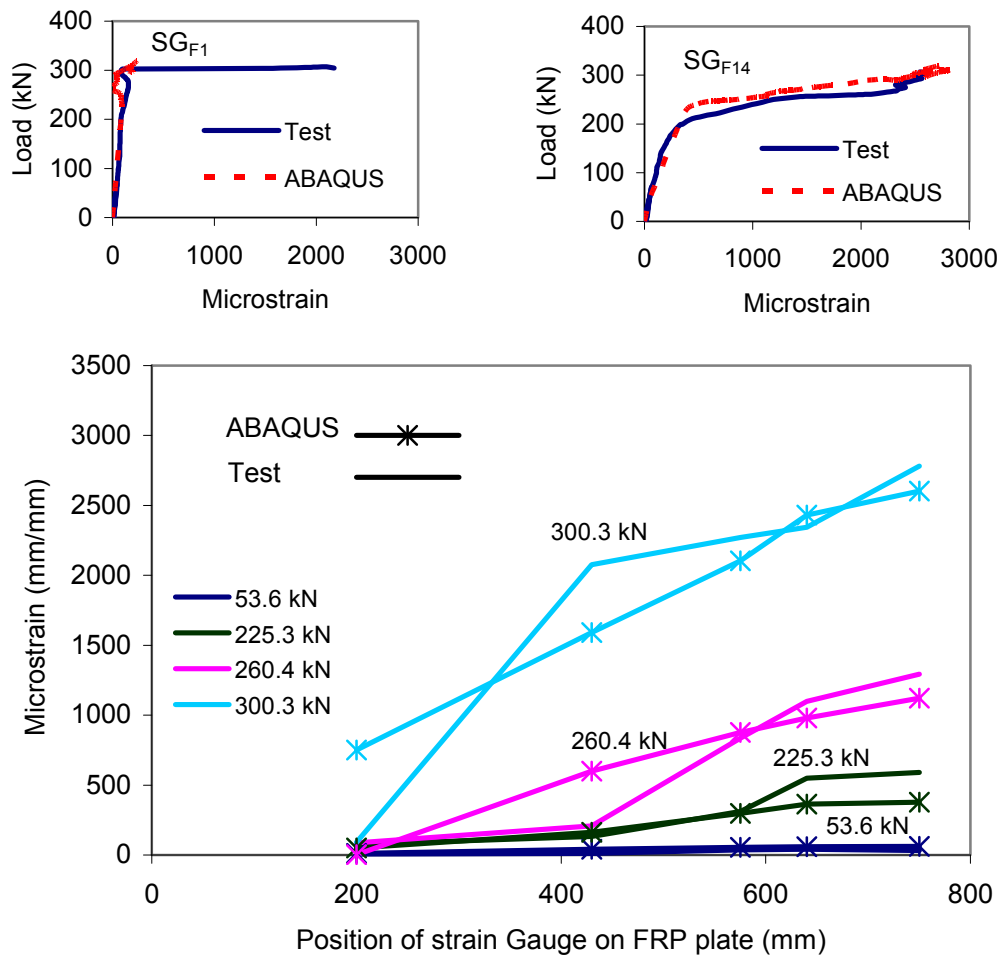


Figure 6-15: Measurement and prediction of FRP strain for Slab (RS-F<sub>30</sub>).

Figure (6-15) shows also the predicted strain distributions along the length of the bonded FRP plate compared to the measured strains at different load levels. The figure shows that the FE predictions deviate from the measured strains at certain locations. That is the profile reflects the same behaviour of the individual load-strain curves of strain gauges.

### **6.3.3. Concrete strains**

Figure (6-16) shows the concrete strain numerical predictions of the prestressed slabs at the designated locations. The FE analysis predicts reasonably well the measured concrete strains for slab (RS-F<sub>15</sub>). However, it shows some discrepancy for the strain measurement of slab (RS-F<sub>30</sub>).

The major contributor to the variation in concrete strains of this slab could be the early debonding of certain strips during the loading history which may be a result of low bond strength at certain sections. So, how could the bond interaction affect the concrete strain measurement? Again, it is known that the deflection is related to curvature which may be defined as the element rotation divided by the effective depth. This rotation can be simplified as the summation of average reinforcement and extreme-fibre compressive concrete strains. Although this definition is applicable for flexural members, the main principle could be applied in the discontinuity region (shear region) with low reinforcement ratios. Thus, if the FRP starts to debond from the concrete substrate, the slab stiffness decreases and, at the same time, the rotation increases. This increase is reflected in one or more of the constitutive parameters, such as the concrete strain. In the FE analysis an average value for the bond strength is used for the whole member, where it is not logical to use different values for different areas within the slab model. So, in the areas with low bond strength, the model will overestimate the FRP strains and underestimate the concrete strain.

Several factors may also contribute to the discrepancy in concrete strains. In the forefront of these factors is the concrete homogeneity. As mentioned before in Section 5.2, the concrete has been judged to be homogeneous at the macro-

scale level. However at the micro-scale level, where the concrete strains are measured, concrete is considered a heterogeneous material. So, the reading of the strain gauge positioned unintentionally on a stone is expected to be much lower than that positioned on the filling cement past. Moreover, the penetration and development of in-between cracks could also affect the strain measurement. In reality concrete strains are expected to be more localized around a crack as it deeply penetrates and widens. However, in the smeared modelling approach the strain is averaged over the element which is much larger than the aggregate size [77].

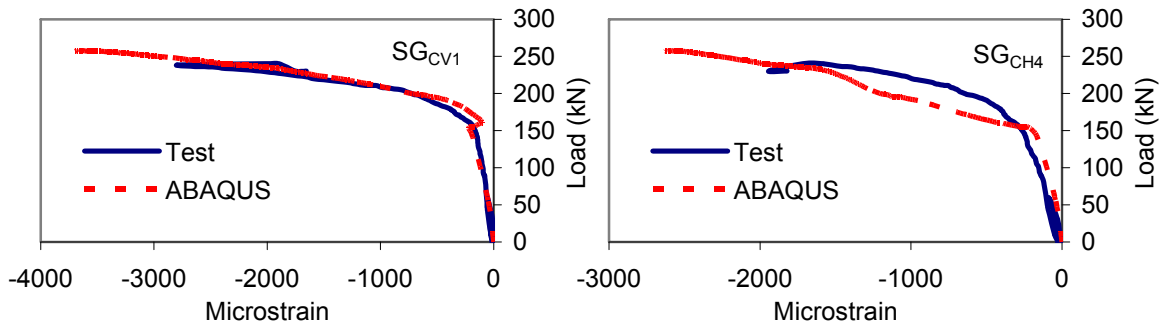


Figure 6-16: Radial and tangential concrete strains for slab (RS-F<sub>15</sub>) at positions  $SG_{CV1}$  and  $SG_{CH4}$ , respectively.

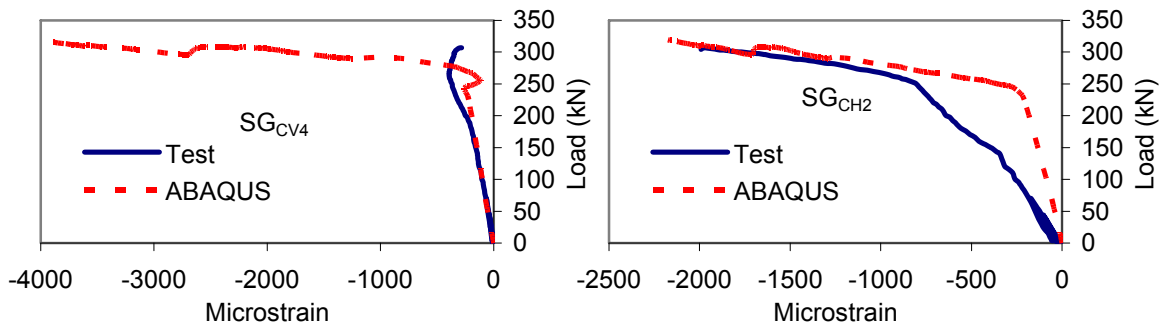


Figure 6-17: Radial and tangential concrete strains for slab (RS-F<sub>30</sub>) at positions  $SG_{CV4}$  and  $SG_{CH2}$ , respectively.

Although some predicted strains show some discrepancy when compared to the measured strains, many others were in a good agreement as shown before in Section 6.2.3 and Appendix B. Furthermore, the effect of bond strength on the response of the compressive zone may be more pronounced in the prestressed slabs with high prestressing force than in the low prestressed or non-prestressed slabs. In general, the higher gradient of interfacial shear stresses results in early development of cracks, and hence rapid growth of concrete strains at the extreme compression fibres. In contrast, in non-prestressed slabs only after the yield of the internal steel reinforcement the cracks become wider and deeper. Therefore, the measured concrete strains are considered representative.

From the above discussion, it could be seen that the response of the compressive concrete zone is related to bond interface which affects the deflection behaviour as well; see Section 6.3.1. So, it is necessary to investigate the FRP-concrete interface which is discussed in the following section.

#### **6.3.4. FRP-concrete interfacial behaviour**

Figures (6-18) and (6-19) show the numerical predictions of the interfacial shear stress distribution for the prestressed slabs (RS-F<sub>15</sub>) and (RS-F<sub>30</sub>), respectively, at different load levels. Their behaviour, to some extent, is similar to the non-prestressed slab (RS-F<sub>0</sub>). That is the bond starts from the slab centre towards the slab edges. However, at early stages of loading before cracking, the shear stress levels along the plate length were high compared to the non-prestressed slab (RS-F<sub>0</sub>), especially near the anchor plate. Accordingly, the shear stress is noticed to increase as it moves towards the plate end. It seems that the high prestressing force in the FRP plate helps more stress concentration at the plate end. The stress concentration near the plate end is a well-known phenomenon, which has been studied by many researchers before. It is caused by a sudden change in the strengthened section due to the termination of the FRP plate. For instance, for slabs (RS-F<sub>15</sub>) and (RS-F<sub>30</sub>), the shear stress levels near the anchor plate, corresponding to a load level of 56.4 kN and 53.2 kN, were 0.04

and 0.12 MPa, respectively, while the shear stress levels near the slab centre are close to zero, as could be shown in Figures (6-18) and (6-19).

In the same vein, the interfacial shear stress near the maximum radial moment area increases significantly after cracking due to the localized concrete cracking. A change in the slope of the interfacial shear stress distribution at the overlapping area is developed, as shown in the circled area on the figures. The shear stress near the anchor plate has got a big increase as well, so the shear stress level at the plate end is still higher than that near the slab centre, as shown by the second lowest curve (171.4 kN) and (258.5 kN) in Figures (6-18 a) and (6-19 a), correspondingly.

It is noticed that the fluctuation of the shear stress profile is less severe than the stress profile of slab (RS-F<sub>0</sub>). That is the high prestressing force was able to distribute the stresses across the plate width. As a result, the time difference between the debonding of the nodes across the FRP plate is considerably diminished. This can be easily identified from the crack pattern of the slabs, as shown in Appendix B.

When the load is further increased, the shear stress at the slab centre reached the peak value 1.6 MPa then descended gradually, as shown from the figures. However, the interfacial shear stress at the overlapping position did not progress negatively, but still with lower stress levels than the surrounding points. This could be attributed to the high prestressing force which was able to reduce the rate of slip changes at the plate overlapping. At the later stages of loading (load level 233.9 kN and 306.9 kN for slab (RS-F<sub>15</sub>) and (RS-F<sub>30</sub>), respectively) the interfacial shear stress just after the overlapping position reaches the bonding strength, while the shear stress near the plate end is still lower than the bond strength (0.92 and 1.04 MPa for slab (RS-F<sub>15</sub>) and (RS-F<sub>30</sub>), respectively). Most interestingly, the debonding progression of the prestressed slabs was very fast compared to the non-prestressed slab (RS-F<sub>0</sub>). One can easily identify that the debonding of 525 mm of the FRP plate occurred in the last ten kNs before failure.

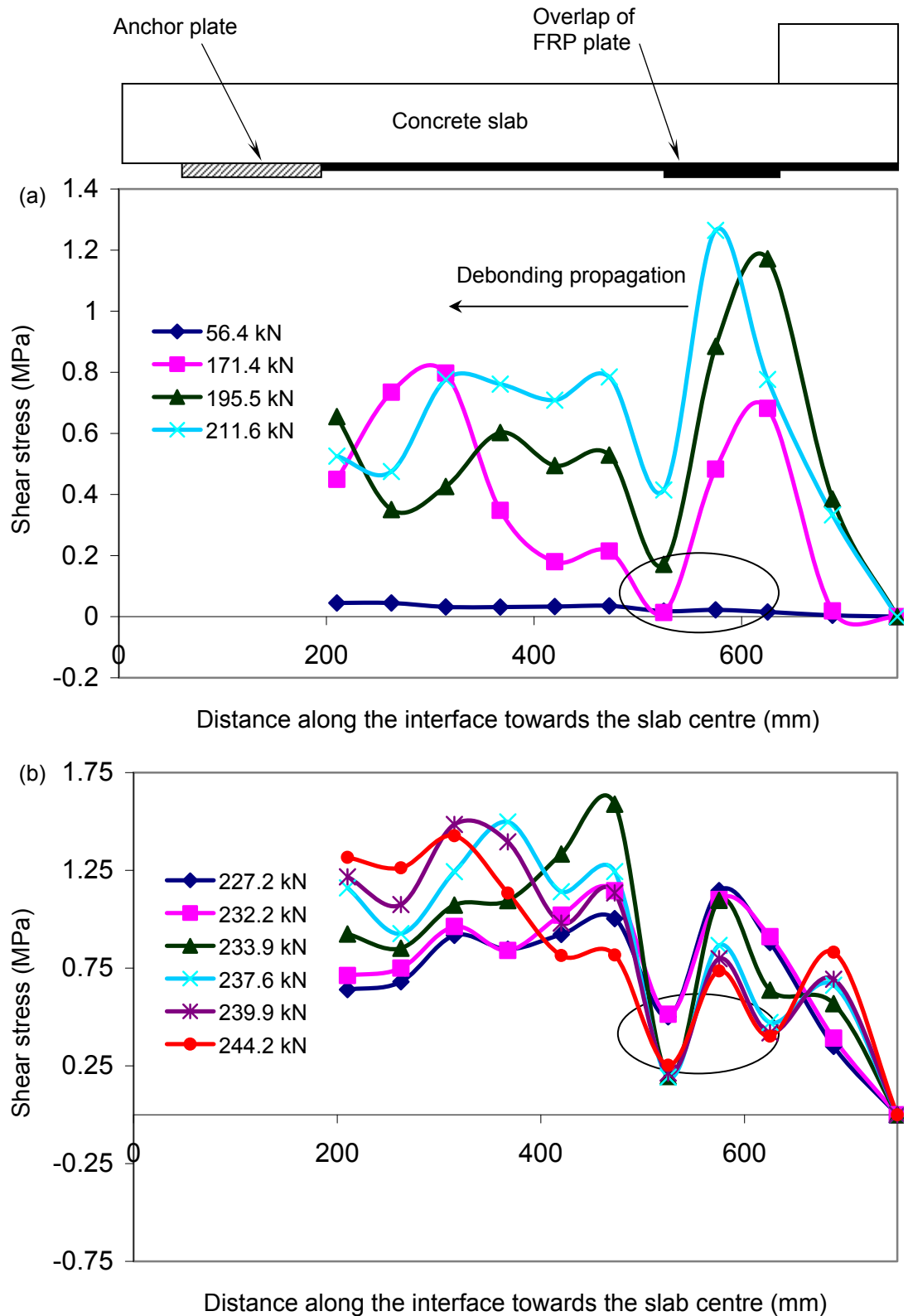


Figure 6-18: FRP-concrete interfacial behaviour of slab (RS-F<sub>15</sub>): (a) before cracking; (b) later stages of loading.

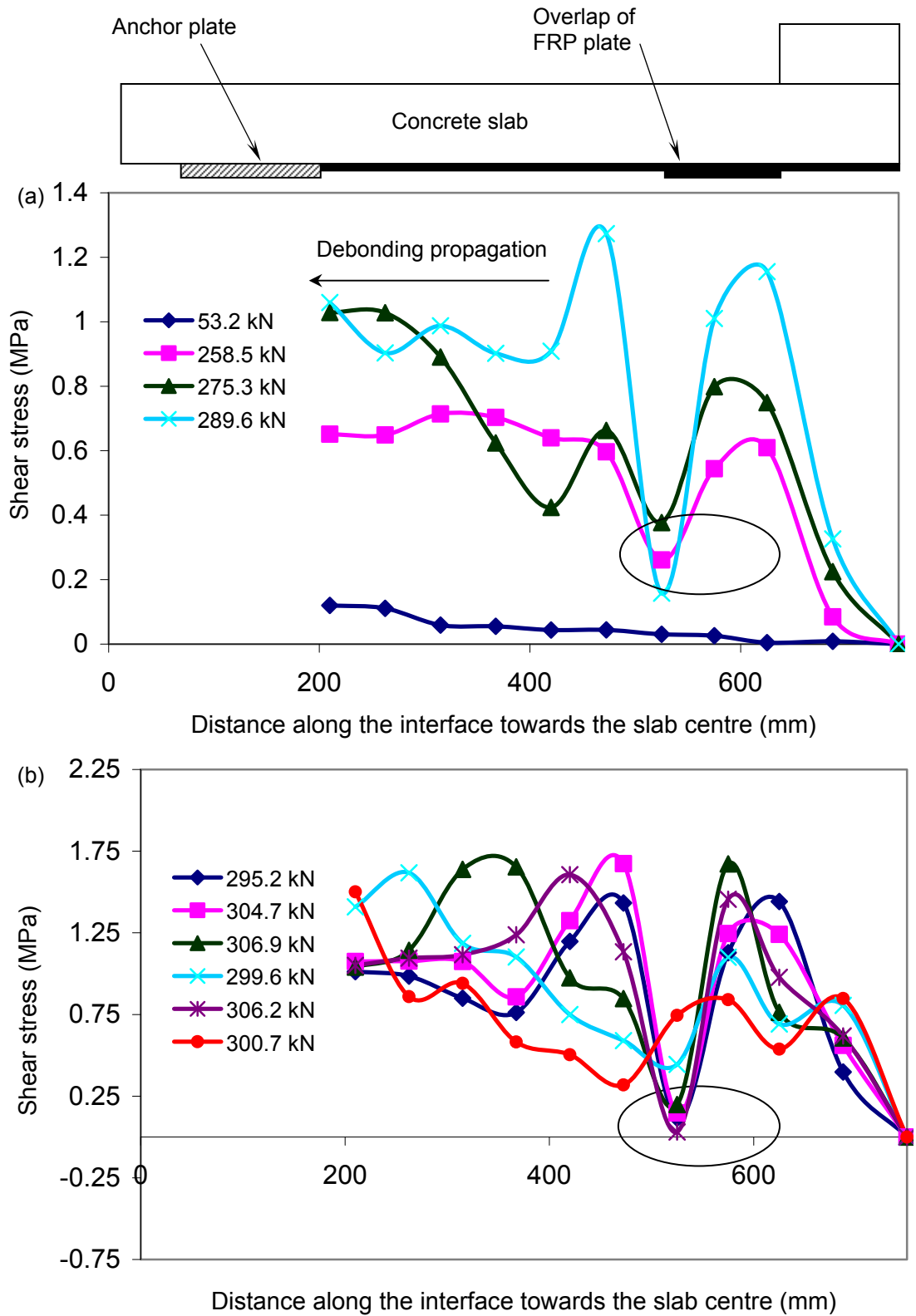


Figure 6-19: FRP-concrete interfacial behaviour of slab (RS-F<sub>30</sub>): (a) before cracking; (b) later stages of loading.

Similar to slab (RS-F<sub>0</sub>), the above figures show that the debonding failure initiates near the slab centre and propagates towards the end of the FRP plate which implies that the debonding failure mode of the prestressed slabs can be classified as intermediate crack induced debonding (IC). However, the experimental results of these slabs showed that the position of the critical shear cracking has been shifted outside the area implying critical diagonal crack induced debonding (CDC). As discussed before, this does not malign the validity of the predicted results since the model was able to pick the main features of the interfacial behaviour such as the stiffness degradation and slip concentration at the FRP overlapping position. So, such difference could be overlooked.

#### **6.3.5. Crack pattern**

The cracking of the prestressed slabs followed a different behaviour from the non-prestressed slab (RS-F<sub>0</sub>) and the reference slab (RS<sub>0</sub>). At zero load level, the FE analysis shows that there is some development of tensile cracks near the plate end. These cracks are a result of the sudden termination of the FRP plate, which carries a high tensile force by the anchors. The model prediction is quite logical. However, in the experimental tests such cracks were not visible by the naked eye. It could be possible that the model shows such cracks due to the use of low tensile strength to validate the deflection behaviour.

For all prestressed slabs, the development of cracking then passed nearly the same stages, but at different load levels for each slab. This was depending on the amount of the prestressing force used. Firstly, the crack strains started to occur tangentially at the area of the maximum bending moment near the column then spread radial towards the slab edges as the predicted load increases. Noticeable large crack strains started to occur at the outer edges of the FRP plates, while relatively small strains occurred at the area just beneath the plates where they are bonded to the concrete substrate. This was accompanied with more stress concentration at the plate end. Within a few kNs later, cracks started to appear along the inner edges of the FRP plate and extended up to the slab edges. As the load was further increased, another crack path parallel to



the inner edge of the FRP plate was noticed. This crack line was extending to the slab edges, to the points which determine the length of the slab edge that does not contact the support. This crack pattern was then kept until failure occurred. It should be mentioned that there is some tiny differences between the crack patterns of the prestressed slabs themselves. For example, the length of the slab edge that does not contact the support due to the corners uplift in slab (RS-F<sub>15</sub>) is shorter than slab (RS-F<sub>30</sub>). This is attributed to the effect of the prestressing force which makes the slab stiffer as the prestressing force is increased. Also noticeable is that increasing the prestressing force results in extending the crack lines around the FRP edges beyond the anchor plate, up to the slab edges. This might explain the slippage problem in the second FRP strip in slab (RS-F<sub>30</sub>).

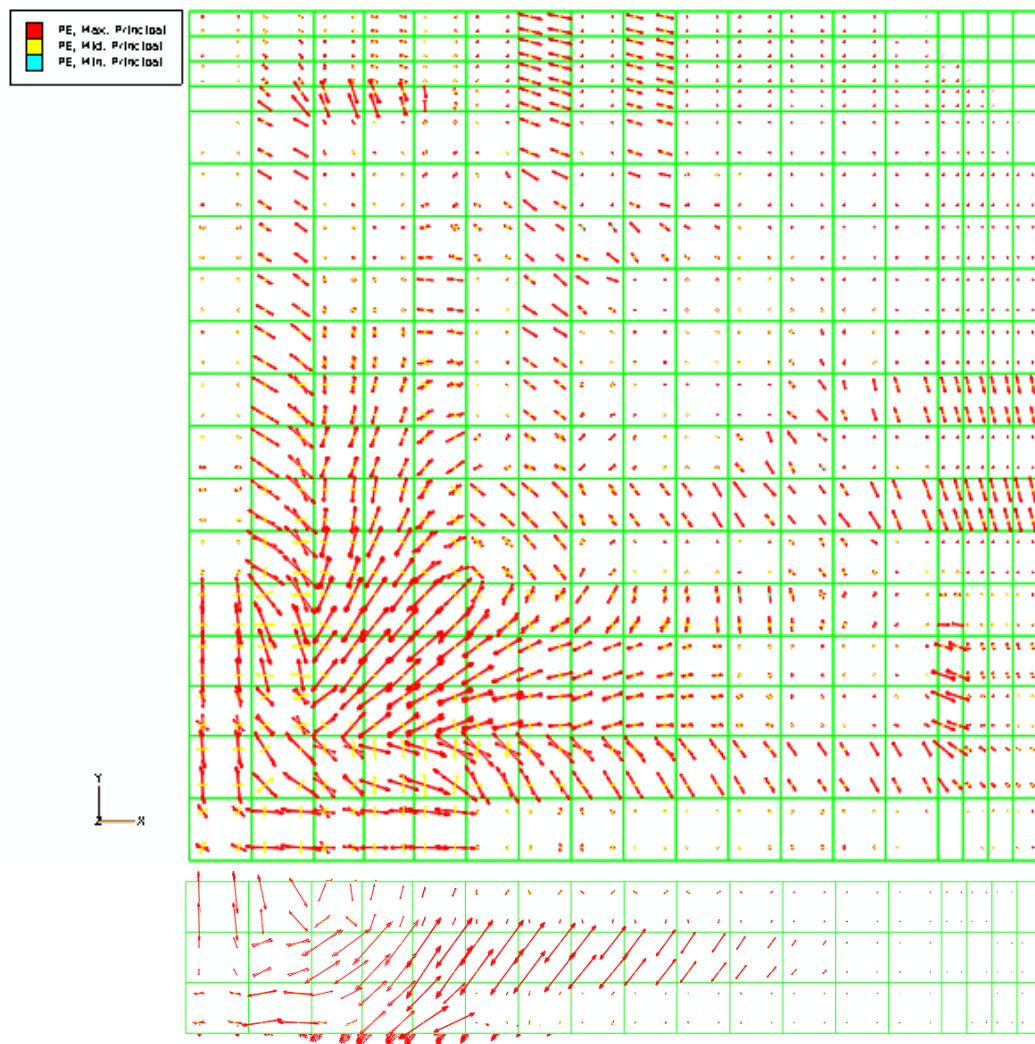


Figure 6-20: Crack pattern of slab (RS-F<sub>15</sub>) at load level 239.9 kN.

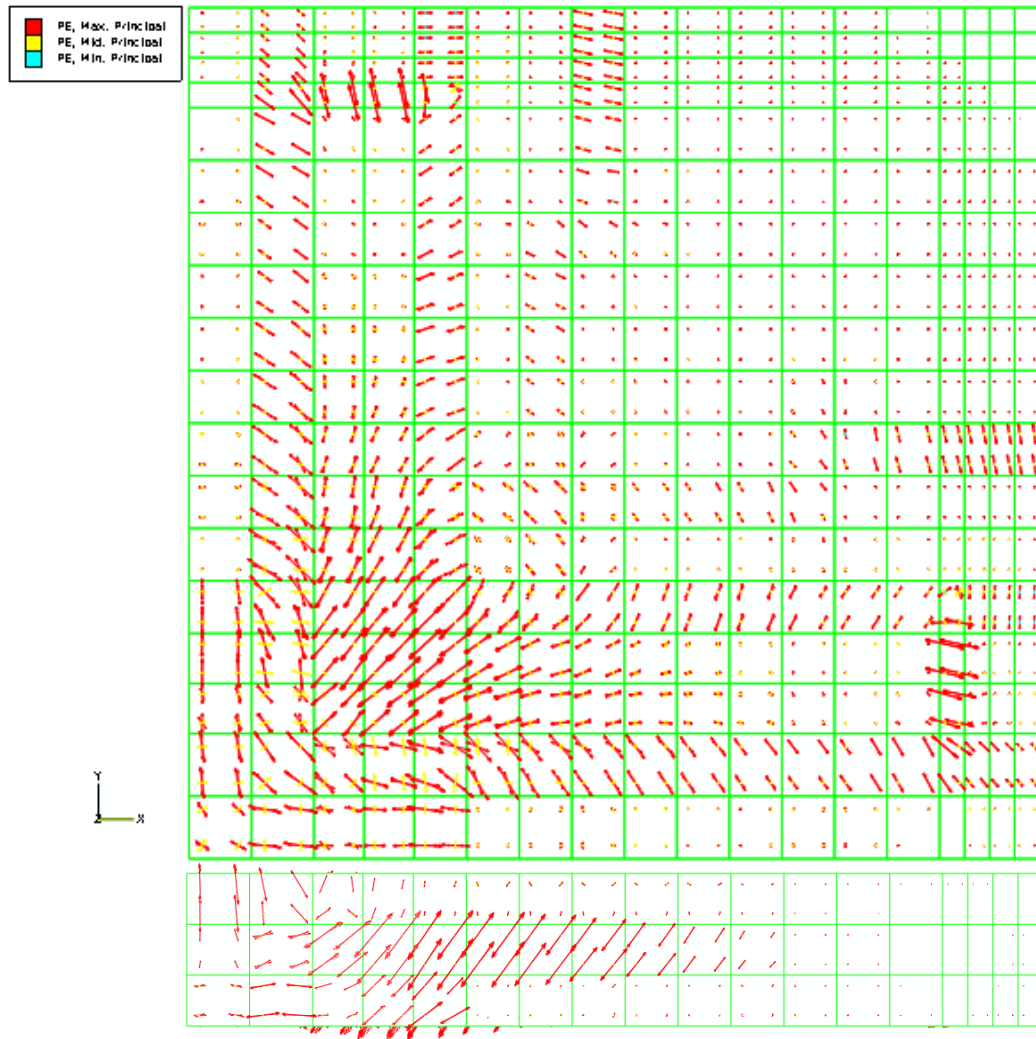


Figure 6-21: Crack pattern of slab (RS-F<sub>30</sub>) at load level 305.7 kN.

By comparing the loads corresponding to the stages of cracking development between the prestressed slabs, it could be concluded that the higher the prestressing force used the more crack resisting capability is obtained. Also, the initial cracking area and intensity is reduced as the prestressing force is increased. Thus, the crack resisting capability of the prestressed slabs has remarkably increased. Figures (6-20) and (6-21) show the crack pattern of the bottom surface and central cross section of slabs (RS-F<sub>15</sub>) and (RS-F<sub>30</sub>), at the predicted failure loads of 239.9 and 305.7 kN, respectively.

### 6.3.6. Crack opening displacement

Figure (6-22) shows the load-(CMOD) curves of the prestressed slabs (RS-F<sub>15</sub>) and (RS-F<sub>30</sub>), predicted by the FE analysis. These curves were obtained at the same position used in slabs (RS-F<sub>0</sub>) and (RS<sub>0</sub>). Again, it is clear that the application of the FRP reinforcement reduced the crack opening displacement. Moreover, increasing the prestressing force resulted in more reduction in the crack opening which implies more enhancement in the serviceability of the strengthened member. This can be easily identified by comparing the crack opening at a certain load level. For example, at load level 200 kN the corresponding opening displacement for slabs (RS<sub>0</sub>), (RS-F<sub>15</sub>) and (RS-F<sub>30</sub>) are 0.26, 0.18 and 0.005 mm, respectively, which clearly reflect the effect of changing the prestressing force. However, by comparing the opening displacement in the early stages of loading such as 90 kN, which is usually the common service load for slabs with such design, no significant difference could be identified for the prestressing effect in reducing the CMODs, compared to the non-prestressed slab (RS-F<sub>0</sub>).

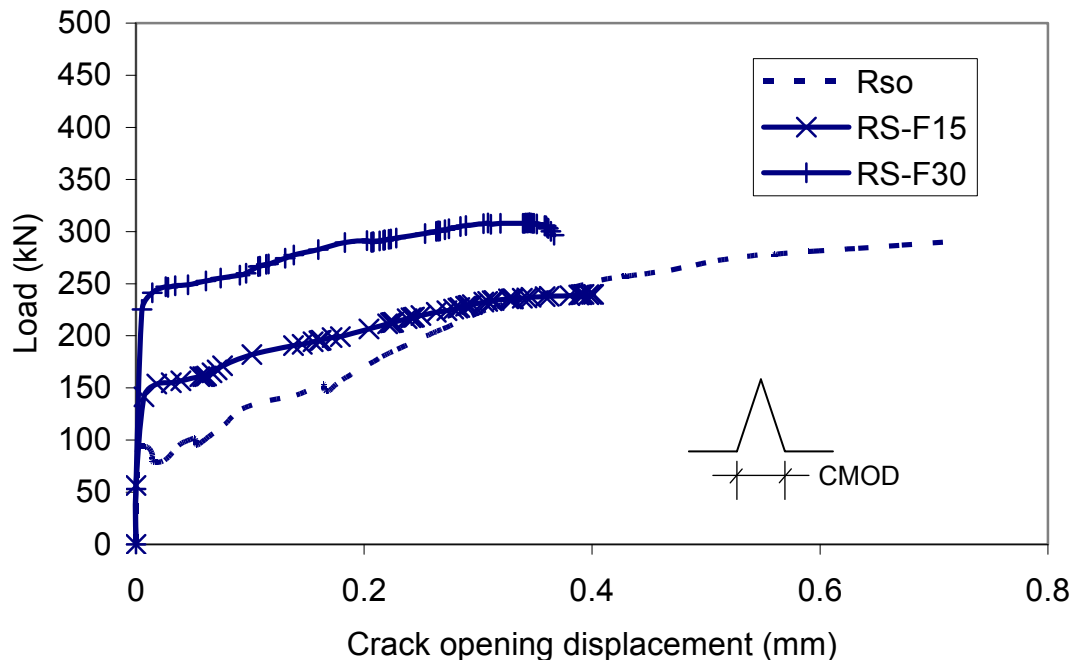


Figure 6-22: Load-CMOD obtained at distance 1.5d from the column face along the centreline of the slab.

### 6.3.7. Ultimate load and failure mode

Table (6-2) summarises the measured and FEA-predicted failure loads for the prestressed slabs, along with their failure modes. The reference slab (RS<sub>0</sub>) and non-prestressed slab (RS-F<sub>0</sub>) results are reprinted here for convenience. For the prestressed slabs, the predicted failure mode is debonding of FRP plates, and the corresponding failure load predicted by FEA is within only 5% of the actual failure load. This indicates an excellent agreement between the numerical and experimental results. These slabs are said to fail in debonding as the damage parameter at the interface reaches a value of 0.99 of the interface strength, while the principal compressive strain around the column does not exceed the value of 0.0035.

Table 6-2: Experimental and FEM predictions of ultimate load and failure mode.

Specimen	Test		FEM		Ultimate Load ratio FEM/Test
	Ultimate load (kN)	Failure mode	Ultimate load (kN)	Failure mode	
RS <sub>0</sub>	284	Flexural punching	253.7	Flexural punching	0.89
RS-F <sub>0</sub>	405.2	Punching	361.3	Debonding	0.89
RS-F <sub>15</sub>	240	Debonding	236.5	Debonding	0.99
RS-F <sub>30</sub>	307	Debonding	292.4	Debonding	0.95
RS-F <sub>30F</sub>	220	Debonding	215.7 <sup>(1)</sup>	Debonding	0.98

(1) The prestressing level used for prediction of the ultimate load is 7.5%

For the prestressed slab (RS-F<sub>15</sub>), neither the concrete nor the steel reached the ultimate compressive strain or the yield strain. At the predicted debonding failure load, the corresponding average concrete strain around the column was within a value of 0.0021, while the levels of the steel strain were less than 0.0027. Similar to slab (RS-F<sub>15</sub>), both the ultimate compressive concrete strain and yield strain margins were not violated for slab (RS-F<sub>30</sub>). The average concrete strain around the column was within a value of 0.0018, and the levels of steel strain were less than 0.0025. Nonetheless, only strain gauge SG<sub>S5</sub> was close to the yield strain. As discussed before, this may be attributed to the

slippage problem of the second FRP strip which allowed the steel reinforcement around the column area to carry more force to compensate the force lost by debonding. The prestressed slab (RS-F<sub>30F</sub>) continued showing unexpected results. At failure, the concrete strain exceeded the ultimate compressive strain near the column corner at position SG<sub>CH2</sub>. Moreover, the steel strain at position SG<sub>S5</sub> exceeded the yield strain as well. This further supports that the prestressing force was not fully transferred to the concrete substrate in this slab. That is the effect of prestressing should be reflected in the results as a low levels of steel strain.

It can be seen that slab (RS-F<sub>30F</sub>) showed some symptoms of the flexural behaviour. However, these indications could not spread over large area of the slab and vanished early due to the rapid development of the debonding failure. Such indications would not appear if there was enough confinement from the prestressing force. Thus, apart from slab (RS-F<sub>30F</sub>), the results indicate that increasing the prestressing force increases the ultimate load, but reduces the member ductility. Moreover, the bond characteristics were the main reason for not attaining higher ultimate load in the prestressed slabs, compared the non-prestressed slab.

#### **6.3.8. Conclusion**

The fairly detailed discussion of the prestressed FRP slabs' results may be conducive to important aspects of behaviour. Bonding prestressed FRP reinforcement to the tension face of concrete column-slab connections enhances the serviceability of the connection in terms of higher cracking loads and stiffness, but does not increase the ultimate load as much as the non-prestressed FRP reinforcement. The high strain levels in the FRP plate due to the prestressing effect is the main reason for not attaining higher ultimate loads as it triggers debonding failure at early stages of loading.

The serviceability is enhanced in terms of stiffer load-deflection behaviour and smaller crack widths, compared to the reference slab and the non-prestressed applications. The level of strain of the steel reinforcement is lower than that of

the non-prestressed application. This attributed to the confinement effect of the prestressing forces.

The percentage increase in the ultimate load is only 8% that of the reference slab. Moreover, slab (RS-F<sub>30F</sub>) shows unexpected behaviour. It shows a low load level at corresponding displacement, compared to other slabs with the supposed prestressing ratio. This is believed to be as a result of improper transfer of the prestressing force to the concrete substrate.

## **Chapter 7**

### **Conclusion and recommendations**

#### **7.1. Introduction**

This study has investigated the punching shear behaviour of RC column-slab connections strengthened with externally bonded FRP reinforcement, both experimentally and analytically. Experimentally, five full-scale RC slabs strengthened with non-prestressed or prestressed FRP plates were tested under concentrated loading. The main variables considered were the prestressing ratio and the anchorage bond length. The experimental study examined deflection profiles together with steel and FRP strains, compressive concrete strains and crack width.

All the slabs tested were analysed by using FE analysis with smeared modelling of cracks. A rigid element was used to model the support to mimic a horizontally unrestrained slab with its corners free to lift, while a connector element was used to model the interface between the FRP plate and the concrete substrate. The sensitivity of each parameter in the slab model and its effect on the predicted slab behaviour was examined. The analytical part looked into the numerical analysis technique used and evaluated its prediction of deflection, crack width, as well as steel, FRP and concrete strains. Furthermore, the FRP-concrete interface was investigated representatively.

This study also evaluated the prediction of punching shear strength in the ACI and Eurocode 2 codes of practice. Modes of failure and punching shear strength were also addressed. The following conclusions and recommendations can be drawn from the present study.

## **7.2. Punching shear behaviour of FRP strengthened slabs**

### **7.2.1. Load-deflection response**

The deflection of slabs with low reinforcement ratios is mainly caused by flexural curvatures. The rigid body rotation, caused by deep penetration of shear cracks, also makes a small contribution to slab deflection. However, this contribution may be negligible for FRP strengthened slabs.

The deflection profile of the strengthened slabs shows that the strengthened members experience low deflection values, compared to the unstrengthened slab, over the whole loading history. Within the service load range, the deflection of the FRP strengthened members is considerably lower than the unstrengthened slab. The measured deflections of the strengthened slabs at the slab centre were 30%, 25% and 26% for the non-prestressed slab (RS-F<sub>0</sub>) and the prestressed slabs (RS-F<sub>15</sub>) and (RS-F<sub>30</sub>), respectively, relative to the reference slab (RS<sub>0</sub>). This implies that the application of prestressed FRP plates marginally reduces the deflection level of the strengthened members, compared to the application of non-prestressed reinforcement. Another important implication is that the effect of increasing the prestressing force can be considered as if it is similar to the effect of increasing the reinforcement ratio; as the prestressing force is increased the cracking load increases.

After cracking, deflection follows an almost linear relationship with load up to failure. The load-deflection curves of the prestressed slabs have lower slope than that of the non-prestressed slab which is a result of the early debonding initiation due to the high prestressing forces applied. At later stages of loading, only the loading area experiences high deflection values, while the rest of the slab still has low deflection values.

FE analysis with smeared modelling of cracks cannot account for deflection due to the rigid body rotation around the critical shear crack. Therefore, though the level of tension stiffening in FE analysis can be chosen to match the measured deflection. So, FE analysis may not predict the actual state of strain in the member. Hence, the average reinforcement strains inside the truncated cone



may be overestimated, while the strains outside this cone may be underestimated. Such phenomenon, which also affects the response of the compressive concrete zone, requires further research.

The deflection behaviour of the strengthened slabs is more governed by concrete, rather than the reinforcement or interface properties. The shape of the tension stiffening curve could significantly affect the solution of the global load-deflection relationship for structures with low reinforcement ratios, in particular where there is a strain localisation in certain areas. They resemble the behaviour of plane concrete. Therefore, the energy require to open unite area of crack is not too much at the beginning of the analysis. However, more energy may be needed at later stages of loading to increase the crack area due to the effect of bond interaction and other toughening mechanisms. Scanlon model well describe such phenomenon.

### **7.2.2. Steel strain**

The steel strains nearly follow the same trend of the load-deflection curves. A stiffer behaviour is noticed for the prestressed and non-prestressed specimens compared to the reference specimen ( $RS_0$ ). The prestressed slabs did not experience extensive yielding and their strain level is much lower than the level of strain in the non-prestressed slab ( $RS-F_0$ ) and the reference slab ( $RS_0$ ).

The FE prediction of the steel strain can be affected by two factors; the amount of tension stiffening used in the model and the interface material properties. Lower material properties for the interface increase the steel strain and vice versa.

### **7.2.3. FRP strain**

Within the range of service load the strain compatibility in the slab cross section is maintained and the strain levels of the FRP are comparable to the steel strains. After debonding initiation, the rate of strain increase for the prestressed specimens ( $RS-F_{15}$ ), ( $RS-F_{30}$ ) and ( $RS-F_{30F}$ ) is higher than that of the none-

prestressed slab (RS-F<sub>0</sub>). This higher rate is attributed to the sudden transfer of forces to the FRP plates at the onset of debonding. The magnitude of the increase in strain is highest at debonding cracks near the slab centre, and gradually reduces away towards the plate end.

The FRP strains are highly dependant on the interface material properties. Higher material properties for the interface increase the level of FRP strain and at the same time reduce the internal steel strain.

#### **7.2.4. Concrete strain**

At the service load level concrete strains are negligible. After debonding, the concrete strain at the extreme compressive concrete fibre increases nonlinearly with load up to failure.

The response of the compressive concrete zone can be noticeably influenced by the width and penetration of shear cracks. Therefore, FE smeared analysis can considerably underestimate the compressive concrete strain, as such analyse does not account for the localised effects of cracks. The difference between the measured and predicted concrete strains reached about 33% for beams slab (RS-F<sub>30</sub>) at position SG<sub>CV2</sub>. However, the model was still able to show that the strain level in the tangential direction is usually higher than that of the radial direction at the same load level.

#### **7.2.5. Cracking**

Bonding FRP plates to the tension surface of concrete slabs reduce the crack widths and shifts the shear cracks positions away from the loading region. Within the service load range, high prestressed FRP reinforcement can delay cracking better than the non-prestressed FRP reinforcement.

The higher the prestressing force used the more crack resisting capability is obtained. Also, the initial cracking area and intensity is reduced as the prestressing force is increased. Thus, the crack resisting capability of the

prestressed slabs has remarkably increased. That implies an enhanced serviceability of the strengthened member.

The bond interface is more susceptible to shear cracks than flexural crack. The former has both pulling and peeling effect on the bond interface which easily spread the debonding, especially if the FRP plate carries high prestressing forces. The FE analysis with interface modelling gave the capability of capturing the gradual activation of the interface debonding.

#### **7.2.6. Mode of failure and ultimate capacity**

Flexural strengthening of column-slab connections using FRP plates increased the load capacity by nearly more than 40% over the unstrengthened slab. The non-prestressed slab showed a better enhancement to the ultimate load compared to the prestressed slabs.

Again, strengthening of concrete slabs by using prestressed FRP plates is similar in behaviour to using high reinforcement ratio. It directs the stress state in the column-slab connection to experience shear failure rather than flexural failure. However, variation of bond length shows no clear effect on the ultimate strength.

The application of the FRP reinforcement increases the punching capacity of the strengthened slabs compared to the reference slab ( $RS_0$ ), but simultaneously decreased the ratio of the punching load to the flexural load, which is translated into smaller rotation at failure. The application of prestressed FRP plates could result in a large reduction in the rotation capacity if there is not enough bonding area to prevent failure by premature debonding. This emphasizes that the design of FRP RC is usually controlled by the serviceability limit state rather than ultimate limit state.

Punching shear failure of slabs strengthened with prestressed EBR is violent and considerations should be given to using more conservative strength reduction factors.

### **7.3. Practical significance of the study**

The current findings add substantially to our understanding of the punching shear behaviour of flat slabs without shear reinforcement and strengthened with externally bonded FRP reinforcement. The application of prestressed FRP reinforcement around the column-slab connection enhances the serviceability of the connection. However, it results in noticeable reduction in the ductility of the member. The main reason of such reduction in ductility is attributed to the development of critical diagonal cracks which result in premature debonding failure prior to the yielding of flexural reinforcement. On the other hand, the application of non-prestressed FRP reinforcement may result in flexural failure, but with low serviceability enhancement compared to the slabs strengthened with prestressed FRP reinforcement.

The FE analysis enables detailed investigation of the interfacial behaviour, and is able to capture the onset of debonding and macro-debonding which is very difficult to identify in the physical tests. As a result, the FE model gives a conservative prediction of the ultimate load. Also, it provides an accurate prediction of the crack patterns which agree to the experimental results. This is attributed to the approach used in modelling the support, so the slab corners are able to lift.

### **7.4. Recommendations and future work**

The current investigation was limited to flat slabs without shear reinforcement and low reinforcement ratios. Therefore, it is recommended that further experimental investigations be undertaken to study the effect of using different reinforcement ratios and arrangements on the punching behaviour of the strengthened connection. Other parameters, related to the strengthening material, can be studied as well such as; the stiffness of the FRP plate, plate geometry and strengthening pattern.

Also, the results of this study indicate that the FRP-concrete interface has a direct impact on the ultimate punching strength. So, it would be interesting to

investigate different measures to enhance the FRP-concrete interfacial behaviour; such as using of FRP sheets with mechanical fasteners.

Another limitation is related to the FE model developed. The model underestimates the effect of the normal stress components around the shear crack at the interface. Also, the model usually starts the crack at the same position of the maximum bending moment. Thus, future work should be conducted with discrete crack modeling to correctly model such phenomena.

The adequacy of code expressions for FRP strengthened members needs to be evaluated against a much wider database of experimental research work, with different test details and FRP reinforcement.

Finally, the adequacy of code expressions for FRP strengthened members needs to be evaluated against a much wider database of experimental research work, with different test details and FRP reinforcement.

## References

1. *Punching of structural concrete slabs (CEB-FIB bulletin No.12)*. 2001.
2. Hollaway, L. and M.B. Leeming, *Strengthening of reinforced concrete structures : using externally-bonded FRP composites in structural and civil engineering*. 2003, Norwich, NY: Knovel.
3. ACI, *Guide for the design and construction of externally bonded FRP systems for strengthening concrete structures (ACI 440.2R-02)*. 2002, American Concrete Institute. p. 45.
4. Norris, T., H. Saadatmanesh, and M.R. Ehsani, *Shear and flexural strengthening of R/C beams with carbon fiber sheets*. Journal of Structural Engineering, 1997. **123**(7): p. 903-911.
5. Quantrill, R.J. and L.C. Hollaway, *Flexural rehabilitation of reinforced concrete beams by the use of prestressed advanced composite plates*. Composites Science and Technology, 1998. **58**(8): p. 1259-1275.
6. Saadatmanesh, H. and M.R. Ehsani, *Fiber composite plates can strengthen concrete beams*. Concrete International ACI, 1990. **12**(3): p. 65-71.
7. Triantafillou, T.C. and N. Plevris, *Strengthening of RC beams with epoxy-bonded fiber-composite materials* Materials and structures, 1992. **25**: p. 201-211.
8. Mirmiran, A. and M. Shahawy, *Behavior of concrete columns confined by fibre composites*. Journal of Structural Engineering, 1997. **123**(5): p. 583-590.
9. Matthys, S. and L. Taerwe, *Concrete slabs reinforced with FRP grids. II: Punching resistance*. Journal of Composites for Construction, 2000. **4**(3): p. 154-161.
10. ISE, *Interim guidance on the design of reinforced concrete structures using fibre composite reinforcement*. 1999, Institution of Structural Engineers (ISE): London.
11. *Externally bonded FRP reinforcement for RC structures (CEB-FIB Bulletin No. 14)*. 2001: Switzerland. p. 138.
12. CSA, *Design and construction of building components with fibre reinforced polymers*. 2002, Canadian Standards Association International (CSA): Toronto.
13. JSCE, *Recommendations for upgrading of concrete structures with use of continuous fiber sheets*, in *Concrete Engineering No. 41*. 2001, Japan Society of Civil Engineers. p. 325.
14. CS, *Design guidance for strengthening concrete structures using fibre composite materials (Technical Report No. 55)*. 2002, Concrete Society: London. p. 102.
15. Binici, B. and O. Bayrak, *Use of fiber-reinforced polymers in slab-column connection upgrades*. ACI Structural Journal, 2005. **102**(1): p. 93-102.
16. Chen, C.C. and C.Y. Li, *Punching shear strength of reinforced concrete slabs strengthened with glass fiber-reinforced polymer laminates*. ACI Structural Journal, 2005. **102**(4): p. 535-542.

17. Moe, j., *Shearing strength of reinforced concrete slabs and footings under concentrated loads*, in *Development Department Bulletin No. D47*. 1961, Portland Cement Association: Skokie. p. 130.
18. Ebead, U. and H. Marzouk, *Fiber-reinforced polymer strengthening of two-way slabs*. ACI Structural Journal, 2004. **101**(5): p. 650-659.
19. Sharaf, M.H., K.A. Soudki, and M. Van Dusen, *CFRP strengthening for punching shear of interior slab-column connections*. Journal of Composites for Construction, 2006. **10**(5): p. 410-418.
20. *CEB-FIP model code 1990*. 1993.
21. *Eurocode 2; Design of concrete structures: BS EN 1992-1-1 and BS EN 1992-1-2*. 2004.
22. BSI, *Structural Use of Concrete: Part 1, code of practice for design and construction, BS 8110*. 1985: London.
23. *ACI 318: Building code requirements for structural concrete*. 2004.
24. *Punching shear failure of flat slab*, [www.sheffield.ac.uk/ci/research/concrete/sb.htmlPunching](http://www.sheffield.ac.uk/ci/research/concrete/sb.htmlPunching) 2003.
25. Criswell, M.E., *Static and dynamic response of reinforced concrete slab-column connections*. ACI Special Publication, 1974. **42**(2): p. 721-746.
26. Guandalini, S., O.L. Burdet, and A. Muttoni, *Punching tests of slabs with low reinforcement ratios*. ACI Structural Journal, 2009. **106**(1): p. 87-95.
27. Vanderbilt, M.D., *Shear strength of continuous slabs*. Proceedings of ASCE, 1972. **98**(ST5): p. 961-973.
28. Elstner, R.C. and E. Hognestad, *Shearing strength of reinforced concrete slabs*. ACI, Proceedings, 1956. **53**(7): p. 29-58.
29. Yitzhaki, D., *Punching strength of reinforced concrete slabs*. ACI, 1966. **63**(5): p. 527-561.
30. Kinnunen, S. and H. Nylander, *Punching of concrete slabs without shear reinforcement, Transactions, No. 158*. 1960, Royal Institute of Technology: Stockholm, Sweden.
31. Criswell, M.E. and N.W. Hawkins, *Shear strength of slabs: Basic principle and their relation to current methods of analysis*. ACI Special Publication, 1974. **42**(2): p. 641-676.
32. *CEB, RC elements under cyclic loading*. 1996.
33. Alexander, S.D.B. and S.H. Simmonds, *Tests of column-flat plate connections*. ACI Structural Journal, 1992. **89**(5): p. 495-502.
34. Hawkins, N.W. and W.G. Corley, *Moment transfer to columns in slabs with shearhead reinforcement*. ACI Special Publication, 1974. **42**: p. 847-880.
35. Pilakoutas, K. and X. Li, *Alternative shear reinforcement for reinforced concrete flat slabs*. Journal of Structural Engineering, 2003. **129**(9): p. 1164-1172.
36. Ghali, A., *An efficient solution to punching of slabs*. Concrete International ACI, 1989: p. 50-54.
37. Ghali, A. and N. Hammill, *Effectiveness of shear reinforcement in slabs*. Concrete International ACI, 1992: p. 60-65.
38. Ebead, U. and H. Marzouk, *Strengthening of two-way slabs using steel plates*. ACI Structural Journal, 2002. **99**(1): p. 23-31.
39. Ghali, A., M.A. Sargious, and A. Huizer, *Vertical prestressing of flat plates around columns*. Shear in Reinforced Concrete, ACI Special Publication, 1974. **42**: p. 905-920.

40. El-Salakawy, E.F., M.A. Polak, and K.A. Soudki, *New shear strengthening technique for concrete slab-column connections*. ACI Structural Journal, 2003. **100**(3): p. 297-304.
41. Taylor, R. and B. Hayes, *Some tests on the effect of edge restraint on punching shear in reinforced concrete slabs*. Magazine of Concrete Research, 1965. **17**(50): p. 39-44.
42. Kuang, J.S. and C.T. Morley, *Punching shear behaviour of restrained concrete slabs*. ACI Structural Journal, 1992. **89**(1): p. 13-19.
43. Rankin, G.I.B. and A.E. Long, *Predicting the enhanced punching strength of interior slab-column connection*. Proc. Inst. Civ. Engr, 1987. **82**: p. 1165-118.
44. Regan, P.E., *Symmetric punching of reinforced concrete slabs*. Magazine of Concrete Research, 1986. **38**(136): p. 115-128.
45. Hawkins, N.M., H.B. Fallsen, and R.C. Hinojosa, *Influence of column rectangularity on the behaviour of flat plate structures*. ACI Special Publication, 1971. **SP-30**: p. 127-146.
46. Bazant, Z.P. and Z. Cao, *Size effect in punching shear failure of slabs*. ACI Structural Journal (American Concrete Institute), 1987. **84**(1): p. 44-53.
47. John, S.L. and I.L. David, *Punching shear behavior of slabs With varying span-depth ratios*. ACI Structural Journal, 1990. **87**(5): p. 507-511.
48. Sissakis, K. and S.A. Sheikh, *Strengthening concrete slabs for punching shear with carbon fiber-reinforced polymer laminates*. ACI Structural Journal, 2007. **104**(1): p. 49-59.
49. Binici, B. and O. Bayrak, *Punching shear strengthening of reinforced concrete flat plates using carbon fiber reinforced polymers*. Journal of Structural Engineering, 2003. **129**(9): p. 1173-1182.
50. Brooms, C.E., *Punching of flat plates-A question of concrete properties in biaxial compression and size effect*. ACI Structural Journal, 1990. **87**(3): p. 292-304.
51. Erki, M.A. and P.J. Heffernan. *Reinforced concrete slabs externally strengthened with fibre-reinforced plastic materials*. in *2nd Symp. on Non-Metalic FRP Reinforcement for Concrete Structures (FRPRCS-2)*. 1995. Ghent, Belg.
52. Wight, R.G., M.F. Green, and M.A. Erki, *Prestressed FRP sheets for poststrengthening reinforced concrete beams*. Journal of Composites for Construction, 2001. **5**(4): p. 214-220.
53. Harajli, M.H. and K.A. Soudki, *Shear strengthening of Interior slab-column connections using carbon fiber-reinforced polymer sheets*. Journal of Composites for Construction, 2003. **7**(2): p. 145-153.
54. El-Salakawy, E., K. Soudki, and M.A. Polak, *Punching shear behavior of flat slabs strengthened with fiber reinforced polymer laminates*. Journal of Composites for Construction, 2004. **8**(5): p. 384-392.
55. Harajli, M.H., K.A. Soudki, and T. Kudsi, *Strengthening of interior slab-column connections using a combination of FRP sheets and steel bolts*. Journal of Composites for Construction, 2006. **10**(5): p. 399-409.
56. Triantafillou, T.C., N. Deskovic, and M. Deuring, *Strengthening of concrete structures with prestressed fiber reinforced plastic sheets*. ACI Structural Journal, 1992. **89**(3): p. 235-244.



57. Garden, H.N. and L.C. Hollaway, *Experimental study of the failure modes of reinforced concrete beams strengthened with prestressed carbon composite plates*. Composites Part B:Engineering, 1998. **29**(4): p. 411-424.
58. Wight, R.G. and M.A. Erki, *Prestressed CFRP sheets for strengthening concrete slabs in fatigue*. Advances in Structural Engineering 2003. **6**(3): p. 175-182.
59. Seim, W., et al., *External FRP poststrengthening of scaled concrete slabs*. Journal of Composites for Construction, 2001. **5**(2): p. 67-75.
60. Kim, Y.J., et al., *Flexure of two-way slabs strengthened with prestressed or nonprestressed CFRP sheets*. Journal of Composites for Construction, 2008. **12**(4): p. 366-374.
61. Menetrey, P., *Relationships between flexural and punching failure*. ACI Structural Journal, 1998. **95**(4): p. 412-419.
62. Bakis, C.E., et al., *Fibre reinforced polymer composites for construction - state of the art review*. Perspectives in Civil Engineering: Commemorating the 150th Anniversary of the American Society of Civil Engineers, 2002: p. 369-383.
63. Lu, X.Z., et al., *Bond-slip models for FRP sheets/plates bonded to concrete*. Engineering Structures, 2005. **27**(6): p. 920-937.
64. Yao, J., J.G. Teng, and J.F. Chen, *Experimental study on FRP-to-concrete bonded joints*. Composites Part B:Engineering, 2005. **36**(2): p. 99-113.
65. Muttoni, A., *Punching shear strength of reinforced concrete slabs without transverse reinforcement*. ACI Structural Journal, 2008. **105**(4): p. 440-450.
66. Menetrey, P., *Synthesis of punching failure in reinforced concrete*. Cement & Concrete Composites, 2002. **24**: p. 497-507.
67. Oh, H. and J. Sim, *Punching shear strength of strengthened deck panels with externally bonded plates*. Composites Part B: Engineering, 2004. **35**(4): p. 313-321.
68. Rochdi, E.H., et al., *Ultimate behaviour of CFRP strengthened RC flat slabs under a centrally applied load*. Composite Structures, 2006. **72**: p. 69-78.
69. Michel, L., et al., *Criteria for punching failure mode in RC slabs reinforced by externally bonded CFRP*. Composite Structures, 2007. **81**(3): p. 438-449.
70. *Cleaning and surface repair of building: BS 6270-3*. 1991.
71. *Testing concrete; Method for determination of compressive strength of concrete: BS1881-Part116*. 1983.
72. *ASTM (C496-96): Standard test method for splitting tensile strength of cylindrical concrete specimen*. 1996.
73. *Testing concrete; Method for determination of static modulus of elasticity in compression: BS1881-Part121*. 1983.
74. *ASTM (D 3039/D 3039M): Standard test method for tensile properties of polymer matrix composite materials*. 2002.
75. *ASTM (A370-97a): Standard test methods and definitions for mechanical testing of steel products*. 1997.
76. Menetrey, P., *Analytical computation of the punching strength of reinforced concrete*. ACI Structural Journal, 1996. **93**(5): p. 1-9.

77. Bazant, Z.P. and B.H. Oh, *Crack band theory for fracture of concrete*. *Materials et constructions*, 1983. **16**(93): p. 155-177.
78. *ABAQUS Theory Manual, User Manual and Example Manual, Version 6.8*, Providence, RI. 2009.
79. Phuvoravan, K. and E.D. Sotelino, *Nonlinear finite element for reinforced concrete slabs*. *Journal of Structural Engineering*, 2005. **131**(4): p. 643-649.
80. Kollár, L.P. and G.S. Springer, *Mechanics of composite structures*. 2003.
81. Rots, J.G. and J. Blaauwendraad, *Crack models for concrete: discrete or smeared? Fixed multi-directional or rotational?* *Heron*, 1989. **34**(1): p. 3-59.
82. Shi, Z., *Crack analysis in structural concrete theory and applications*. 2009.
83. Hillerborg, A., M. Modeer, and P.E. Peterson, *Analysis of crack formation and crack growth in concrete by means of fracture mechanics and finite elements*. *Cement Concrete Res* 1976. **6**(6): p. 773-82.
84. Shah, S.P., S.E. Swartz, and C. Ouyang, *Fracture mechanics of concrete: applications of fracture mechanics to concrete, rock, and other quasi-brittle materials*. 1996.
85. Cornelissen, H.A.W., D.A. Hordijk, and H.W. Reinhardt, *Experimental determination of crack softening characteristics of normal weight and lightweight concrete*. *Heron*, 1985. **31**(2): p. 45-56.
86. Sousa, J.L.A.d.O.e. and R. Gettu, *Determining the tensile stress-crack opening curve of concrete by inverse analysis*. *Journal of Engineering Mechanics*, 2006. **132**(2): p. 141-148.
87. Bazant, Z.P. and P. Gambarova, *Rough cracks in reinforced concrete*. *Journal of the Structural Division*, 1980. **106**(4): p. 819-842.
88. Barzegar, F. and W.C. Schnobrich, *Post-cracking analysis of reinforced concrete panels including tension stiffening*. *Canadian Journal of Civil Engineering*, 1990. **17**(3): p. 311-320.
89. Chen, W.-F., *Plasticity in reinforced concrete*. 2007.
90. Scanlon, A. and D.W. Murray, *Time-dependent reinforced concrete slab deflection*. *Journal of Structural Division*, 1974. **100**: p. 1911-1924.
91. Gilbert, R.I., *Tension stiffening in lightly reinforced concrete slabs*. *Journal of Structural Engineering*, 2007. **133**(6): p. 899-903.
92. *CSA standard A 23.3-04: Design of concrete structures*. 3rd ed. 2006, Ottawa: Cement Association of Canada.
93. Pan, J. and C.K.Y. Leung, *Debonding along the FRP-concrete interface under combined pulling/peeling effects*. *Engineering Fracture Mechanics*, 2007. **74**(1-2): p. 132-150.
94. Niu, H. and Z. Wu, *Numerical analysis of debonding mechanisms in FRP-strengthened RC beams*. *Computer-Aided Civil and Infrastructure Engineering*, 2005. **20**: p. 354-368.
95. Niu, H., V.M. Karbhari, and Z. Wu, *Diagonal macro-crack induced debonding mechanisms in FRP rehabilitated concrete composites Part B: Engineering*, 2006. **37**: p. 627-641.
96. Lu, X.Z., et al., *Intermediate crack debonding in FRP-strengthened RC beams: FE analysis and strength model*. *Journal of Composites for Construction*, 2007. **11**(2): p. 161-174.

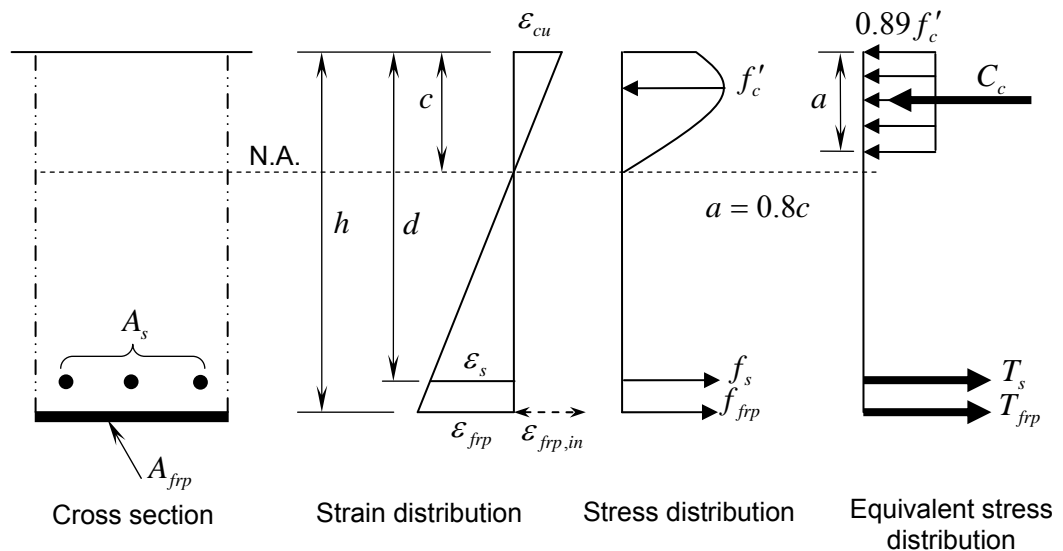
## Appendix A

### Sectional analysis of test slabs

The shear strength corresponding to the ultimate flexural capacity is calculated under the following assumptions:

- (1) Failure is due to concrete crushing at ultimate strain of 0.0035 and the tensile strength of the concrete may be neglected;
- (2) Plane sections before bending remain plane after bending (Bernoulli's principle);
- (3) Perfect bond is assumed between the concrete and both the steel and FRP reinforcement;
- (4) The stress-strain curves of the constitutive material (Concrete, Steel and FRP) are known.
- (5) The area of the FRP is smeared over a breadth equal to the column size plus  $3d$  each side, which is the area where the reinforcement ratio should be calculated according to Eurocode 2.

The neutral axis is obtained iteratively from strain compatibility and the equilibrium of the internal forces until the fulfilment of the following equation;  $C_c = T_s + T_{frp}$ . The ultimate flexural capacity  $V_{flex}$  is then calculated using Equation (2-14) in combination with of Equations (2-16) through (2-18). The final results are summarised in Table (A-1).



$$C_c = 0.89 f'_c a b$$

$$T_s = A_s f_y \text{ if } \varepsilon_s \geq \varepsilon_y \text{ otherwise } T_s = A_s f_s$$

$$T_{frp} = A_{frp} f_{frp}$$

Figure A-1: Stress and strain distribution through the slab thickness.

Table A-1: Summary of sectional analysis

Slab	$c$ (mm)	$C_c$ (N/mm)	$\varepsilon_{frp}$	$T_{frp}$ (N/mm)	$M_r$ (N.mm/mm)	$V_{flex}$ (kN)	$\rho_{equi}$ percent
RS <sub>0</sub>	25	569.6	-----	-----	32178.94	299	-----
RS-F <sub>0</sub>	34.1	776.9	0.012	491.73	40485.17	376.1	1.136
RS-F <sub>15</sub>	36	820.2	0.013	533.3	41102.1	381.9	1.2
RS-F <sub>30</sub>	38.9	886.3	0.014	599.2	48406.4	449.7	1.3
RS-F <sub>30F</sub>	38.9	886.3	0.014	599.2	48406.4	449.7	1.3

## Punching shear strength according to EC2

The punching shear strength is calculated according to Equation (2-28). However, an equivalent reinforcement ratio and depth is used instead of  $\rho$  and  $d$ , respectively as follows:

(1) The equivalent depth is  $d_{equi} = \frac{M_r}{C_c} + \frac{a}{2}$ , but not less than  $0.8h$ ;

(2) The equivalent reinforcement ratio for all strengthened slabs is the equivalent reinforcement ratio of slab (RS-F<sub>0</sub>);  $\rho_{equi} = \frac{C_c}{bd_{equi}f_s}$ . That is the prestressing effect is already taken in a separate term.

## FRP material properties

Table A-2: Summary of material properties for FRP composites

Elastic Modulus (MPa)	Major Poisson's ratio	Shear modulus (MPa)	Tensile/shear strength (MPa)	Thickness of plate (mm)
$E_x = 165000$	$\nu_{xy} = 0.29^{(2)}$	$G_{xy} = 5127.5^{(3)}$	$X_t = 2970$	1.2
$E_y = 14050^{(1)}$	$\nu_{xz} = 0.29$	$G_{xz} = 5127.5$	$Y_t = 69^{(5)}$	
$E_z = 14050$	$\nu_{yz} = 0.6^{(5)}$	$G_{yz} = 4390.6^{(4)}$	$S = 87^{(5)}$	

$$(1) \frac{1}{E_y} = \frac{V_f}{E_{fx}} + \frac{V_m}{E_m}$$

$$(2) \nu_{xy} = V_f \nu_{fxy} + V_m \nu_m$$

$$(3) G_{xy} = \left( \frac{V_f}{G_{fxy}} + \frac{V_m}{G_m} \right)^{-1}$$

$$(4) G_{yz} = \frac{E_y}{2(1 + \nu_{yz})}$$

(5) Other properties of the constitutive materials such as  $\nu_{yz}$ ,  $E_{fxy}$ ,  $\nu_m$  and  $G_m$  are assumed according to typical material properties published in Kollár and Springer [80]. The volume fraction is provided by the manufacturer;  $V_f = 70\%$ .

## Interface material properties

1. The element stiffness is determined as;  $K = \frac{EA}{l}$ , where  $E$  is the modulus of elasticity,  $A$  is the characteristic area of the shell element and  $l$  is the thickness of the interface layer. Similar principals can be applied for the two shear directions.
2. The damage response is defined as a tabular function of the differences between the relative motions at ultimate failure and the relative motions at damage initiation;  $(u_c - u_0)$ .
3. The damage variable  $D$  is determined as shown in the Figure (A-2) as follows;

$$D = \frac{F_{eff} - F_c}{F_{eff}}.$$

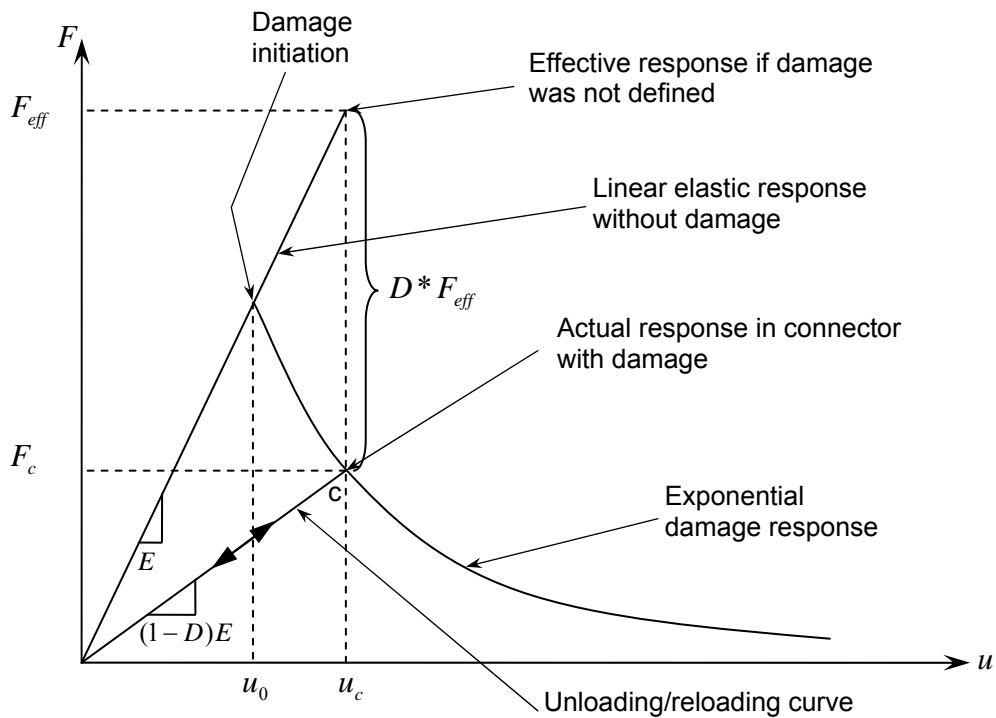


Figure A-2: Exponential damage evolution law for linear elastic connector behaviour.

## Format of the input file

```
*Heading
** Model name: RS-F-50mm-Con-plate
*Preprint, echo=YES, model=YES, history=YES, contact=YES
**

** PARTS
**

*Part, name=FRP-X
*Node
.
.
.
*Element, type=S4
.
.
.
*Elset, elset=FRP, generate
...., ...., ...
*Nset, nset=BC-1
...., ...., ...
*Elset, elset=Bond, generate
1, 6, 1
*Elset, elset=_Surf-Contact-X_SPOS, internal
...., ...., ...., ...., ...., ....
*Surface, type=ELEMENT, name=Surf-Contact-X
_Surf-Contact-X_SPOS, SPOS
*Orientation, name=Ori-1
1., 0., 0., 0., 1., 0.
3, 0.
** Section: FRP
*Shell Section, elset=FRP, material=FRP, orientation=Ori-1
1.2, 5
*End Part
**

*Part, name=FRP-Y
*Node
.
.
.
*Element, type=S4
.
.
.
*Elset, elset=FRP, generate
...., ...., ...
*Nset, nset=BC-2
...., ...., ...
*Elset, elset=Bond, generate
...., ...., ...
*Elset, elset=_Surf-Contact-Y_SPOS, internal
...., ...., ...., ...., ...., ....
*Surface, type=ELEMENT, name=Surf-Contact-Y
_Surf-Contact-Y_SPOS, SPOS
*Orientation, name=Ori-1
0., 1., 0., -1., 0., 0.
3, 0.
** Section: FRP
*Shell Section, elset=FRP, material=FRP, orientation=Ori-1
```

```
1.2, 5
*End Part
**
*Part, name=STEEL-X
*Node
.
.
.
*Element, type=T3D2
.
.
.
*Nset, nset=_PickedSet35, internal, generate
..., ..., ...
*Elset, elset=_PickedSet35, internal, generate
..., ..., ...
*Nset, nset=_PickedSet37, internal, generate
..., ..., ...
*Elset, elset=_PickedSet37, internal, generate
..., ..., ...
*Nset, nset=EMBEDED-X, generate
..., ..., ...
*Elset, elset=EMBEDED-X, generate
..., ..., ...
** Section: STEEL
*Solid Section, elset=_PickedSet37, material=STEEL
113.,
*End Part
**
*Part, name=STEEL-Y
*Node
.
.
.
*Element, type=T3D2
.
.
.
*Nset, nset=_PickedSet32, internal, generate
..., ..., ...
*Elset, elset=_PickedSet32, internal, generate
..., ..., ...
*Nset, nset=_PickedSet34, internal, generate
..., ..., ...
*Elset, elset=_PickedSet34, internal, generate
..., ..., ...
*Nset, nset=EMBEDED-Y, generate
..., ..., ...
*Elset, elset=EMBEDED-Y, generate
..., ..., ...
** Section: STEEL
*Solid Section, elset=_PickedSet34, material=STEEL
113.,
*End Part
**
*Part, name=Slab
*Node
.
.
.
```

```
*Element, type=C3D8
.
.
.
*Nset, nset=Constraint
...., ...., ...., ...., ...., ....
*Nset, nset=DEF
...., ...., ....
*Elset, elset=HOST
...., ...., ....
*Elset, elset=Slab, generate
...., ...., ....
*Nset, nset=Load
...., ...., ....
*Nset, nset=BC-2
...., ...., ....
*Nset, nset=BC-1
...., ...., ....
*Elset, elset=Bolt-house
...., ...., ....
*Elset, elset=Steel
...., ...., ....
*Elset, elset=_Surf-Friction_S1, internal
...., ...., ....
*Surface, type=ELEMENT, name=Surf-Friction
_Surf-Friction_S1, S1
*Elset, elset=_Surf-Pressure1_S1, internal
...., ...., ....
*Surface, type=ELEMENT, name=Surf-Pressure1
_Surf-Pressure1_S1, S1
*Elset, elset=_Surf-Bond-X_S1, internal
...., ...., ....
*Surface, type=ELEMENT, name=Surf-Bond-X
_Surf-Bond-X_S1, S1
*Elset, elset=_Surf-Bond-Y_S1, internal, generate
...., ...., ...., ...., ....
*Surface, type=ELEMENT, name=Surf-Bond-Y
_Surf-Bond-Y_S1, S1
*Elset, elset=_Surf-Contact-X_S1, internal
...., ...., ....
*Surface, type=ELEMENT, name=Surf-Contact-X
_Surf-Contact-X_S1, S1
*Elset, elset=_Surf-Contact-Y_S1, internal
...., ...., ....
*Surface, type=ELEMENT, name=Surf-Contact-Y
_Surf-Contact-Y_S1, S1
** Section: CONCRETE
*Solid Section, elset=Slab, material=CONCRETE
1.,
** Section: Steel-plate
*Solid Section, elset=Steel, material=STEEL

*End Part
**
*Part, name=Steel-plates
*Node
.
.
.
*Element, type=C3D8
```



```
.
.
.
*Nset, nset=_PickedSet5, internal, generate
..., ..., ...
*Elset, elset=_PickedSet5, internal, generate
..., ..., ...
*Elset, elset=Steel-plates, generate
..., ..., ...
** Section: Steel-plate
*Solid Section, elset=_PickedSet5, material=STEEL

*End Part
**

*Part, name=Support
*Node

.
.
.
*Element, type=R3D4
.
.
.
*Node
..., ..., ..., ...
*Nset, nset=Support-RefPt_, internal
..., ..., ...
*Nset, nset=Set-1, generate
..., ..., ...
*Elset, elset=Set-1, generate
..., ..., ...
*Nset, nset=Reaction
..., ..., ...
*Elset, elset=_Surf-Support_SNEG, internal
..., ..., ...
*Surface, type=ELEMENT, name=Surf-Support
_Surf-Support_SNEG, SNEG
*End Part
**
**

** ASSEMBLY
**

*Assembly, name=Assembly
**

*Instance, name=STEEL-X-1, part=STEEL-X
    0.,    0.,    32.
*End Instance
**

*Instance, name=STEEL-Y-1, part=STEEL-Y
    0.,    0.,    32.
*End Instance
**

*Instance, name=Support-1, part=Support
*End Instance
**

*Instance, name=Slab-1, part=Slab
*End Instance
**

*Instance, name=FRP-X-1, part=FRP-X
    0.,    0.,    -1.
```

```
*End Instance
**
*Instance, name=FRP-Y-1, part=FRP-Y
    0.,    0.,    -2.
*End Instance
**
*Instance, name=Steel-plates-1, part=Steel-plates
    0.,    0.,    -2.
*End Instance
**
*Element, type=CONN3D2
1, FRP-X-1.38, Slab-1.1436
.
.
*Connector Section, elset=Wire-1-Set-1, behavior=ConnSect-1, controls=viscosity
Cartesian,
FRP-X-1-Local,
*Nset, nset=_PickedSet100, internal, instance=Support-1
..., ..., ...
*Nset, nset=Wire-1-Set-1, instance=Slab-1
..., ..., ...
*Nset, nset=Wire-1-Set-1, instance=FRP-X-1
..., ..., ...
*Elset, elset=Wire-1-Set-1, generate
..., ..., ...
*Orientation, name=FRP-X-1-Local
    1.,    0.,    0.,    0.,    1.,    0.
1, 0.
** Constraint: Con-plate
*Embedded Element, host elset=Slab-1.Bolt-house, absolute exterior tolerance=5.
Steel-plates-1.Steel-plates
** Constraint: FRP Strengthening-X
*Embedded Element, host elset=Slab-1.Bolt-house, absolute exterior tolerance=5.
FRP-X-1.Bond
** Constraint: FRP Strengthening-Y
*Embedded Element, host elset=Slab-1.Bolt-house, absolute exterior tolerance=5.
FRP-Y-1.Bond
** Constraint: REINFORCEMENT-X
*Embedded Element, host elset=Slab-1.HOST, absolute exterior tolerance=0.05
STEEL-X-1.EMBEDED-X
** Constraint: REINFORCEMENT-Y
*Embedded Element, host elset=Slab-1.HOST, absolute exterior tolerance=0.05
STEEL-Y-1.EMBEDED-Y
** Constraint: Support
*Rigid Body, ref node=_PickedSet100, elset=Support-1.Set-1
*End Assembly
*Connector Behavior, name=ConnSect-1
*Connector Elasticity, component=1
212019.,
*Connector Elasticity, component=2
212019.,
*Connector Elasticity, component=3
2.75625e+06,
*Connector Damage Initiation, component=1
-6641.67, 6641.67
*Connector Damage Evolution, type=Motion,softening=Tabular,affected components
1, 2
    0.,    0.
    ..., ...
*Connector Damage Initiation, component=2
```

```
....  
*Connector Damage Evolution, type=Motion,softening=Tabular,affected components  
1, 2  
0., 0.  
....  
*Connector Damage Initiation, component=3  
....  
*Connector Damage Evolution, type=Energy,affected components  
3  
GII,  
*Section control, name=viscosity, viscosity=0.1d-3, max degradation=0.99  
**  
** MATERIALS  
**  
*Material, name=CONCRETE  
*Density  
2.4e-06,  
*Elastic  
31165., 0.18  
*Concrete Damaged Plasticity  
20., 0.1, 1.16, 0.667, 0.  
*Concrete Compression Hardening  
16.2546, 0.  
17.7465, 7.5997e-06  
21.1373, 3.19128e-05  
24.258, 6.48731e-05  
27.1059, 0.000106572  
29.6781, 0.000157101  
31.9715, 0.000216553  
33.9834, 0.000285025  
35.7106, 0.000362611  
37.1502, 0.00044941  
38.299, 0.000545519  
39.1541, 0.000651038  
39.7121, 0.00076607  
39.9699, 0.000890717  
39.9886, 0.00093442  
39.8526, 0.00106649  
39.4324, 0.00120767  
38.7251, 0.00135804  
37.7277, 0.0015177  
36.437, 0.00168676  
34.85, 0.00186531  
32.9636, 0.00205345  
30.7746, 0.00225128  
28.2797, 0.00245891  
25.4756, 0.00267645  
*Concrete Tension Stiffening, type=DISPLACEMENT  
0.8ft, 0.  
ft, w1  
0.15ft, w2  
0.6ft, w3  
0.01ft, w0  
*Material, name=FRP  
*Elastic, type=LAMINA  
165000., 14050., 0.29, 5127.5, 5127.5, 4390.6  
*Fail Stress  
2970.,-2525., 69., -200., 87., 0., 0.  
*Material, name=STEEL  
*Elastic
```

```
190000., 0.3
*Plastic
570., 0.
650., 0.18
7., 0.2
**
** INTERACTION PROPERTIES
**
*Surface Interaction, name=IntProp-1
1.,
*Friction
0.,
**
** PREDEFINED FIELDS
**
** Name: Prestressing  Type: STRESS
*Initial Conditions, type=STRESS, SECTION POINTS
FRP-X-1.FRP, 1, f, 0., 0.
FRP-X-1.FRP, 2, f, 0., 0.
FRP-X-1.FRP, 3, f, 0., 0.
FRP-X-1.FRP, 4, f, 0., 0.
FRP-X-1.FRP, 5, f, 0., 0.
FRP-Y-1.FRP, 1, f, 0., 0.
FRP-Y-1.FRP, 2, f, 0., 0.
FRP-Y-1.FRP, 3, f, 0., 0.
FRP-Y-1.FRP, 4, f, 0., 0.
FRP-Y-1.FRP, 5, f, 0., 0.
**
** INTERACTIONS
**
** Interaction: Int-1
*Contact Pair, interaction=IntProp-1, small sliding
Slab-1.Surf-Friction, Support-1.Surf-Support
** Interaction: Int-X
*Contact Pair, interaction=IntProp-1, small sliding
FRP-X-1.Surf-Contact-X, Slab-1.Surf-Contact-X
** Interaction: Int-Y
*Contact Pair, interaction=IntProp-1, small sliding
FRP-Y-1.Surf-Contact-Y, Slab-1.Surf-Contact-Y
** -----
**
** STEP: Establish contact
**
*Step, name="Establish contact", nlgeom=YES
*Static
0.1, 1., 1e-17, 1.
**
** BOUNDARY CONDITIONS
**
** Name: BC-1 Type: Symmetry/Antisymmetry/Encastre
*Boundary
Slab-1.BC-1, XSYMM
** Name: BC-2 Type: Symmetry/Antisymmetry/Encastre
*Boundary
Slab-1.BC-2, YSYMM
** Name: BC-3 Type: Displacement/Rotation
*Boundary
Support-1.Reaction, 1, 1
Support-1.Reaction, 2, 2
Support-1.Reaction, 3, 3
```

Support-1.Reaction, 4, 4  
Support-1.Reaction, 5, 5  
Support-1.Reaction, 6, 6  
\*\* Name: BC-6-1 Type: Symmetry/Antisymmetry/Encastre  
\*Boundary  
FRP-X-1.BC-1, XSYMM  
\*\* Name: BC-7-2 Type: Symmetry/Antisymmetry/Encastre  
\*Boundary  
FRP-Y-1.BC-2, YSYMM  
\*\* Name: Slab-cons Type: Displacement/Rotation  
\*Boundary  
Slab-1.Constraint, 3, 3  
\*\*  
\*\* LOADS  
\*\*  
\*\* Name: Pressure1 Type: Pressure  
\*Dsload  
Slab-1.Surf-Pressure1, P, -0.001  
\*\*  
\*\* INTERACTIONS  
\*\*  
\*\* Interaction: Int-X  
\*Model Change, type=CONTACT PAIR, remove  
FRP-X-1.Surf-Contact-X, Slab-1.Surf-Contact-X  
\*\* Interaction: Int-Y  
\*Model Change, type=CONTACT PAIR, remove  
FRP-Y-1.Surf-Contact-Y, Slab-1.Surf-Contact-Y  
\*\*  
\*\* OUTPUT REQUESTS  
\*\*  
\*Restart, write, frequency=0  
\*\*  
\*\* FIELD OUTPUT: General  
\*\*  
\*Output, field  
\*Node Output  
RF, U  
\*Element Output, directions=YES  
LE, PE, PEEQ, PEMAG, S  
\*Contact Output  
CDISP, CSTRESS  
\*\*  
\*\* FIELD OUTPUT: FRP-X  
\*\*  
\*Element Output, elset=FRP-X-1.FRP, directions=YES  
CFAILURE, E, EE  
\*\*  
\*\* FIELD OUTPUT: FRP-Y  
\*\*  
\*Element Output, elset=FRP-Y-1.FRP, directions=YES  
CFAILURE, E, EE  
\*\*  
\*\* FIELD OUTPUT: Slab  
\*\*  
\*Element Output, elset=Slab-1.Slab, directions=YES  
E, IE, PEEQT  
\*\*  
\*\* HISTORY OUTPUT: H-Output-1  
\*\*  
\*Output, history

```
*Energy Output
ALLCD, ALLSD, ALLSE
**
** HISTORY OUTPUT: H-Output-2
**
*Element Output, elset=Wire-1-Set-1
CCU1, CCU2, CCU3, CDIF1, CDIF2, CDIF3, CTF1, CTF2, CTF3
**
** HISTORY OUTPUT: H-Output-3
**
*Element Output, elset=Wire-2-Set-1
CCU1, CCU2, CCU3, CDIF1, CDIF2, CDIF3, CTF1, CTF2, CTF3
**
** HISTORY OUTPUT: H-Output-4
**
*Element Output, elset=Wire-3-Set-1
CCU1, CCU2, CCU3, CDIF1, CDIF2, CDIF3, CTF1, CTF2, CTF3
**
** HISTORY OUTPUT: H-Output-5
**
*Element Output, elset=Wire-4-Set-1
CCU1, CCU2, CCU3, CDIF1, CDIF2, CDIF3, CTF1, CTF2, CTF3
**
** HISTORY OUTPUT: H-Output-6
**
*Element Output, elset=Wire-5-Set-1
CCU1, CCU2, CCU3, CDIF1, CDIF2, CDIF3, CTF1, CTF2, CTF3
**
** HISTORY OUTPUT: H-Output-7
**
*Element Output, elset=Wire-6-Set-1
CCU1, CCU2, CCU3, CDIF1, CDIF2, CDIF3, CTF1, CTF2, CTF3
*End Step
** -----
**
** STEP: Slab releasee
**
*Step, name="Slab releasee", nlgeom=YES
*Static
1., 1., 1e-05, 1.
**
** BOUNDARY CONDITIONS
**
** Name: BC-1 Type: Symmetry/Antisymmetry/Encastre
*Boundary, op=NEW
Slab-1.BC-1, XSYMM
** Name: BC-2 Type: Symmetry/Antisymmetry/Encastre
*Boundary, op=NEW
Slab-1.BC-2, YSYMM
** Name: BC-3 Type: Displacement/Rotation
*Boundary, op=NEW
Support-1.Reaction, 1, 1
Support-1.Reaction, 2, 2
Support-1.Reaction, 3, 3
Support-1.Reaction, 4, 4
Support-1.Reaction, 5, 5
Support-1.Reaction, 6, 6
** Name: BC-6-1 Type: Symmetry/Antisymmetry/Encastre
*Boundary, op=NEW
FRP-X-1.BC-1, XSYMM
```

```
** Name: BC-7-2 Type: Symmetry/Antisymmetry/Encastre
*Boundary, op=NEW
FRP-Y-1.BC-2, YSYMM
** Name: Slab-cons Type: Displacement/Rotation
*Boundary, op=NEW
**
** OUTPUT REQUESTS
**
*Restart, write, frequency=0
**
** FIELD OUTPUT: General
**
*Output, field
*Node Output
RF, U
*Element Output, directions=YES
LE, PE, PEEQ, PEMAG, S
*Contact Output
CDISP, CSTRESS
**
** FIELD OUTPUT: FRP-X
**
*Element Output, elset=FRP-X-1.FRP, directions=YES
CFAILURE, E, EE
**
** FIELD OUTPUT: FRP-Y
**
*Element Output, elset=FRP-Y-1.FRP, directions=YES
CFAILURE, E, EE
**
** FIELD OUTPUT: Slab
**
*Element Output, elset=Slab-1.Slab, directions=YES
E, IE, PEEQT
**
** HISTORY OUTPUT: H-Output-1
**
*Output, history
*Energy Output
ALLCD, ALLSD, ALLSE
**
** HISTORY OUTPUT: H-Output-2
**
*Element Output, elset=Wire-1-Set-1
CCU1, CCU2, CCU3, CDIF1, CDIF2, CDIF3, CTF1, CTF2, CTF3
**
** HISTORY OUTPUT: H-Output-3
**
*Element Output, elset=Wire-2-Set-1
CCU1, CCU2, CCU3, CDIF1, CDIF2, CDIF3, CTF1, CTF2, CTF3
**
** HISTORY OUTPUT: H-Output-4
**
*Element Output, elset=Wire-3-Set-1
CCU1, CCU2, CCU3, CDIF1, CDIF2, CDIF3, CTF1, CTF2, CTF3
**
** HISTORY OUTPUT: H-Output-5
**
*Element Output, elset=Wire-4-Set-1
CCU1, CCU2, CCU3, CDIF1, CDIF2, CDIF3, CTF1, CTF2, CTF3
```

```
**
** HISTORY OUTPUT: H-Output-6
**
*Element Output, elset=Wire-5-Set-1
CCU1, CCU2, CCU3, CDIF1, CDIF2, CDIF3, CTF1, CTF2, CTF3
**
** HISTORY OUTPUT: H-Output-7
**
*Element Output, elset=Wire-6-Set-1
CCU1, CCU2, CCU3, CDIF1, CDIF2, CDIF3, CTF1, CTF2, CTF3
*End Step
** -----
**
** STEP: Loading
**
*Step, name=Loading, nlgeom=YES, inc=10000
*Static, stabilize=0.0002, allsdtol=0.05, continue=NO
0.0005, 1., 1e-17, 0.005
**
** BOUNDARY CONDITIONS
**
** Name: Load Type: Displacement/Rotation
*Boundary
Slab-1.Load, 3, 3,  $\delta$  .
**
** LOADS
**
** Name: Pressure1 Type: Pressure
*Dload, op=NEW
**
** INTERACTIONS
**
** Interaction: Int-X
*Model Change, type=CONTACT PAIR, add
FRP-X-1.Surf-Contact-X, Slab-1.Surf-Contact-X
** Interaction: Int-Y
*Model Change, type=CONTACT PAIR, add
FRP-Y-1.Surf-Contact-Y, Slab-1.Surf-Contact-Y
**
** OUTPUT REQUESTS
**
*Restart, write, frequency=0
**
** FIELD OUTPUT: General
**
*Output, field, frequency=10
*Node Output
RF, U, VF
*Element Output, directions=YES
LE, PE, PEEQ, PEMAG, S
*Contact Output
CDISP, CSTRESS
**
** FIELD OUTPUT: FRP-X
**
*Element Output, elset=FRP-X-1.FRP, directions=YES
CFailure, E, EE
**
** FIELD OUTPUT: FRP-Y
**
```



```
*Element Output, elset=FRP-Y-1.FRP, directions=YES
CFAILURE, E, EE
**
** FIELD OUTPUT: Slab
**
*Element Output, elset=Slab-1.Slab, directions=YES
E, IE, PEEQT
**
** HISTORY OUTPUT: H-Output-1
**
*Output, history
*Energy Output
ALLCD, ALLIE, ALLSD, ALLSE
**
** HISTORY OUTPUT: H-Output-2
**
*Output, history, frequency=10
*Element Output, elset=Wire-1-Set-1
CCU1, CCU2, CCU3, CDIF1, CDIF2, CDIF3, CTF1, CTF2, CTF3
**
** HISTORY OUTPUT: H-Output-3
**
*Element Output, elset=Wire-2-Set-1
CCU1, CCU2, CCU3, CDIF1, CDIF2, CDIF3, CTF1, CTF2, CTF3
**
** HISTORY OUTPUT: H-Output-4
**
*Element Output, elset=Wire-3-Set-1
CCU1, CCU2, CCU3, CDIF1, CDIF2, CDIF3, CTF1, CTF2, CTF3
**
** HISTORY OUTPUT: H-Output-5
**
*Element Output, elset=Wire-4-Set-1
CCU1, CCU2, CCU3, CDIF1, CDIF2, CDIF3, CTF1, CTF2, CTF3
**
** HISTORY OUTPUT: H-Output-6
**
*Element Output, elset=Wire-5-Set-1
CCU1, CCU2, CCU3, CDIF1, CDIF2, CDIF3, CTF1, CTF2, CTF3
**
** HISTORY OUTPUT: H-Output-7
**
*Element Output, elset=Wire-6-Set-1
CCU1, CCU2, CCU3, CDIF1, CDIF2, CDIF3, CTF1, CTF2, CTF3
*End Step
```

## Appendix B

### Numerical results of slab (RS<sub>0</sub>)

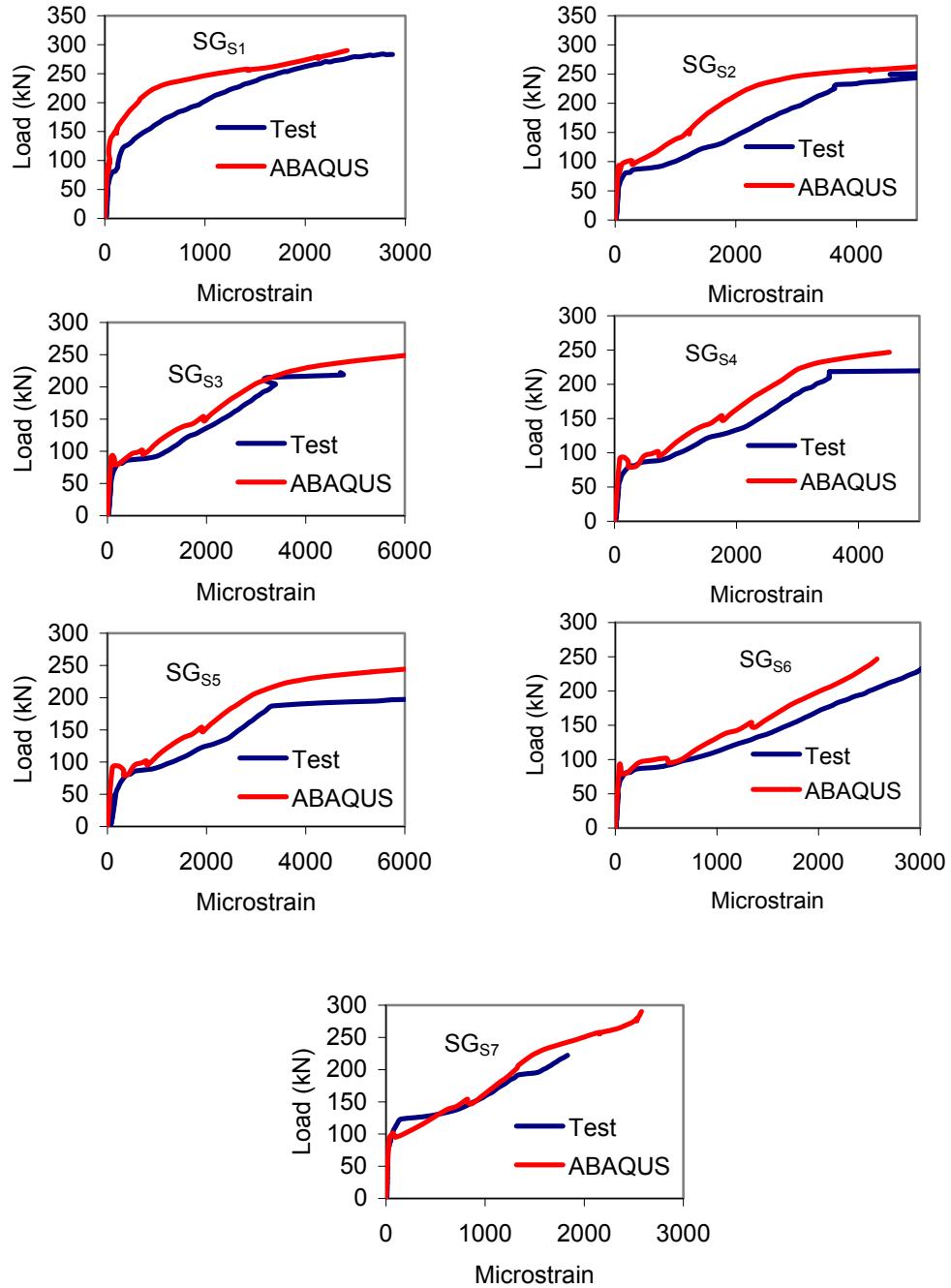


Figure B-1: Predicted strains compared to measured strains of slab (RS<sub>0</sub>).

## Numerical results of slab (RS-F<sub>0</sub>)

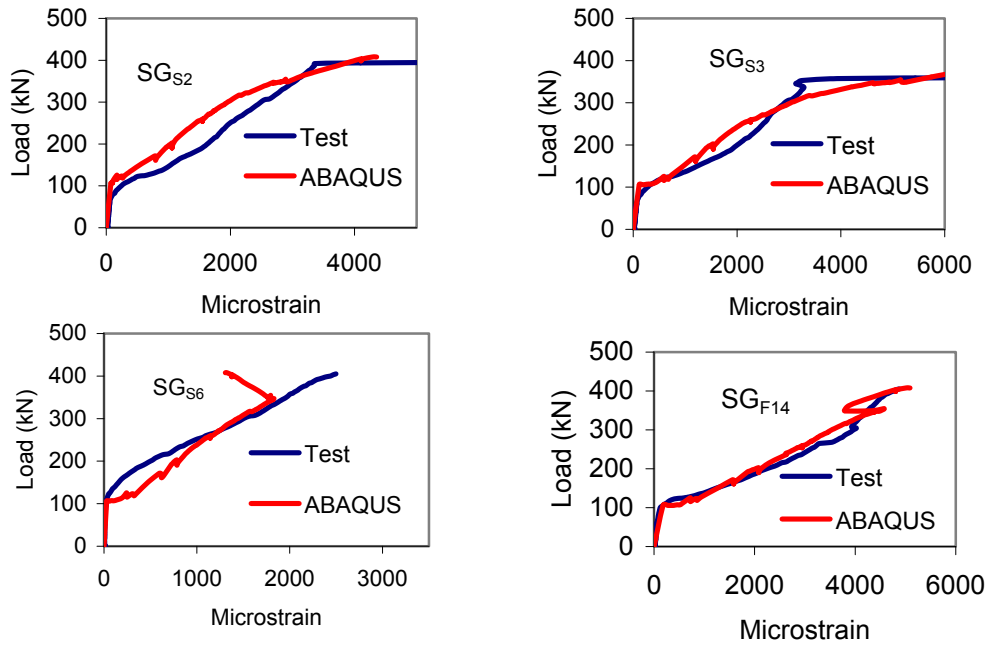


Figure B-2: Predicted strains compared to measured strains of slab (RS-F<sub>0</sub>).

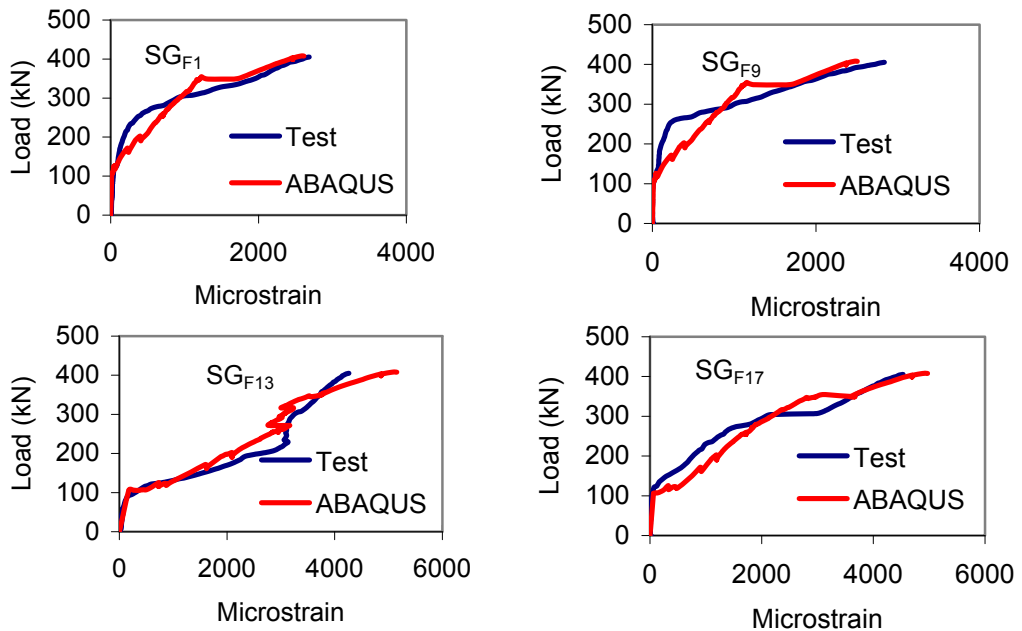


Figure B-2: Predicted strains compared to measured strains of slab (RS-F<sub>0</sub>).

## Numerical results of slab (RS-F<sub>15</sub>)

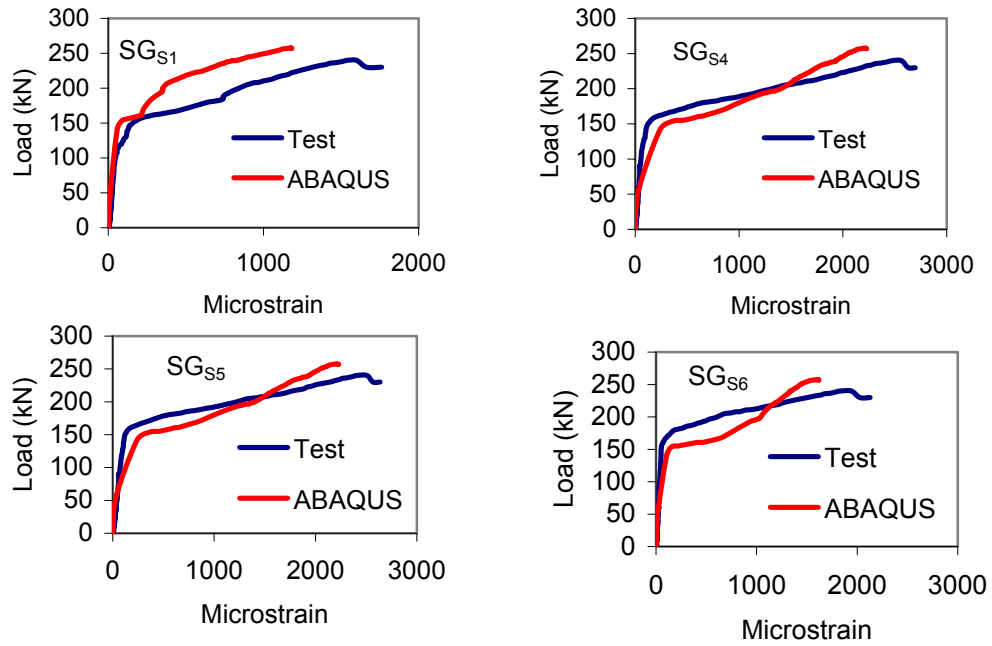


Figure B-3: Predicted strains compared to measured strains of slab (RS-F<sub>15</sub>).

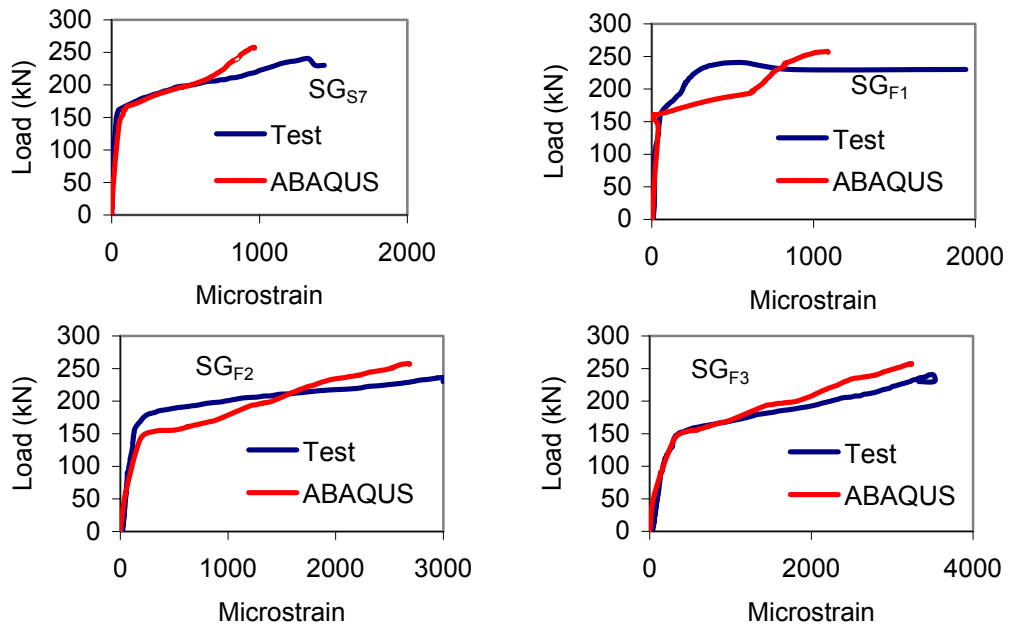


Figure B-3: Predicted strains compared to measured strains of slab (RS-F<sub>15</sub>).

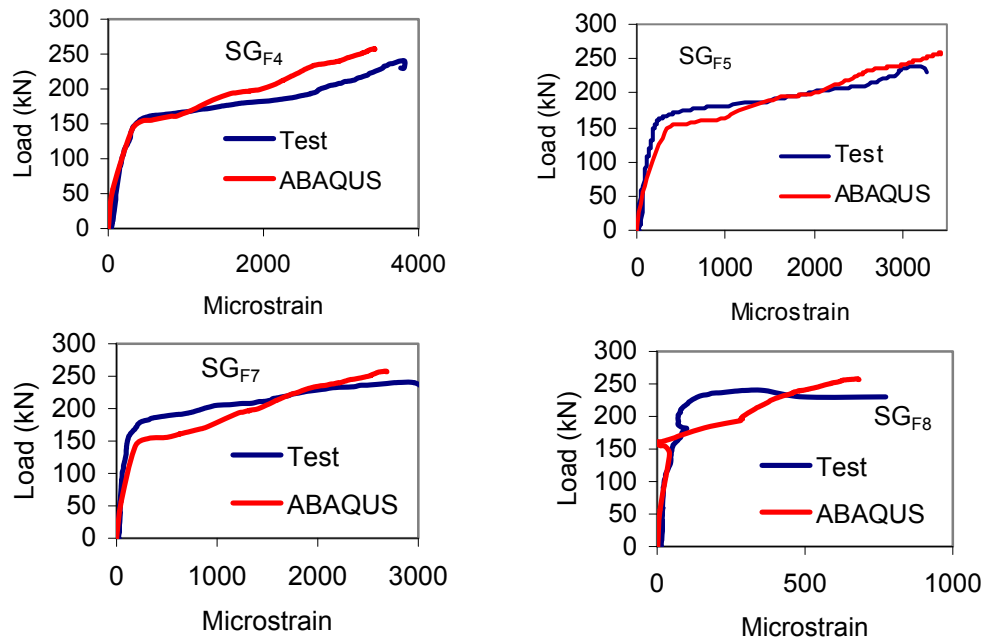


Figure B-3: Predicted strains compared to measured strains of slab (RS-F<sub>15</sub>).

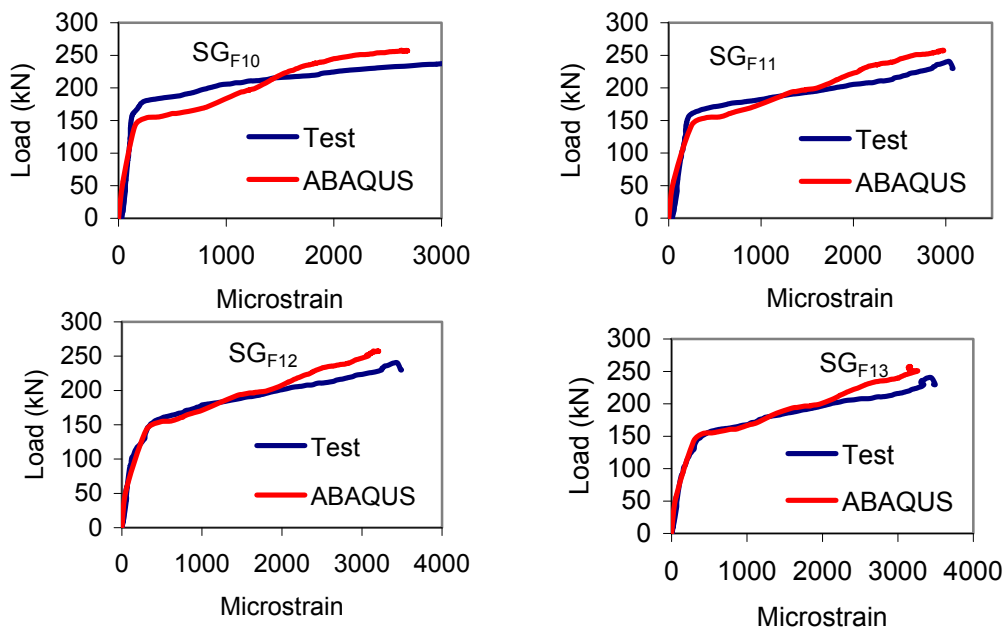


Figure B-3: Predicted strains compared to measured strains of slab (RS-F<sub>15</sub>).

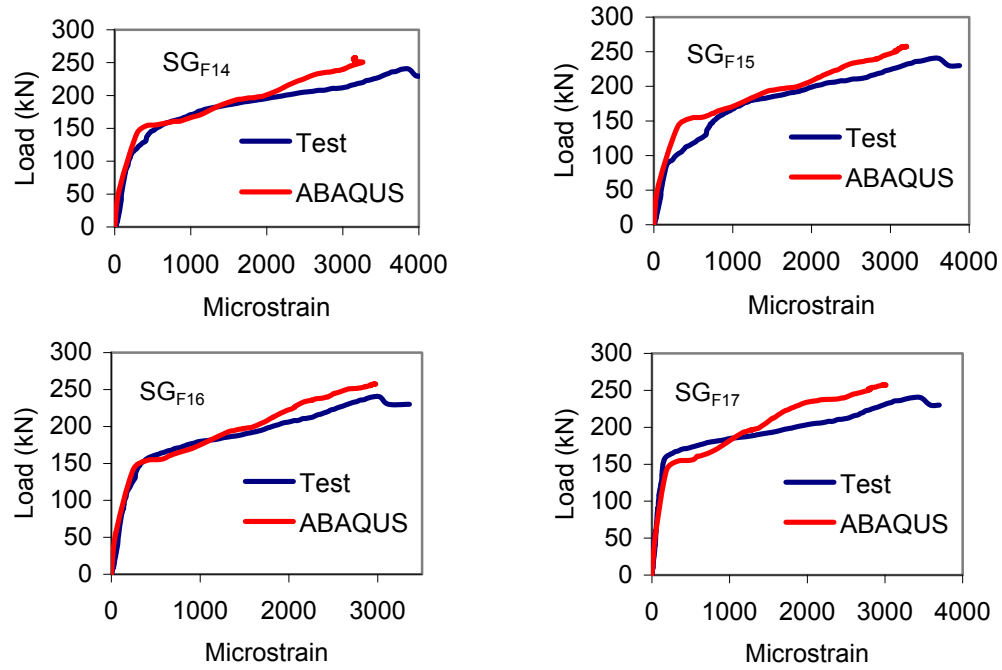


Figure B-3: Predicted strains compared to measured strains of slab (RS-F<sub>15</sub>).

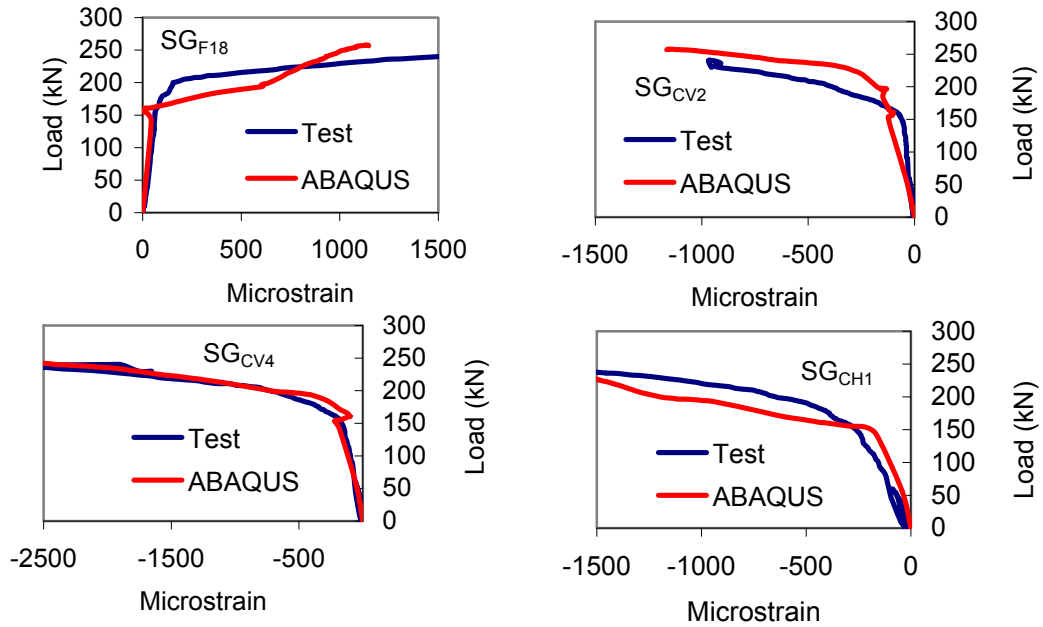


Figure B-3: Predicted strains compared to measured strains of slab (RS-F<sub>15</sub>).

## Numerical results of slab (RS-F<sub>30</sub>)

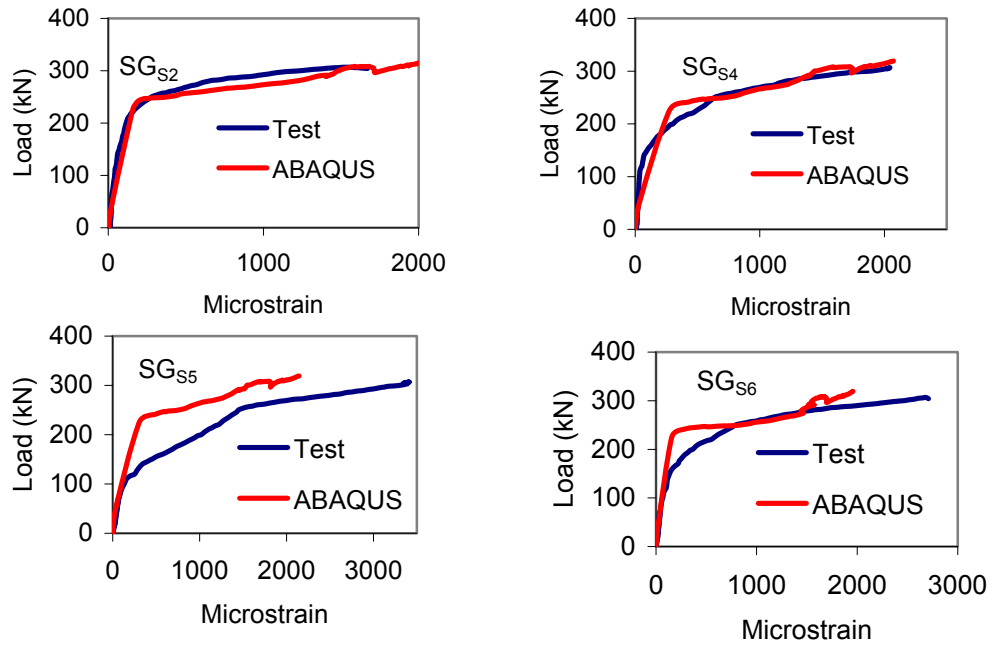


Figure B-4: Predicted strains compared to measured strains of slab (RS-F<sub>30</sub>).

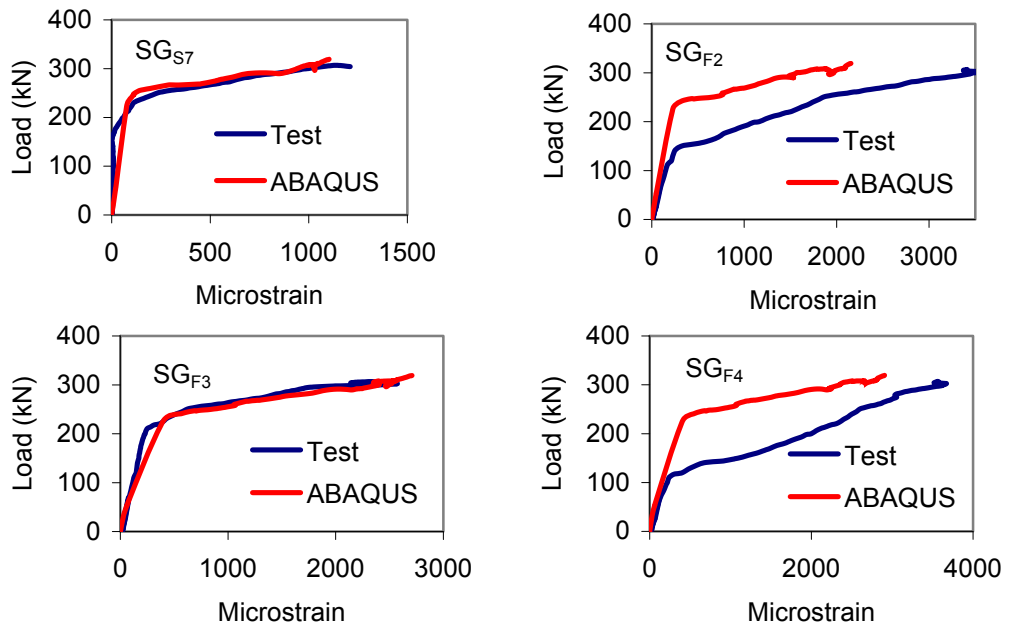


Figure B-4: Predicted strains compared to measured strains of slab (RS-F<sub>30</sub>).

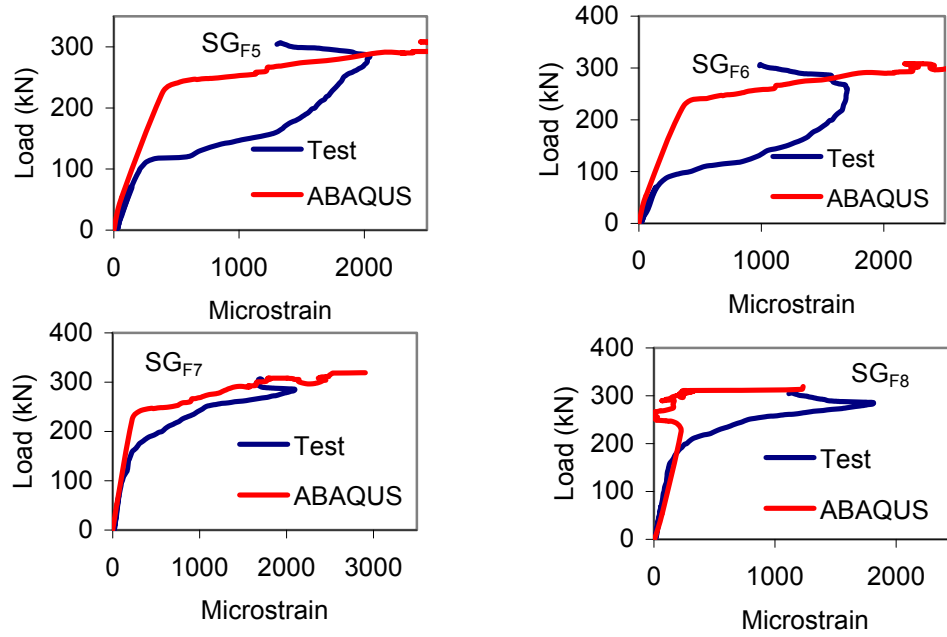


Figure B-4: Predicted strains compared to measured strains of slab (RS-F<sub>30</sub>).

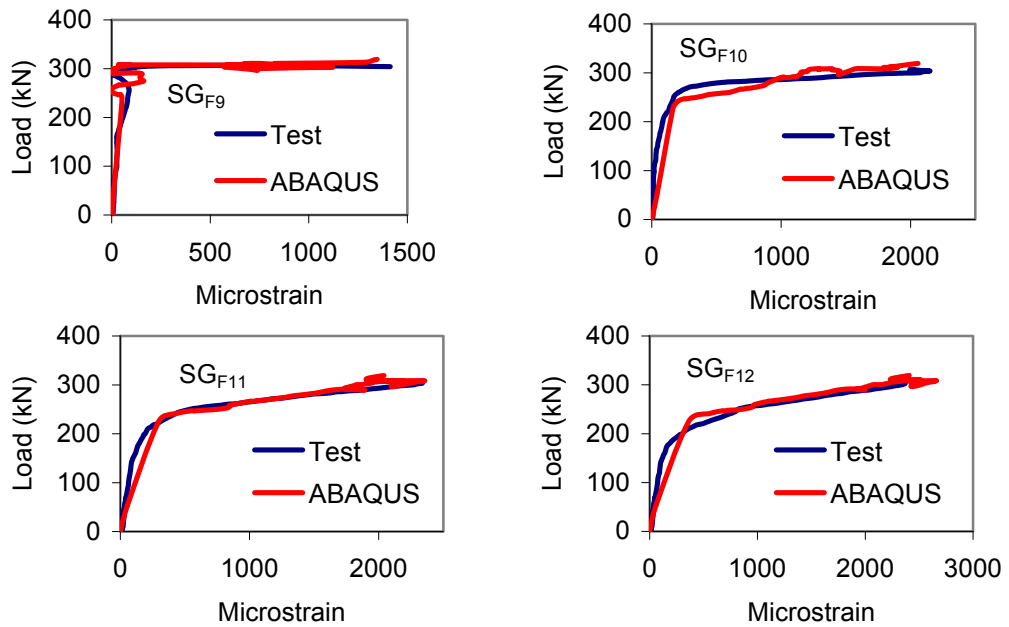


Figure B-4: Predicted strains compared to measured strains of slab (RS-F<sub>30</sub>).



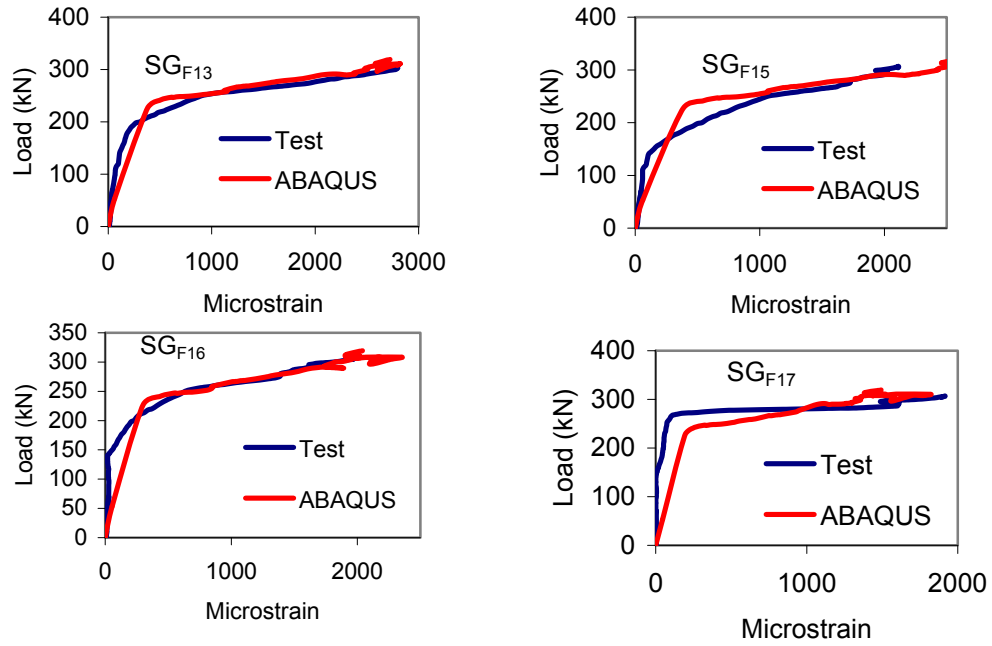


Figure B-4: Predicted strains compared to measured strains of slab (RS-F<sub>30</sub>).

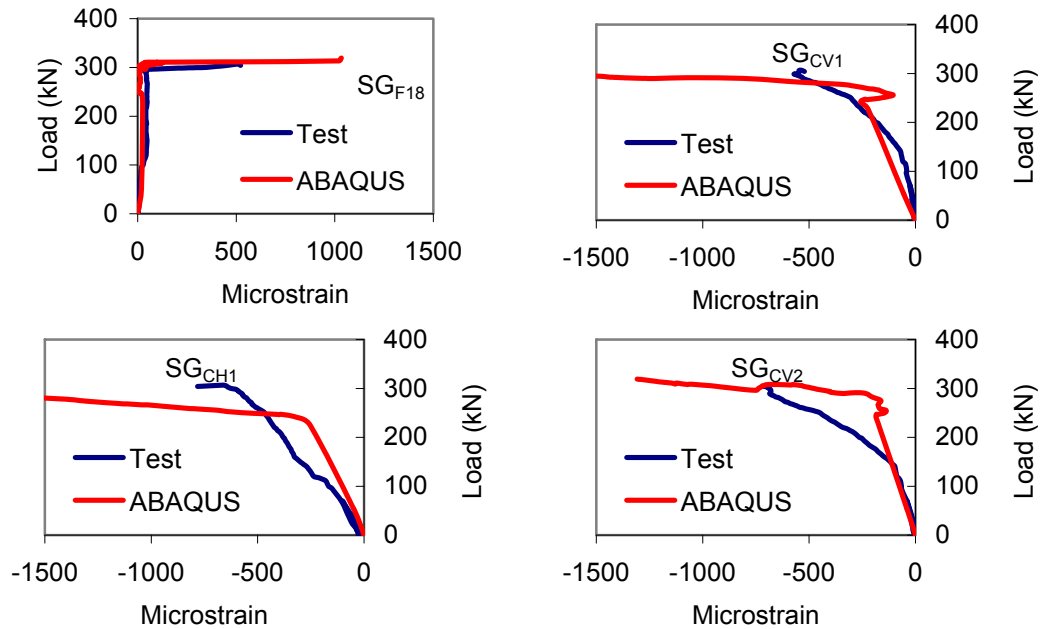


Figure B-4: Predicted strains compared to measured strains of slab (RS-F<sub>30</sub>).

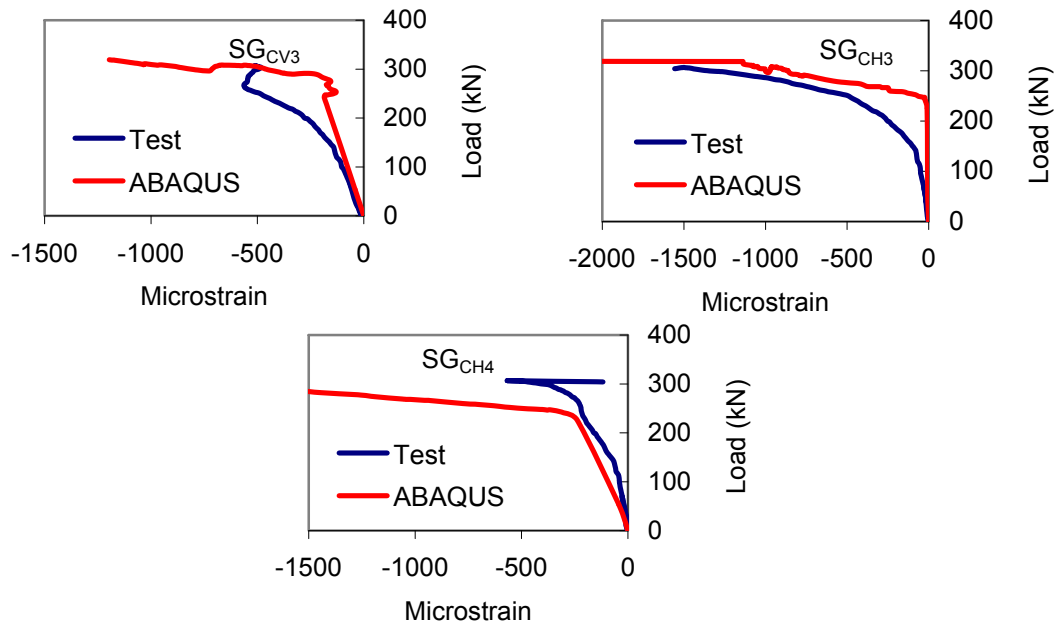


Figure B-4: Predicted strains compared to measured strains of slab (RS-F<sub>30</sub>).

## Test results of slab (RS-F<sub>30F</sub>)

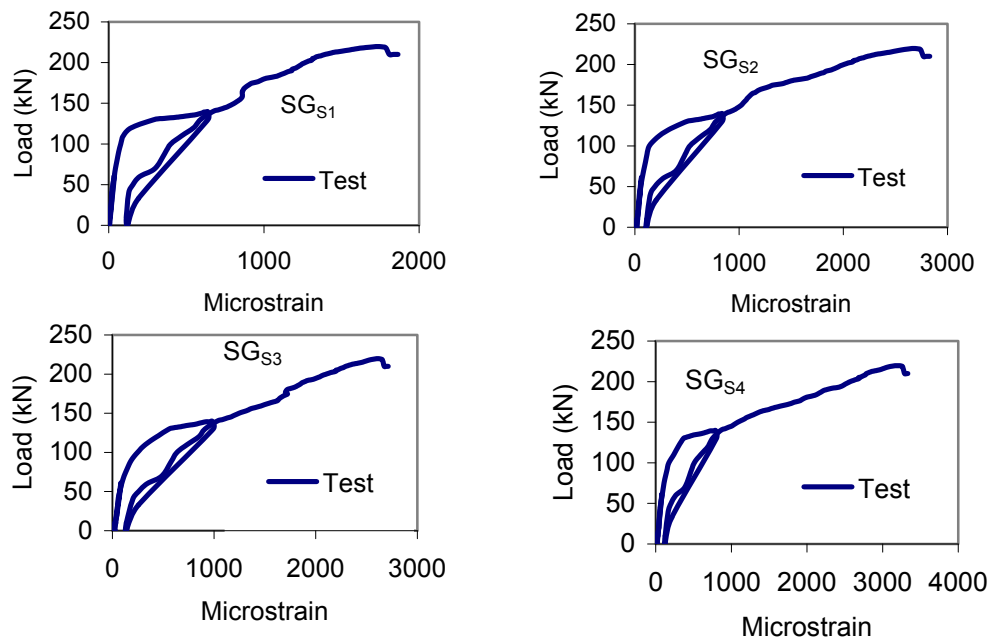


Figure B-5: Measured strains of slab (RS-F<sub>30F</sub>).

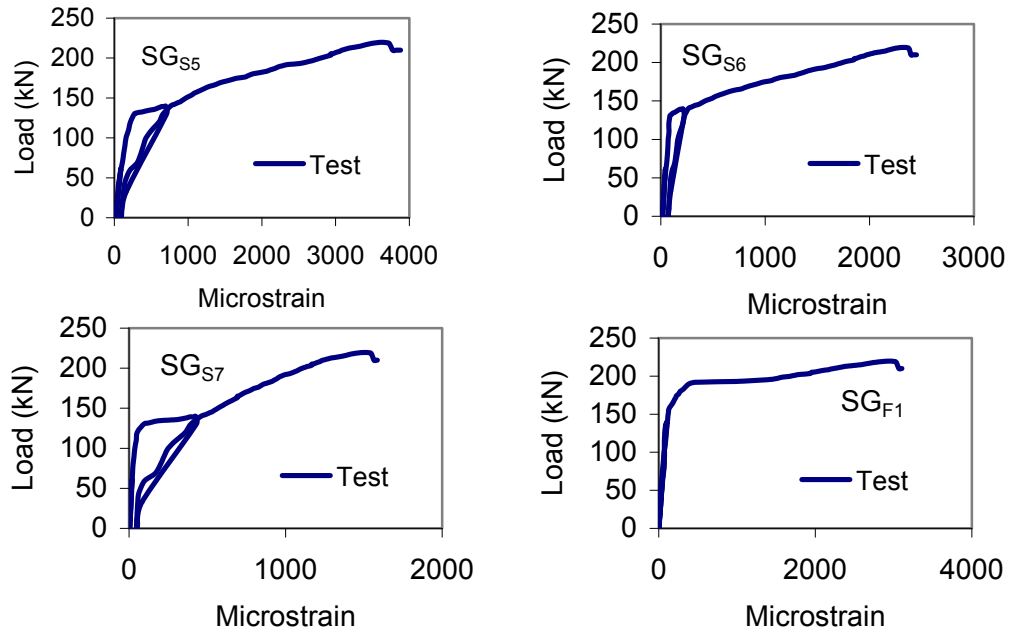


Figure B-5: Measured strains of slab (RS-F<sub>30F</sub>).

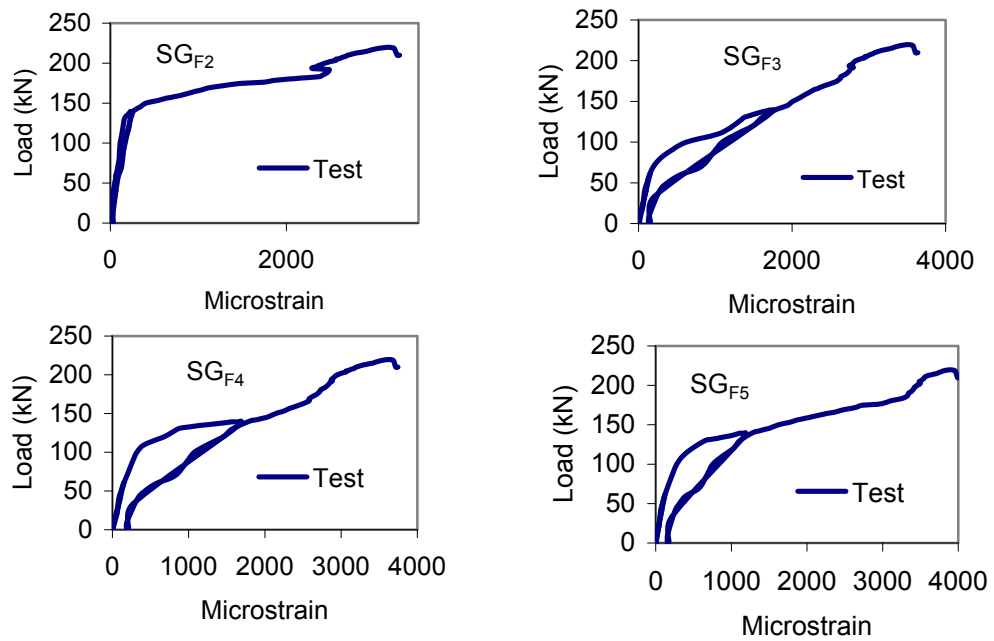


Figure B-5: Measured strains of slab (RS-F<sub>30F</sub>).

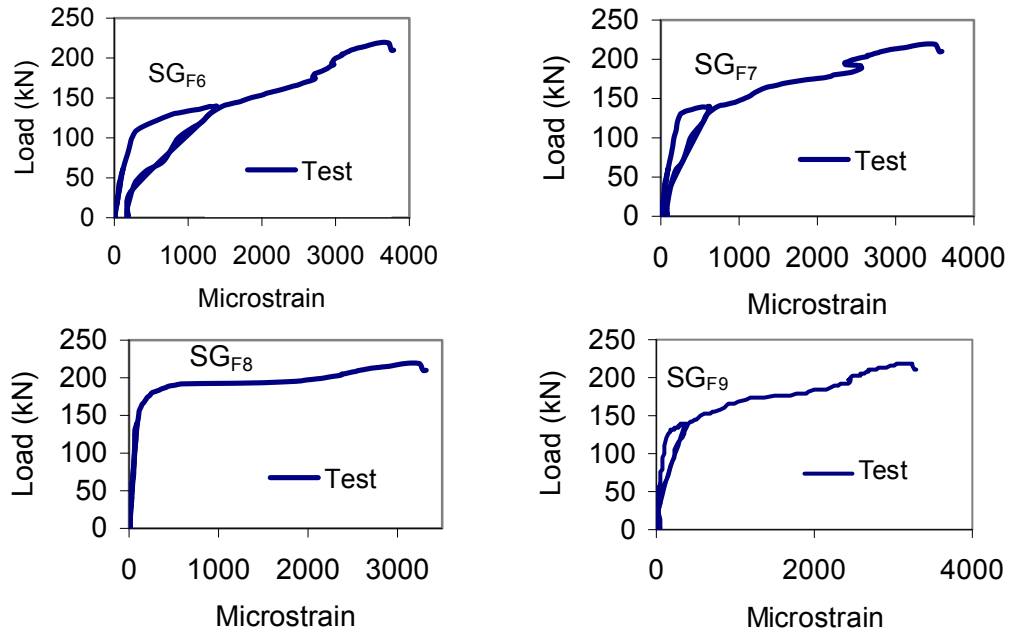


Figure B-5: Measured strains of slab (RS-F<sub>30F</sub>).

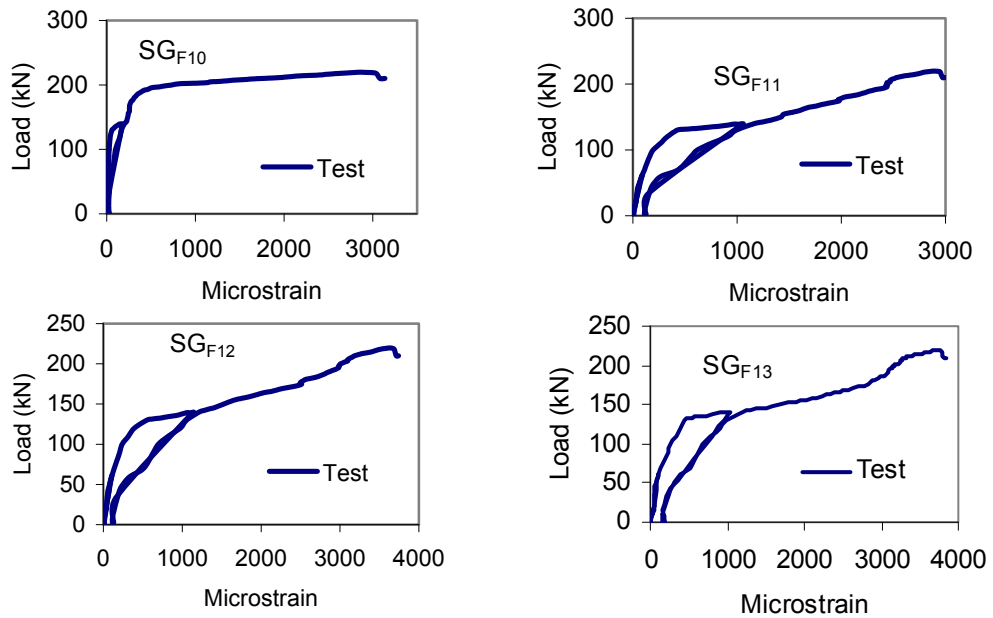


Figure B-5: Measured strains of slab (RS-F<sub>30F</sub>).

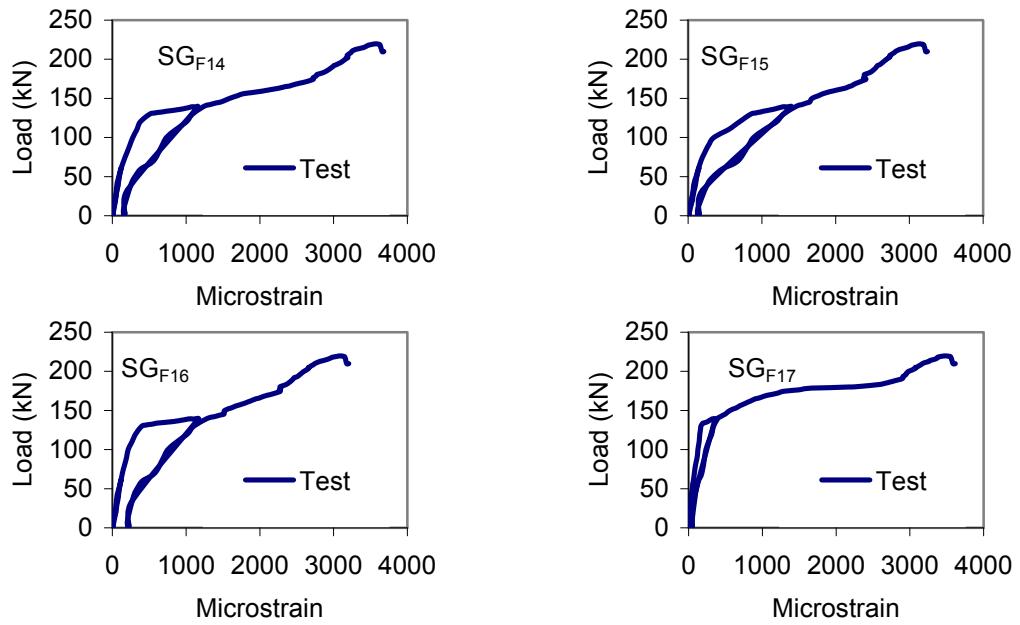


Figure B-5: Measured strains of slab (RS-F<sub>30F</sub>).

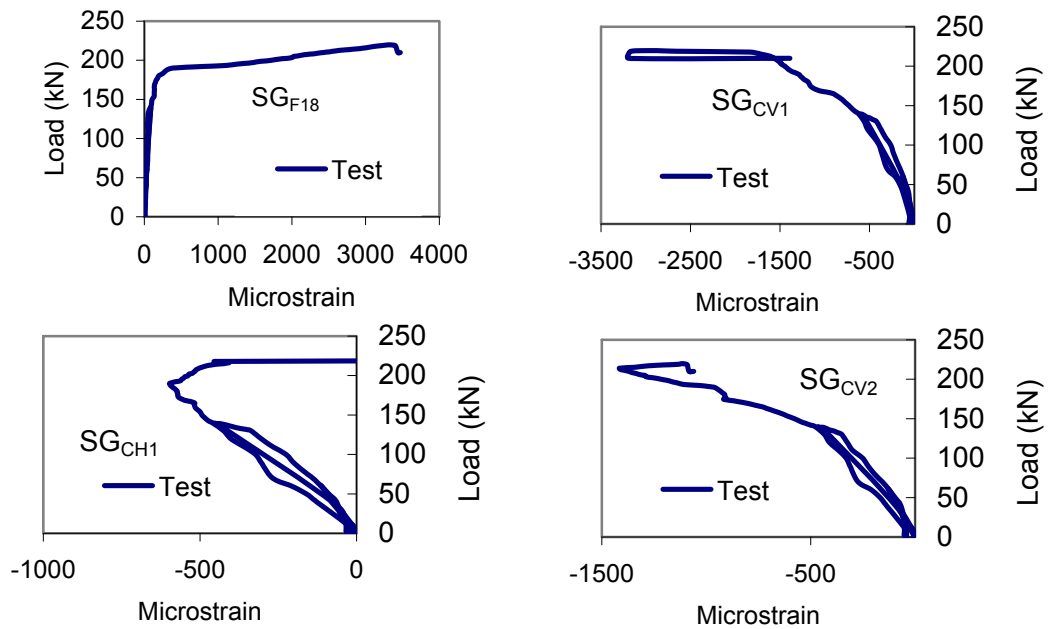


Figure B-5: Measured strains of slab (RS-F<sub>30F</sub>).

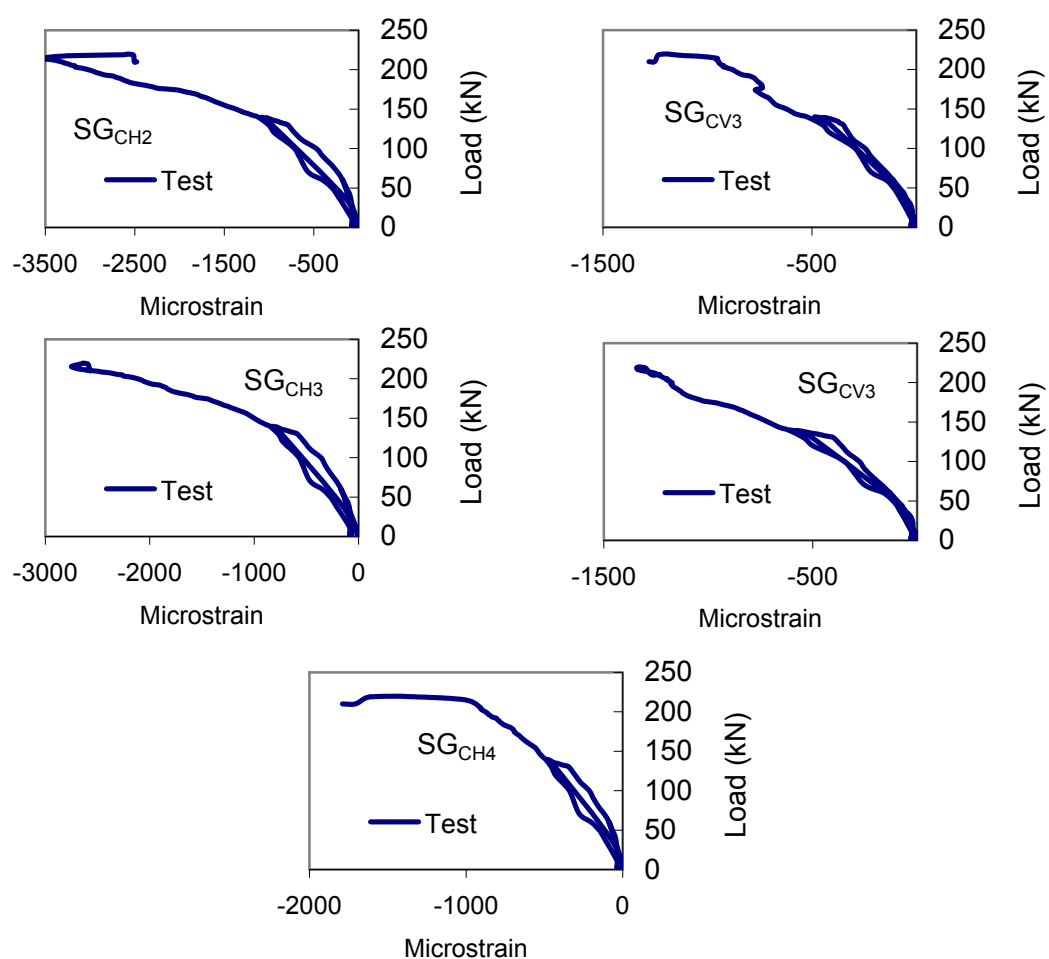


Figure B-5: Measured strains of slab (RS-F<sub>30F</sub>).

## Crack pattern of slab (RS<sub>0</sub>)

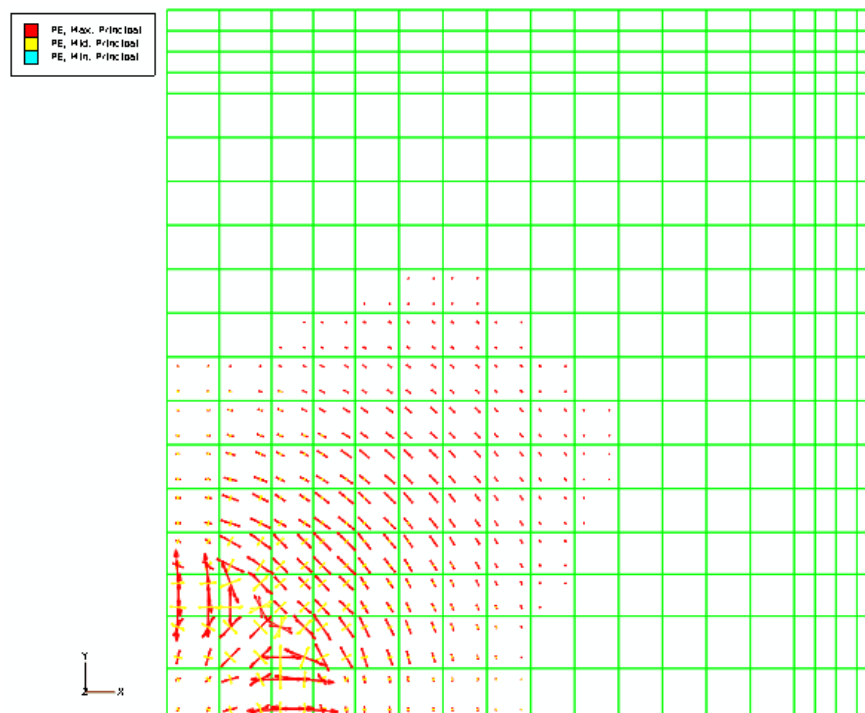


Figure B-6: Crack pattern of slab (RS<sub>0</sub>) at predicted cracking load 91.5 kN.

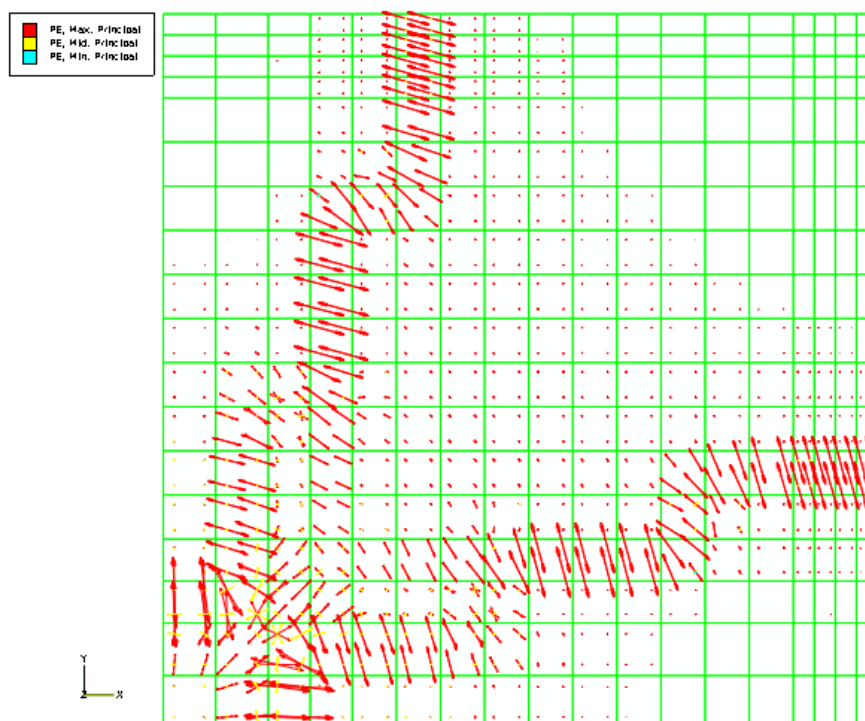


Figure B-7: Crack pattern of slab (RS<sub>0</sub>) at predicted load 95.2 kN.

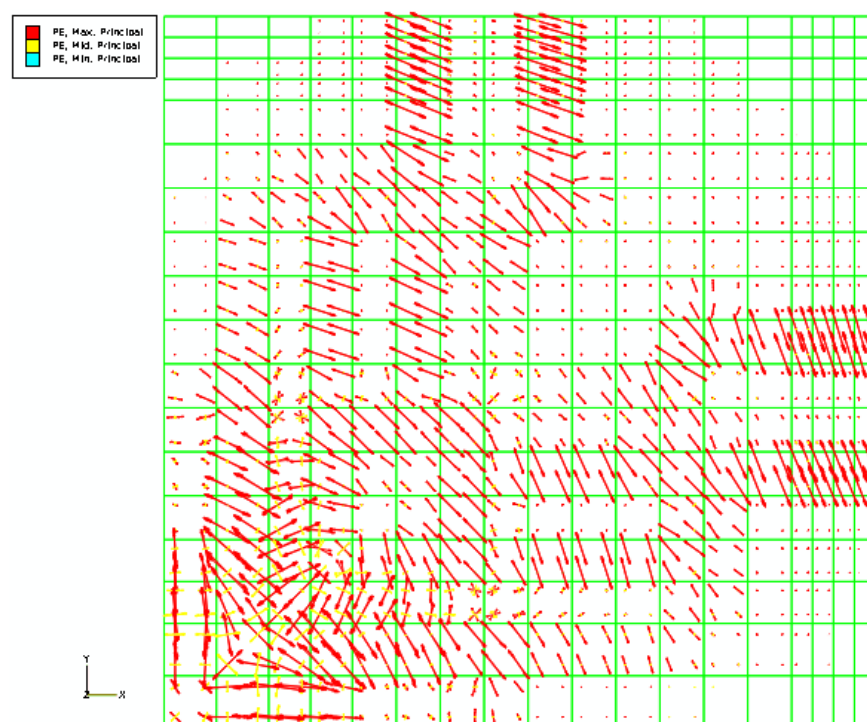


Figure B-8: Crack pattern of slab (RS<sub>0</sub>) at predicted load 138.5 kN.

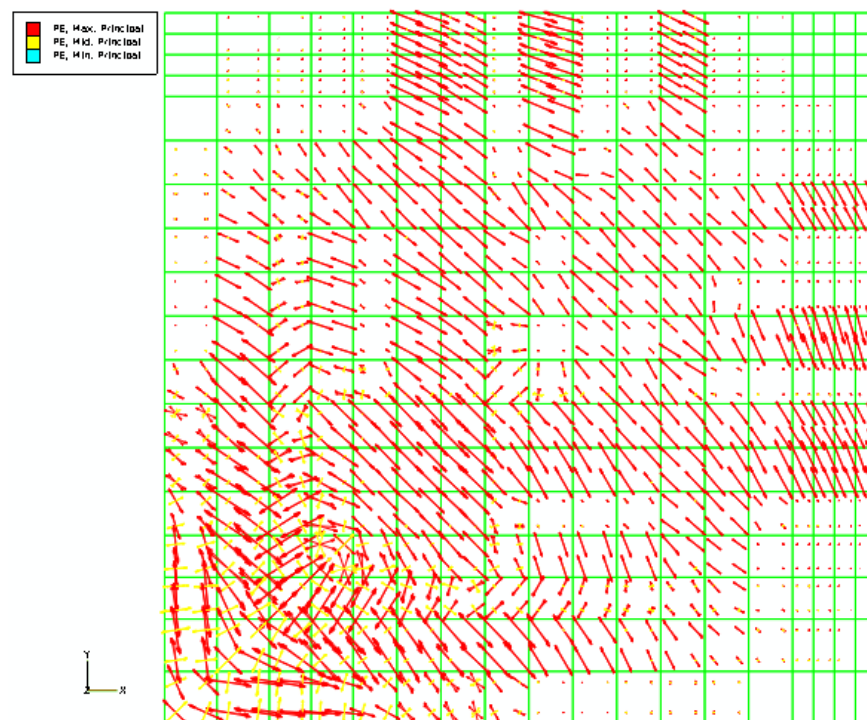


Figure B-9: Crack pattern of slab (RS<sub>0</sub>) at predicted load 202.1 kN.



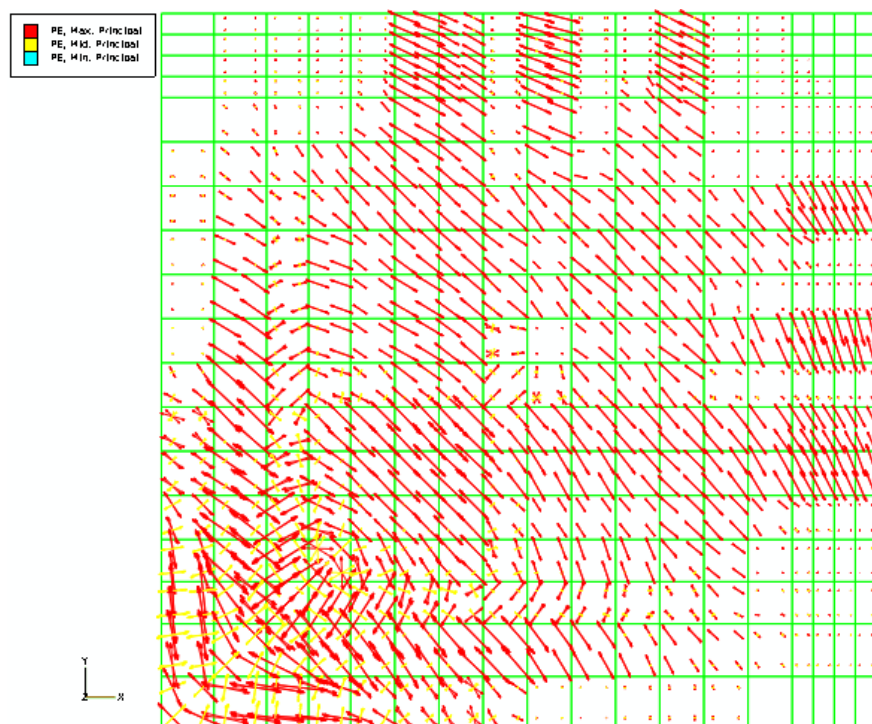


Figure B-10: Crack pattern of slab (RS<sub>0</sub>) at predicted failure load 226.75 kN.

## Crack pattern of slab (RS-F<sub>0</sub>)

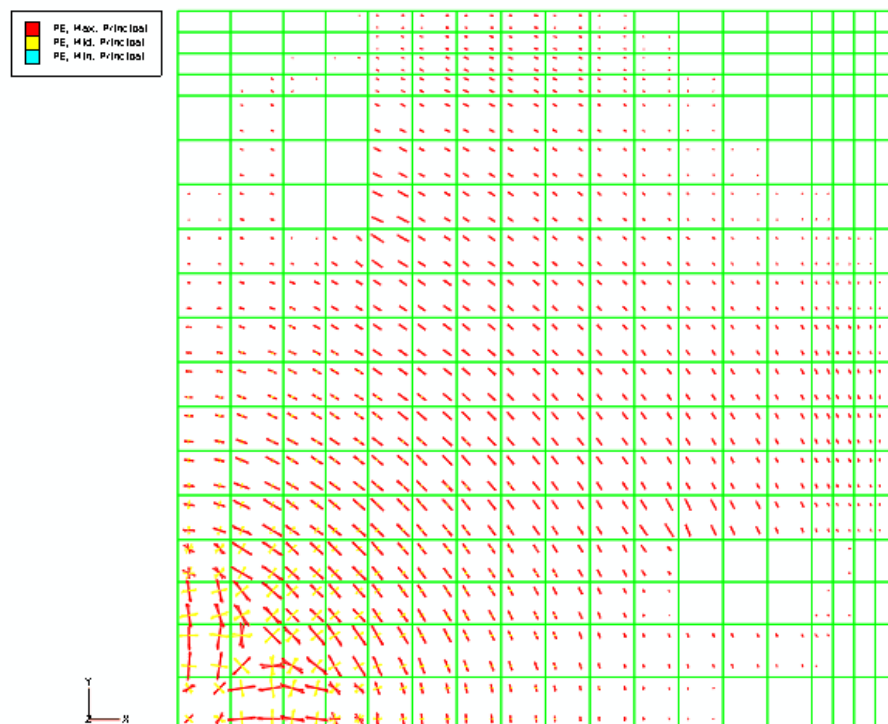


Figure B-11: Crack pattern of slab (RS-F<sub>0</sub>) at cracking load 106.3 kN.

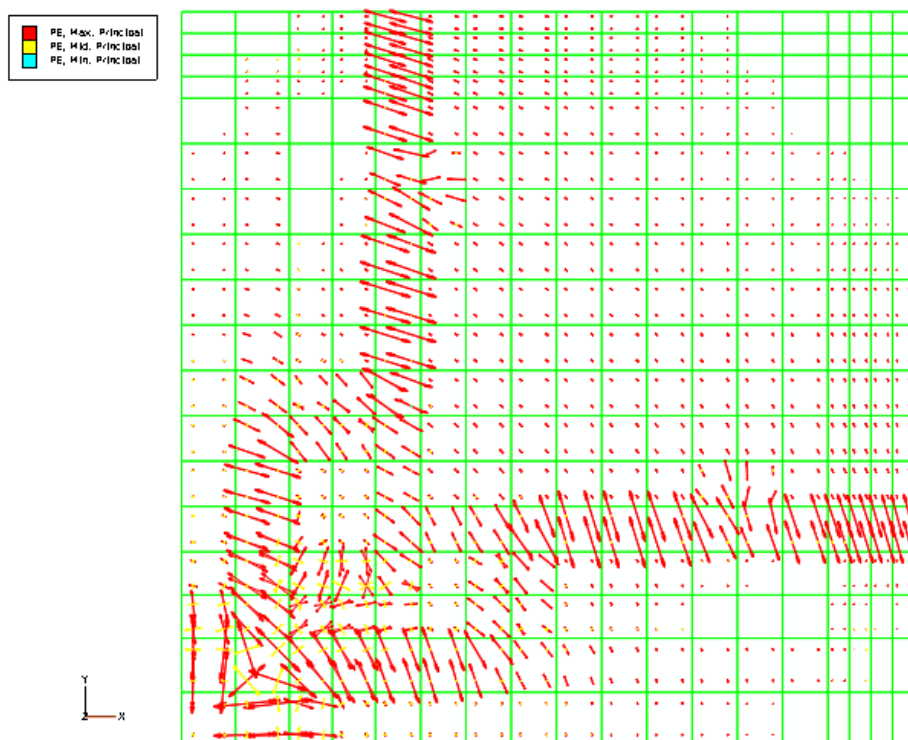


Figure B-12: Crack pattern of slab (RS-F<sub>0</sub>) at load 113.9 kN.

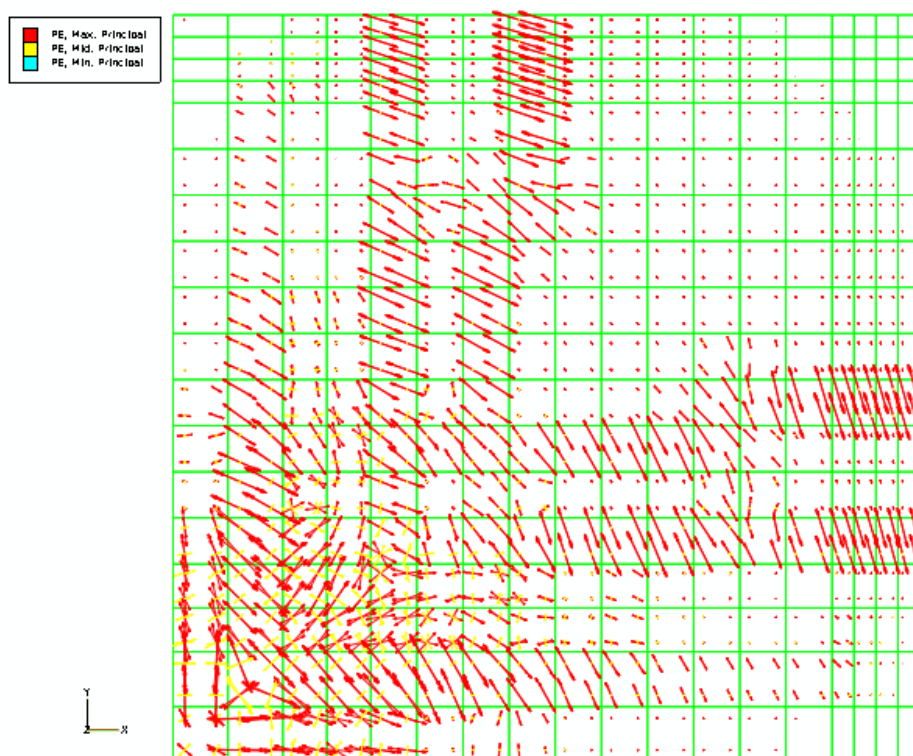


Figure B-13: Crack pattern of slab (RS-F<sub>0</sub>) at load 150.1 kN.

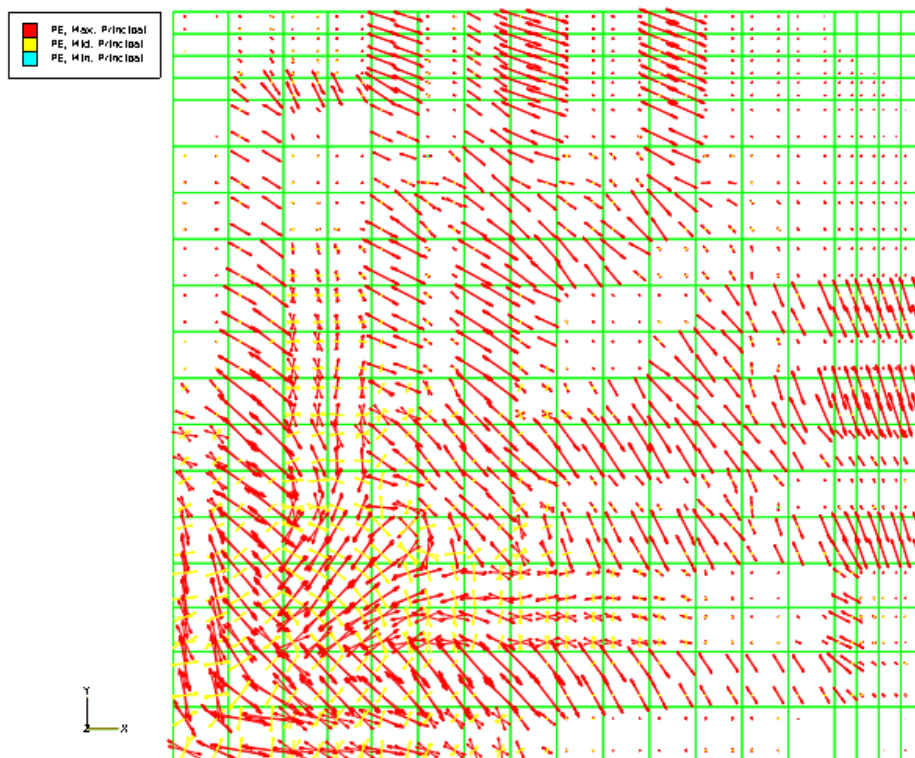


Figure B-14: Crack pattern of slab (RS-F<sub>0</sub>) at load 236 kN

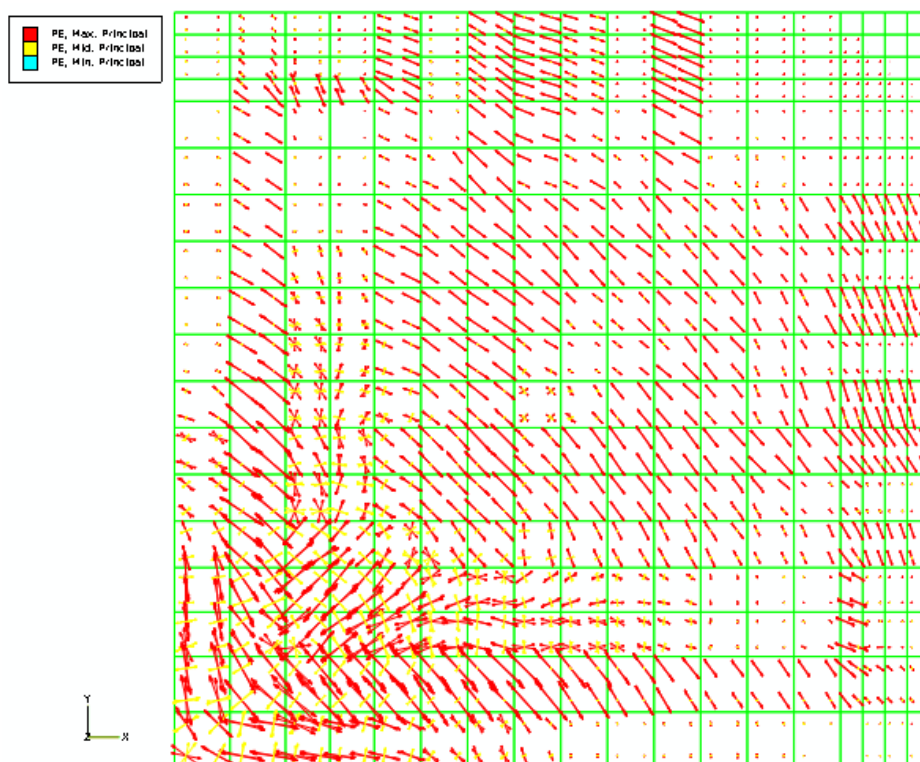


Figure B-15: Crack pattern of slab (RS-F<sub>0</sub>) at load 329.7 kN.

## Crack pattern of slab (RS-F<sub>15</sub>)

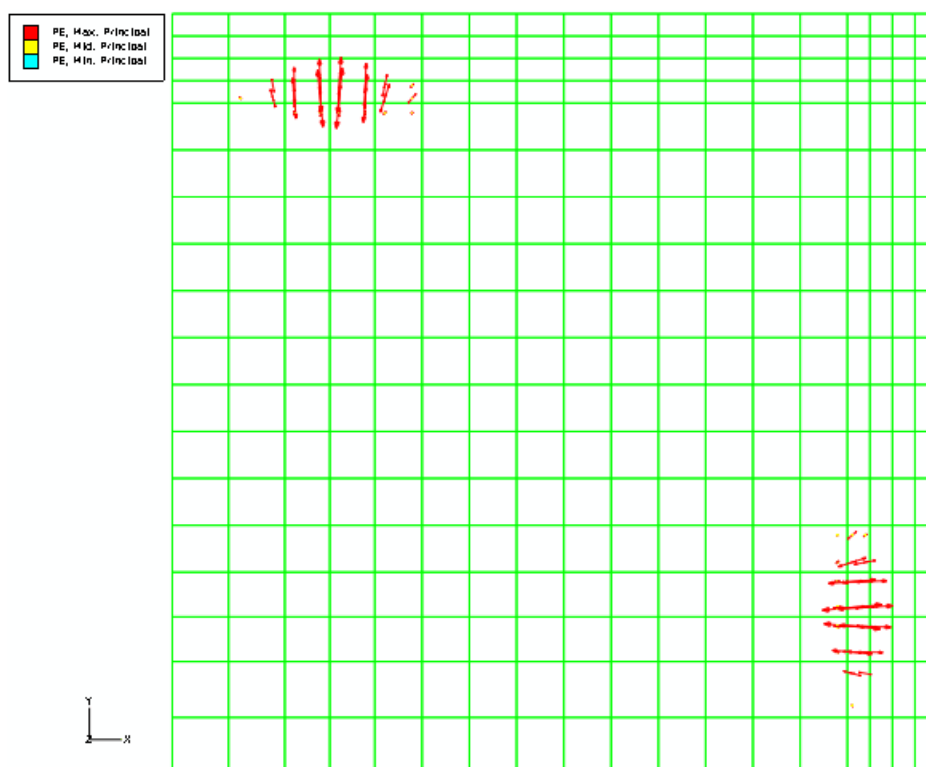


Figure B-16: Crack pattern of slab (RS-F<sub>15</sub>) at zero kN.

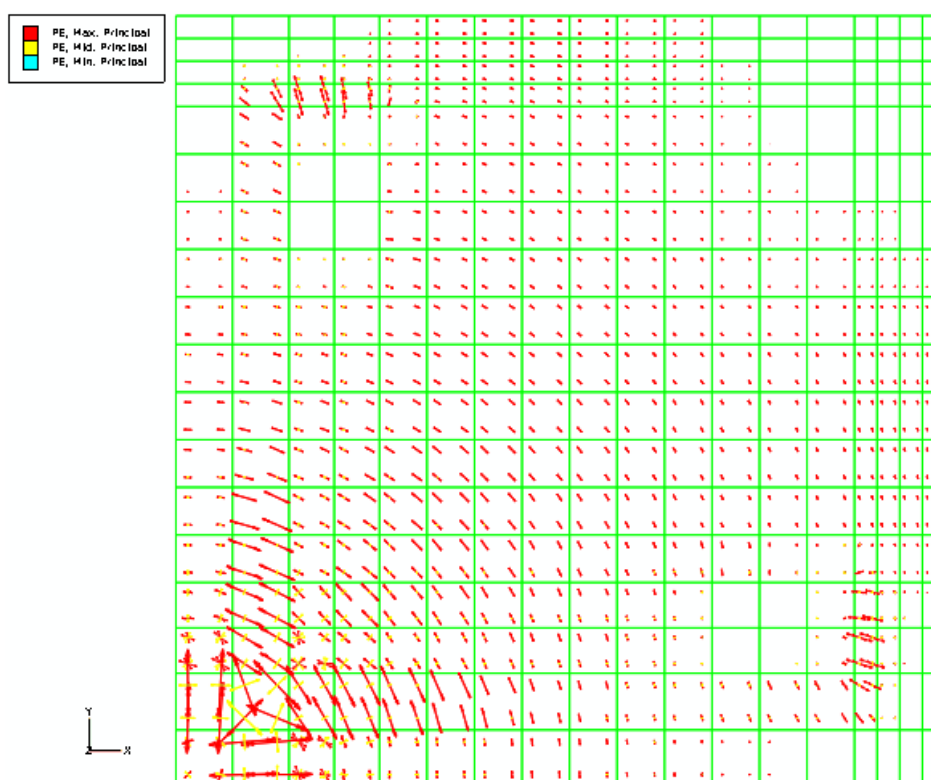


Figure B-17: Crack pattern of slab (RS-F<sub>15</sub>) at cracking load 141.7 kN.

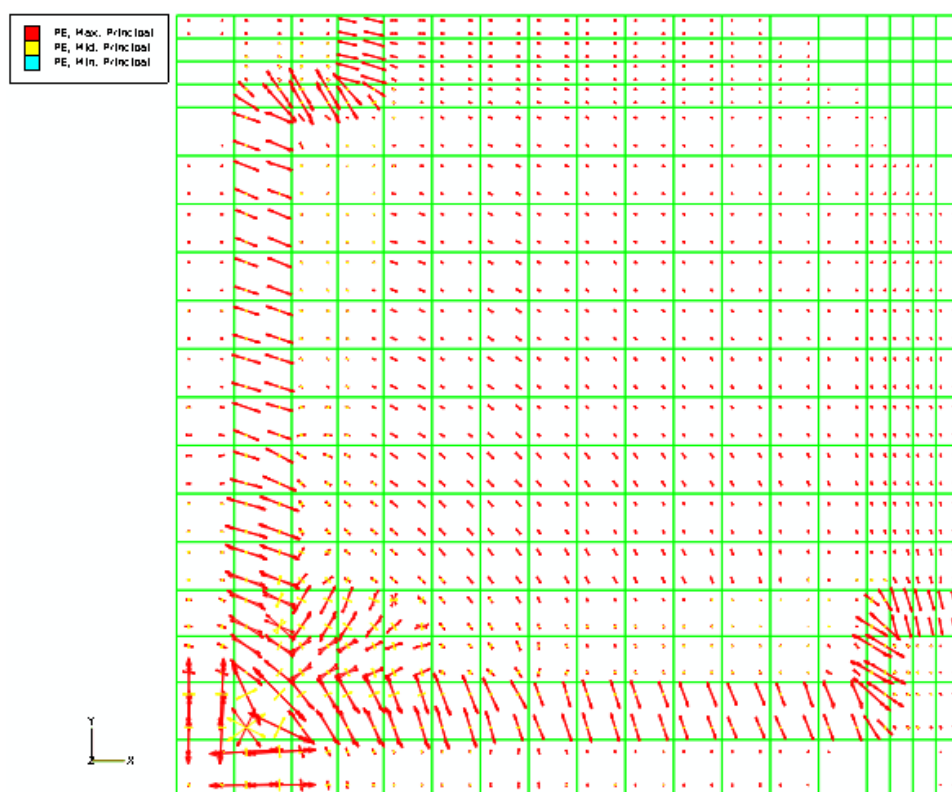


Figure B-18: Crack pattern of slab (RS-F<sub>15</sub>) at load 155.6 kN.

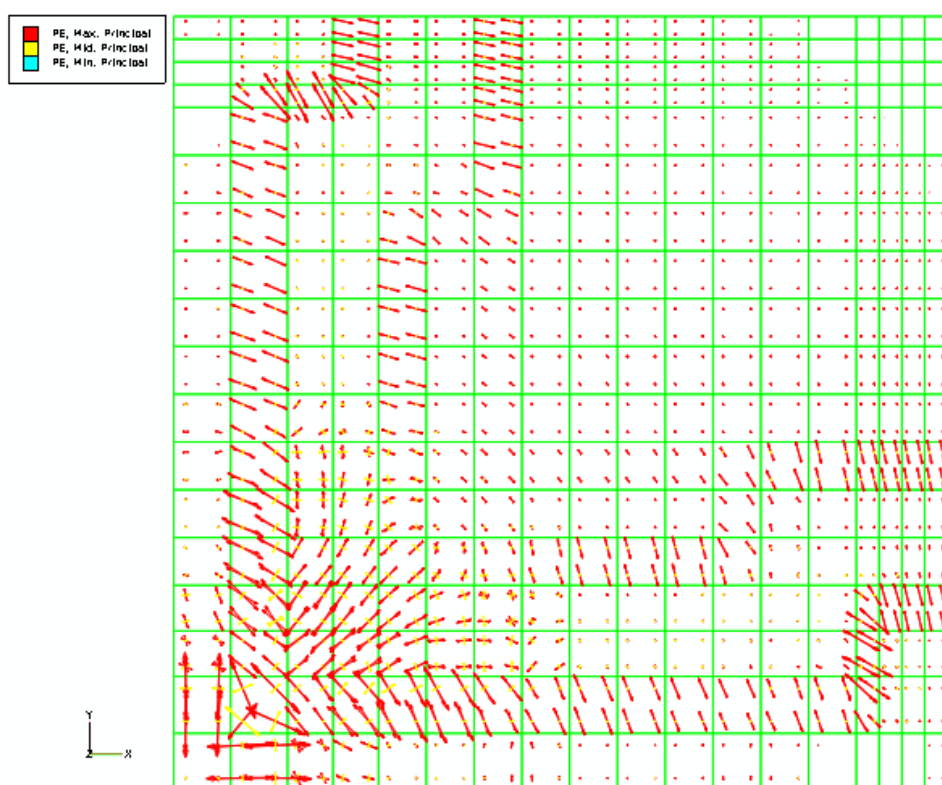


Figure B-19: Crack pattern of slab (RS-F<sub>15</sub>) at load 159.3 kN

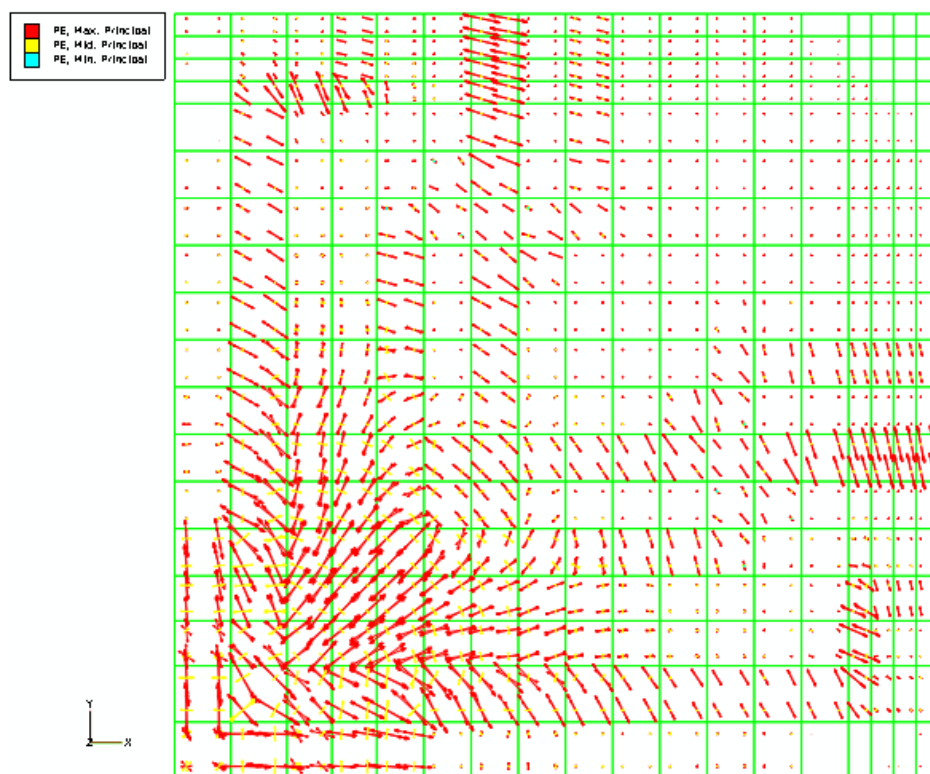


Figure B-20: Crack pattern of slab (RS-F<sub>15</sub>) at load 206.8 kN.

## Crack pattern of slab (RS-F<sub>30</sub>)

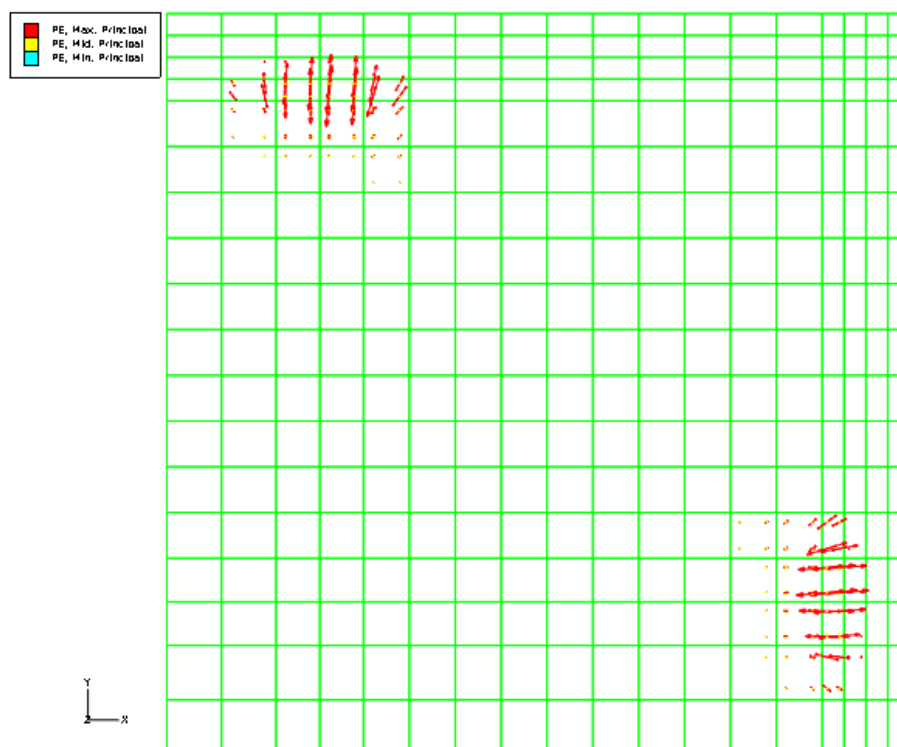


Figure B-21: Crack pattern of slab (RS-F<sub>30</sub>) at zero kN.



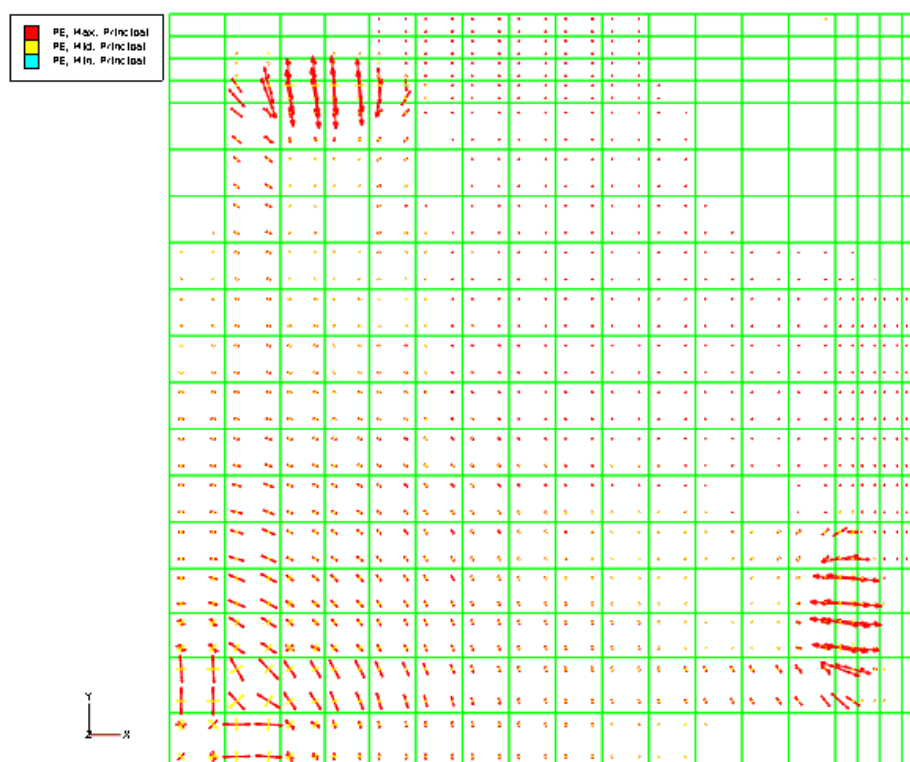


Figure B-22: Crack pattern of slab (RS-F<sub>30</sub>) at cracking load 225.7 kN.

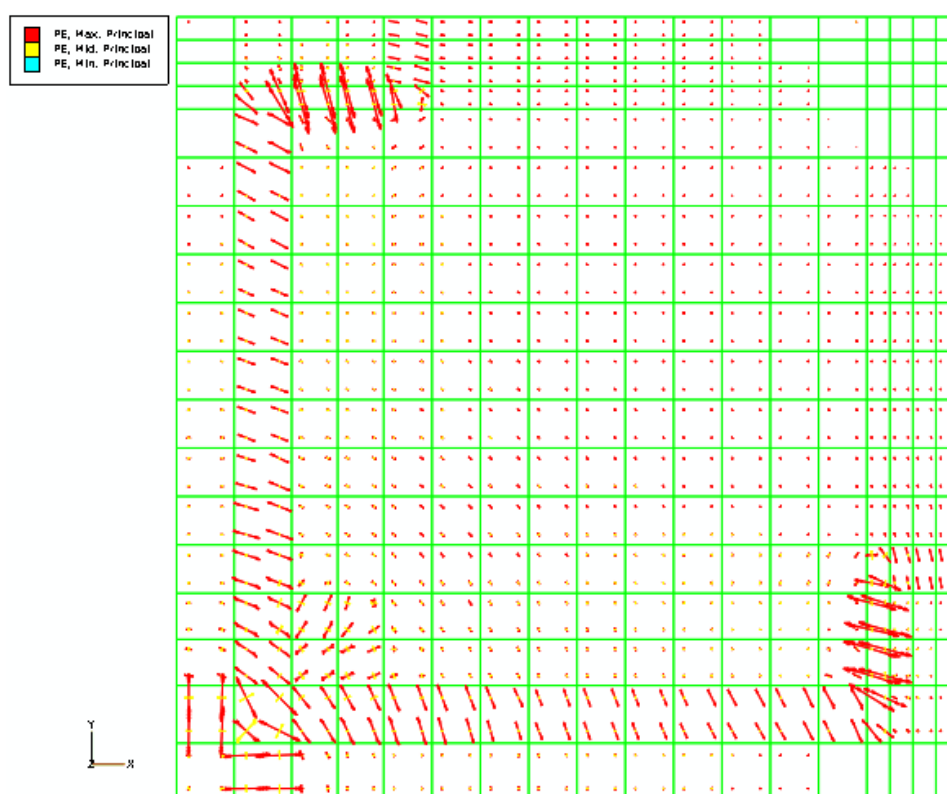


Figure B-23: Crack pattern of slab (RS-F<sub>30</sub>) at load 247.9 kN.

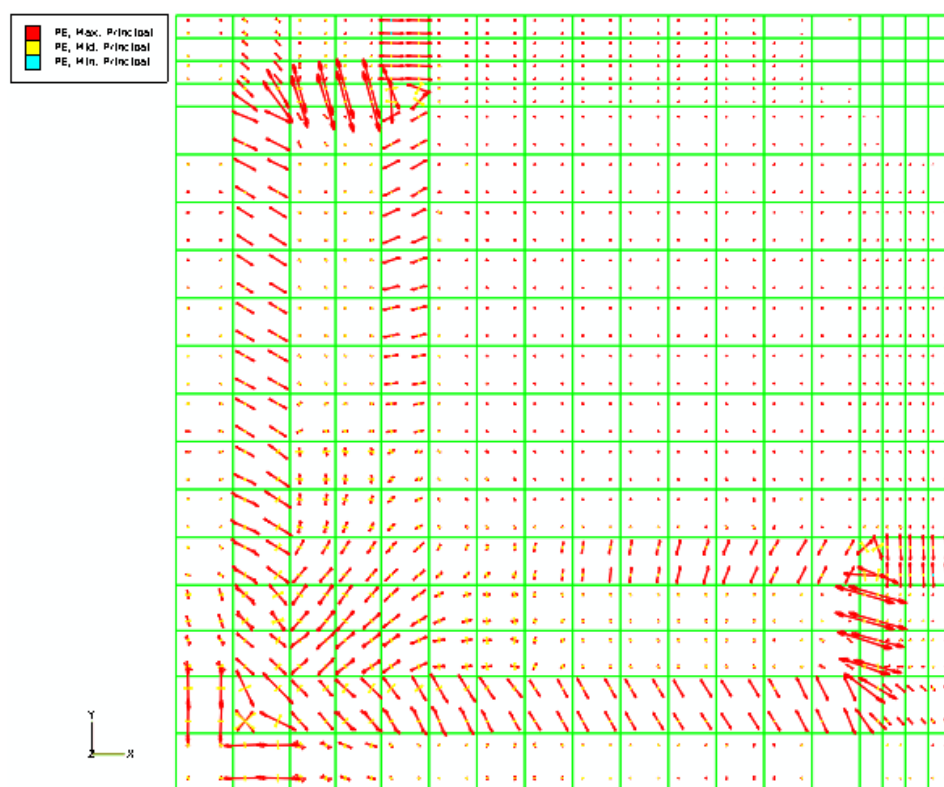


Figure B-24: Crack pattern of slab (RS-F<sub>30</sub>) at load 260 kN

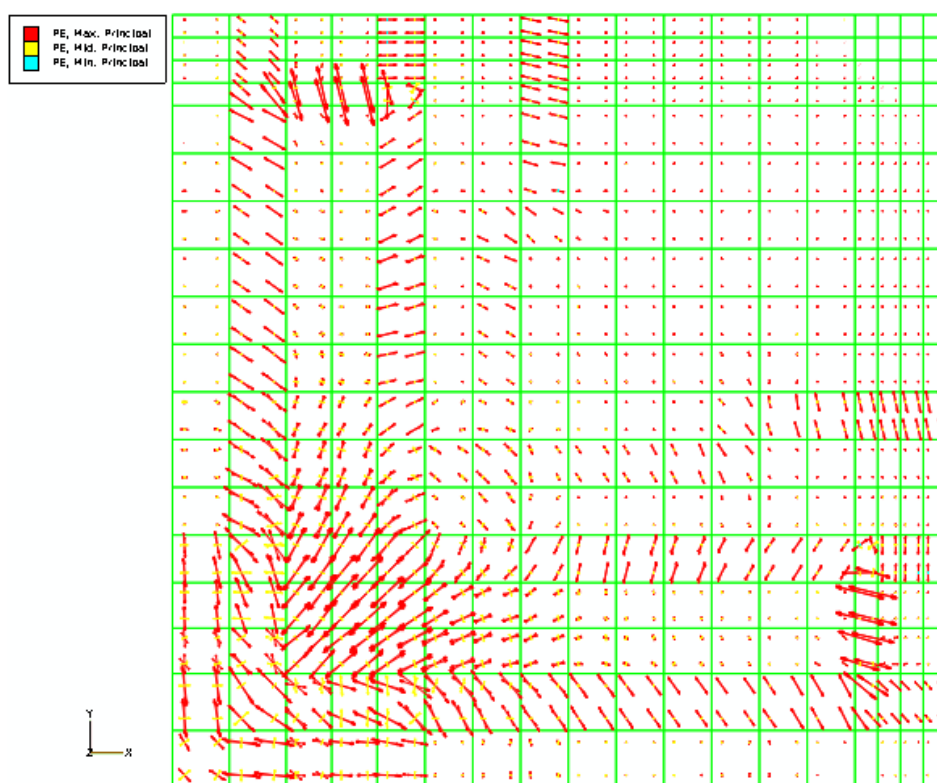


Figure B-25: Crack pattern of slab (RS-F<sub>30</sub>) at load 291.4 kN.